How To Build A Cluster

The formation and evolution of galaxies in high-redshift clusters and protoclusters

Elizabeth Anne Cooke

The University of Nottingham

Thesis submitted to the University of Nottingham
for the degree of Doctor of Philosophy, May 2016

"If a man ascended into heaven and gazed upon the whole workings of the universe and the beauty of the stars, the marvellous sight would give him no joy if he had to keep it to himself."

– Marcus Tullius Cicero

Supervisor: Dr. Nina Hatch

Examiners: Dr. Sean McGee *University of Birmingham*

Prof. Alfonso Aragón-Salamanca *University of Nottingham*

Abstract

High redshift galaxy protoclusters are the precursors of today's massive clusters; the sites of formation of the most massive galaxies in the present-day Universe. By studying these immature structures we can directly analyse the formation of galaxies in the densest environments without relying on extrapolations from low redshift. Finding protoclusters is challenging due to the need for very wide and deep surveys. Radio-loud active galactic nuclei (RLAGN) have been shown to preferentially reside in overdense environments at $z > 1$. By using these bright radio sources as beacons, protoclusters may be efficiently selected, without the need for large, blind surveys. In this thesis I study the properties of galaxies in high redshift ($z > 1.3$) clusters and protoclusters selected around RLAGN.

Using a sample of 37 clusters and protoclusters from the Clusters Around Radio-Loud AGN (CARLA) survey, I show that the protocluster galaxies have an approximately unevolving, red observed-frame $i' - [3.6]$ colour across $1.3 < z < 3.2$. This is at odds with the simple models which are commonly used to explain the cluster red sequence in the local Universe, which predict cluster galaxy colours to become more blue at higher redshifts. Taking the full cluster population into account, I show that the formation of stars within the majority of massive cluster galaxies occurs over at least 2 Gyr, and peaks at $z \sim 2$–3. This is consistent with the cosmic star formation history, with star formation ending in clusters at $1 < z < 2$. I further show that massive galaxies at $z > 2$ must have assembled within 0.5 Gyr of them forming a significant fraction of their stars. This means that few massive galaxies in $z > 2$ protoclusters could have formed via dry mergers.

Some of the CARLA structures exhibit signs of being mature, collapsed clusters. In a pilot project, I report on the discovery of a $z = 1.58$ cluster with a strong red sequence

around the RLAGN 7C 1753+6311. I demonstrate that the cluster has an enhanced quiescent galaxy fraction that is three times that of the control field. I also show that this enhancement is mass dependent: $91 \pm 9\%$ of the $M_* > 10^{10.5}\,\mathrm{M}_\odot$ cluster galaxies are quiescent, compared to only $36 \pm 2\%$ of field galaxies, whereas the fraction of quiescent galaxies with lower masses is the same in the cluster and field environments. This is in contrast to low redshift studies which have shown that mass and environmental effects on quenching star formation are separable.

In the literature there is some debate as to whether RLAGN preferentially reside in clusters of a certain stage of collapse. The presence of a dense core and a well-formed, quiescent red sequence suggest that 7C 1753+6311 resides within a mature cluster. This means that distant RLAGN do not solely reside in young, uncollapsed protoclusters, rather they can be found in clusters in a wide range of evolutionary states.

Finally I present results from surveys of Hα emitters in the fields around three high redshift RLAGN. I find that there is more dust-obscured star formation in protocluster galaxies than in similarly-selected control field galaxies at $z \sim 2.5$ and there is tentative evidence of a higher fraction of starbursting galaxies in the denser environment. However, on average I do not find a difference between the star formation rate (SFR)-mass relations of the protocluster and field galaxies and so conclude that the SFR of these galaxies at $z \sim 2.5$ is governed predominantly by galaxy mass and not the host environment. The stellar mass distribution of the protocluster galaxies is also skewed towards higher masses and there is a significant lack of low mass ($M < 10^{10} M_\odot$) galaxies within the protocluster core.

These results have implications for future protocluster surveys. The lack of low mass galaxies affects the level of overdensity which is detected. If only high mass galaxies are considered, the density of the protocluster field may be over-estimated. This means that it is important when quantifying protoclusters to compare their mass functions, rather than simply number overdensities. I also find that some radio galaxies do not reside in the centre, or densest region of the surrounding structure, meaning the overdensity measured in an aperture centred on the RLAGN will be underestimated. This means that future studies of (proto)clusters around RLAGN should use larger fields of view in order to establish the existence of a (proto)cluster.

Published work

The work presented in this thesis has been published in the following papers:

(i) Cooke E. A., Hatch N. A., Muldrew S. I., Rigby E. E., Kurk J. D., 2014, *A $z = 2.5$ protocluster associated with the radio galaxy MRC 2104−242: star formation and differing mass functions in dense environment*, MNRAS, 440, 3262.

(ii) Muldrew S. I., Hatch N. A., Cooke E. A., 2015, *What are protoclusters? - Defining high-redshift galaxy clusters and protoclusters*, MNRAS, 452, 2528.

(iii) Cooke E. A., Hatch N. A., Rettura A., Wylezalek D., Galametz A., Stern D., Brodwin M., Muldrew S. I., Almaini O., Conselice C. J., Eisenhardt P. R., Hartley W. G., Jarvis M., Seymour N., Stanford S. A., 2015, *The formation history of massive cluster galaxies as revealed by CARLA*, MNRAS, 452, 2318.

(iv) Cooke E. A., Hatch N. A., Stern, D., Rettura, A., Brodwin, M., Galametz, A., Wylezalek, D., Bridge, C., Conselice, C. J., De Breuck, C., Gonzalez, A. H., Jarvis, M., 2016, *A mature galaxy cluster at $z = 1.58$ around the radio galaxy 7C 1753+6311*, ApJ, 816, 83.

(v) Cooke E. A., Hatch N. A., Kurk J. D., Best P., Muldrew S. I., *Hα emitters in $z \sim 1.6$ protoclusters*, in preparation.

Chapter 2 contains material published in Paper iii. Chapter 3 is based on material published in Paper iv. The contents of Paper i, with contributions from Paper ii, are described in Chapter 4. Finally, Chapter 5 describes work which will appear in Paper v.

The work presented in this thesis was performed by the author, with advice from the coauthors listed above. Where material is taken from the literature, this is mentioned explicitly in the relevant chapter. Some figures have been adapted from papers for which the author is a contributor, this is mentioned explicitly in the relevant figure captions.

Acknowledgements

At the very start of this I want to thank Nina. For all your patience and commitment and the fun you brought to my whole Ph.D. I am incredibly grateful. Even if you are still wrong about the best type of cake.

To my family and friends—thank you for pretending to understand what I've been talking about, and bonus points to Dad for actually proof-reading some of this thesis for me. Mum—thank you for always being interested and looking through the telescope, or at the pictures, even when it was just "fuzzy blobs". Dave—thank you for helping me with all my coding problems and providing the best suggestions for what to do whilst stuck up a mountain in the rain. Thank you to those people who encouraged me to do a Ph.D. and, once started, to continue; in particular Cat, Claire, Rachel, Annie and the Cake Time crew from St Andrews.

I am very grateful for all the financial support I have received to attend conferences and observing trips from the Royal Astronomical Society and the Nottingham Astronomy group, and to the Science Technology Facilities Council for my Ph.D. funding. To Simon and Meghan in particular—thank you for continuing to sign off on all my many observing runs.

And finally, thank you to my office mates, and others throughout the department—Evelyn, Lyndsay, Ross, Carl, James, KK, Berta, Martha, Rachel, Becky, Miguel (and the coffee club)—for providing useful conversations, answering (stupid) questions and being willing to be distracted from work for a while.

Contents

List of Figures

List of Tables

How To Build A Cluster

The formation and evolution of galaxies in high-redshift clusters and protoclusters

Chapter 1

Introduction

1.1 Galaxy clusters

The Universe is arranged in a tangle of dark matter and baryonic matter in the form of gas, dust and stars. From tiny fluctuations at the beginning of the Universe, structure evolved under gravity's influence and in today's Universe is observed in the form of a web of intersecting filaments and sheets. At the intersections, the densest parts of the Universe, galaxy clusters formed. These galaxy clusters are the most massive collapsed structures in the Universe and are excellent laboratories for a wide variety of physical studies, including galaxy evolution, cosmology and gas physics. Before the 1980s the extent of our knowledge of clusters extended to just $z \sim 0.2$ (Abell, 1958). Now we are pushing the study of these massive structures out to higher and higher redshifts: the furthest confirmed cluster is at $z \sim 2$ at the time of writing (Gobat *et al.*, 2011). We also now have increasingly larger samples of clusters. This has allowed for measurements of the cluster mass function and its evolution with redshift, providing constraints on cosmological parameters such as Ω_M and σ_8 (e.g. Bahcall *et al.*, 2003; Benson *et al.*, 2013). These larger samples are also increasing our ability to statistically measure the effects of a cluster environment on its member galaxies, minimising the effects of cluster-to-cluster variation. At redshifts higher than $z \sim 1.5$, the number of known collapsed *clusters* rapidly decreases and the study of clusters and the evolution of their member galaxies turns to the progenitors of today's massive collapsed structures: protoclusters.

1.1.1 Clusters at $z \lesssim 0.3$

Clusters are comprised of massive dark matter haloes, dominating the total mass budget, with a hot gas intracluster medium (ICM), galaxies and free-floating stars that have been stripped from their hosts. Though galaxies represent only $\sim 2\%$ of the mass budget of clusters, they emit the majority of the visible light. Thus our initial observations of clusters were focused on their member galaxies.

Early cluster studies noticed very quickly that the populations of galaxies in clusters were different to those in the field. Hubble noted elliptical "nebulae" and early-type spirals were more common in the Virgo cluster than in the field (Hubble & Humason, 1931). Dressler (1980) revealed clear trends of increasing elliptical and S0 fractions, and decreasing spiral fractions, with increasing local density. Giovanelli, Haynes & Chincarini (1986) confirmed these trends with a large study of morphological types as a function of a range of environments. Cluster galaxies are also on average more massive than the general galaxy population (e.g. Kauffmann *et al.*, 2004; Bamford *et al.*, 2009), although are similar in size (e.g. Weinmann *et al.*, 2009; Guo *et al.*, 2009; Nair, van den Bergh & Abraham, 2010; Huertas-Company *et al.*, 2013, see also Valentinuzzi *et al.* 2010).

In addition to morphological and mass differences, cluster galaxies contain different stellar populations from field galaxies. Cluster galaxies are more red in colour (e.g. Balogh *et al.*, 2004; Bamford *et al.*, 2009), and are less star-forming (e.g. von der Linden *et al.*, 2010; Peng *et al.*, 2010). They have older stellar populations (e.g. Smith *et al.*, 2006; Cooper *et al.*, 2010), even when compared as a function of galaxy type: Terlevich & Forbes (2002) found that cluster ellipticals are older than their field counterparts by $\sim 1.9\,$Gyr.

These old, massive, early-type cluster galaxies form a tight relationship in colour-magnitude space called the "red sequence". This sequence corresponds to a relationship between stellar mass and metallicity, with metal-rich, massive galaxies residing at the bright end of the sequence (Kodama & Arimoto, 1997). The intrinsic scatter in the red sequence corresponds to the scatter in galaxy ages (Bower, Lucey & Ellis, 1992). The linearity of the red sequence means it may be characterised by its slope, scatter and zero-point (normalisation). Measurements of these parameters have shown that

the slope does not evolve with redshift, whereas the zero-point evolves to bluer colours at higher redshifts (Aragon-Salamanca *et al.*, 1993; Ellis *et al.*, 1997; Kodama, Bower & Bell, 1999).

In a hierarchical framework, the differences between cluster and field galaxies can be explained by cluster galaxies forming earlier than those in the field, and being influenced by the growth of the large-scale structure around them at early times. In hierarchical models, overdense regions form their haloes earlier on average (Gao, Springel & White, 2005), meaning galaxies within these haloes form their stars earlier than those in more average density regions (De Lucia *et al.*, 2006). However, formation time and assembly time are two different things: while present-day cluster galaxies formed their stars earlier, their assembly was not complete until much later, through many dry mergers (De Lucia *et al.*, 2006; Vulcani *et al.*, 2016).

Although much of a galaxy's final state depends on its early formation, there are also environmental effects which take place at late times. Cluster galaxies can undergo stripping of their cold gas by the ICM as they move through the intracluster gas (Gunn & Gott, 1972). Harassment from many close encounters with other cluster members can also occur (Moore, Lake & Katz, 1998), as well as mergers (Mihos & Hernquist, 1994). There are various studies showing active stripping of the gas from low mass galaxies falling into the cluster (e.g. Kenney, van Gorkom & Vollmer, 2004; Crowl *et al.*, 2005; Abramson *et al.*, 2011). The fraction of galaxies classified as S0s also increases at $z < 0.4$, corresponding to a decrease in the spiral fraction (Dressler *et al.*, 1997; Postman *et al.*, 2005; Desai *et al.*, 2007), suggesting that gas is stripped from spiral galaxies as they enter the cluster environment (e.g. Poggianti *et al.*, 2001; Jaffé *et al.*, 2011).

1.1.2 Clusters at $0.3 < z < 1$

With the advent of larger, more powerful telescopes, the study of clusters was pushed out to $z \sim 1$. Clusters at these intermediate redshifts showed very similar properties to those in the local Universe; the relative fractions of morphological types remain similar in this redshift range (Dressler *et al.*, 1997; Desai *et al.*, 2007), the colour-density relation is still in place out to at least $z \sim 1$, although weakening in significance at

higher redshifts (e.g. Cucciati *et al.*, 2006; Cooper *et al.*, 2007), and the red sequence is ubiquitous in $z < 1$ clusters (Eisenhardt *et al.*, 2008). The colour of the red sequence moves to bluer colours at higher redshifts, and the scatter and slope remain consistent with $z < 1$ measurements, all of which is consistent with red sequence galaxies evolving passively from higher redshift (e.g. Cerulo *et al.*, 2016).

In contrast to these results, some evolution in the latter half of the Universe has been observed. The first indication of evolution at higher redshifts was in the fraction of galaxies with blue colours: distant clusters had a higher fraction of blue galaxies (Butcher & Oemler, 1978, 1984). This corresponds to a higher number of star-forming galaxies in clusters at intermediate redshift compared to locally (e.g. Couch & Sharples, 1987; Saintonge, Tran & Holden, 2008). In addition, dust-obscured star formation increases in clusters from $z = 0.3$ to $z > 1$ (e.g. Alberts *et al.*, 2014).

Although the slope and scatter of the red sequence do not evolve significantly at $z < 1$, at higher redshifts ($z \sim 0.8$) the faint end of the red sequence is under-populated compared to present-day clusters, with the fraction of faint-to-luminous red galaxies in clusters increasing with decreasing redshift (e.g. De Lucia *et al.*, 2007; Rudnick *et al.*, 2009, although see Cerulo *et al.* 2016 and references therein). This means that the luminous red sequence galaxies locally were quenched earlier than those at fainter magnitudes (Muzzin *et al.*, 2012). Indeed, red sequence galaxies at $0.3 < z < 1$ have colours consistent with an early formation time ($z \sim 3$) and passive evolution (e.g. Mei *et al.*, 2009; Eisenhardt *et al.*, 2008). Late-time effects, such as ram pressure stripping, may therefore play a more prominent role in populating the faint end of the quiescent luminosity function. Some studies are now looking at transition objects, such as post-starbursts or K+A galaxies, in clusters at intermediate redshift to search for evidence of environmental effects as they are happening. Poggianti *et al.* (2009) found that the fraction of post-starburst galaxies is higher in clusters than the field by a factor of ~ 2, indicative of environmental quenching of these objects.

At low and intermediate redshifts we have an abundance of known clusters, which lend themselves to large statistical in-depth studies with incredible detail. Clusters are well-established and recognisable by $z \sim 1$, although there is still evolution: the red sequence is ubiquitous in clusters at $z < 1$, although the faint end builds up at

lower redshift; the relative fractions of early and late-types have been established, but the fraction of S0s increases at $z < 0.4$. Although much can be inferred from such studies, they indicate that the majority of cluster galaxies formed their stars at $z > 1$. It is therefore important to explore the high redshift regime in order to study galaxy formation histories in detail, at the epoch where the vast majority of their stars are being formed. Examining cluster galaxies at $z > 1$ may also reveal when trends such as the colour-density relation or the red sequence, seen ubiquitously in the second half of the Universe, appeared.

1.1.3 High redshift clusters

To probe the formation history of cluster galaxies at the epoch where they form the majority of their stars, we need to observe them at $z > 1$. At these redshifts the number of confirmed clusters rapidly decreases to a handful and we enter the regime of protoclusters.

Historically $z > 1$ clusters were hard to find due to the amount of telescope power required. We now have several large surveys at $1 < z < 1.5$: the *XMM* Distant Cluster Project (XDCP; Fassbender *et al.*, 2011), the *Spitzer* Adaptation of the Red-sequence Cluster Survey (SpARCS; Muzzin *et al.*, 2009), the Gemini Cluster Astrophysics Spectroscopic Survey (GCLASS; Muzzin *et al.*, 2012), and the IRAC Shallow (and Deep) Cluster Surveys (ISCS/IDCS; Eisenhardt *et al.*, 2008) to name a few. At $z > 1.5$ the samples comprise individual studies of serendipitously-discovered clusters.

At these redshifts, large cluster-to-cluster variation makes it difficult to draw broad conclusions on the properties of cluster galaxies, and often leads to conflicting results. For example, Brodwin *et al.* (2013) found that the sSFR-M_* planes of cluster and field galaxies are the same, and follow a similar evolution from $z = 1.5$ to $z = 1$. On the other hand, Muzzin *et al.* (2012) found that the sSFR of galaxies in clusters is systematically lower than those in the field at all stellar masses. Still, some trends from low redshift persist: cluster galaxies are redder in colour than those in the field, and the quiescent fraction is higher in clusters (e.g. Muzzin *et al.*, 2012). However, at $z > 1$, there is more star formation in cluster cores than at lower redshifts (e.g. Hilton *et al.*, 2010; Tran *et al.*, 2010; Zeimann *et al.*, 2013; Brodwin *et al.*, 2013), and the

luminosity function deviates from the passive evolution expected from lower redshift studies (Mancone *et al.*, 2010). The fraction of active galactic nuclei (AGN) increases in clusters at $z > 1$ (Galametz *et al.*, 2010a; Martini *et al.*, 2013) and there is a higher rate of merging between galaxies (Mancone *et al.*, 2010; Lotz *et al.*, 2013). There is also evidence for a reversal in the SFR-density relation (Elbaz *et al.*, 2007; Tran *et al.*, 2010), although this is still contested (Quadri *et al.*, 2012). This all points to clusters being more active at higher redshift, as we approach the epoch where they are theorised to be forming most of their galaxies.

In addition to these studies at $1 < z < 1.5$, a handful of individual clusters are known at $z > 1.5$ (e.g. Papovich *et al.*, 2010; Tanaka, Finoguenov & Ueda, 2010; Gobat *et al.*, 2011; Spitler *et al.*, 2012; Andreon *et al.*, 2014). From these, there are tentative hints that cluster galaxies are slightly more dominated by spheroid than disc galaxies (Newman *et al.*, 2014). There is also a higher quiescent fraction in the densest regions, compared to the field (Newman *et al.*, 2014). Individual clusters have been found to exhibit mature red sequences, with some studies claiming that the red sequence is populated even at the faint end (e.g. Andreon *et al.*, 2014). The scatter of the red sequence, however, may be larger than clusters at $z < 1$, indicating that at these redshifts we are approaching the formation epoch of red sequence galaxies (Gobat *et al.*, 2011).

$1 < z < 2$ is clearly a transition period where clusters first start to appear as the collapsed, virialised structures we recognise. The future of cluster surveys is promising, with several key telescopes/instruments coming online in 2018-2023 which will provide incredibly large, detailed samples of clusters at these redshifts. The Gemini Observations of Galaxies in Rich Early ENvironments survey (GOGREEN; PI M. Balogh) is now obtaining spectra and deep photometric observations of over 1000 galaxies in 21 clusters at $1 < z < 1.5$. The Dark Energy Survey (DES) will discover hundreds of thousands of clusters at $z < 1.3$ over 5000 square degrees and provide deep optical data with which to select high-redshift galaxies and study their properties. *Euclid* (Amendola *et al.*, 2013) is predicted to discover $10,000$ galaxy clusters at $z > 1$, imaging them in the NIR and overlapping with ground-based optical surveys such as DES. The extended ROentgen Survey with an Imaging Telescope Array (eROSITA; Pillepich, Porciani & Reiprich, 2012) will select tens of thousands of clusters at X-ray

wavelengths, allowing measures of cluster masses even at $z > 1$.

These surveys will hopefully allow us to come to statistically meaningful conclusions, sorting clusters by mass and state of collapse in order to compare them. In order to fully understand the variety of cluster properties we observe, we also need to examine clusters in light of their progenitors. The redshift regime $1 < z < 2$ also marks the beginning of the study of these structures: protoclusters.

1.1.4 Protoclusters

Before they have collapsed and virialised, clusters exist in an agglomeration of smaller groups and filaments known as "protoclusters". In semi-analytic models, a protocluster consists of all the haloes that will eventually merge to become the $z = 0$ cluster (Muldrew, Hatch & Cooke, 2015). In observations it is considerably more difficult to use this definition, so typically a protocluster is defined as an overdensity of galaxies which has sufficient mass to be able to form a cluster ($M \geq 10^{14}\,\mathrm{M}_{\odot}$), and a density such that the structure will collapse by $z = 0$ (Hatch *et al.*, 2011a).

The seminal study of a high-redshift protocluster focused on the structure surrounding the Spiderweb galaxy. The Spiderweb protocluster is still one of the best-studied protoclusters, with spectroscopic confirmation of several members, as well as extensive photometry covering the optical u-band through to radio wavelengths (e.g. Kurk *et al.*, 2000; Pentericci *et al.*, 2000; Kurk *et al.*, 2004b,a; Hatch *et al.*, 2011b; Seymour *et al.*, 2012; Koyama *et al.*, 2013a; Rigby *et al.*, 2014). As well as the Spiderweb, $\sim$ 20–30 confirmed protoclusters exist at $z > 1.5$ (e.g. Venemans *et al.*, 2007; Hatch *et al.*, 2011a; Kodama *et al.*, 2007). The highest redshift protocluster observed to date is at $z \sim 8$ (Trenti *et al.*, 2012). At the highest redshifts ($z > 3$), very little is known about protocluster galaxy properties, due to the difficulty in gaining sufficient observations of them, and their scarcity. They appear to consist of overdensities of star-forming galaxies, with a high fraction of starburst galaxies, sub-millimeter galaxies and "Lyman-α blobs" (e.g. Venemans *et al.*, 2007; Overzier *et al.*, 2008, 2009; Kuiper *et al.*, 2010, 2011).

At $1 < z < 3$ several studies have compared protocluster galaxies to field galaxies at

the same redshifts, as well as trying to map their evolution towards cluster galaxies. Some of the trends from low redshift are still observable—protocluster galaxies are twice as massive as those in the field (Hatch *et al.*, 2011b; Steidel *et al.*, 2005; Koyama *et al.*, 2013a), and on average older than field galaxies at similar redshifts (Steidel *et al.*, 2005). However, protocluster and field galaxies lie on the same SFR-mass relation, implying a constant sSFR irrespective of environment (Koyama *et al.*, 2013a,b; Cooke *et al.*, 2014). In some protoclusters red sequences have been observed, implying that the red sequence appears before the global virialisation of the cluster, perhaps in the central halo or cluster core (Kodama *et al.*, 2007; Galametz *et al.*, 2010b). There is also evidence that high redshift protoclusters contain a population of early-type galaxies, although the fraction of early-types ranges from $\sim 50\%$, similar to the field fraction, to 80% (Papovich *et al.*, 2012; Zeimann *et al.*, 2012; Mei *et al.*, 2015).

As with $z > 1.5$ clusters, these studies have all been undertaken with individual or small samples of protoclusters. This results in confusing and sometimes contradictory results due to cluster-to-cluster variation. To overcome these issues, it is important to move beyond individual studies and instead examine large samples of clusters and protoclusters at $z > 1$. It is difficult to detect protoclusters at the highest redshifts due to their nature and the techniques employed to find them. In the next section I will discuss methods used to find and select (proto)clusters, highlighting key surveys past, present and future.

1.2 How to find galaxy clusters

Several techniques are now employed to locate clusters and protoclusters at $z > 1$, such as large photometric surveys (e.g. Chiang, Overzier & Gebhardt, 2014; Stanford *et al.*, 2014), surveys exploiting the Sunyaev Zel'dovich effect (e.g. Hasselfield *et al.*, 2013; Bleem *et al.*, 2015; Planck Collaboration *et al.*, 2015), and X-ray detections of the intracluster medium (ICM) (e.g. Willis *et al.*, 2013). Unfortunately, many of these methods are expensive, requiring deep coverage of large fields-of-view in order to locate the rare overdensities. A targeted approach reduces the strain on telescope time and can pinpoint clusters even at the highest redshifts. However, the right beacon needs

to be used. In the following subsections I will discuss the different cluster selection techniques.

1.2.1 X-ray and SZ detections

The ICM comprises $\sim 15\%$ of the baryonic content in clusters. It produces characteristic signals at opposite ends of the spectrum: X-rays due to the hot gas, and millimetre to radio due to up-scattering of transiting photons. Both of these effects have been used to detect clusters, as well as measure properties such as their masses and temperatures.

The ICM has a temperature of 10^7-10^8 K and emits at X-ray wavelengths through both line emission from the hot gas and thermal Bremsstrahlung ("braking") radiation: a process in which a free electron gets decelerated by an ion, emitting an X-ray photon. Since the advent of space-based telescopes, surveys such as the ROSAT Deep Cluster Survey (RDCS; Rosati *et al.*, 1998) and the MAssive Cluster Survey (MACS; Ebeling *et al.*, 2010) have utilised X-ray telescopes to search for extended X-ray emission characteristic of the ICM, and thus selected clusters. Contamination can come from bright X-ray sources such as AGN, which must be removed and accounted for. This can sometimes be difficult as high angular resolution is required to distinguish between point-like sources and extended sources such as clusters. X-ray detections are useful for measuring the mass of the cluster, as well as providing information about the dark matter profiles. Clusters can be broadly categorised into cool-core and non-cool-core clusters based on the temperature profiles of their gas; cool-core clusters exhibit a drop in temperature in the central $\sim$ 50-100 kpc, associated with a slightly higher central surface brightness in X-ray. X-ray signals have been detected out to at least $z = 1.6$, but it becomes increasingly difficult beyond this as the X-ray signal decreases as $(1 + z)^4$. At $z < 1.5$, of order 2000 clusters have had their ICM detected at X-ray wavelengths (Piffaretti *et al.*, 2011), which will increase dramatically in the next few years once *eROSITA* is launched.

The ICM can also cause photons from the cosmic microwave background (CMB) to up-scatter via the inverse-Compton effect (approximately 1% of CMB photons), producing a signal at shorter wavelengths/higher energies (Sunyaev & Zeldovich, 1972). Through this Sunyaev-Zel'dovich (SZ) effect, observations of the CMB allow us to

detect clusters with an ICM sufficient to cause this scattering. As the change in flux from the CMB is fractional, the SZ effect is independent of the cluster's redshift and is therefore particularly useful for detecting clusters at higher redshifts, where the X-ray signal is too weak. The *Planck* satellite has observed ~ 1200 cluster candidates across the whole sky, which are now being confirmed (Planck Collaboration *et al.*, 2015). Similarly, the South Pole Telescope (SPT; Vanderlinde *et al.*, 2010; Carlstrom *et al.*, 2011; Bleem *et al.*, 2015) and the Atacama Cosmology Telescope (ACT; Marriage *et al.*, 2011; Hasselfield *et al.*, 2013) have detected ~ 500 and ~ 100 candidates respectively out to $z \sim 1.5$. In addition, clusters known from optical and NIR work have been found to have an SZ signal from an ICM once targeted by millimeter telescope arrays.

Massive clusters have been found with the SZ effect out to $z \sim 1.5$, with a few candidates at even higher redshifts (e.g. Tozzi *et al.*, 2015, see also Brodwin *et al.*, 2012). These, however, are rare systems; SZ and X-ray surveys struggle to find the more typical, lower mass clusters at $z > 1.5$ since the signal from these methods scales with cluster mass. The high-redshift progenitors of the majority of local $M \sim 10^{14}\,\mathrm{M}_{\odot}$ clusters will be missed since they lack sufficiently massive cluster cores at $z \gtrsim 1.5$ to be detectable with current instruments (Chiang, Overzier & Gebhardt, 2013; Muldrew, Hatch & Cooke, 2015). At the highest redshifts, the ICM is not dense enough to produce an observable signal in either X-ray or SZ. Thus, at $z > 2$ we rely on overdensities of galaxies to pinpoint forming clusters.

1.2.2 Optical and NIR overdensities

The first clusters discovered were found as overdensities of galaxies (Abell, 1958). The Abell catalogue consists of nearly 3000 clusters, extended to over 4000 clusters including the Southern skies (Abell, Corwin & Olowin, 1989). With the advent of 4 m-class telescopes, as well as photometric plates, and then CCDs, making scrutinising the skies easier, cluster surveys advanced to $z \sim 0.9$ (Gunn, Hoessel & Oke, 1986). This is still the basis of many cluster surveys today, both using photometric and spectroscopic data. Large field surveys such as the Sloan Digital Sky Survey (SDSS; Adelman-McCarthy *et al.*, 2008), the Galaxy And Mass Assembly survey (GAMA; Robotham *et al.*, 2011),

the Cosmological Evolution Survey (COSMOS; Bellagamba *et al.*, 2011), and the Ultra Deep Survey (UDS; Lani *et al.*, 2013), have identified overdensities of galaxies within their catalogues and thus selected groups and clusters within the survey region. Rather than scanning the images by eye, searching for overdensities of galaxies, overdensities are typically identified using measures of local density such as n^{th} nearest neighbour or density measures in a certain aperture (Muldrew *et al.*, 2012). The n^{th} nearest neighbour method can be used to define the local environment of a galaxy and probes substructure within clusters and small groups well. Aperture measures are useful when a measure of the global environment is required. This involves placing an aperture of a set size on a region of interest and measuring the number of galaxies within that region. By placing many apertures, the denser regions are identifiable and clusters may be selected. Once overdensities have been identified, confirmation is usually via further follow-up with spectroscopic measurements of cluster members or detections of the ICM from X-ray or SZ measurements.

Without spectroscopic redshift information, photometric redshifts are typically used. When the available photometry is limited to only a few wavebands, however, the redshift distribution of galaxies can be very broad. This causes true overdensities to be "blurred out" and spurious detections of overdensities due to line-of-sight projections. As most clusters at $z < 1$ are populated by old, red early-type galaxies, photometry can be targeted to select galaxies which are more likely to be cluster members and remove some of the projection effects (Gladders & Yee, 2005). By selecting observational wavebands to lie either side of the 4000 Å break, red, quiescent galaxies are easier to separate from blue, star-forming galaxies. With this method, the characteristic red sequence of galaxy clusters can be selected with relatively few wavebands. Optical surveys have used this "red sequence matching" method out to $z \sim 1$ (Gladders *et al.*, 2007), and with the advent of the *Spitzer Space Telescope* these studies are feasible using the IR bands to bracket the 4000 Å break at $z > 1$ (Wilson *et al.*, 2009). Red sequence matching becomes increasingly difficult at higher redshifts as the red sequence is not fully formed at $z > 1.5$, except for a few systems. Searching for overdensities at $z > 1.5$ therefore requires precise photometric redshifts or extensive spectroscopy in order to accurately find (proto)cluster members. We therefore rely on wide, deep surveys to find the rare clusters at such high redshifts. These wide, deep surveys require

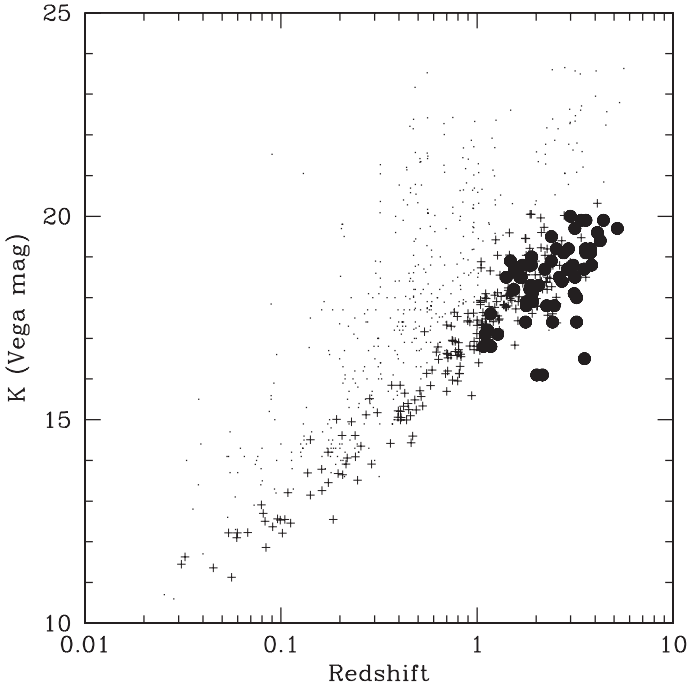

Figure 1.1: From Seymour *et al.* (2007): the observed NIR K versus redshift diagram for radio sources. Radio-loud sources (from De Breuck *et al.*, 2002) are indicated by the pluses and filled circles, radio-quiet galaxies (from the Hawaii survey and the Hubble Deep Field North; Songaila *et al.*, 1994; Dickinson *et al.*, 2003) are shown by the points. The filled circles show the 69 $z > 1$ radio galaxies that comprise the SHzRG sample (Section 1.4).

a lot of telescope time and so there are only a handful of known structures detected in this way at high redshift (e.g. Douglas *et al.*, 2010; Spitler *et al.*, 2012).

1.2.3 Radio-Loud AGN as beacons for protoclusters

Most (proto)cluster candidates at $z > 1.5$ have been found using a targeted approach. By pinpointing certain targets likely to lie within clusters and overdensities, telescope time and expenses can be drastically reduced as a much smaller area needs to be observed. The clusters and protoclusters I examine in this thesis have all been selected because they contain a radio-loud active galactic nucleus (RLAGN) in, or near, their core.

RLAGN are super-massive black holes (SMBHs) which emit strongly at radio wavelengths. SMBH may produce highly-collimated jets. These jets produce synchrotron radiation due to relativistic electrons accelerating around the magnetic field lines. Synchrotron radiation is produced at all wavelengths, but is most obvious at radio wavelengths. The exact conditions required for a SMBH to produce such jets are still un-

clear, but they are more likely to occur with SMBH that are rapidly rotating (Blandford & Znajek, 1977) and have high accretion rates (e.g. Fernandes *et al.*, 2011). The most rapidly spinning SMBHs are caused by mergers between two black holes (e.g. Fanidakis *et al.*, 2011), due to a merger between their host galaxies. Such mergers are more frequent at high redshift in forming cluster environments (e.g. Lotz *et al.*, 2011).

Studies since the 1960s have shown that RLAGN are hosted by the most massive galaxies in the Universe, out to at least $z = 5$ (e.g. Matthews, Morgan & Schmidt, 1964; Best, Longair & Röttgering, 1998; Pentericci *et al.*, 2001). They trace the bright envelope of radio-quiet galaxies in the observed NIR K versus redshift diagram for powerful radio sources, with remarkably low scatter (Figure 1.1; Lilly & Longair, 1984; De Breuck *et al.*, 2010). These massive radio-loud galaxies are therefore theorised to reside in the most dense environments at every epoch. In addition, RLAGN are often suggested to be the progenitors of local brightest cluster galaxies (BCGs; Miley & De Breuck, 2008). Recent simulation work also points to the use of radio galaxies as beacons for forming clusters (Orsi *et al.*, 2016) and targeted searches around these powerful RLAGN have resulted in the discovery of dozens of $z > 1$ clusters and protoclusters (e.g. Pentericci *et al.*, 2000; Venemans *et al.*, 2007; Galametz *et al.*, 2009; Hatch *et al.*, 2011a; Cooke *et al.*, 2014).

It is still unclear why radio galaxies preferentially reside in overdense environments. Hatch *et al.* (2014) showed that the environments around RLAGN were denser on average than those around radio-quiet galaxies of the same stellar mass. This means that the tendancy for RLAGN to reside in overdense environments is not solely due to their large stellar masses, and the associated clustering of massive galaxies. Simpson & Rawlings (2002) suggested that radio galaxies may be triggered by a merger of two group-sized objects. They studied two systems containing RLAGN and proposed a model whereby a merger of groups or clusters causes a merger of two massive galaxies which triggers the radio jets. X-ray observations of these two clusters does indeed suggest that they have undergone a recent major merger. Larger samples comparing clusters with and without RLAGN are required to draw firm conclusions (see also Chapter 3).

The benefit of using bright RLAGN as beacons for (proto)clusters is that the redshift

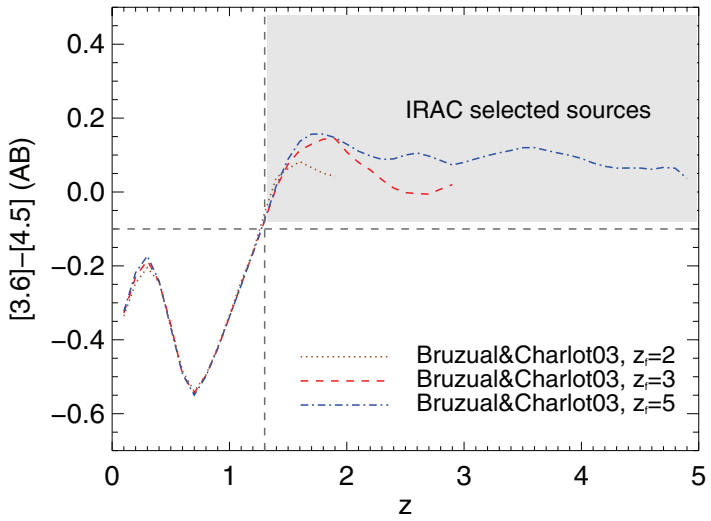

Figure 1.2: The evolution of the IRAC $[3.6] - [4.5]$ colour as a function of redshift, taken from Wylezalek *et al.* (2013). Plotted are Bruzual & Charlot (2003) stellar population models for three formation redshifts, z_f, assuming a Salpeter (1955) IMF and an exponentially declining burst of star formation with $\tau = 0.1$ Gyr. At $z > 1.3$, 90% of galaxies have IRAC colours redder than -0.1 (grey shaded region, Papovich, 2008).

of the cluster is known; it is assumed to be the redshift of the radio galaxy. This allows targeted photometric and spectroscopic follow-up in appropriate wavebands. In the following sections I will discuss two surveys utilising RLAGN to select protocluster candidates: the *Spitzer* High-redshift Radio Galaxy (SHzRG) and Clusters Around Radio-Loud AGN (CARLA) surveys. SHzRG was the precursor to CARLA. The latter has now discovered ~ 200 cluster and protocluster candidates at $1.3 < z < 3.2$; the largest sample at such high redshifts. The (proto)clusters I present in this thesis were all selected from these radio galaxy cluster surveys.

1.3 The *Spitzer* High-redshift Radio Galaxy survey

It is now well-established that RLAGN are known to preferentially reside in overdense environments at high redshift (e.g. Venemans *et al.*, 2007), which are more dense than those of radio-quiet galaxies of similar mass (Hatch *et al.*, 2014). This makes them ideal targets for $z > 1$ cluster studies, as they provide an efficient way to find high redshift (proto)clusters without the need for extremely wide and deep field surveys.

The *Spitzer* High-redshift Radio Galaxy survey (SHzRG; Seymour *et al.*, 2007) was a Cycle 1 *Spitzer* survey of 69 $1 < z < 5$ high-redshift RLAGN (Figure 1.1), examining

the properties of the RLAGN and their host galaxies. Galametz *et al.* (2012) studied the fields of 48 RLAGN at $1.2 < z < 3$ from this survey to search for high redshift (proto)clusters. High-redshift galaxies were selected using the well-tested Papovich (2008) colour-cut of $[3.6] - [4.5] > -0.1$ (Figure 1.2). This criterion selects galaxies at $z > 1.3$ almost independently of galaxy type or age, due to the 1.6 μm peak of stellar emission moving into the IRAC bands at $z > 1$. 90% of $z > 1.3$ galaxies have colours $[3.6] - [4.5] > -0.1$ (Papovich, 2008). Most stars have $[3.6] - [4.5] \sim -0.5$ and so are successfully removed by this cut, however some contamination can come from brown dwarfs, strongly star-forming galaxies at $z \sim 0.3$ and powerful AGN (Galametz *et al.*, 2012).

The SHzRG fields are covered at 3.6 μm and 4.5 μm to depths of $[3.6] = 21.3$ and $[4.5] = 21.1$ (5σ AB; Galametz *et al.*, 2012). From the SHzRG sample, overdense fields were selected as those with > 15 sources with red[1] IRAC colours within a cell of $1'$ radius around the radio galaxy. This corresponds to $> 2\sigma$ outliers from the mean field density, measured from $20,000$ one arcmin radius cells in the *Spitzer* Wide-Infrared Extragalactic survey (SWIRE; Lonsdale, 2003). More than 70% of the studied RLAGN were surrounded by environments that were denser than the average SWIRE field. Twenty-three percent fit the criterion of being surrounded by more than 15 sources, including five previously-known structures. MRC 2104−242 (studied in Chapter 4) was found to have 14 sources within $1'$ of the radio galaxy.

Galametz *et al.* (2012) showed that the IRAC criterion is a successful and efficient method of selecting high-redshift (proto)clusters. Their pilot study found 11 fields highly likely to contain protoclusters, as well as numerous fields more dense than the average field which warrant further investigation into the wide-field structure. This study of 48 RLAGN with *Spitzer* paved the way for the much larger CARLA survey.

1.4 The CARLA survey

Based on the success of the SHzRG pilot study, the Clusters Around Radio-Loud AGN survey (CARLA; Wylezalek *et al.*, 2013) imaged the environment of 420 powerful

[1] i.e. $[3.6] - [4.5] > -0.1$

RLAGN with a 500 MHz luminosity $\geq 10^{27.5}$ W Hz^{-1} at $1.3 < z < 3.2$. The aim was to discover as many clusters and protoclusters as possible with which to study galaxy and cluster evolution.

The following description of the selection of (proto)clusters is adapted from the work of Wylezalek *et al.* (2013, 2014). High-redshift radio galaxies (HzRGs) were selected from the compendium of Miley & De Breuck (2008), radio surveys (e.g., MRC, 3C, 6C, 7C) and ultra-steep spectrum surveys (e.g. Roettgering *et al.*, 1997; De Breuck *et al.*, 2001). Radio-loud quasars (RLQs) were also selected from the Sloan Digital Sky Survey (SDSS; Schneider *et al.*, 2010) and the 2dF QSO Redshift Survey (Croom *et al.*, 2004). In total the CARLA sample is composed of 209 HzRGs and 211 RLQs, uniformly covering $1.3 < z < 3.2$.

The fields around the RLAGN targeted by CARLA were imaged with the *Spitzer* Infrared Array Camera (IRAC; Fazio *et al.*, 2004) at 3.6 μm and 4.5 μm in a ~ 400 hour Cycle 7 and 8 *Warm Spitzer* snapshot program, reaching 95% completeness at 22.6 mag ($= 3.45\,\mu$Jy) and 22.9 mag ($= 2.55\,\mu$Jy) at 3.6 μm and 4.5 μm, respectively. Each field has an area of $5.2' \times 5.2'$, which is approximately 2.5 Mpc$\times 2.5$ Mpc (physical coordinates) at $1.3 < z < 3.2$. Sources were detected using the 4.5 μm data, and photometry extracted at 3.6 μm using SExtractor in dual-image mode (Bertin & Arnouts, 1996). Sources were selected as high-redshift sources ("IRAC-selected sources", Figure 1.2) with the following criteria: (i) 4.5 μm $> 2.55\,\mu$Jy (95% completeness limit) (ii) 3.6 μm $> 2.8\,\mu$Jy (3.5σ detection limit); and (iii) $[3.6] - [4.5] > -0.1$. Alternatively, sources were included if they matched the following criteria: (i) 4.5 μm $> 2.55\,\mu$Jy (ii) 3.6 μm $< 2.8\mu$Jy but (iii) $[3.6] - [4.5] > -0.1$ at the 3.5σ detection limit. A full description of the data, reduction and source extraction is given in Wylezalek *et al.* (2013).

Galaxy densities were measured in an aperture of radius 1 arcmin around the RLAGN. Contaminants such as cool brown dwarfs are not expected to significantly contribute to the signal in such a small area, especially in fields at high Galactic latitudes (Galametz *et al.*, 2012). To select (proto)cluster candidates, the *Spitzer* UKIDSS Ultra Deep Survey (SpUDS; PI J. Dunlop) was used as a comparison control field. Over 400 random apertures of 1 arcmin were placed on the 1 deg^2 SpUDS field and the density

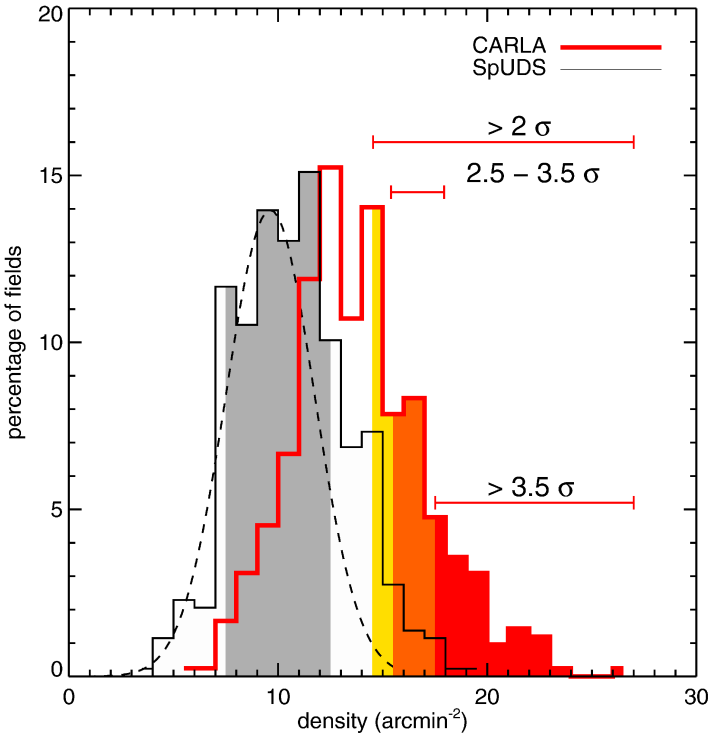

Figure 1.3: From Wylezalek *et al.* (2014): the surface densities of IRAC-selected sources (coloured histogram) within 1 arcmin of the CARLA RLAGN, compared to the field distribution of SpUDS fields (black line). The dashed black line shows a Gaussian fit to the lower half of the SpUDS distribution. The peak of this Gaussian is taken as the average field density: 9.6 ± 2.1 arcmin^{-2}. The grey shaded region shows the SpUDS regions with surface density 9.6 ± 2.1 arcmin^{-2} (i.e. $\pm 1\sigma$). The yellow, orange and red shaded regions show CARLA targets which are 2-2.5σ, 2.5-3.5σ and $> 3.5\sigma$ denser than the field average.

of IRAC-selected sources (those with $[3.6] - [4.5] > -0.1$) was measured. Figure 1.3, adapted from Wylezalek *et al.* (2014), shows the surface densities of the SpUDS random fields and the CARLA fields. Nearly half (190, 45%) of these RLAGN are surrounded by significant ($> 2\sigma$) excesses of galaxies with red $[3.6] - [4.5]$ colours that are likely associated with the RLAGN and therefore are likely to be high redshift clusters and protoclusters. These overdensities show an increase in surface density towards the RLAGN, meaning they are indeed associated with the RLAGN, rather than a random distribution. With nearly 200 candidates, the CARLA sample is the largest coherent sample of cluster and protocluster candidates at $z > 1.5$ for studies of the properties of high-redshift clusters and their member galaxies.

1.5 Results from the CARLA survey

As the CARLA cluster candidate sample is so large, it lends itself to large statistical studies of cluster properties and their evolution over $3.2 > z > 1.3$. Wylezalek *et al.* (2013) took advantage of the similar numbers of HzRGs and RLQs in the survey to compare the environments of type-1 and type-2 AGN. They found that there is no difference between the environments of RLQs (type-1 AGN) and HzRGs (type-2 AGN). This adds weight to the AGN unified model (Urry & Padovani, 1995), whereby the difference between these two types of RLAGN is simply due to their observed orientation, rather than an intrinsic difference between them, for example, each type representing a different stage in an evolutionary sequence. This study, however, is limited to very powerful RLAGN.

The 4.5 μm luminosity functions of the CARLA cluster galaxies were investigated in Wylezalek *et al.* (2014). The luminosity function has the form of a Schechter (1976) function:

$$n(x)\mathrm{d}x = \phi^* x^{\alpha} \mathrm{e}^{-x} \mathrm{d}x \tag{1.1}$$

where $x = L/L^*$, ϕ^* is the normalization of the function and L^* is the characteristic luminosity, corresponding to the "knee" of the function, where the power law ends. Wylezalek *et al.* (2014) found that the faint-end slope, α, of the cluster luminosity function does not deviate significantly from $\alpha = -1$ out to $z = 3.2$. They also measured the knee of the $4.5\,\mu$m luminosity function, m_*, up to $z \sim 3.2$ and showed that the observations were consistent with passive galaxy evolution models. The measured values of m_* allowed for less than 40% contribution to the luminosity function from star-forming galaxies. Below $z = 1.5$, the CARLA clusters have little-to-no contribution to their luminosity functions from star formation. By contrast, Mancone *et al.* (2010) found that clusters found at $1 < z < 1.5$ in the IRAC Shallow Cluster Survey (ISCS; Eisenhardt *et al.*, 2008) showed significant differences between their measured luminosity functions and passive evolution models, suggesting on-going mass assembly in these clusters. The lowest richness CARLA fields have luminosity functions with forms more similar to those from the ISCS, suggesting that the majority of CARLA clusters are more evolved and more massive than the ISCS clusters.

These studies used just two photometric wavebands (3.6 μm and 4.5 μm), with no way of selecting cluster members exactly. A strength of the CARLA survey is the large number of cluster candidates: such studies may rely on statistics with 10-30 galaxy clusters in any given bin, so that the overall trends can be analysed without knowing cluster membership explicitly. By using a control field (in the case of the CARLA survey, the UDS was used), field contamination can be removed by using statistical background subtraction, revealing the cluster properties (see Chapters 2 and 3).

Ongoing projects within the CARLA collaboration are now working to confirm more of the CARLA cluster candidates, and characterise the galaxy populations within these overdense structures. To date several CARLA (proto)clusters have been confirmed from ground-based spectroscopy (Galametz *et al.*, 2013; Cooke *et al.*, 2016, A. Rettura *et al.* in preparation) and there is an ongoing *HST* programme to confirm 20 of the densest CARLA cluster candidates (G. Noirot *et al.* submitted). In Chapter 2 I describe my optical follow-up study of 37 of the densest CARLA (proto)clusters, using $i' - [3.6]$ colours to measure the evolution of the average cluster galaxy.

1.6 Outline of this thesis

In this thesis I aim to study the properties of galaxies in high redshift ($z > 1.3$) clusters and protoclusters. I will compare them to field galaxies at similar epochs, and also study the evolution of their properties across cosmic time.

Chapter 2 contains my optical follow-up study of 37 of the most promising CARLA (proto)cluster candidates. I will present the $i' - [3.6]$ colours of these structures and show the evolution of the average cluster galaxy colour from $z = 3.2$ to $z = 1.3$. Comparing these colours to simple galaxy formation models I will discuss the average formation history of cluster galaxies, for the first time probing the $z > 1.5$ Universe in this way.

In Chapter 3 I will present a study of a $z = 1.58$ cluster around the RLAGN 7C 1753+6311. This cluster was selected from my optical study (Chapter 2) as an extremely overdense structure consisting of many red galaxies. In this chapter I show the clear red sequence of quiescent galaxies around 7C 1753+6311 and measure the quiescent

fraction as a function of mass and environment.

Chapter 4 describes my study of the field around the RLAGN MRC 2104−242 at $z = 2.49$. This field was found to contain 14 high-redshift sources within $1'$ of the RLAGN in Galametz *et al.* (2012) (Section 1.3). In Chapter 4 I examine star-forming galaxies in the wider field using narrowband observations designed to select Hα emitters at $z = 2.5$. I will show the masses, star formation rates and dust extinction of the protocluster galaxies, and compare them to field samples at similar redshifts.

Finally, in Chapter 5, I will describe a project which aimed to compare the properties of star-forming galaxies in protoclusters around RLAGN to those in protoclusters with no central RLAGN. This project was awarded 50% of the telescope time requested, and was plagued with poor weather. As such, only two of the planned five RLAGN fields were observed. Therefore, in Chapter 5 I will present the data on these two fields and examine the properties of the galaxies surrounding the RLAGN.

Throughout this thesis I assume a ΛCDM cosmology with $h = 0.70$, $\Omega_M = 0.3$ and $\Omega_\Lambda = 0.7$, unless stated otherwise. I adopt a Chabrier (2003) initial mass function (IMF) for all my calculations and magnitudes are given in the AB photometric system unless stated otherwise.

Chapter 2

The formation history of massive cluster galaxies as revealed by CARLA

2.1 Introduction

In the local Universe, most massive cluster galaxies are old and have little-to-no ongoing star formation (e.g. Oemler, 1974). They form a very homogeneous, slowly-evolving population, exhibiting similar, red colours. When viewed in colour-magnitude space, these massive, old galaxies form a characteristic "red sequence". Such red sequences of galaxies are nearly ubiquitous in low redshift clusters, and persist out to $z \sim 1.5$ (e.g. Blakeslee *et al.*, 2003; Holden *et al.*, 2004; Mei *et al.*, 2006; Eisenhardt *et al.*, 2008). Red sequences have commonly been used to examine the formation history of massive cluster galaxies. The colour, slope and low scatter of the red sequence within $z < 1$ clusters are consistent with early-type cluster galaxies forming concurrently in a short burst of star formation at high redshift ($z > 2$) and passively evolving thereafter (e.g. Bower, Lucey & Ellis, 1992; Eisenhardt *et al.*, 2007), although there are indications that further star formation occurs within galaxies towards the outskirts of the cluster (Ferré-Mateu *et al.*, 2014).

The red sequences of low redshift clusters indicate a high formation redshift, though it is difficult to determine the exact epoch and history of galaxy formation using their galaxy colours. This is because the colours of galaxies that have been passively evolv-

ing for more than a few billion years are very similar (Kauffmann *et al.*, 2003). Thus it is difficult to differentiate between formation redshifts if the time between the galaxy's formation and observation is several Gyr. It is possible to measure galaxy ages more accurately by observing them early in their formation. By measuring the colours of galaxies within high redshift clusters we can determine the exact epoch and history of formation and break the degeneracies between single collapse models and those which include extended periods of galaxy growth (e.g. Snyder *et al.*, 2012).

The scatter in colour of early-type cluster galaxies at $z > 1$ is low and consistent with passive evolution for $z \lesssim 2.3$ (e.g. Stanford, Eisenhardt & Dickinson, 1998; Blakeslee *et al.*, 2003; Mei *et al.*, 2006; Lidman *et al.*, 2008). However, when examining the full cluster population, it is no longer possible to model the galaxy formation history with a single formation timescale, but rather there is a scatter in the inferred ages (e.g. Eisenhardt *et al.*, 2008; Kurk *et al.*, 2009). Clusters at $z > 1$ were much more active than they are today; they exhibited significant ongoing star formation (Snyder *et al.*, 2012; Brodwin *et al.*, 2013; Zeimann *et al.*, 2013; Alberts *et al.*, 2014), merging between galaxies (Mancone *et al.*, 2010; Lotz *et al.*, 2013) and increased AGN activity (Galametz *et al.*, 2010a; Martini *et al.*, 2013). The red sequence of clusters and protoclusters was much less populated at $z > 1$ than today (e.g. Kodama *et al.*, 2007; Hatch *et al.*, 2011a; Rudnick *et al.*, 2012), which means some of the progenitors of local red sequence galaxies would have bluer colours and lie below the red sequence at $z > 1$. Thus, when tracing the evolution of just the galaxies that already lie on the red sequence, high redshift studies are prone to progenitor bias (van Dokkum & Franx, 2001). To robustly trace the evolution of cluster galaxies it is important to study all the progenitors; those that are already passive at high redshift, and those that only become passive at a later time.

To trace the early formation history of massive cluster galaxies, I have taken the cluster sample from the CARLA survey (Wylezalek *et al.*, 2013, Section 1.4), and pushed the study of galaxy colours to even higher redshifts. My sample extends from $z = 1.3$ out to $z = 3.2$, covering the full timescale of massive cluster galaxy formation measured from previous works (e.g. Blakeslee *et al.*, 2003).

In the study of the cluster luminosity function with the CARLA sample, Wylezalek

et al. (2014) showed that passive galaxy evolution models were consistent with their measured m_* up to $z \sim 3.2$. In this chapter I investigate the formation epoch and star formation history of the cluster galaxies. I observed 37 of the densest CARLA fields in the i' band and calculated the average observed $i' - [3.6]$ colour of the cluster galaxies. To avoid progenitor bias I measured the colours of all $M_* > 10^{10.5}\,\mathrm{M}_\odot$ cluster galaxies to estimate the overall average colour evolution of massive cluster galaxies. Although using average colours loses information about the individual cluster galaxies, if they are formed as concurrent bursts, then averaging will reduce photometric errors. If the galaxy population is more diverse, then by modelling that diversity we can compare to the average colour, which still contains information about the population. The scatter in colours can also be used to reduce the effect of degeneracies between models.

In Section 2.2 I describe my data and control fields, as well as the methodology of measuring cluster galaxy properties. Section 2.3 presents my key results, the implications of which are discussed in Section 2.4. My conclusions are summarised in Section 2.5.

2.2 Method

In this Section I describe my methodology and datasets. I use two cluster samples: a high redshift ($1.3 < z < 3.2$) sample from the CARLA survey (Section 2.2.1), and a low and intermediate redshift sample ($0.1 < z < 1.8$) taken from the IRAC Shallow Cluster Survey (ISCS, described in Section 2.2.5). I also utilise a control field sample, from the UKIDSS Ultra Deep Survey (Section 2.2.2), in order to statistically subtract field contaminants from our cluster samples. The selection of high redshift galaxies and cleaning of foreground interlopers is described in Section 2.2.3. My method for calculating the colours of (proto)cluster galaxies is described in Section 2.2.4.

Table 2.1: Details of i' band observations for the 37 CARLA fields observed with ACAM on the WHT and GMOS-S on Gemini South.

Field	RA	DEC	z	Instrument	Exp. time (s)	5σ i' depth	Seeing (arcsec)	Density[a]
J085442.00+57572	08:54:42.00	57:57:29.16	1.317	ACAM	6600	24.59	1.00	4.1
J110020.21+09493	11:00:20.16	09:49:35.00	1.321	GMOS-S	2405	24.86	0.65	3.3
J135817.60+57520	13:58:17.52	57:52:04.08	1.373	ACAM	8400	24.95	0.89	6.2
MRC0955−288	09:58:04.80	−29:04:07.32	1.400	GMOS-S	2645	25.02	0.58	2.7
7C1756+6520	17:57:05.28	65:19:51.60	1.416	ACAM	10205	24.26	1.73	4.4
6CE1100+3505	11:03:26.40	34:49:48.00	1.440	ACAM	9600	25.19	1.12	6.3
TXS 2353−003	23:55:35.87	−00:02:48.00	1.490	ACAM	6000	24.99	0.81	5.6
J112914.10+09515	11:29:14.16	09:51:59.00	1.519	GMOS-S	2645	24.78	0.44	6.3
MG0122+1923	01:22:30.00	19:23:38.40	1.595	ACAM	7200	24.83	0.79	3.2
7C1753+6311	17:53:35.28	63:10:49.08	1.600	ACAM	6000	25.08	0.74	4.5
BRL1422−297	14:25:29.28	−29:59:56.04	1.632	GMOS-S	2689	24.87	0.62	3.5
J105231.82+08060	10:52:31.92	08:06:07.99	1.643	GMOS-S	2645	25.04	0.56	5.0
TNJ0941−1628	09:41:07.44	−16:28:03.00	1.644	GMOS-S	2645	25.03	0.58	4.7
6CE1141+3525	11:43:51.12	35:08:24.00	1.780	ACAM	10187	24.89	1.59	4.5
6CE0905+3955	09:08:16.80	39:43:26.04	1.883	ACAM	7200	25.09	0.89	4.1

[a] Density is the number of standard deviations from the average field density of red IRAC sources, as calculated in Wylezalek *et al.* (2014).

[*] i' imaging of J140445.88−013021.8 was taken with the new Hamamatsu CCDs on GMOS-S, with reduced fringing effects.

Table 2.1 – continued from previous page

Field	RA	DEC	z	Instrument	Exp. time (s)	5σ i' depth	Seeing (arcsec)	Density[a]
MRC1217−276	12:20:21.12	−27:53:00.96	1.899	GMOS-S	2645	24.96	0.69	3.5
J101827.85+05303	10:18:27.84	05:30:29.99	1.938	ACAM	7200	25.19	0.81	5.0
J213638.58+00415	21:36:38.64	00:41:53.99	1.941	ACAM	6300	25.00	0.69	5.7
J115043.87−00235	11:50:43.92	−00:23:54.00	1.976	GMOS-S	2645	25.04	0.62	2.7
J080016.10+402955.6	08:00:16.08	40:29:56.40	2.021	ACAM	6600	25.16	0.93	6.3
J132720.98+432627.9	13:27:20.88	43:26:27.96	2.084	ACAM	7200	25.03	0.75	4.1
J115201.12+102322.8	11:52:01.20	10:23:22.92	2.089	ACAM	7200	25.18	1.13	4.2
TNR 2254+1857	22:54:53.76	18:57:03.60	2.154	ACAM	9000	25.41	1.10	5.6
J112338.14+052038.5	11:23:38.16	05:20:38.54	2.181	GMOS-S	2645	25.00	0.64	4.7
J141906.82+055501.9	14:19:06.72	05:55:01.92	2.293	ACAM	7800	24.56	1.28	4.5
J095033.62+274329.9	09:50:33.60	27:43:30.00	2.356	ACAM	7200	24.92	1.31	4.4
4C 40.02	00:30:49.00	41:10:48.00	2.428	ACAM	8700	25.26	0.94	4.2
J140445.88−013021.8	14:04:45.84	−01:30:21.88	2.499	GMOS-S*	2640	25.08	0.38	2.7
J110344.53+023209.9	11:03:44.64	02:32:09.92	2.514	ACAM	7800	24.76	1.33	4.1
TXS 1558−003	16:01:17.28	−00:28:46.00	2.520	GMOS-S	2405	24.94	0.91	2.4
J102429.58−005255.4	10:24:29.52	−00:52:55.43	2.555	GMOS-S	2645	25.14	0.53	4.5

[a] Density is the number of standard deviations from the average field density of red IRAC sources, as calculated in Wylezalek *et al.* (2014).

*i' imaging of J140445.88−013021.8 was taken with the new Hamamatsu CCDs on GMOS-S, with reduced fringing effects.

Table 2.1 – continued from previous page

Field	RA	DEC	z	Instrument	Exp. time (s)	5σ i' depth	Seeing (arcsec)	Density[a]
J140653.84+343337.3	14:06:53.76	34:33:37.44	2.566	ACAM	7800	25.19	0.73	3.3
6CSS0824+5344	08:27:59.04	53:34:14.88	2.824	ACAM	7200	24.65	1.17	4.1
J140432.99+072846.9	14:04:32.88	07:28:46.96	2.864	ACAM	8400	25.06	1.02	4.1
B2 1132+37	11:35:06.00	37:08:40.92	2.880	ACAM	7200	25.19	0.98	5.9
MRC 0943−242	09:45:32.88	−24:28:50.16	2.922	GMOS-S	2645	24.83	0.44	4.7

[a] Density is the number of standard deviations from the average field density of red IRAC sources, as calculated in Wylezalek *et al.* (2014).

[*] i' imaging of J140445.88−013021.8 was taken with the new Hamamatsu CCDs on GMOS-S, with reduced fringing effects.

2.2.1 High redshift cluster sample: CARLA

2.2.1.1 Data

Infrared (IR) data at 3.6 μm and 4.5 μm for the CARLA sample were taken using *Spitzer's* IRAC instrument (Section 1.4). The 4.5 μm data is slightly deeper; 95% completeness is reached at magnitudes of $[3.6] = 22.6$ and $[4.5] = 22.9$. For a full description of the IR observations and data reduction see Wylezalek *et al.* (2013).

I complemented our existing *Spitzer* dataset with i' band imaging. The i' and $3.6\,\mu$m bands bracket the 4000 Å break at the redshifts covered by the CARLA survey, and allow direct comparison to previous work at lower redshifts (Eisenhardt *et al.*, 2008). The extra i' band also allows me to refine the selection of cluster member galaxies, providing more detail in order to study the evolution of clusters more thoroughly than before.

I obtained optical i' band data for 37 of the densest CARLA fields with the auxiliary-port camera (ACAM) on the 4.2 m William Herschel Telescope (WHT) in La Palma and the Gemini Multi-Object Spectrograph South instrument (GMOS-S; Hook *et al.*, 2004) on Gemini-South in Chile. These fields were selected as the CARLA targets which contained the highest densities of sources with red IRAC $[3.6] - [4.5]$ colours that were visible at the latitudes of each telescope. Densities of most of these fields are 4–6σ denser than an average blank field (see Table 2.1), as calculated in Wylezalek *et al.* (2014), with a few at 2–3σ due to higher density fields not being observable.

I selected targets for the WHT observations according to their density, as above. I then rejected fields with bright stars ($m_{i'} \leq 10$) in the field of view to avoid saturation and bleeding in the images. I also rejected fields with known low-redshift clusters within the field of view to avoid biasing our measurements of overdensities.

I imaged twenty-three fields with ACAM during the period 2013 September–2014 December. This consisted of three visitor-mode (VM)[1] observing runs and one service programme (PI N. Hatch). The field of view of ACAM is circular, with a diameter of 8.3 arcmin and pixel scale 0.25 arcsec pixel^{-1}. ACAM was used, rather than the Prime

[1] VM: 2013 Sept 5–6, 2014 Jan 3,7–8 (1 night lost due to poor weather), 2014 Feb 21–27 (2 nights lost due to poor weather).

Focus Imaging Platform (PFIP), as the Cassegrain focus positioning of ACAM allows for more flexible scheduling, as well as the use of other instruments if there are poor weather conditions during the observing run.

The remaining 14 fields were imaged with GMOS-S through a service programme (PI A. Rettura). The majority of the GMOS-S data was taken using the EEV detectors between February and April 2014, though one field (J140445−013021.8) was imaged in June 2014 with the new Hamamatsu CCDs. GMOS-S covers an area of $5.5 \times 5.5\,\mathrm{arcmin}^2$ with a pixel scale of $0.146\,\mathrm{arcsec\,pixel}^{-1}$. During visitor-mode observations, I adapted the exposure times to take varying seeing into account, in order to obtain a consistent depth across all fields (see Table 2.1). In service-mode the seeing was relatively stable due to the restraints requested in the proposals.

2.2.1.2 Data reduction

I reduced the i' band images from both WHT/ACAM and Gemini-South/GMOS-S using the publicly available THELI software (Erben *et al.*, 2005; Schirmer, 2013). I de-biased and flatfielded the data using a superflat created from median-combining all images taken on the same night. I created a fringing model and subtracted this and the sky background from the images. Fringing occurs in some CCDs due to internal reflections creating interference patterns. Strong sky emission lines, in particular OH lines at wavelengths longer than $\sim 700\,\mathrm{nm}$, may reflect within a layer of silicon in the CCD and interfere with further incoming photons. Fringing may be reduced by applying an anti-reflection layer to the back of the CCD. The GMOS-S data taken with the old EEV detectors exhibited bad fringing (typically $\sim 67\%$ of the background), whereas the data taken with the Hamamatsu CCDs has significantly reduced fringing effects ($< 1\%$ of the background). The ACAM data had very low fringing effects: $< 1\%$ of the background.

I derived astrometric solutions for the images with SCAMP (Bertin, 2006) within THELI, using catalogues from the Sloan Digital Sky Survey (SDSS), or the Two Micron All Sky Survey (2MASS) where fields were not covered by the SDSS. I mean-combined each field using SWARP (Bertin *et al.*, 2002) within the THELI software. I flux calibrated the reduced images by comparing unsaturated stars in each field to

the SDSS where possible. Two WHT fields were not covered by SDSS and were flux calibrated with unsaturated stars in SDSS-covered exposures taken immediately before and after the observations. For the GMOS-S fields not covered by SDSS I used standard star observations for the flux calibration. I compared the different calibration methods for fields with both SDSS coverage and standard star observations and found that calibrations with standard stars differ from calibrations with SDSS by ≤ 0.05 mag. Details of the i' band data for each of the 37 CARLA fields are given in Table 2.1.

2.2.1.3 Source extraction

To produce object catalogues, source extraction was performed by D. Wylezalek using SExtractor (Bertin & Arnouts, 1996) in dual image mode, using the 4.5 μm images for detection and performing photometry on the 3.6 μm images. IRAC fluxes were measured in 4 arcsec apertures and corrected to total fluxes using aperture corrections of 1.42 and 1.45 for 3.6 μm and 4.5 μm respectively (Wylezalek *et al.*, 2013). At the RA and DEC of each source detected at 4.5 μm, I measured i'-band fluxes using the IDL APER routine. These fluxes were measured in either 2.5 arcsec or 3.2 arcsec diameter apertures, depending on the full-width half-maximum (FWHM) of the image. I chose the aperture sizes to be $\sim 2.5\times$ the seeing, which was a compromise between including as much flux as possible, and avoiding blending. The larger aperture was used for images with seeing > 1.15 arcsec (see Table 2.1). I then corrected these i' fluxes to total flux using correction factors (typically 1.15 and 1.04 for ACAM and GMOS-S data respectively) measured from the growth curves of unsaturated stars in the images.

I calculated image depths, shown in Table 2.1, by measuring the flux in $\sim 100,000$ random apertures, with the aperture size dependent on the FWHM of each image (as above). The median 1σ depth of the WHT data is $i' = 26.79$ mag, and for the Gemini data is $i' = 26.75$ mag. Due to the similarity in depth of all the fields, I used the overall median depth of $i' = 26.76$ mag ($= 1\sigma_{med}$) for all fields.

I calculated colours from aperture-corrected $i'-$ aperture-corrected $3.6\,\mu$m magnitudes. I derived the colours from the control field (see Section 2.2.2) in exactly the same way as the (proto)cluster sample. The distribution of colours of all galaxies in

the (proto)cluster fields are consistent with the control field so there are no systematic errors in my colour measurements.

2.2.2 Control field: UDS and SpUDS

I utilised the UKIDSS Ultra Deep Survey (UDS; PI O. Almaini) to statistically subtract contamination from fore- and background galaxies in the cluster fields. The UDS is a deep 0.8 deg^2 near-infrared survey, which overlaps part of the Subaru/*XMM-Newton* Deep Survey (SXDS; Furusawa *et al.*, 2008).

Galaxies in the UDS have photometric redshift information derived in Hartley *et al.* (2013) using 11 photometric bands. The K-band selected catalogue incorporates U-band data from the Canada-France-Hawaii Telescope, optical $BVRi'z'$ photometry from the SXDS, JHK photometry from the 8th data release (DR8) of the UDS, and *Spitzer* Ultra Deep Survey 3.6 and 4.5 μm data (SpUDS; PI J. Dunlop). Photometric redshifts were determined by fitting spectral energy distribution (SED) templates to the photometric data points. The resulting dispersion is $\Delta z/(1+z) = 0.031$.

The SpUDS survey is a 1 deg^2 Cycle 4 *Spitzer* Legacy program that encompasses the UDS field. I used the SpUDS 3.6 and $4.5\,\mu$m catalogues created by D. Wylezalek, detailed in Wylezalek *et al.* (2013). These were extracted from the public mosaics in the same way as for the CARLA survey. She created catalogues using SExtractor in dual-image mode, using the $4.5\,\mu$m image as the detection image. The SpUDS data reach 3σ depths of ~ 24 mag at both 3.6 and 4.5 μm, but in this work I only use sources down to the shallower depth of the CARLA data.

The i' band data covering the 0.8 deg^2 UDS was obtained as part of the SXDS and resampled and registered onto the UDS K-band image by the UDS team (PI O. Almaini, see Cirasuolo *et al.*, 2010). The 5σ limiting depth is $i' = 27.2$ mag, but I only use sources down to the shallower depth of the CARLA fields. Any source with i' magnitude fainter than the median depth is limited to $1\sigma_{med}$. I measured fluxes in the same way as for the CARLA sample, using positions from the $4.5\,\mu$m catalogue and measuring fluxes using the IDL APER routine with 2.5 arcsec diameter apertures.

2.2.3 Selection of high redshift galaxies

The cluster membership of the galaxies in the CARLA fields is not yet known, therefore I determined the average $i' - [3.6]$ colours of the cluster members by statistically subtracting the back- and foreground galaxies. Statistical subtraction is most accurate when the cluster members are the dominant population in the sample; however, for the high redshift CARLA clusters, the number of interloping galaxies outweighs the number of cluster members. I therefore made a spatial cut and two colour cuts to pre-select galaxies that are most likely to be cluster members. These cuts are explained in the following two subsections.

2.2.3.1 Spatial selection

To select the highest fraction of (proto)cluster galaxies to interlopers, I only considered sources within 1 arcmin of the central RLAGN for each CARLA field because Wylezalek *et al.* (2013) showed that the galaxy density was highest within this region. At these redshifts, 1 arcmin is ~ 500 kpc in physical coordinates. In co-moving coordinates this corresponds to ~ 1.8 Mpc radius at $z \sim 3$ and ~ 1.2 Mpc radius at $z = 1.3$. This decreasing co-moving radius with time traces the expected collapse of the cluster. Although protoclusters always collapse in the co-moving reference frame, in physical and angular coordinates the size of the protocluster remains approximately constant across $1.3 < z < 3.2$ as gravity is almost balanced by the Hubble expansion (for a full explanation see Muldrew, Hatch & Cooke, 2015). Whilst my 1 arcmin aperture can only capture a fraction of these protoclusters, it encloses approximately the same fraction at all redshifts between $z = 1.3$ and $z = 3.2$. Assuming the CARLA clusters all have approximately the same $z = 0$ mass (see Section 2.3.2.2), this means that I select the same fraction of the (proto)clusters at each redshift.

2.2.3.2 Colour cuts at $z > 1.3$

Without spectroscopic measurements I cannot ascertain true cluster membership; however, with the available photometry I can remove low redshift foreground contaminants. I used the *Spitzer* IRAC colour cut $[3.6] - [4.5] > -0.1$ (Papovich, 2008) to

select sources at $1.3 < z < 3.2$. Hereafter I refer to these mid-infrared colour-selected sources as "IRAC-selected sources", as explained in Section 1.4. This colour cut effectively selects galaxies at $z > 1.3$, with only 10–20% contamination from foreground sources (Muzzin *et al.*, 2013). Potential contaminants include strongly star-forming galaxies at $0.2 < z < 0.5$ and powerful AGN at all redshifts. To remove these bright interlopers, as well as other bright foreground sources, I applied a further cut of $i' - [3.6] > -0.5 \times [3.6] + 11.4$, shown in Figure 2.1 by the red line. I derived this line from UDS data, using the photometric redshift information to determine where foreground contaminants are most likely to lie in colour-magnitude space. From the UDS, I derived contours of the probability of a source lying at $z < 1.3$. This cut is a linear fit to the contour corresponding to a $\geq 80\%$ likelihood of a source lying at $z < 1.3$. This cut removes the brightest foreground contaminants while retaining 99% of the IRAC-selected sources, likely to lie at $z > 1.3$. Throughout the rest of this chapter I refer to the IRAC-selected sources which have colours above these cuts as my "high redshift sample". After applying these colour cuts, the CARLA fields are 1.5–2 times the density of the average field. Given the fact that I am observing a very deep cylinder (from $z \sim 1.3$), and a typical protocluster is at most ~ 40 Mpc (co-moving diameter) deep (Muldrew, Hatch & Cooke, 2015), an overdensity level of 2 times the field is quite extreme, meaning these structures are highly likely to be forming clusters.

2.2.3.3 Mass cuts

The CARLA survey covers a wide redshift range, from 2 Gyr to 7 Gyr after the Big Bang ($1.3 < z < 3.2$), to the same flux limit, so we are likely to detect more low-mass galaxies at low redshifts than at high redshifts. This may bias our results by giving a bluer average colour at low redshift simply because we can probe further down the mass function than at high redshift, and there is a correlation between mass and red fraction (Bamford *et al.*, 2009; Foltz *et al.*, 2015). In order to better compare these clusters across redshift, we select galaxies with stellar masses of $M_* > 10^{10.5}\,\mathrm{M}_\odot$ at each redshift[2].

[2]Note that taking a $10^{10.5}\,\mathrm{M}_\odot$ mass cut does not fully account for progenitor bias (Mundy, Conselice & Ownsworth, 2015). The lower mass progenitors of $M_* = 10^{10.5}\,\mathrm{M}_\odot$ galaxies at low redshift will not be selected by my mass cut at high redshift. This means that there will be additional galaxies that enter the sample at low redshift that are not detected at high redshift. These low mass objects will typically

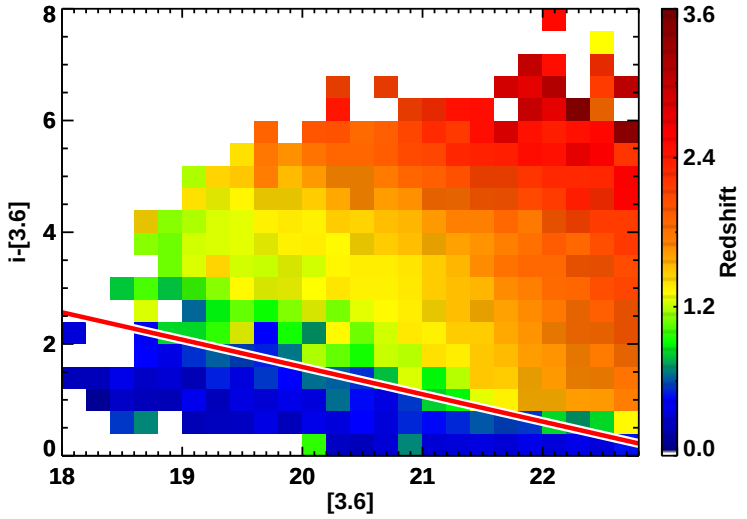

Figure 2.1: Distribution of UDS sources by redshift in colour-magnitude space. Each pixel's colour represents the mean redshift of all the sources within that pixel. I employ a colour-magnitude cut, shown by the red line, to remove bright foreground contaminants, whilst retaining 99% of the IRAC-selected sources.

I used the $[3.6]$ magnitude and $i' - [3.6]$ colour as a mass proxy to approximate stellar mass. For redshifts $0.1 < z < 3.2$ in steps of $\Delta z = 0.1$, I determined a line in the $(i' - [3.6])$-$[3.6]$ plane for a $10^{10.5}\,\mathrm{M}_{\odot}$ galaxy using Bruzual & Charlot (2003) models. I used stellar population models with exponentially declining star formation models following $\mathrm{SFR} \propto e^{-t/\tau}$ with τ of 0.01, 0.1, 0.5, 1 and $10\,\mathrm{Gyr}$. For all models solar metallicity and a Chabrier (2003) initial mass function are assumed. These models were created by N. Hatch, who produced SEDs of these models at a variety of ages since the onset of star formation, ranging between 0.5 and $12\,\mathrm{Gyrs}$ in $0.5\,\mathrm{Gyr}$ steps (but not allowing the model to be older than the age of the Universe). I then fit a best-fit line to these models and used these as the mass cuts for each redshift bin. I applied these mass cuts to each (proto)cluster, according to its redshift, which are shown as dotted lines in Figure A.1. For clusters with $z < 1.3$, an evolving $[3.6]$ magnitude limit was also applied, to avoid faint, low mass galaxies entering the sample. This magnitude limit was calculated, using the same models as above, as the faintest possible magnitude that a $10^{10.5}\,\mathrm{M}_{\odot}$ galaxy could have at each redshift.

have bluer colours, which may cause the measured colours to be progressively bluer at lower redshifts. An evolving mass cut, or a constant number density selection would provide a more accurate measure of the evolution of the $\langle i' - [3.6] \rangle$ colour, however these cuts are dependent on the galaxy evolution model adopted and are beyond the capabilities of the current data.

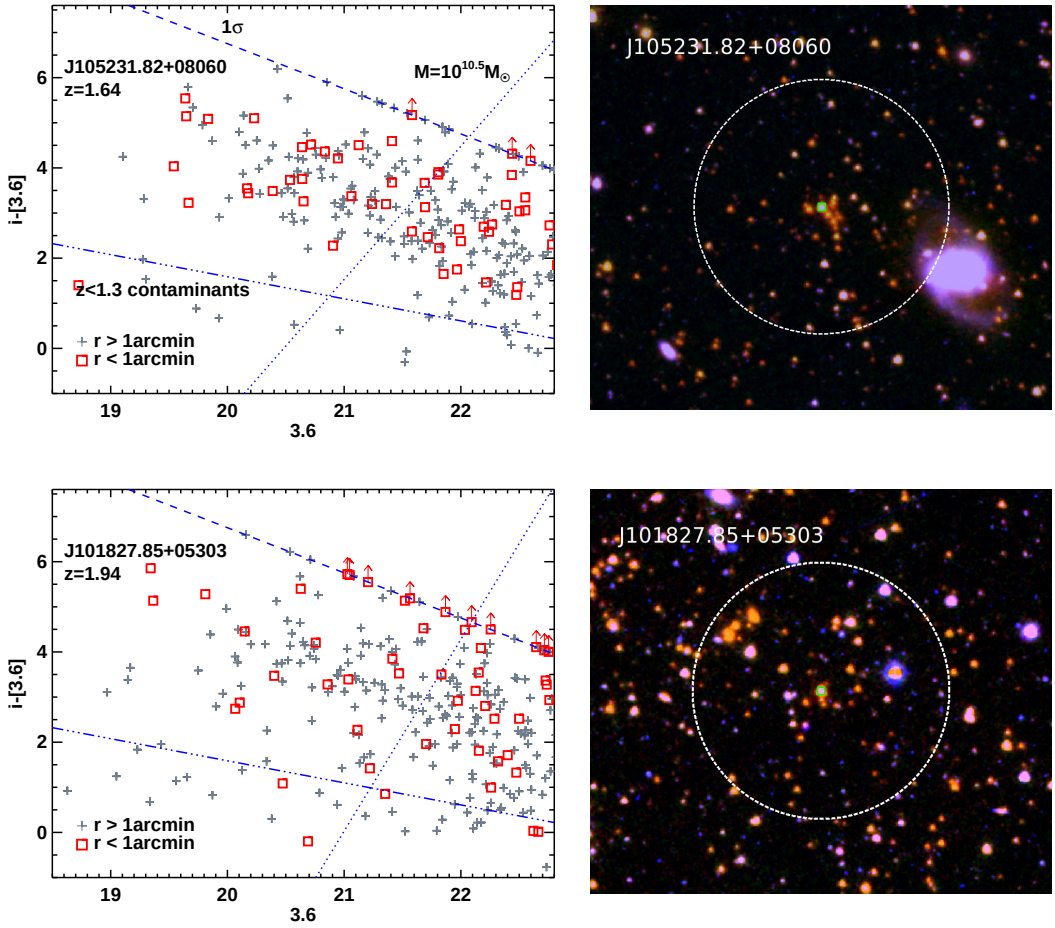

Figure 2.2: *Left:* $i' - [3.6]$ colour-magnitude diagrams for J105231.82+08060 at $z = 1.64$ and J101827.85+05303 at $z = 1.94$, two of the 37 CARLA fields. J105231.82+08060 appears to show a dense core of red galaxies, indicating that the red sequence is being populated, whereas the red sources in J101827.85+05303 are more spread out across the field. Red squares show sources within 1 arcmin of the RLAGN. Grey plus symbols show those sources lying further than 1 arcmin from the RLAGN, which are more likely to be contaminants. The blue dashed lines show the 1σ i' median depth. Sources fainter than the 1σ median depth are set to $1\sigma_{med}$ and shown as lower limits. The dotted blue lines show a $M_* > 10^{10.5}$ M$_\odot$ mass cut and the dash-triple dotted blue lines show the cut used to remove low redshift contaminants. The RLAGN in these fields are too bright to fit on this scale and are not shown. No sources have been removed through statistical subtraction here. The colour-magnitude diagrams of the other 35 CARLA targets are shown in Appendix A. *Right:* i',[3.6],[4.5] three-colour images of J105231.82+08060 and J101827.85+05303, showing the 1 arcmin radius apertures, within which cluster galaxies are selected. The central RLAGN is marked with a green square.

2.2.4 Colours of (proto)cluster galaxies

In Figure 2.2 I show the colour-magnitude diagrams of two of the CARLA fields, J105231.82+08060 (imaged with GMOS-S) and J101827.85+05303 (imaged with ACAM) at $z = 1.64$ and $z = 1.94$, along with their i', $[3.6]$, $[4.5]$ three-colour images. Red squares show sources within 1 arcmin of the RLAGN, and grey plus symbols show those sources lying further than 1 arcmin from the RLAGN, which are likely to contain a higher fraction of field contaminants. The blue dashed lines show the 1σ i' median depth. Due to the depth of the i' data I cannot probe the faint red population, although at these redshifts the red sequence is depleted at faint magnitudes (e.g. Papovich *et al.*, 2010). The faint red sources shown as limits are also likely to be cluster members. The dotted blue lines in Figure 2.2 show the mass cut used to select galaxies with $M_* > 10^{10.5}\,\mathrm{M}_\odot$, as described in Section 2.2.3.3. The colour-magnitude diagrams of the remaining CARLA clusters are shown in Appendix A.

I measured the median $i' - [3.6]$ colour of the CARLA cluster galaxies (used in Section 2.3) by dividing the colour-magnitude diagram of the clusters into grid cells (see Figure 2.3) and statistically subtracting the expected number of field galaxies in each grid cell before taking the median colour of the remaining galaxies. The full method is as follows:

I used the UDS data to derive the average number of sources expected from field contamination, and their expected distribution in $i' - [3.6]$ vs. $[3.6]$ colour-magnitude space. Colour-magnitude diagrams were calculated for 401 randomly located 1 arcmin radius regions in the UDS. The colour-magnitude diagrams of the 401 random UDS regions were then divided into twelve grid cells (Figure 2.3) and the mean number of sources in each cell was measured ($\mu_{cell}^{\mathrm{UDS}}$).

In order to statistically remove field contaminants, I removed randomly-selected sources from each (proto)cluster field before calculating the median $i' - [3.6]$ colour of the remaining sources. The total number of randomly-selected sources removed each time was taken from a Gaussian centred on $\mu_{total}^{\mathrm{UDS}}$ with a width of $\sigma_{total}^{\mathrm{UDS}}$, helping to deal with sample variance in interloper galaxies[3]. This was repeated for 1001 iterations to give

[3] $\sigma_{total}^{\mathrm{UDS}}$ was measured from the number distribution of all sources in the 401 random regions, before applying the grid.

an overall median colour.

To vary the number of interlopers subtracted from each cell so that overall $\mu_{total}^{\rm UDS} \pm \sigma_{total}^{\rm UDS}$ were subtracted, the standard deviation of the number of sources per cell was used and normalised such that $\sum \sigma_{cell}^{\rm UDS} = \sigma_{total}^{\rm UDS}$. This ensures that the distribution of field galaxies in colour-magnitude space was taken into account, but field contamination was not overestimated and only $\mu_{total}^{\rm UDS} \pm \sigma_{total}^{\rm UDS}$ sources were subtracted. All values were calculated after applying the appropriate mass cut for the CARLA field being investigated, so the field and cluster were treated in the same way throughout.

I calculated the mean colours in the same way, though sources with i' band magnitudes fainter than $1\,\sigma_{med}$ were set equal to $1\,\sigma_{med}$ value (shown as lower limits in Figure 2.2). The mean $i' - [3.6]$ colours typically differ by ~ 0.13 mag compared with the median colours and at most differ by ~ 0.34 mag. The median colours are typically redder than the means, with seven exceptions ($> 80\%$ are redder). In the remainder of this chapter I use the median colours in order to avoid biasing my results, but there is good agreement between the mean and median colours.

The median and mean $[3.6] - [4.5]$ colours were measured similarly, dividing the $([3.6] - [4.5])$-$[3.6]$ colour-magnitude diagrams into cells and statistically removing field contamination. The median $[3.6] - [4.5]$ colours are used throughout this chapter.

2.2.5 Low & intermediate redshift cluster sample

In order to compare the results of the high redshift CARLA clusters presented in this chapter to lower redshift clusters, I use photometric catalogues, created by M. Brodwin, from the IRAC Shallow Cluster Survey (ISCS; Eisenhardt *et al.*, 2008), covering the Boötes region of the NOAO Deep Wide-Field Survey (NDWFS; Jannuzi & Dey, 1999). In Eisenhardt *et al.* (2008) 335 cluster and group candidates were identified spanning $0 < z \lesssim 2$. These form a low and intermediate redshift cluster comparison sample. I also include in my sample two higher redshift clusters discovered in the same sky region by the IRAC Distant Cluster survey (IDCS; the deeper IRAC extension of the ISCS), at $z = 1.75$ (Stanford *et al.*, 2012; Brodwin *et al.*, 2012; Gonzalez *et al.*, 2012) and $z = 1.89$ (Zeimann *et al.*, 2012).

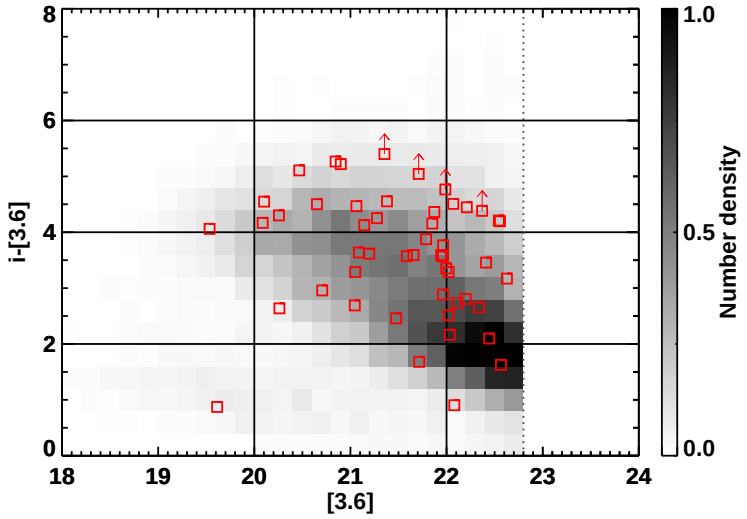

Figure 2.3: Example of the grid cells used in calculating the average $i' - [3.6]$ colour of each cluster. In each cell, $\mu_{cell}^{\rm UDS} \pm \sigma_{cell}^{\rm UDS}$ sources from each cluster field were removed iteratively before calculating the average colour, in order to statistically remove the field sources in each CARLA (proto)cluster candidate region. This grid is as fine as possible, whilst still ensuring a significant number of sources in each cell. To guide the eye, shading shows the normalised number density distribution of IRAC-selected UDS sources. The depth of the 3.6 μm images is shown by the dotted line. Also overlaid are red points showing the colour-magnitude diagram of J213638.58+00415 at $z = 1.94$. See Appendix A for full details of the colour-magnitude diagrams.

I converted the I magnitudes from the NDWFS[4] (Eisenhardt *et al.*, 2008) to SDSS i' magnitudes using the $R - I$ colours:

$$i' = 0.004 + 0.46(R - I) + I \tag{2.1}$$

I derived this conversion using Bruzual & Charlot (2003) models with both exponentially declining star formation models following a star formation rate $({\rm SFR}) \propto e^{-t/\tau}$ with τ of 0.01, 0.1, 0.5, 1 Gyr and simple stellar population models where stars form in a single burst at high redshift and passively evolve thereafter. I convolved these models with the appropriate KPNO/Mosaic-1 and Sloan filters to measure magnitudes. A linear equation was then fit to the model galaxy $(R - I)$ and $(i' - I)$ colours.

For the low and intermediate redshift sample, galaxies were selected if they reside within 1 arcmin of the cluster centre and have a *Spitzer* IRAC colour of $[3.6] - [4.5] \leq 0$ for clusters with $0 < z < 1.3$, thus removing contaminants at higher redshifts.

[4]The NDWFS used the Kitt Peak National Observatory Mayall 4 m telescope with the Mosaic-1 camera.

Selecting galaxies within a constant 1 arcmin radius of the cluster centre at $z < 1.3$ corresponds to an increasingly smaller fraction of the (proto)cluster towards lower redshift (Muldrew, Hatch & Cooke, 2015). This effect is small (at most an 8% decrease in the area observed between $z = 1.3$ and $z = 0.5$; Muldrew, Hatch & Cooke, 2015), however it may bias my selection towards the very core of the lowest redshift clusters, and potentially bias my colours to those of the most massive cluster galaxies, with the reddest colours, due to the SFR-density relation. This effect is unlikely to cause a bias in my results for two reasons: first, I am only selecting the most massive cluster galaxies in each cluster, which are likely to be in the central cluster regions anyway. Secondly, Eisenhardt *et al.* (2008) used a constant physical radius for their cluster galaxy selection. This would have the opposite effect: selecting a larger fraction of the lower redshift clusters. My results for the ISCS clusters agree with the results found in Eisenhardt *et al.* (2008) and thus are unlikely to be biased by my choice of aperture size.

I treated the clusters at $z > 1.3$ in exactly the same way as the 37 CARLA clusters, as described above. Mass cuts of $M_* > 10^{10.5}\,\mathrm{M}_\odot$ were taken for all clusters, as I have described in Section 2.2.3.3.

2.2.5.1 Testing the method

The average $i' - [3.6]$ colours for the ISCS clusters are shown in Figure 2.4. Although no cluster membership information is used in this study, the average cluster galaxy colours agree well with those found in Eisenhardt *et al.* (2008) who used photometric and spectroscopic redshifts to determine cluster membership. The trend of increasing $i' - [3.6]$ colour with redshift agrees with a formation redshift for these cluster galaxies of $z_f \sim 3$, showing larger scatter in the colours at higher redshift, as found in Eisenhardt *et al.* (2008). This proves that the statistical subtraction method I used to measure average cluster galaxy colours can replicate the results found when cluster membership information is taken into account.

Four clusters lie significantly off the $z_f = 3$ trend at $z \sim 0.4$ (shown with light grey crosses in Figure 2.4). I visually inspected the colour-magnitude diagrams for these clusters and found they showed secondary structures at higher redshift, which have

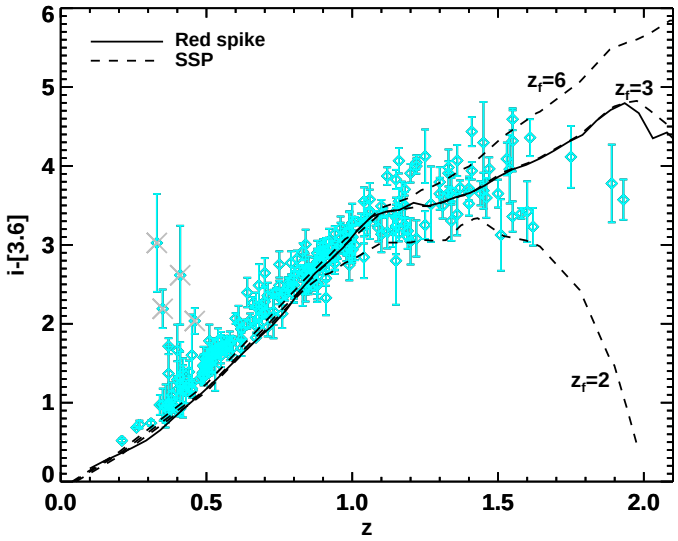

Figure 2.4: Average $i' - [3.6]$ colours for the ISCS clusters, measured in the same way as for the 37 CARLA clusters. Overlaid is a "red spike" model (solid line), where stars are formed in a 0.1 Gyr burst beginning at $z_f = 3$, as in Eisenhardt *et al.* (2008). Also shown are simple stellar population (SSP) models, where stars form in a delta burst at $z_f = 2$, 3, 6 (dashed lines). There is very little difference in the resulting colours of the red spike model and a SSP with $z_f = 3$. The measured colours agree with a formation redshift for these cluster galaxies of $z_f \sim 3$, in agreement with Eisenhardt *et al.* (2008), however note the degeneracies between the different models at $z \lesssim 1$. Points overlaid with grey crosses show low redshift clusters whose colours are affected by secondary overdensities at higher redshift, which have colours of $i' - [3.6] \sim 4$.

colours of $i' - [3.6] \sim 4$. Since I cannot separate out and remove these potential higher redshift clusters using my method, I instead removed these four clusters from the ISCS sample. At $z < 1$ the ISCS data lies slightly above the model. This is due to the mass cut I employed, which selects just the most massive galaxies in order to be consistent with the higher redshift data. This slight offset is expected from Eisenhardt *et al.* (2008), where the most luminous (massive) cluster galaxies were systematically redder than simple stellar population models due to the mass-metallicity relation.

2.3 Results

2.3.1 Median colours of the CARLA cluster galaxies

The median $i' - [3.6]$ and $[3.6] - [4.5]$ colours of the CARLA clusters are plotted as a function of redshift in Figure 2.5. For each field, I used the redshift of the central RLAGN as the cluster redshift. I also plot the colours for two spectroscopically con-

firmed clusters, for comparison: CLG 0218.3−0510 at $z = 1.62$ (Tanaka, Finoguenov & Ueda, 2010; Papovich *et al.*, 2010) and the protocluster around the Spiderweb radio galaxy, PKS 1138−262 at $z = 2.156$ (Pentericci *et al.*, 2000). I measured their colours in the same way as described in Section 2.2.4.

In the bottom panels of Figure 2.5 I plot the characteristic $[4.5]$ magnitude, $m^*_{[4.5]}$, measured by Wylezalek *et al.* (2014). Wylezalek *et al.* (2014) studied the luminosity functions of CARLA clusters within three density bins. Since most of the CARLA clusters in our present study are more than 4σ denser than the average field, I use the $m^*_{[4.5]}$ derived for the highest density bin used in the Wylezalek *et al.* (2014) study.

To determine the galaxy formation history of the clusters I compare the average $i' - [3.6]$, $[3.6] - [4.5]$ colours and $m^*_{[4.5]}$ values to three simplistic models (see Figure 2.6): simple burst models (SSP; Section 2.3.2), exponentially declining models (CSP; Section 2.3.3) and multiple burst models (mSSP; Section 2.3.4). I generated model galaxies using the publicly available model calculator, EzGal (Mancone & Gonzalez, 2012), with Bruzual & Charlot (2003) models[5] normalized to match the observed m^* of galaxy clusters at $z \sim 0.82$, $[4.5] = 19.82$ (AB) (Mancone *et al.*, 2012). The scatter in the average $[3.6] - [4.5]$ colours is very large, ~ 0.2 mag, meaning it is difficult to constrain a formation history using these colours. They are consistent with all the models I examine in the following sections and therefore I do not discuss them further.

In Section 2.2.3.3 I used Bruzual & Charlot (2003) models with exponentially declining star formation rates to ascertain mass cuts in colour-magnitude space for each of the CARLA fields. In the following sections I examine different star formation histories. Here I briefly examine the effect of using different models in the mass cuts to those fit to the average colours. I consider two extremes: using an exponential model with $\tau = 10$ Gyr and an SSP model, with an effective $\tau \leq 0.01$ Gyr. Using just an exponential model with $\tau = 10$ Gyr would cause the mass cut line to move to brighter $[3.6]$ magnitudes, and redder $i' - [3.6]$ colours. This would cause the average cluster galaxy colour to be redder in Figure 2.5. This would result in large discrepancies between the data colours and those predicted by the models. On the other hand, using an exponential model with $\tau = 0.01$ Gyr would result in a mass cut which selected

[5] I have also tested my models using Maraston (2005) models (see Section 2.3.5) but find that the Bruzual & Charlot (2003) models provide a better fit to my data.

fainter and bluer galaxies, causing a shift to bluer colours in the data, although only very slightly, within the errorbars at the highest redshifts as the mass cut line is already selecting very faint and blue galaxies. This would thus not solve the discrepancy between the data and SSP models at $z > 2.5$. It is likely that the true star formation histories of the CARLA clusters are varied and so taking an average mass cut from a range of star formation histories is reasonable, and does not affect our conclusions.

2.3.2 Comparing the CARLA clusters to a Simple Stellar Population model

2.3.2.1 Model description

The first model I examined is a single simple stellar population (SSP), where galaxies form in an instantaneous burst (hereafter referred to as a delta burst) at z_f and passively evolve thereafter (see the top panel of Figure 2.6). Such a model is commonly used in the literature to estimate the formation epoch of cluster galaxies and provides a good fit to the $z < 1.5$ data (see Figure 2.4).

In the left hand column of Figure 2.5 I compare the SSP models with a range of formation redshifts to the average $i' - [3.6]$ colours of the CARLA clusters, as well as the average $[3.6] - [4.5]$ colour and the characteristic magnitudes $m^*_{[4.5]}$. Whereas the SSP model with $z_f = 3$ agrees with the $m^*_{[4.5]}$ values well at all redshifts, no SSP with a single formation redshift is able to match the $i' - [3.6]$ colour data. For the CARLA clusters at $z \lesssim 2.5$ a formation redshift of $z_f \sim 2.5$–3 seems to fit the average $i' - [3.6]$ colours well. For clusters at higher redshifts, however, the measured average colour seems to imply a higher formation redshift. This means that, either the basic SSP model is a poor representation of the galaxy formation history of clusters above $z \sim 1.3$; or the CARLA clusters selected at $z \sim 3$ formed earlier than those at $z \sim 1.5$, and thus they do not all lie on one evolutionary sequence. I explore which of these scenarios is likely to be the case in the following section.

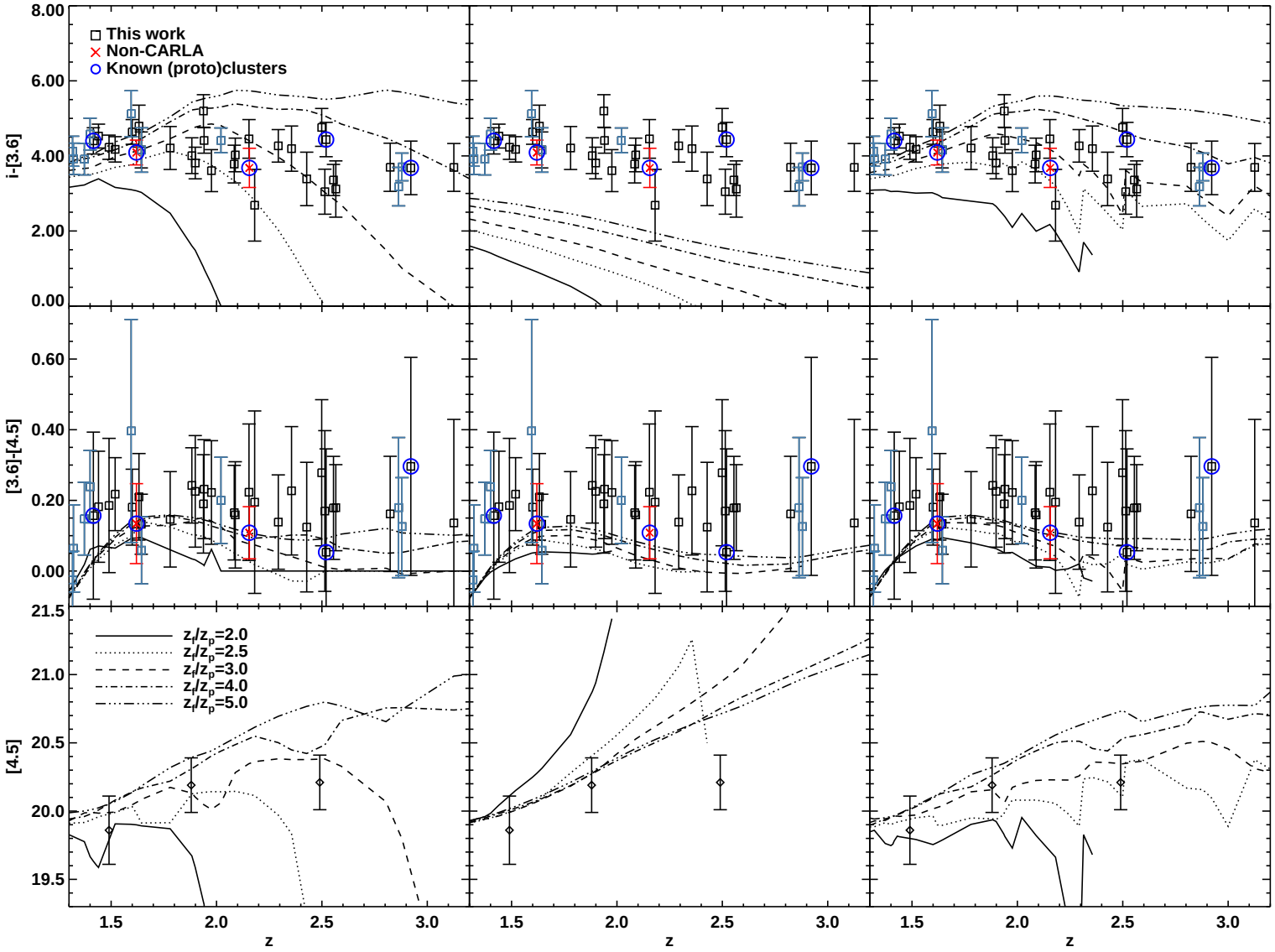

Figure 2.5: *Left:* SSP models. *Centre:* CSP models: exponentially declining models with an e-folding time of 1 Gyr. *Right:* mSSP models: multiple, normally distributed, bursts of star formation with $z_{peak} = z_p$ and FWHM = 1 Gyr. Each column shows the predicted $i' - [3.6]$, $[3.6] - [4.5]$ and $m^*_{[4.5]}$ for z_f (z_p for mSSP) $= 2.0, 2.5, 3.0, 4.0, 5.0$. Overlaid are the data points from the CARLA clusters (black squares), as well as two non-CARLA (proto)clusters from previous studies (red crosses). Confirmed (proto)clusters are circled in dark blue. *Top:* The $i' - [3.6]$ colours. The points show the median and errorbars represent the standard deviation of the median from 1001 iterations plus a 10% error in the fluxes. *Middle:* The $[3.6] - [4.5]$ colours. Points show the median source colour and the error on the median. A 20% error on the flux measurements is not shown, but would add 0.3 mag to the error bars. *Bottom:* The $m^*_{[4.5]}$ data points in the highest density bin from Wylezalek *et al.* (2014). In the top two panels, grey-blue points show those (proto)clusters which lie significantly off the trend found in Figure 2.7.

2.3.2.2 Are CARLA clusters an evolutionary sequence?

The CARLA survey imaged over 400 high redshift RLAGN across the entire sky. From this survey, nearly 200 RLAGN appear to be located in regions denser than 2σ above average (Wylezalek *et al.*, 2013). Finally, from these $\sim$ 190 (proto)cluster candidates I selected the 37 most overdense observable candidates in every redshift bin. Therefore, through my selection method, I have isolated some of the most overdense (proto)clusters across $1.3 \leq z \leq 3.2$. According to hierarchical structure formation, the most overdense regions at $z = 3$ should evolve into the most overdense regions at $z = 1.3$ (and subsequently $z = 0$), albeit with a large amount of scatter (Chiang, Overzier & Gebhardt, 2013). So I expect the CARLA (proto)clusters in this study to form an approximate evolutionary sequence, with the high redshift protoclusters being the statistical ancestors of the lower redshift clusters in my sample.

To test this hypothesis, I examined the galaxy growth within the CARLA clusters. With the red crosses in Figure 2.7, I show the overdensity (left panel) and abundance (right panel) of $M_* > 10^{10.5}\,\mathrm{M}_\odot$ galaxies within $1\,\mathrm{Mpc}$ of the RLAGN. These red points show a trend of increasing overdensity and abundance towards lower redshift, with a Spearman's rank correlation coefficient of $r = -0.72$. This is a highly significant trend with a p-value of 5.5×10^{-7}.

This trend was not artificially introduced by the mass cuts, which evolve with redshift. I tested this by randomly reassigning the redshifts to the 37 CARLA clusters, which in turn randomised the mass cut line taken for each cluster. I iterated this 1000 times and re-examined the trend of increasing overdensity with redshift. The randomized samples produce a very weak correlation of median value $r = -0.29$, which is not significant (median p$= 0.08$). Therefore, randomising the redshifts (and therefore the mass cut) for each cluster does not produce a significant trend with redshift.

Furthermore, this trend is not due to massive galaxies entering the cluster from the outskirts region, because the 1 arcmin apertures contain the same fraction of the (proto) clusters at all redshifts between $z = 3.2$ and $z = 1.3$. Chiang, Overzier & Gebhardt (2013) show that most of cluster collapse occurs at $z > 1$ when viewed in the co-moving reference frame. However, in physical units, the cluster's effective radius stays relatively stable until $z \leq 1$ because gravity is almost balanced by the Hubble ex-

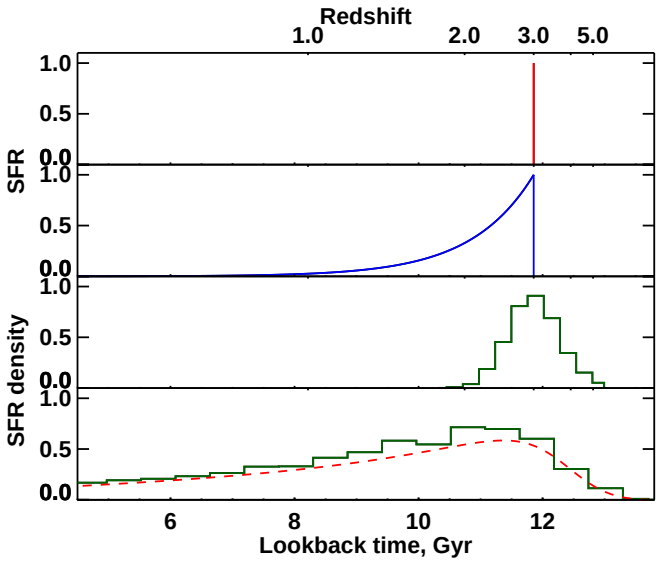

Figure 2.6: Cartoon representation of the three models described in Sections 2.3.2–2.3.4, as well as a model based on the star formation rate density of the Universe, described in Section 2.4.2. *Top:* SSP model: stars form in a single delta burst at $z_f = 3$ and passively evolve thereafter. *Upper middle:* CSP model: the galaxy undergoes an exponentially decaying SFR ($SFR \propto \exp -t/\tau$) starting at $z_f = 3$, with $\tau = 1$ Gyr. *Lower middle:* mSSP model: galaxies are formed in multiple bursts of star formation, normally distributed in time around $z_{peak} = 3$ with FWHM$= 1$ Gyr. The green histogram illustrates the relative fraction of galaxies that are formed in each time interval. *Bottom:* Multiple burst model where the distribution of galaxies follows the cosmic star formation rate density, see Section 2.4.2 for details. As above, the histogram illustrates the relative fraction of galaxies that are formed in each time interval.

pansion (Muldrew, Hatch & Cooke, 2015). The 1 arcmin radius (~ 0.5 Mpc physical) apertures used in this chapter track the same fraction of the (proto)clusters across the $1.3 < z < 3.2$ epoch. Thus, the trend in Figure 2.7 is not caused by cluster collapse, but rather is due to galaxy growth within the (proto)clusters.

In hierarchical cosmology it takes time for massive galaxies to assemble, therefore we can use the abundance of massive galaxies as a proxy for cluster maturity. The increase in massive galaxy abundance therefore suggests an increase in cluster maturity. To test this hypothesis I compared the trend in Figure 2.7 to the expected galaxy growth within semi-analytic models. I use the Guo *et al.* (2011) semi-analytic model built upon the Millennium Dark Matter Simulation (Springel *et al.*, 2005). A full description of the models and identification of (proto)cluster members is provided in Chapter 4 and Muldrew, Hatch & Cooke (2015). This catalogue was created by S. Muldrew; he traced 1938 clusters with $z = 0$ halo masses of $> 10^{14}\,h^{-1}\,\mathrm{M}_{\odot}$ back in time and traced their member galaxies. At each output redshift he counted the number of progenitor galaxies with $M_* > 10^{10.5}\,h^{-1}\,\mathrm{M}_{\odot}$. I then used this catalogue to create the solid black line in

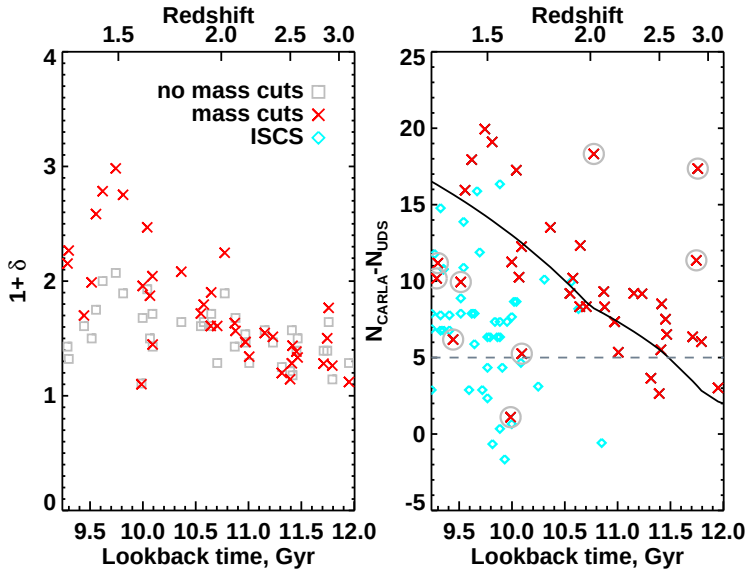

Figure 2.7: Left: $1+\delta = N_{\rm CARLA}/N_{\rm UDS}$ for the clusters as a function of time. Grey points show the original densities, without taking any mass cuts. Red points show the densities after taking a $10^{10.5}\,{\rm M}_{\odot}$ mass cut. There is a significant trend of increasing density over time. Clusters which do not lie on this trend are unlikely to be the progenitors/descendants of those on the trend. Right: $N_{\rm CARLA} - N_{\rm UDS}$. This shows how the number of galaxies within 1 arcmin of the RLAGN with M$> 10^{10.5}\,{\rm M}_{\odot}$ increases with time. The black line shows the expected evolution of the number of massive (proto)cluster galaxies from semi-analytic models. Blue points show the ISCS clusters, discussed in Section 2.4.5. Highlighted with grey circles are clusters that lie significantly off the expected trend for the CARLA clusters and thus are unlikely to form part of the evolutionary sequence.

Figure 2.7. This shows the evolution of the number of $M_* > 10^{10.5}\,{\rm M}_{\odot}$ (proto)cluster galaxies from the semi-analytic models, normalised to the least squares fit to the data. Although the detailed physics of the semi-analytic models is uncertain, the general trend is in good agreement with the data. This provides compelling evidence that the growth in abundance of massive galaxies within these CARLA clusters suggests that they are likely to form an evolutionary sequence: the high redshift protoclusters could be the statistical ancestors of the lower redshift clusters in this sample.

2.3.2.3 High redshift cluster colours are not well-explained by SSP models

I have shown that the increase in abundance of massive galaxies within the CARLA clusters follows the expected trend of galaxy growth within forming clusters. I therefore suggest that these CARLA clusters lie on an approximate evolutionary sequence, i.e. the lower redshift clusters have the expected properties of the descendants of the higher redshift protoclusters in our sample. Therefore the colour data in Figure 2.5

must be fit by a single formation model. However, although a single SSP of any $z_f > 2$ fits the colours of $z < 1.5$ cluster galaxies, at high redshift, one formation epoch cannot be fit to all the data across $1.3 < z < 3.2$. This implies that cluster galaxies did not form concurrently at high redshift, but rather a more complex formation history is required.

2.3.3 Composite Stellar Population model

2.3.3.1 Model description

In order to try to fit the unevolving colour in the data, I next examined a composite stellar population (CSP), where each of the galaxies undergo an exponentially decaying SFR ($SFR \propto \exp -t/\tau$) starting at z_f, with an e-folding timescale τ. This is represented by the upper-middle panel of Figure 2.6. CSP models were examined with τ =0.1, 1 and 10 Gyr. All galaxies are assumed to have formed concurrently. The short e-folding time of $\tau = 0.1$ Gyr gives similar results to the SSP models, and the $\tau = 10$ Gyr models cannot produce $i' - [3.6]$ colours redder than 1.5. The CSP models with $\tau = 1$ Gyr are shown in the centre column in Figure 2.5. Formation redshifts of $z_f > 5$ were also tested, but also produce colours which are too blue to fit the data, with a $z_f = 10$ model reaching a maximum colour of $i' - [3.6] \sim 2$ at $z = 2.5$. CSP models with $z_f > 2$ fit the $m^*_{[4.5]}$ values at low redshift, however they cannot explain the bright magnitudes at $z = 2.5$. Although this model succeeds in producing a flatter $i' - [3.6]$ colour trend with redshift, the colours are still too blue to fit the CARLA data. This means that massive cluster galaxies could not have formed their stars gradually in one long period of star formation unless there is a large amount of dust attenuation.

2.3.3.2 The effect of dust extinction

Dust attenuation in the cluster galaxies will cause their colours to appear redder. Adding dust to the CSP models would make the models redder. Because the models get bluer at higher redshift, in order to fit the flat colour trend of the data, I require a varying amount of dust extinction (A_V) with redshift. Assuming the Calzetti extinction law, to

match the CSP models[6], I would require $A_V \sim 1.8$ at $z = 3$, $A_V \sim 1.3$ at $z = 2$ and $A_V \sim 1.1$ at $z = 1.3$. This level of dust extinction is not extreme for these redshifts (Garn & Best, 2010; Cooke *et al.*, 2014).

A number of recent studies have found large numbers of dusty, star-bursting galaxies in high-redshift (proto)clusters (e.g. Santos *et al.*, 2014, 2015; Dannerbauer *et al.*, 2014). These large numbers do not necessarily mean that the dusty star-forming population represent the majority of the cluster population. Indeed, despite the increase in star-formation rates, Papovich *et al.* (2012) found that the majority of cluster galaxies in the central regions are passive.

The colours plotted in Figure 2.5 are the median values for each cluster. This means that a large fraction of the galaxies would need to be dusty in order to affect the overall median colour I measure. Up to 10% of UDS sources (with all my selection criteria and cuts applied) are detected at $24\,\mu$m. This suggests that the fraction of galaxies in my CARLA sample that are extremely dusty, star-forming galaxies is less than 10%, and therefore are unlikely to affect my measured median colour.

2.3.3.3 CSP models cannot explain CARLA cluster colours

The CSP models shown here do not produce colours which are red enough to explain the observed $\langle i' - [3.6] \rangle$ data. In order to match the data, we require a significant fraction of the cluster population to be dusty, highly star-forming galaxies, and have an average dust attenuation that increases with redshift. Previous studies have shown that a significant fraction of the massive cluster population are likely to be passive (at least up to $z \sim 1.6$), so it is unlikely that these CSP models are correct for this massive cluster galaxy population. Furthermore, significant dust extinction would bring further discrepancy between the models and the values of $m^*_{[4.5]}$.

[6] In order to match the SSP models, I would require a varying amount of dust extinction with redshift, with $A_V \sim 1.8$ at $z = 3$, and $A_V \leq 0.7$ at $z = 1.3$. This amount of dust extinction in passively evolving galaxies is unlikely, due to the lack of on-going star formation.

2.3.4 Multiple Simple Stellar Populations model

I have shown that the epoch of massive cluster galaxy formation has to be extended, but the CSP models which extend the period of star formation cannot fit the data unless I incorporate a significant amount of dust. In order to produce the observed red $\langle i' - [3.6] \rangle$ colours at $z = 3$, at least some of the cluster population must already be passive at high redshift.

2.3.4.1 Model description

In order to produce passive $M > 10^{10.5}\,\mathrm{M}_{\odot}$ galaxies by $z = 3$, I again model galaxy formation as single bursts of star formation. To extend the period of cluster galaxy formation, and produce an approximately unevolving colour trend with redshift, I use multiple simple stellar populations (mSSP), where cluster galaxies are formed in individual, short bursts, with their formation redshifts distributed in time so that the total cluster population forms over the course of a few Gyr. This model is illustrated in the lower-middle panel of Figure 2.6. The green histogram represents the relative fraction of galaxies being formed.

I created mSSP models with 16 model galaxies[7], which each form their stars in delta-bursts, with their formation redshifts normally distributed in time around a peak at redshift z_{peak}. The normal distribution's FWHM is set to 1 Gyr. I then took the median colour of these model galaxies at each redshift. The right hand column of Figure 2.5 shows the mSSP models for the $i' - [3.6]$, $[3.6] - [4.5]$ and $m^*_{[4.5]}$ values with different z_{peak}. Including multiple bursts of star formation flattens the expected $i' - [3.6]$ colour over redshift and provides good agreement with the CARLA data. The $[3.6] - [4.5]$ and $m^*_{[4.5]}$ values are also consistent with $z_{peak} > 2.5$. I also tested this model with varying FWHM and find that the FWHM has to be > 0.9 Gyr in order to provide a good fit to the CARLA data.

[7] On average there are 16 cluster galaxies within 1 arcmin of the RLAGN in each of the 37 CARLA fields, once field contaminants are statistically removed.

2.3.4.2 mSSP model provides a good description of the data

The mSSP model describes the observed $i' - [3.6]$ colours of these CARLA clusters well, and also agrees with the $m^*_{[4.5]}$ values. I conclude that a more extended period of burst-like galaxy formation, spanning at least 1 Gyr, is required to explain the colours of the CARLA cluster galaxies. I have modelled these galaxies as forming in single bursts, but due to the scatter in our data I cannot constrain the individual star formation histories of the cluster members. The median $i' - [3.6]$ colours mean that the galaxies must have ceased their star formation rapidly in order to produce red colours. This bursty appearance could also be produced with a variety of star formation histories, so long as the star formation is rapidly terminated. Investigating these formation histories is beyond the scope of these data; the scatter in the individual colours, as well as the cluster-to-cluster scatter are consistent with most such formation histories. In this chapter I just examine the most basic, burst models. Further work examining the individual colours of confirmed cluster galaxies, rather than the statistical average for the cluster, will be able to further distinguish between different formation histories.

2.3.5 Maraston models

At high redshift ($1.4 < z < 2.7$), the treatment of the asymptotic giant branch (AGB) phase of stellar evolution becomes important in the *Spitzer* wavebands. At these redshifts, the AGB effect is expected to be at a maximum. Maraston *et al.* (2006) showed that the AGB phase of stellar evolution can affect the measured age and mass of high redshift galaxies and produce systematically younger ages than Bruzual & Charlot (2003) models. This effect is unlikely to be significant, as Kriek *et al.* (2010) showed that Bruzual & Charlot (2003) provide better fits to post-starburst galaxy spectral energy distributions than Maraston (2005) models which take into account the effects of AGB stars.

I reproduced the mSSP models (Section 2.3.4) using Maraston (2005) models (Figure 2.8). Models with a Chabrier (2003) IMF were not available for the Maraston (2005) models so I used a Kroupa (2001) IMF, which produces similar results. Qualitatively the Maraston (2005) models show the same trends as the Bruzual & Charlot (2003)

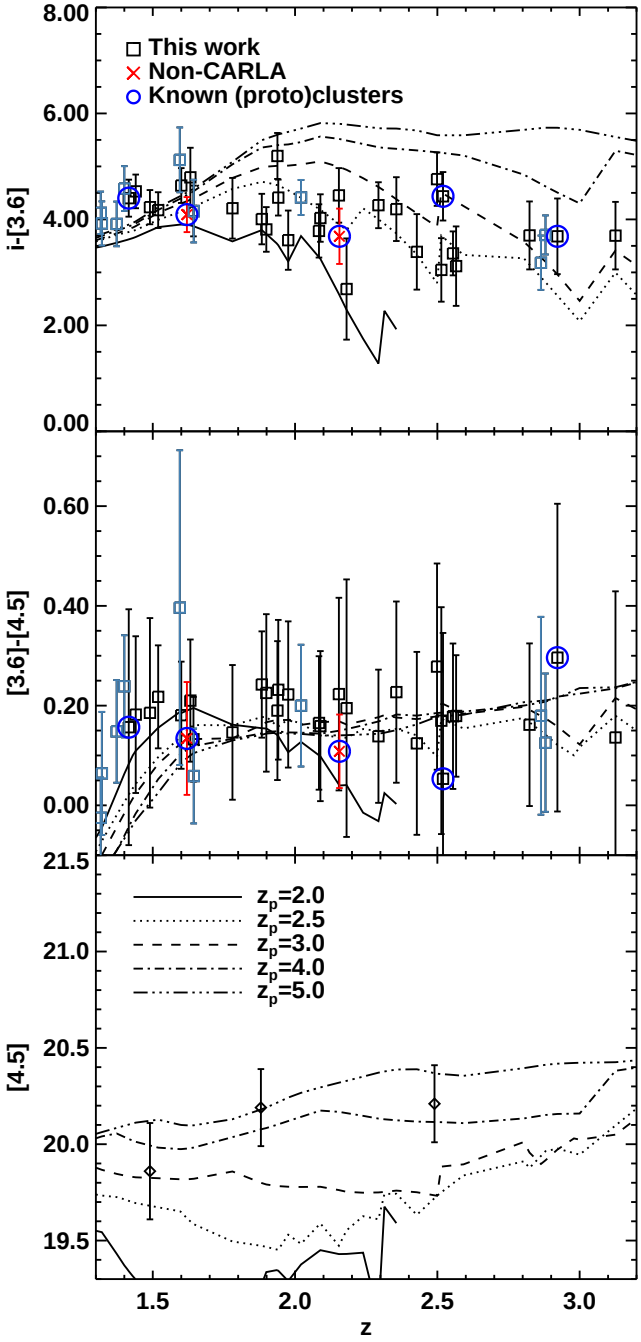

Figure 2.8: The same as the right hand column of Figure 2.5, with Maraston (2005) mSSP models used instead of Bruzual & Charlot (2003) models.

models for the $i' - [3.6]$ colours. The CARLA IRAC colours are better fit by Maraston (2005) models, however the Bruzual & Charlot (2003) models are also consistent within scatter in the colours and flux errors. I used Bruzual & Charlot (2003) models in my analysis as the models of the $[4.5]$ magnitudes and $i' - [3.6]$ colours give a consistent estimate of z_{peak} for the CARLA cluster data, whereas the Maraston (2005) models for the $[4.5]$ magnitudes suggest a much higher z_{peak} than the $i' - [3.6]$ colours.

2.4 Discussion

2.4.1 Clusters undergo extended periods of galaxy formation

I have examined three model star formation histories to fit the colour evolution of (proto)cluster galaxies: a single stellar population, an exponentially declining SFR, and multiple bursts of star formation distributed normally around a peak period at z_{peak}. I find that SSP models (left hand column of Figure 2.5) are unable to account for the red $i' - [3.6]$ colours of cluster galaxies at $z > 2.5$ and the flat colour trend I find at $z > 1.3$ (assuming that these clusters represent one evolutionary sequence; see Section 2.3.2.2). By examining the colours of cluster galaxies at $z > 1.3$ I am able to distinguish the cluster formation histories and have shown that the epoch of galaxy formation in clusters has to be extended; a single formation redshift is not sufficient to produce the colour trend we observe.

I have shown that the $\langle i' - [3.6] \rangle$ colours of these cluster galaxies agree well with a model in which they formed in multiple short bursts over approximately 2 Gyr, peaking at $z \sim 3$. This is consistent with a model where different populations of galaxies form in individual bursts at different times, building up the galaxy population over time, rather than in one, short burst. This model is similar to the composite model from Wylezalek *et al.* (2014) used to explain the luminosity functions of CARLA clusters. Although I claim that the cluster galaxies formed over an extended period of time, my data are not sufficient to further constrain the galaxy formation history due to the relatively large scatter in the average colours. In addition, the large wavelength range probed by the $i' - [3.6]$ colours allows for a variety of star formation histories. A

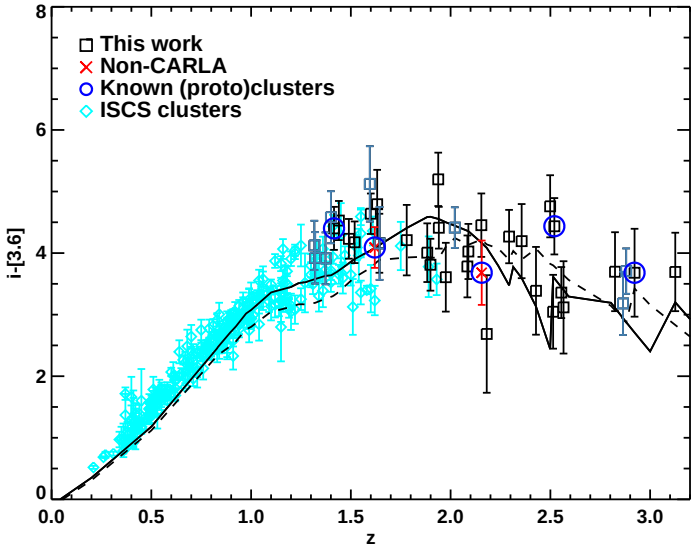

Figure 2.9: The points are the same as in Figure 2.5, also showing the ISCS clusters at lower redshift as cyan diamonds. Overlaid are the mSSP model with multiple bursts of star formation normally distributed around $z_{peak} = 3$, with FWHM$= 1$ Gyr (solid line), and a multiple-burst model following the cosmic star formation history (dashed line). These extended galaxy formation models provide the best fit to our CARLA clusters at high redshift, and also account for the colours observed at lower redshift. The scatter in our data is too large to allow any further distinction between the two extended models.

number of extended galaxy formation models could fit these data (e.g. Figure 2.9).

In order to further analyse the formation history of massive cluster galaxies, I must adopt a model. I choose to follow recent literature (e.g. Snyder *et al.*, 2012) in assuming the cluster galaxies follow the star formation rate density trend of the Universe. My following analysis does not strongly depend on the exact form of this extended model. I tested this by using a range of extended models, and found that the results qualitatively do not change.

I expand the mSSP model to follow the cosmic star formation rate by producing 500 model galaxies, each formed in a single short burst, distributed in time according to the star formation history of the Universe from Hopkins & Beacom (2006):

$$\rho_* = \frac{(a + bz)h}{1 + (z/c)^d} \tag{2.2}$$

where ρ_* is the star formation rate density, $a = 0.017$, $b = 0.13$, $c = 3.3$, $d = 5.3$, and $h = 0.7$. The bottom panel of Figure 2.6 illustrates this multiple-burst model. The red dashed line shows the overall shape of the cosmic star formation rate, the

green histogram indicates the relative fraction of galaxies that are formed in each time interval.

In Figure 2.9 I show this model, as well as the mSSP model (Section 2.3.4), with multiple bursts of star formation around $z_{peak} = 3$ (normally distributed bursts across $\sim 2\,$Gyr). This figure illustrates that I do not have sufficient data to distinguish between different extended models. Both models can also account for the colours of lower redshift clusters, providing a consistent explanation for the formation of all massive cluster galaxies.

2.4.2 Formation timescale of massive galaxies

In this section I examine the period of time between high redshift cluster galaxies forming their stars and assembling into $M_* > 10^{10.5}\,\mathrm{M}_\odot$ objects. In hierarchical merging models (e.g. De Lucia *et al.*, 2006) galaxies form in small entities and subsequently merge. Therefore there may exist a long time delay between the period of star formation and their assembly epoch. If galaxies merge with little gas and no significant star formation (a "dry merger"), then the resulting massive galaxies will appear red. If the merger included a lot of gas (i.e. a "wet merger", or if the galaxies formed via monolithic collapse; Eggen, Lynden-Bell & Sandage, 1962), and induced further star formation, then the resulting galaxies will have bluer colours. Thus I can use my data to estimate the time between star formation and assembly into $M_* > 10^{10.5}\,\mathrm{M}_\odot$ galaxies.

To do this I formed 500 model galaxies distributed in redshift according to the cosmic star formation rate density (Equation 2.2) and calculated an average $i' - [3.6]$ colour at each redshift. To simulate galaxies growing in mass through dry mergers and entering my sample only after a certain period of time, I impose a restriction whereby galaxies are only included in my sample after a time delay Δt.

Figure 2.10 shows this model with different values of Δt. The CARLA data at $z > 2$ are only consistent with a maximum time delay of $\Delta t \approx 0.5\,$Gyr. This short delay between galaxies forming their stars and growing massive enough to enter our sample is in agreement with studies of the luminosity function of galaxies at high redshift,

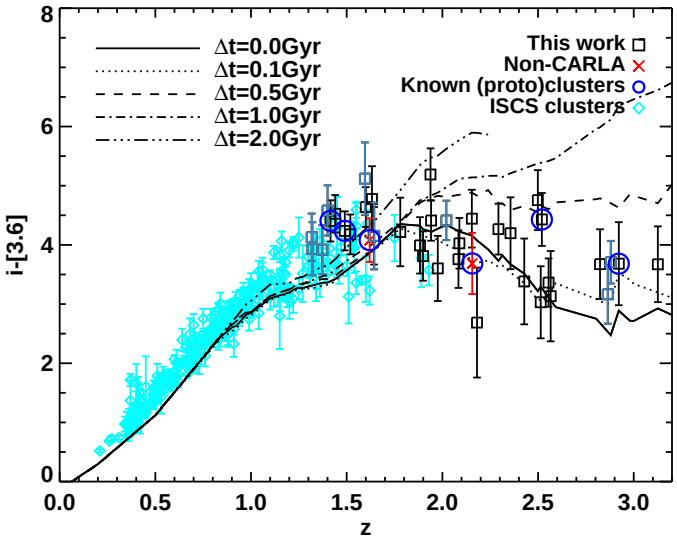

Figure 2.10: The expected average $i' - [3.6]$ colours of clusters when the component galaxies are formed in single bursts, distributed according to the star formation rate density of the Universe. The points are the same as in Figure 2.9. The models here include a time delay Δt between galaxies forming and being included in our selection. Different lines correspond to different values of Δt. Values of Δt larger than ~ 0.5 Gyr produce average cluster colours that are too red to explain the observations at $z > 2$.

which show that the bright end of the luminosity function is established within 5 Gyr of the Big Bang (e.g. De Propris *et al.*, 2003; Andreon, 2006; Muzzin *et al.*, 2008; Mancone *et al.*, 2010; Wylezalek *et al.*, 2014).

These results do not depend on the exact form of the cluster's assembly history. I tested different assembly histories (the best-fit normally distributed model from Section 2.3.4 and a model with the same form as the cosmic star formation rate density, but shifted to higher redshifts) and found no qualitative difference in these results. Individual galaxies must still have assembled within 0.5 Gyr of formation of the majority of their stars.

In summary, $z > 2$ massive ($M_* > 10^{10.5}\,\mathrm{M}_\odot$) cluster galaxies must have assembled within 0.5 Gyr of forming their stars. This could have happened in a number of different ways, such as: formation through a single massive burst; merging into massive galaxies soon after they formed their stars; undergoing a merging event which triggered a massive starburst which dominated the observed colours of the galaxy thereafter.

At $z < 2$, there can be a long delay (several Gyr) between galaxies forming their stars and assembling into massive galaxies. Dry galaxy merging is likely to become a much

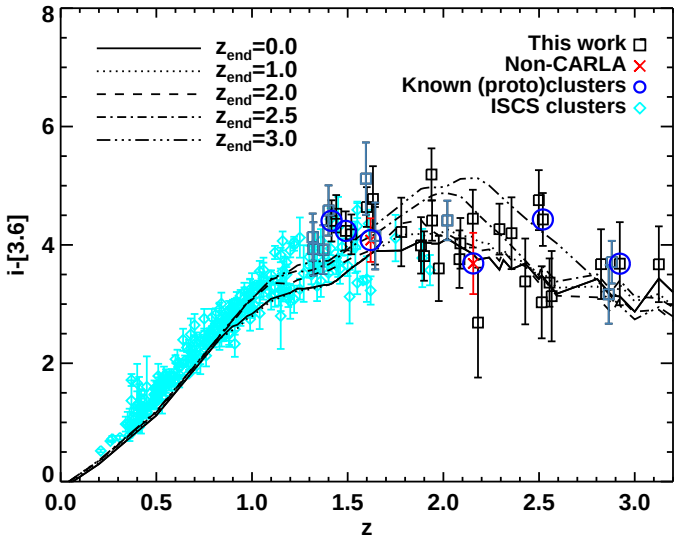

Figure 2.11: The same as Figure 2.10, but the different lines here correspond to different cut-offs in star formation, i.e. star formation is allowed to continue down to z_{end}, following the cosmic star formation rate density, and then terminated. The choice of z_{end} has little effect on the expected colours, suggesting that the cosmic star formation rate density itself is sufficient, requiring no cut-off.

more important route by which massive galaxies form at $z \lesssim 2$.

2.4.3 Cessation of star formation within massive cluster galaxies

Massive galaxies at $z = 0$ are passive and contain old stellar populations which suggest that they finished forming stars at $z > 2$ (e.g. Bower, Lucey & Ellis, 1992). The cosmic star formation model forms stars up to the present-day. In this section I test whether a cut-off in galaxy formation at higher redshifts provides a better fit to the data.

To test when massive galaxy formation ceased in clusters, I formed 500 model galaxies following the cosmic star formation rate density (Equation 2.2), down to a defined redshift z_{end}, i.e. with no more star formation occurring in massive galaxies at $z < z_{end}$. Throughout this section, I use $\Delta t = 0$. Figure 2.11 shows the average $i' - [3.6]$ colour of the model galaxies with various different values of z_{end}. Higher values of z_{end} predict slightly redder colours at $1 < z < 2.5$, however the scatter in the data does not allow us to quantify whether a termination of star formation at any particular z_{end} is required. The reddening of galaxy colours is entirely due to the peak epoch of star formation occurring at $2 \leq z \leq 3$ and few stars forming in massive galaxies thereafter. To determine when star formation in massive cluster galaxies ceased, I would

require measurements of the individual star formation rates of the cluster members. The average $i' - [3.6]$ colours alone do not contain enough information.

2.4.4 Is an extended galaxy formation history within clusters consistent with previous studies?

Previous studies have modelled the formation of cluster galaxies as a single concurrent event. Lower redshift data agree well with these models (e.g. Blakeslee *et al.*, 2003; Mei *et al.*, 2009). In this section I test whether an extended period of galaxy formation is consistent with the observational data from previous work.

In Figure 2.12 I examine the trend of the rest-frame $(U - B)_0$ average colour and scatter predicted from the extended model from Section 2.4.3, following the cosmic star formation density, with different cut-off redshifts, z_{end}. Overlaid in red in Figure 2.12 are findings from previous studies (Bower, Lucey & Ellis, 1992; Ellis *et al.*, 1997; van Dokkum *et al.*, 1998; Blakeslee *et al.*, 2003; Mei *et al.*, 2009; Papovich *et al.*, 2010; Snyder *et al.*, 2012) at $0 < z < 1.6$.

The $\langle U - B \rangle_0$ colour and scatter depend on the adopted value of z_{end}. Stopping galaxy formation at higher z_{end} decreases the scatter and reddens the expected $(U - B)_0$ colours. My model colours and scatters were calculated taking the whole cluster population into account, whereas the data points were measured from red sequence galaxies only. Therefore the data are expected to have a redder colour and smaller scatter than the models, however almost all massive cluster galaxies at $z < 1.5$ exhibit red colours (e.g. Kajisawa & Yamada, 2006). The models with $z_{end} \sim$ 1–2 show good agreement with these previous results, although there is large scatter in the data, suggesting that my simple burst model following the cosmic star formation rate density of the Universe, with some reasonable $z_{end} \sim$ 1–2, provides a possible explanation for the formation history of massive cluster galaxies.

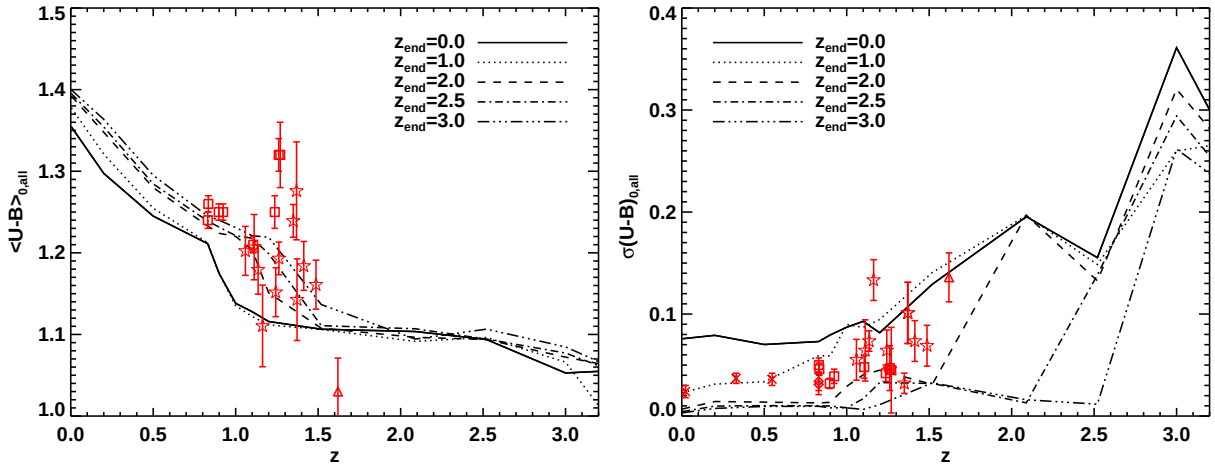

Figure 2.12: Predicted evolution of rest-frame $(U-B)_0$ colours for model galaxies forming as described in Section 2.4.2 with different values of z_{end}. *Left:* The average colours for all cluster galaxies. *Right:* The scatter in the $(U-B)_0$ colours for cluster galaxies. Overplotted in red are results from previous studies: Mei *et al.* (2009) (squares), Blakeslee *et al.* (2003) (diamonds), Papovich *et al.* (2010) (triangle), Snyder *et al.* (2012) (stars). Three studies at low redshift are shown by the red crosses; these are data taken from Bower, Lucey & Ellis (1992); Ellis *et al.* (1997); van Dokkum *et al.* (1998), adapted to rest-frame $(U-B)_0$ by Mei *et al.* (2009).

2.4.5 Estimation of cluster masses in comparison to ISCS clusters

The luminosity functions of CARLA clusters are significantly different from the ISCS clusters, with the CARLA clusters having brighter $m^*_{[4.5]}$ values than those from the ISCS (Wylezalek *et al.*, 2014). The lowest density bin examined in Wylezalek *et al.* (2014) showed results more consistent with the ISCS sample, suggesting that the lower-richness CARLA clusters are more similar to the clusters from ISCS. In this chapter I only examine the densest CARLA clusters and in Figure 2.7 I confirm that members of this subset are richer than the $z > 1.3$ ISCS clusters.

In the right hand panel of Figure 2.7 I plot the number of massive ($M_* > 10^{10.5}\,\mathrm{M}_\odot$) galaxies in the CARLA fields. I also show the excess number of galaxies in the ISCS clusters at $z > 1.3$. The majority of the high redshift ISCS clusters have systematically fewer massive galaxies than the CARLA sample. This indicates that the CARLA clusters are more overdense than the ISCS sample and are therefore likely to be more massive clusters and protoclusters.

Brodwin *et al.* (2007) found that the correlation function of ISCS clusters indicates they reside in dark matter haloes of $\sim 10^{13.9}\,\mathrm{M}_\odot$, and will evolve into clusters of 2–$3 \times 10^{14}\,\mathrm{M}_\odot$ by $z = 0$. Figure 2.7 suggests that the majority of the 37 CARLA clusters

in this study will collapse to become more massive clusters ($\gtrsim 5 \times 10^{14}\,\mathrm{M}_{\odot}$) by the present day.

Brodwin *et al.* (2013) suggest that the formation history of massive cluster galaxies depends on the overall mass of the cluster in which they reside. They found that the lower-mass ISCS clusters were undergoing a major epoch of merging and galaxy formation peaked around $z \sim 1.4$, and predicted that the formation epoch would peak at higher redshifts for more massive clusters. The CARLA data are consistent with a peak formation and assembly epoch of $z \sim 2$–3 for the more massive CARLA clusters, in agreement with a higher assembly epoch for more massive clusters. With the $\langle i' - [3.6] \rangle$ data, however, I find that the cluster density does not affect the measured average colour. This is perhaps due to the broad range of rest-frame colours covered by the observed $i' - [3.6]$ colour at these redshifts.

In summary, the CARLA fields studied here are unlikely to be the progenitors of the lower redshift ISCS clusters. They are likely to evolve into more massive clusters ($\gtrsim 5 \times 10^{14}\,\mathrm{M}_{\odot}$). However, I do not think this will affect the results of Figures 2.9-2.11 as both populations exhibit similar average $i' - [3.6]$ colours.

2.4.6 Caveats

2.4.6.1 CARLA sample are not yet spectroscopically confirmed (proto)clusters

Most of the CARLA clusters studied here are not yet spectroscopically confirmed, which may affect my conclusions on the evolution of clusters. There is an on-going *HST* programme spectroscopically confirming 20 of the densest CARLA (proto)cluster candidates (G. Noirot *et al.*, submitted; G. Noirot *et al.*, in preparation), but spectroscopic confirmation is a time- and labour-intensive process, so at present we rely on large statistical samples of likely (proto)clusters. The fields in this study were selected as the most dense CARLA fields, which are significantly denser than the average field at a $\gtrsim 4\sigma$ level, and thus are likely to contain protoclusters (Wylezalek *et al.*, 2013). Also, in Figure 2.7, the trend of increasing density towards lower redshifts suggests that most of my sample are indeed (proto)clusters. Some fields in my sample have clear evidence for a forming red sequence (see Figure A.1) and five of the sample

are spectroscopically confirmed structures: 7C1756+6520 (Galametz *et al.*, 2010a), 7C1753+6311 (Cooke *et al.*, 2016), J080016.10+402955.6 (G. Noirot *et al.*, submitted), TXS 1558−003 (Hayashi *et al.*, 2012), and MRC 0943−242 (Venemans *et al.*, 2007). These clusters, as well as the two non-CARLA clusters from Papovich *et al.* (2010) and Pentericci *et al.* (2000), follow the same flat trend in colour as the unconfirmed clusters at all redshifts. This all provides strong evidence that the majority of the CARLA fields in this study are likely to be (proto)clusters.

2.4.6.2 AGN may cause incorrect colour measurements

The presence of AGN may cause redder colours in my cluster sample. The fraction of AGN in clusters is known to be enhanced compared to the field (e.g. Galametz *et al.*, 2010a), which may affect the IRAC bands. My use of median colours throughout should prevent small numbers of AGN significantly affecting the measured average colours.

2.4.6.3 Blending of sources

The FWHM of the *Spitzer* 3.6 and $4.5\,\mu$m data is ~ 1.7 arcsec. This means that source fluxes may be affected by blending with nearby sources, particularly in crowded fields. The i' data, although having a small FWHM, may also experience some blending. If blending occurs between galaxies at similar redshifts, i.e. between cluster members, my conclusions will be unaffected, as I measure median colours of clusters throughout. Blending with fore- or background sources may cause inaccuracies in the measured colours. Further data with better resolution is required to gain more accurate measurements of galaxy colours.

2.5 Conclusions

I have used a sample of 37 clusters and protoclusters across $1.3 \leq z \leq 3.2$ from the CARLA survey of high-redshift clusters to study the formation history of massive cluster galaxies. These fields are the densest targets of the CARLA survey, and as

such are likely to be the sites of formation for massive clusters. I have used optical i'-band and infrared $3.6\,\mu$m and $4.5\,\mu$m images to statistically select sources likely to lie within these (proto)clusters and examined their average observed $i'-[3.6]$ colours. The abundance of massive galaxies within these (proto)clusters increases with decreasing redshift, suggesting these CARLA (proto)clusters form an evolutionary sequence, with the lower redshift clusters in the sample having similar properties to the descendants of the high redshift protoclusters. This sequence allows us to study how the properties of their galaxy populations evolve as a function of redshift. By comparing the abundance of massive galaxies in these CARLA (proto)clusters to those of $z > 1.5$ ISCS clusters I have shown that the CARLA sample are likely to collapse into more massive clusters, typically $\gtrsim 5 \times 10^{14}\,\mathrm{M}_{\odot}$.

I have compared the evolution of the average colour of massive cluster galaxies with simple galaxy formation models. Taking the full cluster population into account, I have shown that cluster galaxies did not all form concurrently, but rather formed over the course of a few Gyr. The overall colour evolution is consistent with the stars in each galaxy forming in a single burst, although more complex individual star formation histories that are rapidly truncated may produce this effect. This galaxy formation history is consistent with galaxies within different groups of the (proto)cluster forming concurrently, but the whole cluster population building up over a longer period of time. Overall this produces an approximately unevolving average observed $i' - [3.6]$ colour for cluster galaxies at $z = 1.3$ to $z \sim 3$.

In summary, my main conclusions are as follows:

1. The average colours of massive cluster galaxies are relatively flat across $1.3 < z < 3.2$. It is not possible to describe the formation of these galaxies with a burst model at a single formation redshift. Cluster galaxies formed over an extended period of time.

2. The formation of the majority of massive cluster galaxies is extended over at least 2 Gyr, peaking at $z \sim 2$–3. From the average $i' - [3.6]$ colours we cannot determine the star formation histories of individual galaxies, but their star formation must have been rapidly terminated to produce the observed colours.

3. Massive galaxies at $z > 2$ must have assembled within 0.5 Gyr of them forming a significant fraction of their stars. This means that few $M > 10^{10.5}\,\mathrm{M}_{\odot}$ galaxies in $z > 2$ clusters could have formed via dry mergers.

Chapter 3

A mature galaxy cluster at $z = 1.58$ around the radio galaxy 7C 1753+6311

3.1 Introduction

In Chapter 2 I analysed a sample of 37 clusters and protoclusters from the CARLA survey. These (proto)clusters had red observed average colours. Such colours can be produced in two different ways: firstly, by passively-evolving, quiescent galaxies with intrinsically red stellar populations; secondly, by dust extinction in star-forming galaxies causing them to appear red. In Chapter 2 I concluded that at least some of the population must be quiescent in the CARLA clusters as the amount of dust extinction required to produce the observed red colours would also cause a large discrepancy between the observed $i' - [3.6]$ colours and measured values of $m^*_{[4.5]}$. The rest-frame UVJ colours of galaxies are able to distinguish between quiescent galaxies and those which are red due to dust extinction. In this chapter I will analyse one of the CARLA fields, around the RLAGN 7C 1753+6311, to distinguish between galaxies obscured by dust and those that are quiescent. This field was also identified as having a very dense core and indications of a red sequence already forming, which made it an ideal candidate on which to pilot this study of the galaxy populations in CARLA (proto)clusters.

It is also important for high redshift protocluster studies that the selection bias is un-

derstood. It is well documented in the literature that RLAGN preferentially lie in overdense environments and can be used as beacons for (proto)clusters at $z > 1$ (e.g. Galametz *et al.*, 2012; Wylezalek *et al.*, 2013), which are significantly denser than the environments of radio-quiet galaxies of the same stellar mass (Hatch *et al.*, 2014). This is also predicted in studies employing semi-analytic models (e.g. Orsi *et al.*, 2016). These RLAGN provide one of the most efficient ways to find and study large-scale structure formation, particularly at the highest redshifts. However, if RLAGN preferentially reside in clusters of a certain age or stage of collapse, then our view of cluster formation will be biased. For example, Simpson & Rawlings (2002) and van Breukelen *et al.* (2009) suggest distant radio galaxies pinpoint merging clusters.

Most confirmed cluster progenitors have been identified with Lyα emitters, Hα emitters, or Lyman-break galaxies, which are tracers of young systems (e.g. Overzier *et al.*, 2005; Venemans *et al.*, 2007, see also Chapter 4). So the methods by which protoclusters have been identified preferentially pinpoint young, forming galaxies, and clusters that contain mature, passively evolving galaxies may be missed.

By contrast, large cluster surveys using *Spitzer* data are not intrinsically biased to star-forming galaxies (Simpson & Eisenhardt, 1999; Eisenhardt *et al.*, 2008; Muzzin *et al.*, 2009; Galametz *et al.*, 2012; Wylezalek *et al.*, 2013; Rettura *et al.*, 2014). The criterion proposed by Papovich (2008) uses a $3.6\,\mu$m $-4.5\,\mu$m colour selection to isolate all types of galaxies at $z > 1.3$, thanks to the peak of stellar emission near $1.6\,\mu$m in galaxy spectral energy distributions (SEDs) moving into these bands at $z > 1$. This feature is present in galaxies of all types so selecting only on this criteria does not greatly bias the galaxy selection. Using the *Spitzer* wavebands to select both star forming and passively evolving cluster members, CARLA clusters are the ideal sample to investigate whether RLAGN are biased tracers of clusters that reside preferentially in younger structures, or whether the young structures discovered to date are due to the protocluster confirmation techniques used.

In this chapter I will present an analysis of the properties of the red galaxies surrounding 7C 1753+6311 (Figure 3.1). If the red galaxies in this field are quiescent then RLAGN can indeed be found in a wide variety of structures. If, on the other hand, the red colours are due to dusty star-forming galaxies, then RLAGN may pinpoint clus-

ters of a certain age or stage of evolution which is characterised by high levels of star formation, and few quenched galaxies, for example merging clusters.

Lacy *et al.* (1999) tentatively assigned a redshift to 7C 1753+6311 of $z = 1.95$ based on an uncertain emission line at 4854Å assumed to be He II $\lambda 1640$ and the possible detection of an associated Lyα break. This redshift was assigned a quality "γ", indicating an "uncertain" redshift. Here I report the first robust spectroscopic redshift for 7C 1753+6311, confirming it to instead be at $z = 1.58$, and examine the surrounding cluster environment.

In the following, Section 3.2 outlines my data and methods used. In Section 3.3 I present a new, deep, optical spectrum of 7C 1753+6311 which confirms its redshift as being $z = 1.58$. Section 3.4 then investigates the properties of the galaxies surrounding 7C 1753+6311, and Section 3.5 presents my conclusions.

3.2 Data and Method

3.2.1 Imaging

The field surrounding 7C 1753+6311 was imaged at $3.6\,\mu$m and $4.5\,\mu$m by the CARLA survey (Section 1.4), reaching a 3σ depth of $[3.6] = 23.8$ mag and $[4.5] = 24.4$ mag. This field was identified as a protocluster candidate with a 4.5σ overdensity by Wylezalek *et al.* (2013) and was followed up in i' and J using the William Herschel Telescope in La Palma. I obtained the i' band image with the auxiliary-port camera (ACAM), with an exposure time of 6000 s. Full details of the i' data are available in Table 2.1. I obtained the J band image with the long-slit intermediate resolution infrared spectrograph (LIRIS) in service mode (PI E. Cooke), with an exposure time of 8160 s. I reduced this data in the standard way using the publicly available program THELI (Erben *et al.*, 2005; Schirmer, 2013). A 3σ depth is reached at $i' = 26.0$ mag and $J = 23.6$ mag, with seeing of ~ 0.76 arcsec for both images.

The IRAC images have a much broader point-spread function (PSF) than the i' and J images, so selecting sources using the $4.5\,\mu$m image is prone to blending and some galaxies may be missed which are distinct in the i' or J bands. Using solely the i'

band to detect sources would result in biasing the selection towards intrinsically blue sources, whereas the J image is relatively shallow, so I used a deep F140W image as a detection image. The field around 7C 1753+6311 was imaged with the F140W filter of the *Hubble Space Telescope* Wide-Field Camera 3 (*HST*/WFC3) in July 2015 as part of an on-going 40-orbit spectroscopic program (PI D. Stern). The *HST* spectra and photometry will be discussed in a future paper (A. Rettura *et al.* in preparation). I retrieved the calibrated, dither-combined (drizzled) image from MAST[1] to use as a detection image. This image has 0.5 ksec exposure and is complete[2] to at least 24 mag.

I detected and measured fluxes for sources using SExtractor (Bertin & Arnouts, 1996) in dual-image mode. I used the *HST* F140W detection image to detect sources, and obtained photometry on the i', J, $3.6\,\mu$m and $4.5\,\mu$m images in 2 arcsec diameter apertures. I was unable to use large apertures to measure the IRAC fluxes (e.g. 4 arcsec) due to the high spatial density of sources in the cluster core (galaxies are typically ~ 2 arcsec apart). So I measured the fluxes in 2 arcsec diameter apertures and corrected for the broader PSF of the IRAC data compared to the ground-based data using the ratio of the flux in the J band image to the J image convolved with a Gaussian kernel matching the IRAC PSF, following Hartley *et al.* (2013). Fluxes were corrected to total fluxes using the growth curves of bright, unsaturated stars in the field-of-view. This method assumes that the blended sources have the same $J-\mathrm{IRAC}$ colour, so may provide inaccurate colours for some sources.

3.2.2 High redshift galaxy selection

To select sources likely to lie at high redshift, I employed two colour cuts. The well-tested IRAC cut of $[3.6]-[4.5] > -0.1$ (Papovich, 2008) selects sources at $z > 1.3$ due to the $1.6\,\mu$m peak of stellar emission moving into the IRAC bands at these redshifts. I adjusted this cut to $[3.6]-[4.5] > -0.2$ in order to be sure of selecting as complete a cluster sample as possible, although this also allows more lower-redshift sources to contaminate the sample. Most stars have $[3.6]-[4.5] \sim -0.5$ and so will be successfully removed by this cut (Galametz *et al.*, 2012). A second cut of

[1] Mikulski Archive for Space Telescopes: https://archive.stsci.edu

[2] The histogram of number counts per magnitude bin starts to decrease after 25 mag in F140W.

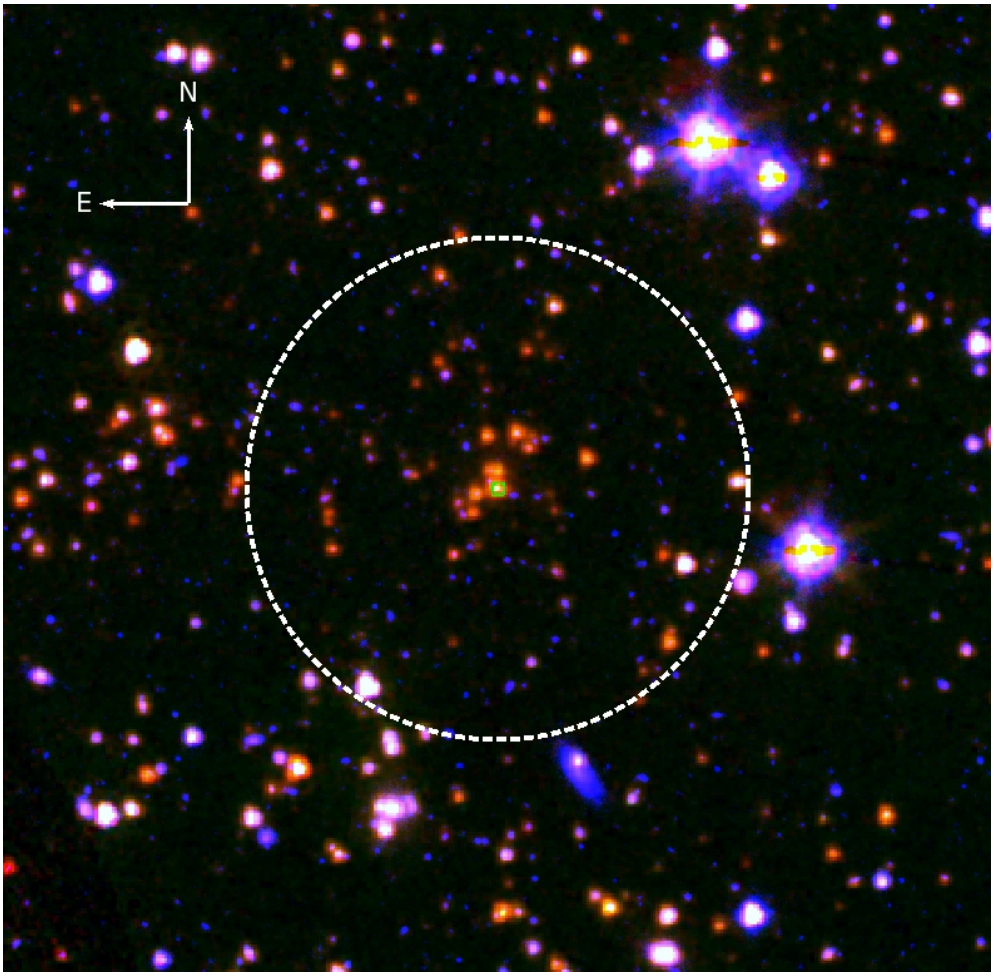

Figure 3.1: $i', [3.6], [4.5]$ three-colour image of the field around 7C 1753+6311. The central RLAGN is marked with a green square. There are several red sources clustered around the RLAGN. The white dashed circle shows a 0.9 arcmin radius around the RLAGN. 0.9 arcmin at $z = 1.58$ corresponds to 0.46 Mpc in physical coordinates.

$i' - [3.6] > -0.5 \times [3.6] + 11.4$ (derived in Chapter 2) was applied to further remove bright low-redshift interlopers and contaminating AGN. This cut removes the brightest foreground interlopers; those which are $\geq 80\%$ likely to lie at $z < 1.3$, whilst retaining 99% of IRAC-selected sources. To remove faint sources with potentially inaccurate flux measurements, I only considered those with magnitudes brighter than 23.8 mag in $4.5\,\mu$m (5σ image depth) and 23.6 mag in J (3σ image depth). Any sources referred to hereafter are those that match these criteria. To maximise the overdensity of (proto)cluster sources to field contaminants, I only consider sources within 0.9 arcmin of the central RLAGN.

The completeness of my catalogue is a function of F140W magnitude. This image is deeper than the ground-based imaging and is 100% complete to the J band limit of

23.6 mag. This means I detect all sources with $J \leq 23.6$ mag and am not missing any sources in the following analysis.

3.2.3 Statistical subtraction

3.2.3.1 Control field used to remove fore/background contamination

Throughout this study, I used the eighth data release (DR8) of the UKIDSS Ultra Deep Survey (UDS; Hartley *et al.*, 2013) as a control field. The IRAC fluxes in the UDS catalogue were deblended using the same method described above, using the resolved K images to deblend sources (see Hartley *et al.*, 2013). The UDS has 5σ depths of $i' = 27.0$ mag, $J = 24.9$ mag, $[3.6] = 24.2$ mag and $[4.5] = 24.0$ mag (Furusawa *et al.*, 2008; Hartley *et al.*, 2013). I therefore use the same magnitude cuts for the UDS as for the 7C 1753+6311 field. I do not consider Eddington bias due to the greater depth of the UDS, however I do not expect it to significantly affect my results, particularly regarding the fraction of the most massive galaxies in the cluster that are quiescent.

The UDS is a K-selected survey, whereas I use an F140W selection for 7C 1753+6311. Both selections are done in the infrared, and both are much deeper than our $J \leq 23.6$ mag selection so these methods are unlikely to differ greatly. They would only differ for extremely red sources with very faint F140W magnitudes and bright K magnitudes. I have checked that the different selection methods do not affect my use of the UDS as a control sample by comparing number counts in the two fields as a function of i', J, $[3.6]$ and $[4.5]$ magnitudes and find that they match well within the colour and magnitude cuts stated above.

Where I compare the properties of the cluster galaxies to the field, I use only those galaxies selected in the UDS which have photometric redshifts between $1.5 < z < 1.7$.[3] This ensures I am comparing the cluster properties to those of the field at approximately the same redshift. For statistical subtraction (see below), I use the full UDS with no photometric redshift constraints.

[3] Photometric redshifts determined by W. Hartley from the full 11-band photometry of the UDS, see Hartley *et al.* (2013).

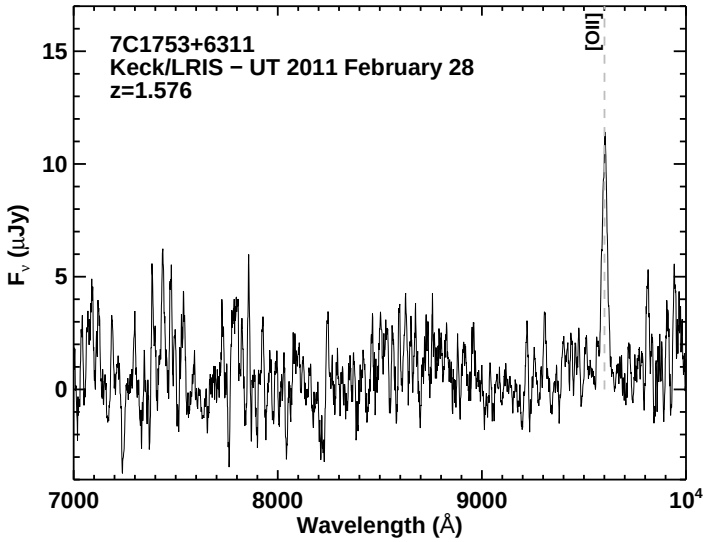

Figure 3.2: The Keck/LRIS spectrum of 7C 1753+6311 obtained on UT 2011 February 28 (smoothed with a boxcar average of 10 Å for clarity). A single, high equivalent width emission line is detected at 9602 Å which we identify as the [O II] λ3727 doublet which places 7C 1753+6311 at $z = 1.576$. This redshift is confirmed with corresponding Hα emission by A. Rettura *et al.* (in preparation).

3.2.3.2 Subtraction of field contaminants

Since I do not identify cluster members with spectra or photometric redshifts, I use statistical subtraction to derive the cluster galaxy properties. The fore- and background population is estimated from $\sim$ 400 random 0.9 arcmin radius regions in the UDS, having applied the same colour and magnitude cuts as above. The field contribution is estimated from the median of these 400 regions and then subtracted from the corresponding number of galaxies around 7C 1753+6311. The uncertainty is the 1σ standard deviation of the 400 field regions.

3.3 Redshift of 7C 1753+6311

A deep optical spectrum of 7C 1753+6311 was obtained using the Low Resolution Imaging Spectrometer (LRIS; Oke et al. 1995) at the Keck I telescope during twilight on UT 2011 February 28 (PI C. Bridge, observers C. Bridge and A. Blain). LRIS is a double spectrograph, and they integrated for 1200 s on the blue arm and 1120 s on the red arm in order to match read-out times. The observations used the $1.5''$ wide longslit and the data were processed by D. Stern using standard procedures and flux

calibrated using an archival sensitivity function from 2011 April. I used a catalogue of wavelengths and flux densities compiled by D. Stern to plot the spectrum in Figure 3.2. Nothing is detected on the blue side, but a single, strong, high equivalent width emission line is detected at 9602 Å on the red side, which we identify with the [O II] $\lambda3727$ doublet at $z = 1.576$ (see Figure 3.2). For the instrument configuration used, the spectral resolving power was $R \equiv \lambda/\Delta\lambda = 1600$ for objects filling the slit at ~ 9600 Å, which is insufficient to resolve the [O II] doublet. However, the redshift is confirmed by the detection of corresponding Hα emission in a Keck near-infrared spectrum reported by A. Rettura *et al.* (in preparation). In comparison to radio galaxies surrounded by protoclusters typically reported in the literature (e.g. Venemans *et al.*, 2007; Galametz *et al.*, 2010a; Hatch *et al.*, 2011a), this is a relatively weak line emitter. There are not any features at 4854 Å and this wavelength does not correspond to any strong spectral features for our measured redshift. The feature noted in Lacy *et al.* (1999) was therefore probably due to noise in their shallow data.

3.4 Cluster properties

3.4.1 A galaxy cluster at $z = 1.58$

Figure 3.3 shows a density map of the field around 7C 1753+6311 and ClG 0218.3−0510, a well-studied cluster at $z = 1.62$ (Papovich *et al.*, 2010; Tanaka, Finoguenov & Ueda, 2010). I produced these maps by measuring the number density of sources (selected using the colour and magnitude criteria described in Section 3.2) within 30 arcsec radius apertures around each 5 arcsec pixel. I mapped the UDS in the same way, and used the mean and standard deviation of densities in the UDS to convert each number density value to a significance above the expected field density. The pixels in Figure 3.3 are therefore correlated as each 5 arcsec pixel indicates the overdensity within a 30 arcsec radius aperture. Using the selection criteria defined in Section 3.2, the peak overdensity around 7C 1753+6311 is an 8.9σ significance of galaxies within a 30 arcsec aperture, centred 16 arcsec (136 kpc) from the radio galaxy. These galaxies appear to be highly clustered around the central RLAGN (Figure 3.1). The source density is so high in the central 0.9 arcmin region that five pairs of sources were blended

in the $4.5\,\mu$m image, and their true nature was only discovered in the higher resolution ground-based data. It is possible that many of the other CARLA cluster candidates which have extremely high galaxy overdensities also suffer from blending.

Follow-up near-infrared Keck spectroscopy of 7C 1753+6311 revealed five galaxies, including the RLAGN, with spectroscopic redshifts between $1.578 < z < 1.587$ within a projected diameter of 2 Mpc (A. Rettura *et al.*, in preparation). This structure therefore satisfies the criteria set out by Eisenhardt *et al.* (2008) for a spectroscopically confirmed $z > 1$ (proto)cluster, and so we refer to the structure as CARLA J1753+6311 from now on.

Besides the RLAGN, there are 29 ± 6 excess galaxies within 0.9 arcmin of 7C 1753+6311 that are selected with the above colour and magnitude criteria[4]. This level of clustering and overdensity is slightly greater than that of the ClG 0218.3−0530 protocluster at $z = 1.62$, which has a galaxy excess of 22 ± 6 using the same criteria. The cluster ClG 0218.3−0530 is a well-studied structure with a tentative 4.5σ X-ray detection potentially indicating a collapsed core (Tanaka, Finoguenov & Ueda, 2010). The comparably high galaxy overdensity surrounding 7C 1753+6311 (Figure 3.3) suggests that this RLAGN is surrounded by a protocluster consisting of a dominant main halo that is already a relatively high-mass group.

The approximate mass of CARLA J1753+6311 can be estimated from the galaxy richness. Andreon & Congdon (2014) reported that galaxy richness was a good proxy for cluster mass, with little dependence on redshift. ClG 0218.3−0530 has an X-ray determined mass of 4–$8 \times 10^{13}\,\mathrm{M}_{\odot}$ (Tanaka, Finoguenov & Ueda, 2010; Pierre *et al.*, 2012), which is consistent with the galaxy velocity dispersion (Tran *et al.*, 2015). Since CARLA J1753+6311 is richer than ClG 0218.3−0530, its mass is likely to be slightly greater. Using equation 3 from Andreon & Congdon (2014), and the calculated value of $m^*_{4.5\mu m} + 1 = 21.2$ from Wylezalek *et al.* (2014) I measure a cluster richness of 10 ± 1 galaxies[5] with $[4.5] \leq 21.2$, and estimate the mass of 7C 1753+6311 to be $(9.2 \pm 4.5) \times 10^{13}\,\mathrm{M}_{\odot}$ within 500 kpc, consistent with this structure being a slightly more massive group than ClG 0218.3−0530.

[4]The number of excess galaxies was calculated by taking the number of field galaxies selected in 400 random 0.9 arcmin fields in the UDS and subtracting this from the number of galaxies selected around 7C 1753+6311, then taking the mean and standard deviation of the resultant distribution.

[5]This is the number of background-subtracted galaxies in the 7C 1753+6311 field.

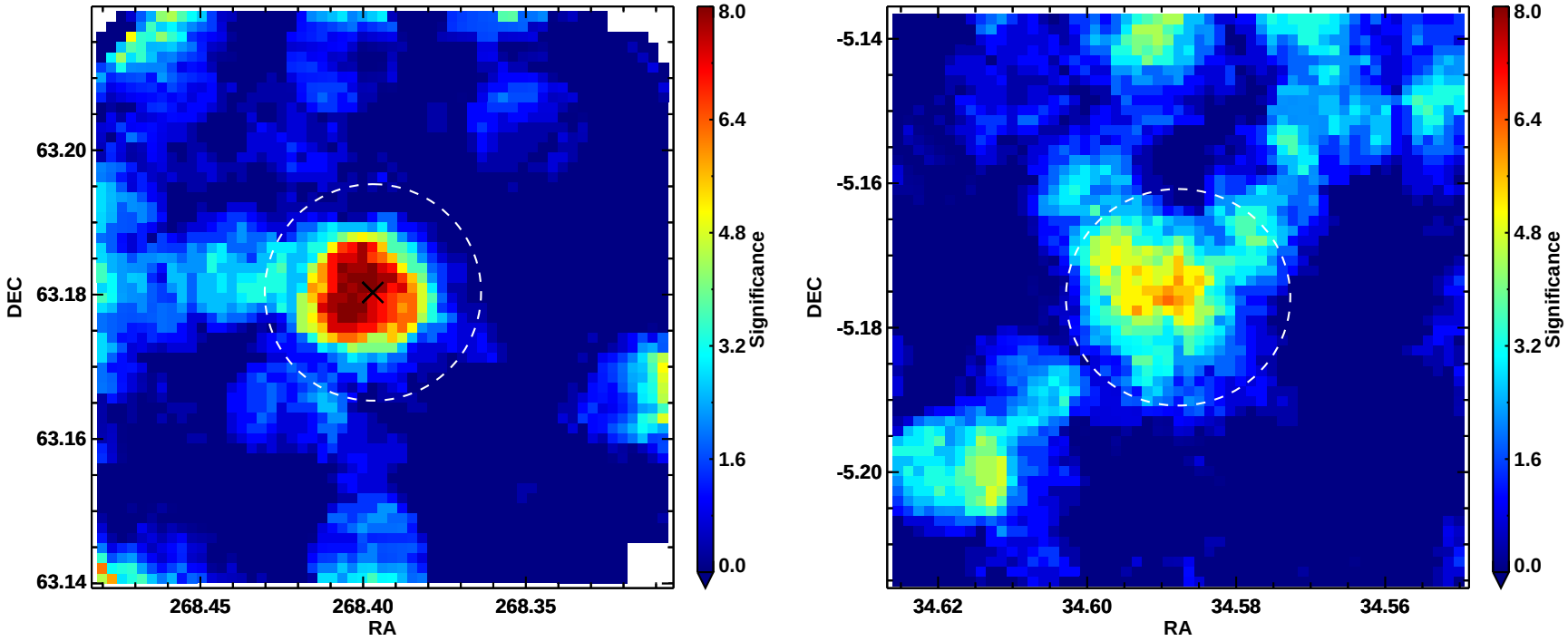

Figure 3.3: *Left*: Density map of colour-selected sources in CARLA J1753+6311. The *HST* image used to detect sources has been supplemented by the i' and J images in the outskirts to show the extended field around 7C 1753+6311. The RLAGN is shown by the black cross and the circle shows a 0.9 arcmin (0.46 Mpc) radius around the RLAGN. Only sources within this circle are considered in this paper. R_{200} at $z = 1.6$ is 0.51 Mpc for a 9.2×10^{13} $M_\odot$ structure. The colourbar shows the overdensity in sigma compared to the average field. *Right*: Density map of colour-selected sources in ClG 0218.3−0510. The white circle has a radius of 0.9 arcmin around centre of the cluster, as measured by Papovich *et al.* (2010).

3.4.2 Red sequence and red fraction

One of the signs of a mature cluster is the presence of a red sequence. Ubiquitous in clusters at $z < 1$, red sequences persist in galaxy clusters out to at least $z = 1.4$ (Stanford *et al.*, 2005; Snyder *et al.*, 2012), and have been found in some dense (proto)clusters at even higher redshifts (e.g. Kodama *et al.*, 2007; Stanford *et al.*, 2012; Newman *et al.*, 2014).

Figure 3.4 shows the $i' - J$ colour-magnitude diagram of sources within 0.9 arcmin of the RLAGN (~ 500 kpc at this redshift)[6]. Larger squares indicate sources that are within 30 arcsec of the radio galaxy. The histogram in the top panel of Figure 3.4 shows the excess number of galaxies in CARLA J1753+6311, compared to the UDS control field. There is a significant overdensity in the field around 7C 1753+6311 at all magnitudes, increasing at the faint end. Although contamination from fore- and background field sources in the colour-magnitude diagram is to be expected, the majority of the red data points are likely to be cluster members, and there is a clear, strong red sequence at $J < 23$ mag, with hints of the sequence continuing to fainter magnitudes.

The red sequence is fit by the line $i' - J = 7.688 - 0.232 \times J$, calculated by iteratively clipping sources more than 1.5σ from the best-fit line, allowing both the slope and normalization to freely vary, until convergence was reached. The fit is shown by the red dotted line in Figure 3.4. If the galaxies are assumed to have formed their stars in single bursts, the colours of sources on this red sequence suggest they formed at redshifts of $2 < z_f < 3$. A cluster formation model in which the member galaxies formed over the course of 2–3 Gyr, with galaxy formation peaking at $z = 3$ predicts an average red sequence colour of $i' - J = 2.7$ mag, consistent with the data (Chapter 2).

I define "red" galaxies as those that lie within 0.5 mag of (or redder than) the red sequence (shown by the lower, grey, dotted line in Figure 3.4); this cleanly divides the red sequence from the blue cloud. I calculated the red fraction for CARLA J1753+6311, statistically removing the expected number of field contaminants as:

$$f_{\rm red} = \langle \frac{(N_{\rm red}^{\rm 7C1753} - N_{\rm red}^{\rm field})}{(N_{\rm total}^{\rm 7C1753} - N_{\rm total}^{\rm field})} \rangle_{\rm median} \tag{3.1}$$

[6]None of our results qualitatively change when we consider a smaller 30 arcsec radius field.

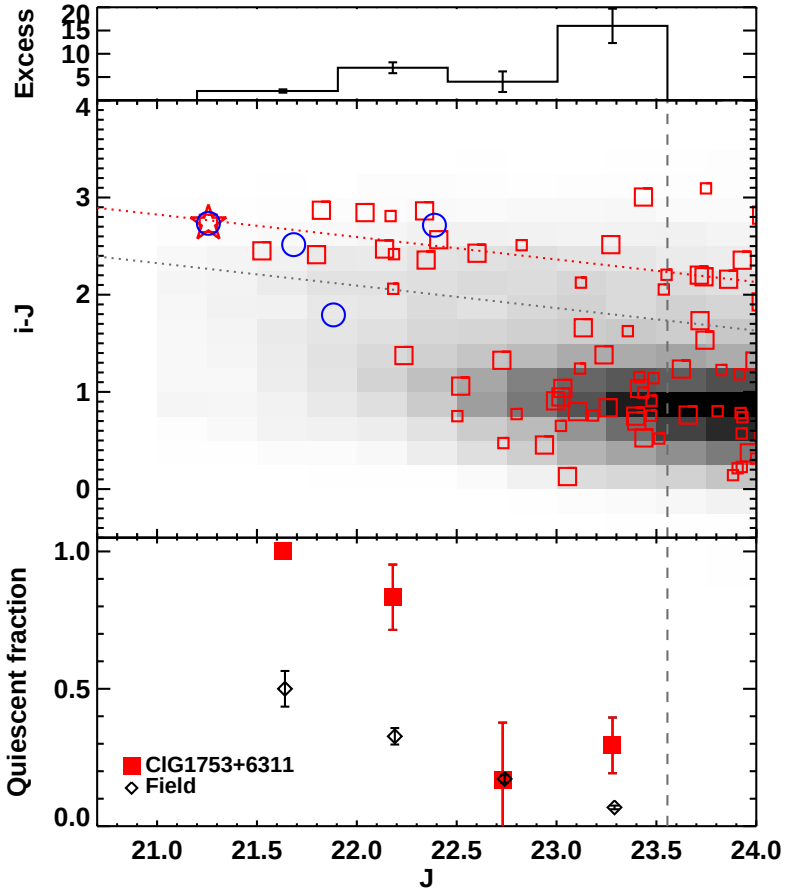

Figure 3.4: *Top*: Histogram showing the number of excess sources within 0.9 arcmin of 7C 1753+6311 compared to the expected numbers in a random blank field, as a function of J band magnitude. *Middle*: Colour-magnitude diagram showing a clear structure of red sources at $i' - J \sim 2.5$. The RLAGN is marked with a red star. All sources within 0.9 arcmin of the RLAGN are marked with red squares. Larger squares indicate those within 0.5 arcmin of the RLAGN. The grey dashed line indicates the 3σ depth of the J band. The best fit to the red sequence is shown by the red dotted line. The grey dotted line indicates 0.5 mag below this line. The background greyscale shows the normalized distribution of the UDS for comparison. Spectroscopic members (A. Rettura *et al.*, in preparation) are highlighted with large blue circles. *Bottom*: The quiescent fraction of galaxies in CARLA J1753+6311 as a function of J band magnitude. Red squares show the cluster values, black diamonds indicate the quiescent fractions measured for field galaxies.

where $N_{\rm red}^{\rm field}$ and $N_{\rm total}^{\rm field}$ are the measured number of "red" and total galaxies that satisfy our colour criteria in ~ 400 random 0.9 arcmin field regions from the UDS. The uncertainty is the 1σ standard deviation in the calculated red fractions for CARLA J1753+6311.

The fraction of red galaxies in the protocluster is significantly larger than in the blank field. The red fraction of CARLA J1753+6311, after statistically removing field contaminants, is $f_{\rm red} = 0.66 \pm 0.13$, compared to the average fraction of $1.5 < z < 1.7$ galaxies in the UDS control field, which is $f_{\rm red} = 0.27 \pm 0.01$ (see Table 3.1).

	CARLA J1753+6311	ClG 0218−0510	UDS
$f_{\rm red}$	0.66 ± 0.13	0.48 ± 0.15	0.27 ± 0.01
$f_{\rm Q}$ ($J \leq 23.6$)	0.50 ± 0.09	0.30 ± 0.08	0.16 ± 0.01
$f_{\rm Q}$ (red galaxies)	0.80 ± 0.06	0.67 ± 0.11	0.61 ± 0.03
$f_{\rm Q}$ ($M_* \geq 10^{10}$M$_\odot$)	0.76 ± 0.13	0.44 ± 0.14	0.28 ± 0.01
$f_{\rm Q}$ ($M_* \geq 10^{10.5}$M$_\odot$)	0.91 ± 0.09	0.38 ± 0.16	0.36 ± 0.02

Table 3.1: Fractions of quiescent galaxies in CARLA J1753+6311, ClG 0218.3−0510 and in the control field UDS at $1.5 < z < 1.7$. $f_{\rm Q}$ gives the quiescent galaxy fraction and $f_{\rm red}$ gives the fraction of galaxies with red colours in each sample.

CARLA J1753+6311 has a similar red fraction to the $z = 1.62$ protocluster ClG 0218.3 −0510, which has $f_{\rm red} = 0.48 \pm 0.15$. So the enhanced red fraction in CARLA J1753+ 6311 seems typical for mature protoclusters. The dense environment of the protoclusters appears to have a strong impact on the colours of their member galaxies.

3.4.3 Quiescent galaxy fraction

In low-redshift clusters the galaxies that lie on the red sequence are predominantly passively evolving, old galaxies. However, dusty star forming galaxies (with $A_V \sim 1$–3) exhibit colours similar to those expected from quenched, passively evolving (i.e. quiescent) galaxies, and these galaxies make up approximately half of the red infrared-selected galaxy population at higher redshifts (Kriek *et al.*, 2008). Furthermore, recent literature has also shown that high-redshift clusters and protoclusters do contain dusty star-forming galaxies (e.g. Brodwin *et al.*, 2013; Dannerbauer *et al.*, 2014; Smail *et al.*, 2014; Santos *et al.*, 2015). The enhanced red fraction of sources in CARLA J1753+6311 could therefore be ascribed to an excess of dusty star-forming galaxies and/or quenched, passively evolving galaxies. Here I use the rest-frame U, B, J colours (observed i', J, $[3.6]$) to separate these two populations.

Using the method outlined in Williams *et al.* (2009), Papovich *et al.* (2012) used the observed-frame z', J and $3.6\,\mu$m bands (rest-frame U, B, J) to separate galaxies in the $z = 1.62$ cluster ClG 0218.3−0510 into quiescent and star forming populations. Using the full spectral energy distribution (SED) fits to the ClG 0218.3−0510 cluster members from Hatch *et al.* (2016), I have converted the Papovich *et al.* (2012) selection criteria to use our i', J and $3.6\,\mu$m bands. This was achieved by selecting quiescent

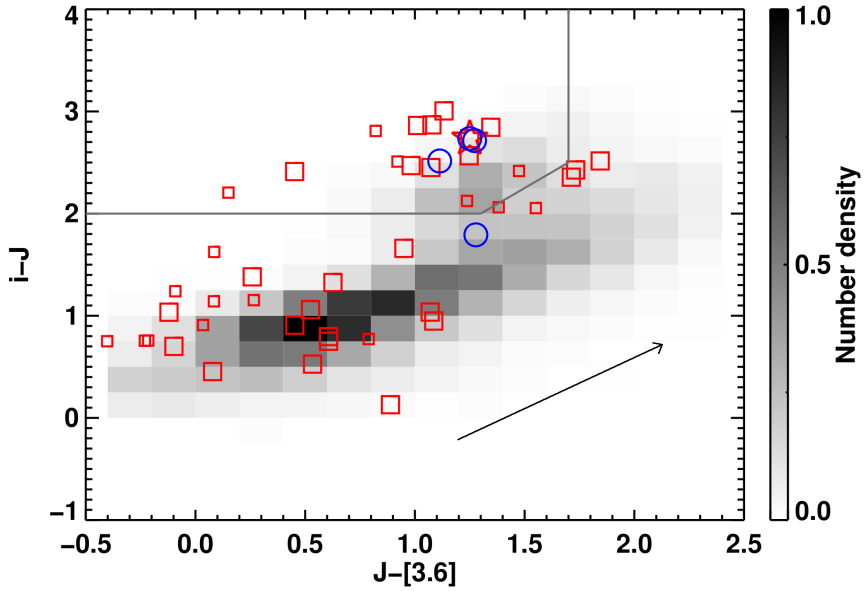

Figure 3.5: Observed $i' - J$ versus $J - [3.6]$ (rest-frame $U - B$ versus $B - J$) colour-colour diagram. The upper left quadrant selects quiescent galaxies at $z \sim 1.6$. Sources further towards the upper-right are dusty star forming objects; the arrow represents the effect of 1 mag of dust extinction (A_V) using the Calzetti *et al.* (2000) dust extinction law. Those at bluer $i' - J$ colours are star forming galaxies. The background density map shows the expected normalized distribution of field sources from the UDS. The symbols are the same as in Figure 3.4.

ClG 0218.3−0510 cluster members using the Papovich *et al.* (2012) criteria, and then using the i', J and $3.6\,\mu$m bands to select the same sample. I then tightened up the selection (selecting an area in colour-colour space which is slightly bluer in $J - [3.6]$ and redder in $i' - J$) so as to have a clean sample of quiescent galaxies, compromising the completeness. These criteria are therefore slightly stricter than those used in Papovich *et al.* (2012). Quiescent galaxies are those which satisfy the following criteria:

$$i' - J \geq 2.0 \tag{3.2}$$

$$J - [3.6] \leq 1.7 \tag{3.3}$$

$$i' - J \geq 0.375 + 1.25 \times (J - [3.6]) \tag{3.4}$$

I caution the reader that these equations were derived specifically for the eighth data release of the UDS and my data. The $3.6\,\mu$m magnitudes may be systematically offset by up to 0.5 mag due to the method by which they were determined and so these criteria may change for different datasets.

Figure 3.5 shows the distribution of all sources selected in CARLA J1753+6311 in $i' - J$ versus $J - [3.6]$ (rest-frame $U - B$ versus $B - J$) colour-colour space. The greyscale shows the expected distribution of the control field. The lines show the $i', J, [3.6]$ criteria used to select quiescent galaxies, which lie in the upper-left quadrant. The full cluster membership of CARLA J1753+6311 is not known, so interlopers were statistically removed in $i'J[3.6]$ colour-colour space using the UDS as the control field. To do this I use ~ 400 random 0.9 arcmin radius regions in the UDS, classifying sources as "quiescent" or "star forming" using the above criteria. Sources in the 7C 1753+6311 field are then classified as "quiescent" or "star forming", and the quiescent fraction calculated as:

$$f_{\rm Q} = \langle \frac{(N_{\rm Q}^{\rm 7C1753} - N_{\rm Q}^{\rm field})}{(N_{\rm total}^{\rm 7C1753} - N_{\rm total}^{\rm field})} \rangle_{\rm median} \tag{3.5}$$

where $N_{\rm Q}^{\rm field}$ is the measured number of rest-frame UBJ-selected quiescent galaxies in ~ 400 random 0.9 arcmin field regions. The uncertainty is the 1σ standard deviation in the calculated quiescent fractions for CARLA J1753+6311.

Without far-IR data, I am unable to locate extremely dust-obscured systems, so these will not be found in either the 7C 1753+6311 field or UDS and would be missing from Figure 3.5. These extremely dusty galaxies are rare, but could be an important population in protoclusters (e.g. Brodwin *et al.*, 2013). In addition, some galaxies (of order $\sim 10\%$) may be misclassified due to very dusty regions within them causing redder colours. Further analysis with submillimeter data would be required to examine the extremely dusty populations in these fields. This means that I cannot analyse the extremely dust-obscured populations in any of the fields considered here, but I am able to do a robust comparison between them as the dusty populations are undetected in all of these fields: CARLA J1753+6311, ClG 0218.3−0510 and the UDS control field.

Half of the detected galaxies in CARLA J1753+6311 are quiescent, with a quiescent fraction (f_Q) for sources with $J \leq 23.6$ of $f_Q = 0.50 \pm 0.09$ (see Table 3.1). Of the "red" galaxies, $80 \pm 6\%$ are quiescent, so the vast majority of these objects are not dust-obscured star forming galaxies, but are already quenched and evolving passively.

ClG 0218.3−0510 contains fewer passively evolving galaxies ($f_Q = 0.30 \pm 0.08$), with

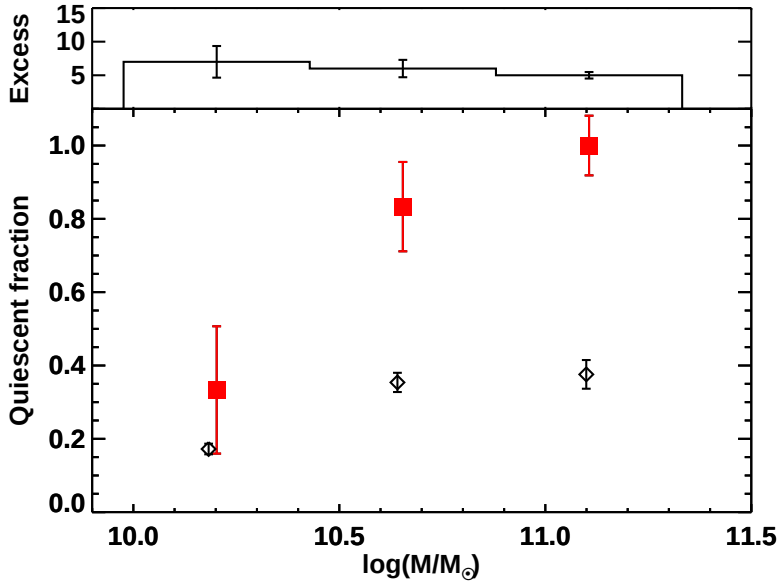

Figure 3.6: The quiescent fraction measured in $4.5\,\mu$m magnitude bins, which correspond to stellar mass bins. Red squares show the cluster values, black diamonds indicate the quiescent fractions measured for field galaxies. The top histogram shows the excess number of sources in CARLA J1753+6311, compared to a random blank field, per mass bin.

$67 \pm 11\%$ of the red galaxies classified as quiescent. These fractions were calculated using the same criteria as in Section 3.2 and within a 0.9 arcmin aperture of the cluster core. CARLA J1753+6311 has a similar fraction of red, quiescent galaxies at a 1σ level.

Both of these protoclusters contain a significantly higher quiescent fraction than the average field, which is $f_Q = 0.16 \pm 0.01$. This means that the star formation rates of many cluster members are greatly suppressed relative to the field.

3.4.4 Quiescent fraction as a function of mass

The quiescent fraction is a strong function of J band magnitude. As shown in the bottom panel of Figure 3.4, the quiescent fraction gradually rises with decreasing magnitude. At $J < 22.5$ mag the fraction of quiescent galaxies in the protocluster rises to $> 80\%$, double the field fraction.

The $4.5\,\mu$m flux provides a better correlation with stellar mass than the J flux, and is nearly independent of galaxy type. Using galaxies with known stellar masses (from full

SED-fitting) in the UDS (Mortlock *et al.*, 2013), I converted the $[4.5]$ magnitudes to stellar mass using $\log(M_*/\mathrm{M}_\odot) = 22.53 - 0.57 \times [4.5]$. I derived this equation empirically by fitting a line to the stellar masses and $[4.5]$ magnitudes from the UDS, which was resampled to have the same $J \leq 23.6$ quiescent fraction as CARLA J1753+6311, i.e. 50%, to remove the slight dependence of this relation on galaxy type. This line has an intrinsic scatter of 0.2 dex. I used this equation to calculate the masses for CARLA J1753+6311. I used a similar equation but for the full UDS with no resampling, to calculate the masses for the field. This simply corresponds to a slight shift in the bin centres in Figure 3.6. Using these equations, I recalculated the quiescent fractions as a function of stellar mass (Figure 3.6). These fractions were calculated as in Section 3.4.3 for sources in $[4.5]$ magnitude bins (corresponding to stellar mass).

There is also a strong correlation between galaxy mass and passivity, with a higher fraction of the massive sources being quiescent. Figure 3.6 shows that this trend is steeper for the protocluster galaxies than for the field galaxies, and there is a divide at $M_* \sim 10^{10.5}\,\mathrm{M}_\odot$. Only 20–30% of galaxies with stellar masses $M_* < 10^{10.5}\,\mathrm{M}_\odot$ are quiescent in both environments, whereas 80–100% of $M_* > 10^{10.5}\,\mathrm{M}_\odot$ galaxies are quiescent in the protocluster, compared to only $\sim 40\%$ in the field (Table 3.1).

I find that the fraction of quiescent galaxies is dependent on environment: CARLA J1753+6311 contains double the quiescent fraction of the control field at $z \sim 1.6$. However, this environmental effect is also mass dependent: only the population of high-mass galaxies has an enhanced quenched fraction relative to the control field. These results are consistent with recent literature on red galaxies in clusters at $z > 1.5$. Rudnick *et al.* (2012) and Fassbender *et al.* (2014) found a strong excess of bright, red galaxies in two $z \sim 1.6$ clusters, but a corresponding lack of faint, red galaxies. However, in contrast to these results, Andreon *et al.* (2014) found a well-populated red sequence down to $\sim 10^{10}\,\mathrm{M}_\odot$ in a $z \sim 1.8$ cluster and Lee *et al.* (2015) find that there is no difference in the quiescent fraction between cluster and field environments at $z > 1$, with a large variation between individual clusters. Therefore the mass dependence of quiescent galaxies needs to be analysed in a larger sample of protoclusters to draw firm conclusions.

van der Burg *et al.* (2013) showed that clusters at $z \sim 1$ also have an increased qui-

escent fraction compared to the field. The quiescent fractions in CARLA J1753+6311 are similar to the $z \sim 1$ fractions at high masses ($M > 10^{10.5}\,\mathrm{M}_{\odot}$), which is further evidence that CARLA J1753+6311 is already a very mature structure, more similar to $z = 1$ clusters than higher redshift protoclusters. The quiescent fraction at lower masses is much higher at $z \sim 1$ than in CARLA J1753+6311. This may suggest a build up of the low mass end of the red sequence in clusters from $z = 1.6$ to $z = 1$. The build up of the low mass end of the red sequence has been well documented below $z = 1$ (e.g. De Lucia *et al.*, 2007; Rudnick *et al.*, 2009, Chapter 1).

3.5 Conclusions

I have presented the first robust spectroscopic redshift of the high redshift RLAGN 7C 1753+ 6311, placing it at $z = 1.58$. I have shown that this radio galaxy is located in an 8.9σ galaxy overdensity, implying that it is embedded in a high redshift galaxy cluster. The cluster core contains 28 ± 6 excess galaxies brighter than $J = 23.6$ mag. This galaxy richness implies a cluster mass of at least several $\times 10^{13}\,\mathrm{M}_{\odot}$. Of these excess galaxies, $66 \pm 13\%$ have red colours and lie on a sequence in colour-magnitude space. The rest-frame UBJ colours of these galaxies show that 80% of the red galaxies are quiescent, therefore this is a mature cluster with a predominantly old stellar population. More than 80% of the galaxies with masses $M_{*} > 10^{10.5}\,\mathrm{M}_{\odot}$ are quiescent in this cluster, compared to only $\sim 40\%$ of field galaxies of this high mass. At lower masses I find no difference between the quiescent fractions of the field and cluster galaxies. This mature structure is similar in the level of clustering, overdensity and red fraction to other clusters at a similar redshift. The presence of a dense core and a well-formed, passively evolving red sequence suggest that RLAGN do not solely reside in young, uncollapsed protoclusters, rather they can be used as beacons for clusters in a wide range of evolutionary states.

Chapter 4

A $z = 2.5$ protocluster associated with the radio galaxy MRC 2104−242: star formation and absence of low-mass galaxies in dense environments

4.1 Introduction

In Chapter 3 I showed that RLAGN can be used to locate clusters in a range of evolutionary states. 7C 1753+6311 resides in a quiescent cluster with a collapsed core at $z = 1.6$; 80% of the red galaxies within 0.9 Mpc of 7C 1753+6311 are quiescent. The majority of RLAGN investigated to date, however, have been found to be surrounded by an excess of star-forming galaxies. In this chapter I examine the properties of star-forming galaxies at $z = 2.5$ in a protocluster and compare them to galaxies in field environments. The high-redshift radio galaxy (HzRG) MRC 2104−242 is surrounded by an overdensity of red galaxies (Hatch *et al.*, 2011a), much like 7C 1753+6311, but also has a significant star-forming population.

At low redshift, cluster galaxies appear different to those in the field in terms of their mass, morphology and luminosity-weighted ages (see Chapter 1). These age differences were instigated above $z \sim 2$, when the galaxies were still forming (Bower, Lucey

& Ellis, 1992; Cimatti *et al.*, 2004). To investigate how these differences occurred, in this chapter I study the star formation rate (SFR)-mass relation for protocluster and field galaxies. This can provide insight into the processes behind star formation and any differences with respect to environment may indicate a different formation mechanism for (proto)cluster galaxies.

Locally, the SFR-mass relation does not change as a function of galaxy environment; the fraction of galaxies which are star forming differs but the specific star formation rate (sSFR) is constant irrespective of environment (Peng *et al.*, 2010). This SFR-mass relation evolves with redshift, however cluster and field galaxies continue to lie on the same relation up to $z = 1$ (Muzzin *et al.*, 2012). At higher redshifts, studies have found that this trend of a constant sSFR between galaxies in the process of forming a cluster (protocluster galaxies) and field galaxies appears to continue, implying a sSFR independent of environment (Koyama *et al.*, 2013a,b). The existence of a "main sequence" for galaxies suggests that star formation in galaxies proceeds in the same way in (proto)clusters as it does in the field, even at redshifts $z > 2$. Protocluster galaxy properties, however, differ from those in the field: the progenitors of low redshift clusters have previously been found to contain member galaxies that are older, more star-forming, more metal-rich and twice as massive as field galaxies at the same redshift (Steidel *et al.*, 2005; Hatch *et al.*, 2011b; Koyama *et al.*, 2013a; Kulas *et al.*, 2013). This implies that cluster galaxies have experienced an accelerated growth in their early years, yet their sSFRs show no difference from the field up to redshift $z = 2$.

Previously, the SFR-mass relation in protoclusters at $z > 2$ has been studied using masses derived from K-band fluxes, and SFRs corrected using mass-dependent dust extinction estimates (Koyama *et al.*, 2013a,b). Using a dust extinction law that is solely dependent on the mass of the object makes it difficult to find extreme starbursts that lie above the main sequence. Using the rest frame UV slope as a direct measure of dust extinction, as well as infrared star formation indicators such as 24 μm and 250 μm fluxes, may help to break this degeneracy between normal star-forming galaxies and heavily dust-obscured star-bursting objects. Combining this with SED-derived masses should provide a better measure of the SFR-mass relation for protocluster and field galaxies at $z > 2$.

In this chapter I investigate the SFR-mass relation in a candidate protocluster field, around the radio galaxy MRC 2104−242. This field was observed as part of an infrared survey of eight HzRGs, described in Galametz *et al.* (2010b) and Hatch *et al.* (2011a). Four of these HzRGs appeared to be surrounded by an overdensity of red galaxies, one of which (MRC 0156−252) has been spectroscopically confirmed to lie within a large-scale structure (Galametz *et al.*, 2013). The subject of this chapter, MRC 2104−242, had a 3σ overdensity of red galaxies ($J - H > H - K + 0.5 \ \cap \ J - K > 1.5$, see Hatch *et al.*, 2011a) and the angular correlation function showed that the galaxies in this field were more clustered than average (Hatch *et al.*, 2011a). MRC 2104−242 lies at $z = 2.49$ (McCarthy *et al.*, 1990), which means the Hα emission line falls directly within the ISAAC narrow-band filter at $2.29\,\mu$m. This allows us to select star-forming galaxies within a narrow redshift range ($\Delta z = 0.05$) around the radio galaxy. Using optical to MIR photometry we have studied the masses and star-forming properties of Hα selected galaxies around MRC 2104−242. We have compared the results in the radio galaxy field to a control field sample, using the same selection techniques throughout.

The structure of this chapter is as follows: Section 4.2 outlines the observations, data reduction and sample selection. Section 4.3 describes my methods in determining the galaxy properties. In Section 4.4 I present my results and look at galaxy properties as a function of environment. Section 4.5 discusses my key results and possible implications and Section 4.6 presents a summary.

4.2 Data

I obtained images of MRC 2104−242 in g', z', J, H, K_s, $3.6\,\mu$m, $4.5\,\mu$m, and $24\,\mu$m bands (described further in the following subsections) as well as narrow-band photometry at $2.29\,\mu$m, covering an area of 2.65 arcmin $\times$ 2.65 arcmin. This narrow-band filter is centred on the Hα emission line at $z = 2.49$, the redshift of the radio galaxy. The width of the filter (324 Å) allows us to select Hα emitters between $2.46 < z < 2.51$. This corresponds to $\Delta v \sim 4300\,\mathrm{km\,s^{-1}}$, so I expect to detect all protocluster members.

4.2.1 Imaging and data reduction

4.2.1.1 NIR observations

MRC 2104−242 was observed in service mode using the High Acuity Wide-field K-band Imager (HAWK-I) (Kissler-Patig *et al.*, 2008) to obtain the J, H and $K_{\rm s}$ images, and ISAAC to obtain the narrow-band (hereafter NB) $2.29\,\mu$m image. Details on the observations and reduction of the J, H and $K_{\rm s}$ data are provided in Hatch *et al.* (2011a), here I use the reduced, flux-calibrated, PSF-matched images. The NB data were obtained in 2011 October 8–10th for a total integration time of 5.6 h (PI N. Hatch). The ISAAC field of view is smaller than the HAWK-I field of view (2.5 arcmin $\times$ 2.5 arcmin compared to 7.5 arcmin $\times$ 7.5 arcmin), so the detector was aligned to match the coverage of the HAWK-I chip containing the radio galaxy. The radio galaxy was positioned in the upper-right section of the ISAAC detector to match the spatial coverage of the deep HAWK-I data.

The NB data were reduced by N. Hatch with the ESO/MVM data reduction pipeline (Vandame, 2004) and the astrometric solutions were derived using a catalogue from the $K_{\rm s}$ HAWK-I data. The pixel scale of the H, J and $K_{\rm s}$ HAWK-I images (0.106 arcsec pixel^{-1}) was degraded to the ISAAC pixel scale of 0.148 arcsec pixel^{-1}. The NB image was convolved to the seeing of the $K_{\rm s}$ of 0.7 arcsec.

To ensure the image depth was approximately consistent across the whole image, I masked out regions which had less than 30 percent of the maximum exposure time. I measured the 3σ image depths given in Table 4.1 by placing 2 arcsec apertures at multiple (~ 10000) random locations. The total overlapping area of the NB, H, J and $K_{\rm s}$ images is 11.8 arcmin^2.

I flux-calibrated the NB image using the HAWK-I $K_{\rm s}$ image (which was flux-calibrated using 2MASS stars in the field of view; see Hatch *et al.* 2011a) and made further adjustments to this calibration by comparing the $NB-K_s$ colour of stars in the images to the predicted colours of stars in the Pickles stellar library. Uncertainties in the flux calibration are < 0.04 mag. No correction was applied to account for Galactic extinction as this is negligible.

Filter	Integration Time	3σ Limit (AB)	Instrument
g'	3.8 h	27.8	GMOS-S
z'	0.67 h	25.1	GMOS-S
J	3.38 h	25.3	HAWK-I
H	0.67 h	24.3	HAWK-I
K_s	1.53 h	24.0	HAWK-I
NB229	5.6 h	21.4	ISAAC
3.6 μm	0.44 h	23.0	IRAC
4.5 μm	0.44 h	22.7	IRAC

Table 4.1: Details of the images used. Limiting magnitudes for the optical and NIR images were measured using randomly placed 2 arcsec apertures. The IRAC image limits were determined from their completeness curves.

4.2.1.2 MIR and FIR observations

I obtained reduced and calibrated mid- and far-infrared images from *Spitzer*/MIPS and *Herschel*/SPIRE, as well as catalogues of sources at $3.6\,\mu$m and $4.5\,\mu$m from *Spitzer*/IRAC. Details of the observations, data and references are below.

IRAC (Fazio *et al.*, 2004) observations at $3.6\,\mu$m and $4.5\,\mu$m were obtained in 2009 during a warm *Spitzer* mission (PID 60112, PI N. Hatch) for a total integration time of $1600\,$s in both bands. Details of the observations and data reduction can be found in Galametz *et al.* (2012). I estimated the limiting magnitudes for the IRAC bands from their completeness curves.

Spitzer MIPS (Rieke *et al.*, 2004) 24 μm data was obtained as part of the *Spitzer* High-redshift Radio Galaxy sample survey. Full details of the observations and data reduction can be found in Seymour *et al.* (2007).

Herschel SPIRE (Griffin *et al.*, 2010) $250\,\mu$m imaging was obtained during the Search for Protoclusters with *Herschel* (SPHer) survey and reduced by E. Rigby. The depth of the SPIRE data of the MRC 2104−242 field is identical to that of the three control fields. A description of the data can be found in Rigby *et al.* (2014).

4.2.1.3 Optical observations

Observations in the optical regime (g' and z' bands) were taken in service mode using the Gemini Multi-Object Spectrograph South (GMOS-S; Hook *et al.*, 2004) instrument on Cerro Pachon, Chile, during the period 2010 August–November (PI N. Hatch). The

z' band total integration time was 40 min, and the total g' band integration time was 3.8 h. I reduced the g' and z' data using the Gemini GEMTOOLS IRAF package. The usual reduction steps were taken: bias subtraction, flat fielding, and trimming of the image. The z' band fringing was removed using IDL to subtract the fringe frame, which had been created using the IRAF package GIFRINGE. I mosaicked and combined the images using IMCOMBINE.

I flux-calibrated the g' image by comparing the $g' - J$ colour of stars in the image to those predicted using the Pickles stellar library (the J image was flux-calibrated using 2MASS stars in the field of view; see Hatch *et al.* 2011a). I then flux-calibrated the z' image similarly, using the $g' - z'$ colour of stars. I measured 3σ image depths by placing ~ 10000 random 2 arcsec apertures on the images.

4.2.2 Control field

Throughout this chapter, I compare the radio galaxy field to three control fields taken from the Ultra Deep Survey (UDS), the Cosmic Evolution Survey (COSMOS) and the Great Observatories Origins Deep Survey-South (GOODS-S). By using three separate control fields I hope to overcome the effects of cosmic variance in my results, however this will still be an issue due to the small fields of view. For each of the control fields, I obtained reduced, calibrated images in approximately the same bands as the radio galaxy field (B, z', J, H, K_s, $3.6\,\mu$m, $4.5\,\mu$m, $24\,\mu$m, $250\,\mu$m). NB images were taken using the HAWK-I H_2 $2.12\,\mu$m filter for the UDS and COSMOS fields and using the NB2090 filter for the GOODS-S field. These filters detect Hα emission at $2.22 \leq z \leq 2.26$ and $2.18 \leq z \leq 2.21$ respectively. When calculating densities I scale the control field results according to the different volumes given by each filter. Each of the control fields is limited by the size of the NB field-of-view and are all approximately 57 arcmin^2. I refer to Hatch *et al.* (2011b) for details on the reduction of the $K_{\rm s}$ and NB images. The remaining photometry was obtained from public archives and is described in Capak *et al.* (2007, 2011); Furusawa *et al.* (2008); Retzlaff *et al.* (2010); McCracken *et al.* (2012); Hartley *et al.* (2013). The *Spitzer* data was obtained from the NASA/IPAC Infrared Science Archive. The *Herschel* $250\,\mu$m data was obtained from the H-ATLAS survey (Eales *et al.*, 2010) and re-reduced by E. Rigby to have the same

depth as the MRC 2104−242 data, see Rigby *et al.* (2014) for details.

4.2.3 Catalogues

To create a photometric catalogue of the data, I used SExtractor (Bertin & Arnouts, 1996)in dual-image mode, using a weighted NB image as the detection image, to obtain fluxes in all bands. The NB image was weighted with the square root of the effective exposure map, which takes background noise into account. I select sources as those with 25 adjoining pixels that are 1σ above the rms background and use apertures of 2 arcsec in diameter for measuring colours. These apertures are significantly larger than the ~ 0.7 arcsec FWHM of point sources in the images.

Individual flux densities were measured using Kron AUTO apertures. I estimated limiting magnitudes for the optical and NIR bands by measuring the standard deviation of the flux densities in 2 arcsec diameter apertures placed randomly on the images (Table 4.1). For the IRAC $3.6\,\mu$m and $4.5\,\mu$m bands, SExtractor was optimised with MINAREA $= 4$ pixels and DETECT_THRESH $= 2.5\sigma$ above the rms background. I matched the NB photometric catalogues with the IRAC catalogues within 1 arcsec using Topcat (Taylor, 2005) to produce the full photometric catalogue. In order to determine what effect the choice of SExtractor parameters had on my results, I checked my methods using three different parameter combinations: 2 arcsec fixed apertures (25 adjoining pixels), AUTO apertures for 25 adjoining pixels and AUTO apertures with 24 adjoining pixels. I found that the choice of selection parameters does not significantly affect my results and does not alter my conclusions.

4.2.4 Selection of NB sources

To obtain a sample of NB-excess sources I followed the method of Bunker *et al.* (1995), selecting sources with excess NB signal relative to the K_s band. Sources with a value of $K_s - NB \geq 2\Sigma$ were selected as NB excess sources, with Σ defined as:

$$\Sigma = \frac{1 - 10^{-0.4(K-NB)}}{10^{-0.4(zp-NB)}\sqrt{\pi r_{ap}^2(\sigma_{NB}^2 + \sigma_K^2)}} \tag{4.1}$$

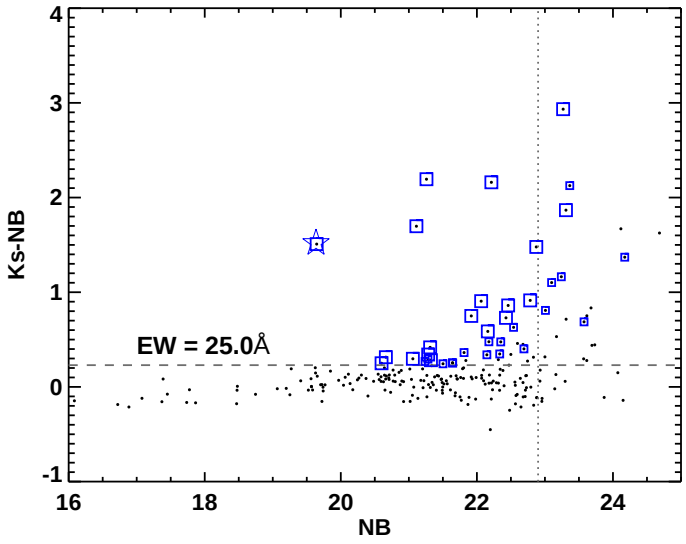

Figure 4.1: Colour-magnitude diagram for the MRC 2104−242 field. Blue points highlight NB-excess sources with $K_s - NB > 2\Sigma$, with larger squares indicating those with $K_s - NB > 3\Sigma$. The radio galaxy is highlighted with a blue star. The dashed line marks a rest-frame EW cut of 25Å. The vertical dotted line shows the 80% completeness limit in the NB.

K and NB are the AB magnitudes in each band, σ values are the SExtractor errors for each band, πr_{ap}^2 is the area of the aperture used and zp is the zero-point of the images; here $zp = 26.9$.

A rest frame equivalent width (EW) cut of 25 Å was also used to avoid contamination due to photometric errors. Figure 4.1 shows the $K_s - NB$ colours against the NB magnitudes for all sources. Σ quantifies the significance of the NB excess and the 2Σ selection corresponds to a completeness cut in star formation rate (SFR) of ~ 7 $M_\odot$ yr^{-1}. I also exclude sources with NB magnitude fainter than 22.9. At this limit the data is $> 80\%$ complete in both the radio galaxy field and all the control fields. Completeness was calculated by comparing the detection catalogues for the NB and deeper K_s images. Figure 4.2 shows the completeness curves for each field in the NB and K_s band. Vertical lines indicate where the NB becomes 80% complete. A $NB > 22.9$ mag cut corresponds to the completeness of the radio galaxy field. In the radio galaxy field I find 31 sources above this limit, 16 of which have values of $K_s - NB > 3\Sigma$. Of these NB excess sources, 14 have detections at 3.6 μm and 4.5 μm.

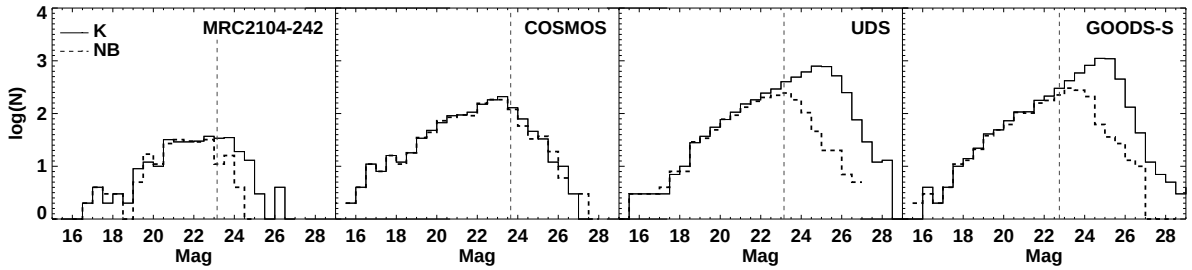

Figure 4.2: Completeness histograms for the K_s (solid lines) and NB (dashed lines) images in the MRC 2104−242 field and control fields. Vertical lines mark the 80% completeness limit for each NB image.

4.2.5 Hα emitters

Excess NB flux could also be produced from low-redshift ($z < 1$) emission line contaminants or [OIII] lines from sources at $z = 3.57$. To remove low-redshift contaminants I used two methods: firstly following the method of Daddi *et al.* (2004), I select Hα emitters as sources with BzK colours ($(z - K_s) - (B - z) > -0.2$, or equivalently gzK colours: $(z - K_s) - \left(\frac{(g'-z')-0.13}{0.87}\right) > -0.2$). The BzK criterion selects sources that lie at redshifts between $1.4 < z < 2.5$ and has a contamination rate of $\leq 13\%$ from galaxies at $z < 1$ (Daddi *et al.*, 2004). I do not have B band photometry in the radio galaxy field so I used the g' band photometry in its place. I converted the selection criteria using model galaxy spectra, redshifted to the lower limit of BzK-selected galaxies ($z = 1.4$) and convolved with B, g' and z' filters. A line was fit to the $g' - z'$ versus $B - z'$ points to obtain the selection conversion. Secondly, for sources with IRAC detections, I took a colour cut of $[3.6] - [4.5] > -0.1$, selecting sources which lie at $z > 1.3$ (Papovich, 2008).

I retain in my sample those sources which are selected by either the BzK or IRAC criterion. I removed two sources because they appeared to be associated with a large, foreground galaxy, possibly a spiral. I have checked my results with and without including these sources and they remain unchanged. I therefore remove the sources to avoid contamination from low redshift interlopers.

Sobral *et al.* (2013) find that 10–20% of sources selected using the BzK method may be high redshift contaminants. However, without spectroscopic information I am unable to identify sources at $z = 3.57$ and cannot remove them from my sample. After applying these selections to my NB excess sources, there are 18 Hα emitters in my

sample (from 31 NB excess sources), including the radio galaxy and three "companion" galaxies, which lie within 3 arcsec of the radio galaxy. Nine of these Hα emitters were selected via the IRAC colour selection, and 11 via the BzK criterion (2 were selected by both criteria). I selected $17/25$, $9/16$, $8/12$ (Hα emitters / NB excess sources) from the COSMOS, UDS and GOODS-S control fields respectively.

4.2.6 AGN

I estimated the contamination rate of AGN in the control fields using the following *Spitzer* IRAC criterion from Donley *et al.* (2012):

$$x = \log\left(\frac{f_{5.8\mu\mathrm{m}}}{f_{3.6\mu\mathrm{m}}}\right), y = \log\left(\frac{f_{8.0\mu\mathrm{m}}}{f_{4.5\mu\mathrm{m}}}\right)$$

$$x \geq 0.08 \cap y \geq 0.15 \tag{4.2}$$

$$y \geq (1.21 \times x) - 0.27 \tag{4.3}$$

$$y \leq (1.21 \times x) + 0.27 \tag{4.4}$$

$$f_{4.5\mu\mathrm{m}} > f_{3.6\mu\mathrm{m}} \tag{4.5}$$

$$f_{5.8\mu\mathrm{m}} > f_{4.5\mu\mathrm{m}} \tag{4.6}$$

$$f_{8.0\mu\mathrm{m}} > f_{5.8\mu\mathrm{m}} \tag{4.7}$$

From this selection I estimate that there are two possible AGN in the COSMOS Hα emitter sample and none in the UDS or GOODS-S samples. I do not have $5.8\,\mu$m and $8\,\mu$m data for the MRC 2104$-$242 field that is deep enough to determine the number of AGN around the radio galaxy. Assuming the AGN fraction in the MRC 2104$-$242 field is the same as in the control fields (AGN/Hα emitters $= 0.03$), I do not expect to find any AGN in this field. The suspected AGN were retained in the control field sample, so the results are not biased, but I discuss how removing them will affect my results in Section 4.4.5.1.

4.3 Determining properties of Hα emitters

4.3.1 Stellar mass

I determined stellar masses by using the SED fitting programme "Fitting and Assessment of Synthetic Templates" (FAST, Kriek *et al.*, 2009) to fit the photometry of my sample of Hα candidates to obtain mass estimates. I assume from now on that the NB excess flux in the Hα candidates is due to Hα+[NII] emission at the redshift of the radio galaxy and I fixed the redshift of the fit to $z = 2.49$. The control field galaxy redshifts were set to $z = 2.24, 2.24,$ and 2.19 for COSMOS, UDS and GOODS-S respectively, assuming Hα emission from the centre of the NB filters. The effect of having control fields at slightly lower redshifts is discussed in Section 4.4.5.2.

I used FAST to fit Bruzual & Charlot (2003) stellar population synthesis models with a Chabrier (2003) IMF to the photometry (B/g',z',J,H,K,[3.6],[4.5]). $12/18$ Hα emitters in the MRC 2104−242 field had detections in the IRAC bands. I fit delayed exponentially declining (SFR $\sim t\exp[-t/\tau]$) star formation histories with dust extinction $0 < A_V < 3$ in steps of 0.2 mag (assuming the Calzetti *et al.* (2000) extinction law), $7.0 < \log_{10}(\tau/\mathrm{yr}) < 10.1$ in steps of 0.1 and $7.5 < \log_{10}(\mathrm{age/yr}) < 9.5$ in steps of 0.2. Metallicities were fixed to solar abundance. As I have rest-frame UV, optical and NIR photometry, the stellar mass output from the SED is well-determined. Due to degeneracies between SFR, dust extinction (A_V) and the assumed star formation histories, I do not use these outputs from FAST as they are likely to be highly unreliable. However, the mass output is robust independent of the exact star formation history template that is assumed (Shapley *et al.*, 2005). Errors in the stellar masses are determined from 100 Monte Carlo simulations performed by FAST, with the photometry being varied within the flux uncertainties. I also added a rest-frame template error function to take into account the uncertainties in the model templates.

Some of the photometry for the control fields is deeper than for the protocluster field. In my analysis only detections to the depth of the MRC 2104−242 field were considered in the control fields. I have checked my results using full-depth magnitudes for the control field and find that my overall conclusions are unaffected by the different depths of the images between fields.

4.3.2 SFRs

4.3.2.1 Hα-derived SFRs

I calculated the K_s continuum and convert the NB signal to an Hα flux using:

$$f(K_{\rm cont}) = \frac{w_{K_s} f(K_s) - w_{\rm NB} f({\rm NB})}{w_{K_s} - w_{\rm NB}} \tag{4.8}$$

$$f({\rm H}\alpha) = w_{\rm NB}[f({\rm NB}) - f(K_{\rm cont})] \tag{4.9}$$

where $f(K_{\rm cont})$ is the continuum flux density in the K_s band, $f({\rm NB})$ and $f(K_s)$ are the flux densities in the NB and K_s bands respectively, $f({\rm H}\alpha)$ is the Hα flux, and w_{K_s} and $w_{\rm NB}$ are the widths of the corresponding filters.

These values are corrected for dust extinction calculated from the $B-z'$ colour[1], which corresponds to the rest-frame UV slope, following the method of Daddi *et al.* (2004):

$$E(B-V) = 0.25(B - z' + 0.1)_{AB} \tag{4.10}$$

Note that here I assume that the extinction for Hα is the same as for the broadband SED. Where sources had g', B or z' magnitudes fainter than the 3σ limiting magnitude (see Table 4.1) I convolved the best fitting SED template for that source with the appropriate filter curve in order to get a magnitude estimate. For the radio galaxy field any sources with g' magnitudes fainter than 3 times the limiting magnitude were convolved with a B filter curve to avoid having to convert the colours. For each of the control fields and for the radio galaxy field z' band, I used the B or z' filter curve of the instrument used to obtain the data.

Dust-corrected Hα luminosities were then calculated, scaling for luminosity distance, and Hα SFRs determined using the Kennicutt (1998) relation, converted to a Chabrier (2003) IMF:

$$SFR({\rm M}_\odot\ {\rm yr}^{-1}) = 4.39 \times 10^{-42} L_{H\alpha}({\rm erg\,s}^{-1}) \tag{4.11}$$

[1]For the MRC 2104−242 field the $B - z'$ colour was calculated using $(B - z') = \left(\frac{(g'-z')+0.09}{0.91}\right)$ at $z = 2.5$

4.3.2.2 MIPS 24 μm SFRs

The *Spitzer* $24\,\mu$m filter transmits between 20.8–25.8μm, which corresponds to rest-frame wavelengths of 6.0–$7.4\,\mu$m for $z = 2.49$ galaxies. This rest-frame wavelength range is dominated by polycyclic aromatic hydrocarbon (PAH) features, which have been shown to provide a good measure of hidden star formation (Siana *et al.*, 2009).

The $24\,\mu$m data have a 3σ detection limit of ~ 0.11 mJy. There is a $> 3\sigma$ detection in $24\,\mu$m for the radio galaxy and its companions (these sources are blended in the $24\,\mu$m image), however the majority of the Hα emitters were not individually detected. I therefore stacked the sources to obtain a median flux density for each field. The radio galaxy and its companions were not included in the stack, however I include the AGN candidates in the COSMOS field as these sources were not individually detected at $> 2\sigma$ and we are not able to identify AGN candidates in the protocluster field.

I created postage stamps of 22×22 pixels (4.5 times the *Spitzer* $24\,\mu$m FWHM) around each Hα source, and median-stacked sources in each field (Figure 4.3). I then measured flux densities from the stacks in 8 pixel (5 arcsec) diameter apertures (Table 4.2).

The rest-frame IR flux densities were converted to SFRs using both the method outlined in Rujopakarn *et al.* (2013) (their section 5) and using equation 14 of Rieke *et al.* (2009):

$$\log\left(SFR_{IR}\right) = 0.108 + 1.711(\log\left(4\pi L_d^2 f\right) - 53) \tag{4.12}$$

where f is the flux density in an 8 pixel diameter aperture, L_d is the luminosity distance in cm. The method from Rujopakarn *et al.* (2013) assumes these galaxies lie on the galaxy main sequence (MS), whereas Rieke *et al.* (2009) calculate the SFR for (ultra) luminous infrared galaxies ([U]LIRGs). Without additional information, such as a measure of the IR bump, I cannot distinguish between the two scenarios for the galaxies in my sample (see Elbaz *et al.*, 2011) and so I use both methods in my analysis. The detection limit of 0.11 mJy corresponds to $\sim 145\,\mathrm{M}_\odot\,\mathrm{yr}^{-1}$ or $\sim 1200\,\mathrm{M}_\odot\,\mathrm{yr}^{-1}$ (MS or ULIRG) at $z = 2.5$.

Field	n	Flux density (μJy)	SFR (MS; $M_\odot$ yr^{-1})	SFR (ULIRG; $M_\odot$ yr^{-1})
MRC 2104−242	14	35.7 ± 10.0	37.3 ± 13.3	171.4 ± 94.6
COSMOS	17	10.3 (9.2) $\pm$ 3.5 (3.8)[a]	6.3 ± 2.6	13.3 ± 8.5
UDS	9	18.1 ± 1.2	12.3 ± 1.4	34.7 ± 5.9
GOODS-S	8	-[b] $\pm$ 0.52	0.63	0.48

Table 4.2: Flux densities measured from the 24μm stacks in an aperture of radius 5 arcsec. The uncertainties are the standard deviation of 1000 sets of n stacked random regions (where n is the number of Hα sources in each field). The SFRs given are calculated from the $24\,\mu$m fluxes using relations based on local ULIRGs and main sequence (MS) estimates.
[a] Numbers in brackets for COSMOS are flux density and error values when the AGN candidates are removed from the stack.
[b] There was no detectable signal in the GOODS-S stack, the 3σ value is used in all SFR calculations.

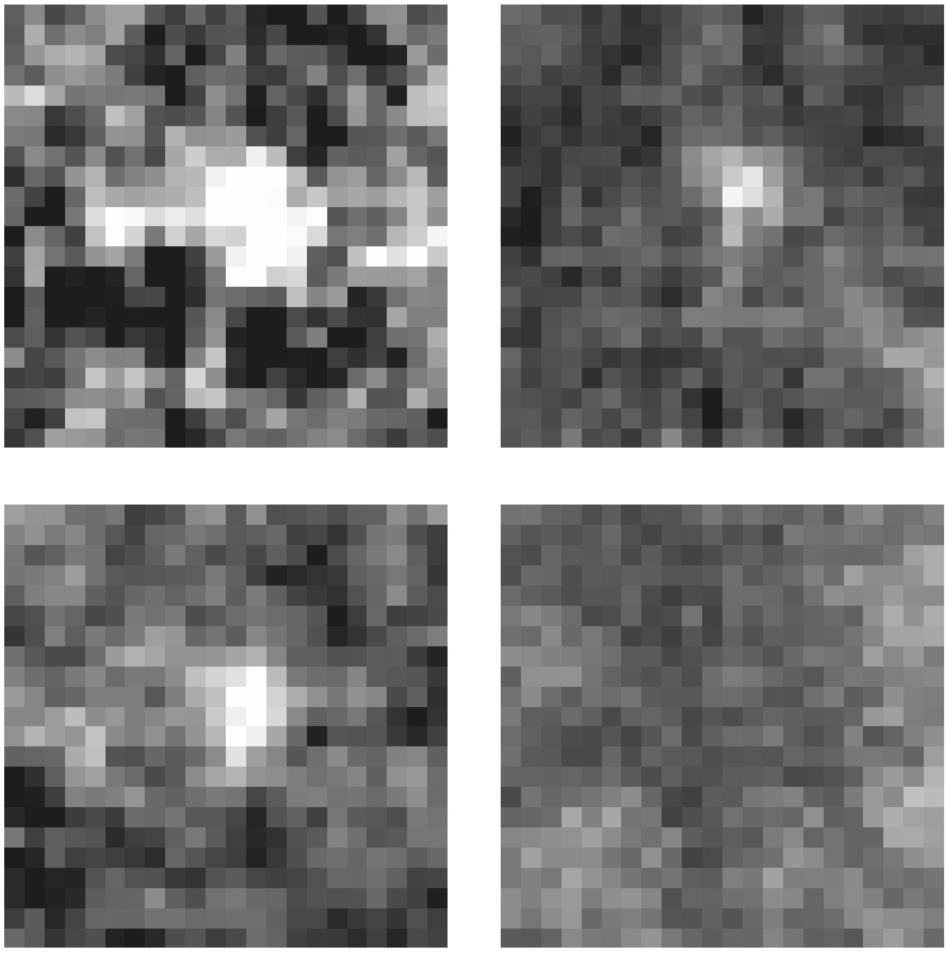

Figure 4.3: Median stacks of MIPS $24\,\mu$m images for Hα emitters. Clockwise from top left: MRC 2104−242 (14 stamps), COSMOS (17 stamps), GOODS-S (8 stamps), UDS (9 stamps). All images have the same scale. Three of the four fields have clear detections, with MRC 2104−242 showing a stronger signal. The radio galaxy and companions are not included in the stack, however the COSMOS AGN candidates are included.

4.3.2.3 *Herschel* 250 μm SFRs

The *Herschel* SPIRE $250\,\mu$m filter probes the far-IR bump for galaxies at $z > 2$, allowing the total IR luminosity of distant galaxies to be measured. These data have a 3σ detection limit of $\sim 375\,\mathrm{M}_{\odot}\,\mathrm{yr}^{-1}$ at $z = 2.5$. The radio galaxy and its companions are detected in the *Herschel* $250\,\mu$m data, and a few other Hα sources had $> 2\sigma$ detections within 10 arcsec, however due to the large beam size of *Herschel* we are unable to robustly identify counterparts. To obtain an estimate of the SFR of the Hα emitters I therefore median stacked all Hα sources (not including the radio galaxy and its companions). A SFR was derived from the median $250\,\mu$m flux by modelling the IR bump as an isothermal body of temperature 35 Kelvin and $\beta = 1.5$ (Smith *et al.*, 2013). This template was normalised to the detected $250\,\mu$m flux and integrated over 8–1000 μm to obtain L_{IR}. The L_{IR} was converted to a SFR using the Kennicutt (1998) relation adjusted to a Chabrier (2003) IMF by dividing the SFRs by 1.6. Median stacks of the Hα emitters in the UDS, COSMOS and GOODS-S fields were produced in the same manner, but none of these stacks resulted in a signal above 3σ significance.

4.4 Results

4.4.1 Galaxy overdensity

The field around MRC 2104−242 has a large overdensity of Hα emitters (Figures 4.4 & 4.5). Excluding the radio galaxy and three nearby companions, there are 14 objects in a 7.09 sq. arcmin field, which is 8.0 ± 0.8 times the density of the control fields, i.e. contains a galaxy overdensity of 7.0 ± 0.8. The field of view around the HzRG is relatively small ($4.5\,\mathrm{Mpc} \times 4.5\,\mathrm{Mpc}$ comoving) compared to the average size of high redshift protoclusters: protoclusters at $z > 2$ typically extend for at least $\sim 10\,\mathrm{Mpc}$ (Venemans *et al.*, 2007; Hatch *et al.*, 2011a). As Chiang, Overzier & Gebhardt (2013) show this means we cannot say anything for certain about the total or future mass of this structure as the vast majority of the mass available for growth will be outside of our field of view (Muldrew, Hatch & Cooke, 2015). This level of overdensity, however, is of the same order that has been found in other protoclusters at similar redshift (e.g.

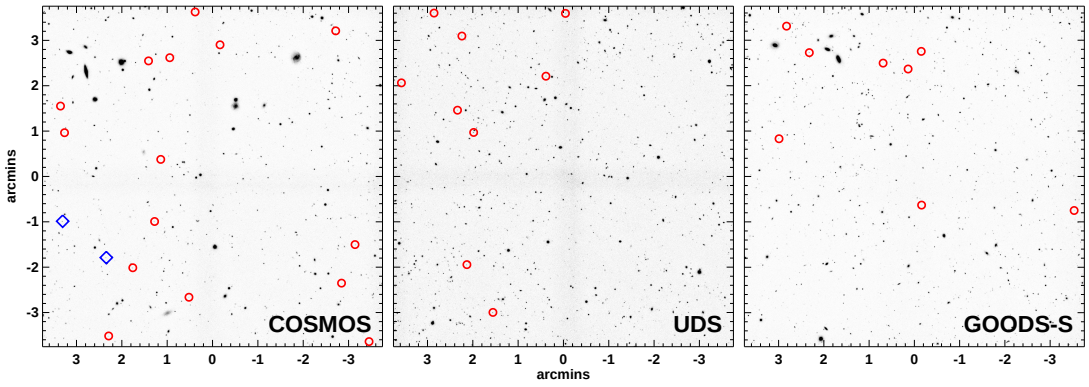

Figure 4.4: The control fields used in this study. From left: COSMOS, UDS, GOODS-S. The figures show the NB images, with detected Hα sources overlaid as red circles. The AGN candidates in the COSMOS field are highlighted with blue diamonds. Each window is 7.5 arcmin $\times$ 7.5 arcmin.

Kurk *et al.*, 2004b; Hatch *et al.*, 2011b; Hayashi *et al.*, 2012). MRC 2104−242 is therefore likely to also lie within a protocluster.

I tested to see if there was any preferential clustering of Hα sources around the radio galaxy by comparing the average distance from the radio galaxy to average distances calculated from random distributions of sources. The average distance of the Hα sources from the radio galaxy differs from that expected from a random distribution at a 2.6 sigma level. However, this includes the three companion galaxies within 3 arcsec of the radio galaxy. When these three sources are excluded from the analysis the significance is only 1.2 sigma. Therefore there is no strong clustering around the radio galaxy.

4.4.2 Red galaxies

Hatch *et al.* (2011a) found a 3σ overdensity of JHK galaxies ($J-H > H-K+0.5 \cap J-K > 1.5$ [Vega]) around MRC 2104−242. The JHK criterion selects red galaxies with low SFRs or star forming galaxies which are heavily obscured by dust, and so probes a different population to the Hα emitters. I find 10 JHK galaxies within the ISAAC field-of-view (Figures 4.5 and 4.7), one of which is the radio galaxy. The spatial distribution of the JHK galaxies is presented in Figure 4.5.

Whilst all of our Hα emitters are likely to lie within the protocluster, the JHK galaxies lie within a much larger redshift range and so it is unclear whether they are associated with the protocluster. Two JHK galaxies, in addition to the radio galaxy, are Hα

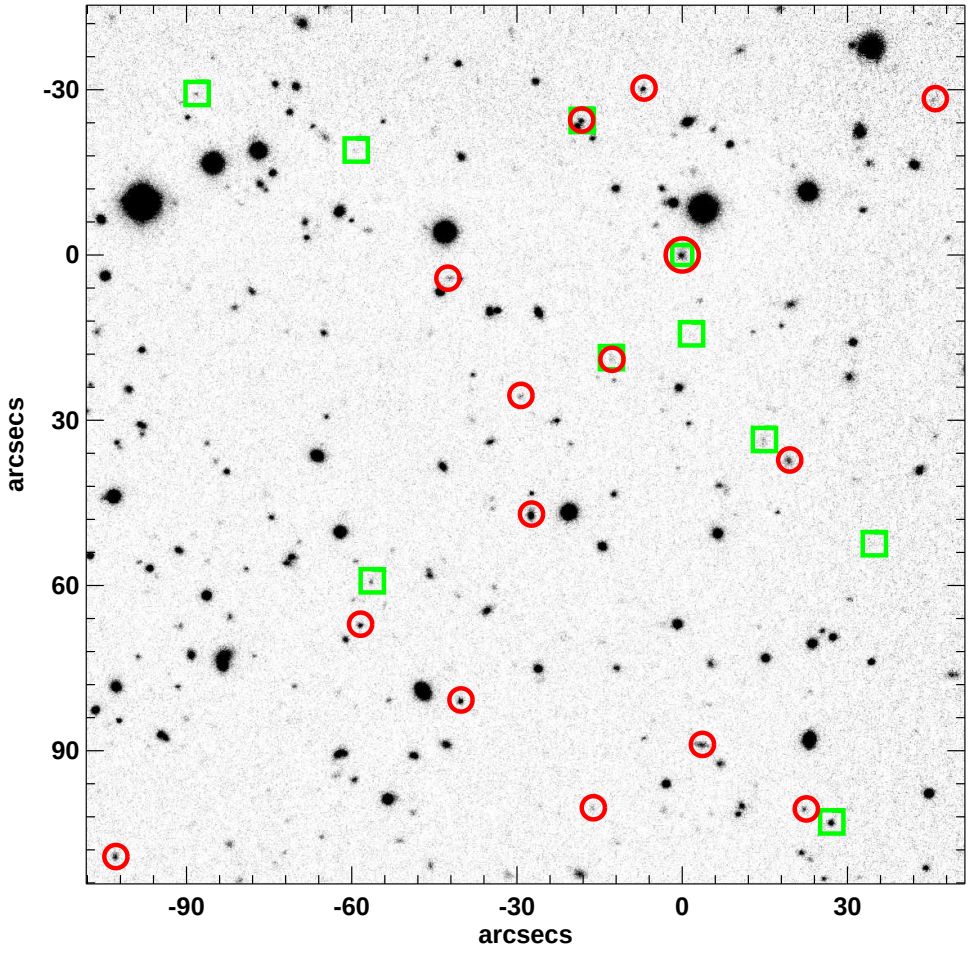

Figure 4.5: K_s image of the field around MRC 2104−242. North is up, East to the left. Detected Hα sources are shown with red circles. The radio galaxy and three companions (see Figure 4.6) lie at the origin, within the larger red circle of radius 3 arcsec. The window size is 2.65 arcmin × 2.65 arcmin. The MRC 2104−242 field is clearly overdense compared to the control fields (see also Figure 4.4), containing 14 Hα emitters in a $\sim$ 7 sq. arcmin field. For comparison we also show galaxies selected by the JHK criterion (green squares, see text for details). The radio galaxy was also selected by the JHK criterion.

emitters, meaning these galaxies are highly dust obscured, star forming galaxies which lie in the protocluster. One of these is the Hα source with a 3σ signal at $24\,\mu$m and 2σ signal at $250\,\mu$m. Stacking the NB images for the remaining 7 JHK galaxies does not produce a signal, giving an upper limit of $SFR \sim 5.5\,\mathrm{M}_\odot\,\mathrm{yr}^{-1}$, and there is no significant detection ($< 2\sigma$) in the stacked MIPS $24\,\mu$m and *Herschel* $250\,\mu$m images. Hence if the remaining 7 JHK galaxies are in the protocluster the lack of NB emission indicates that they are passive, with a sSFR of $\log_{10}(sSFR/\mathrm{yr}^{-1}) \leq -9.7$.

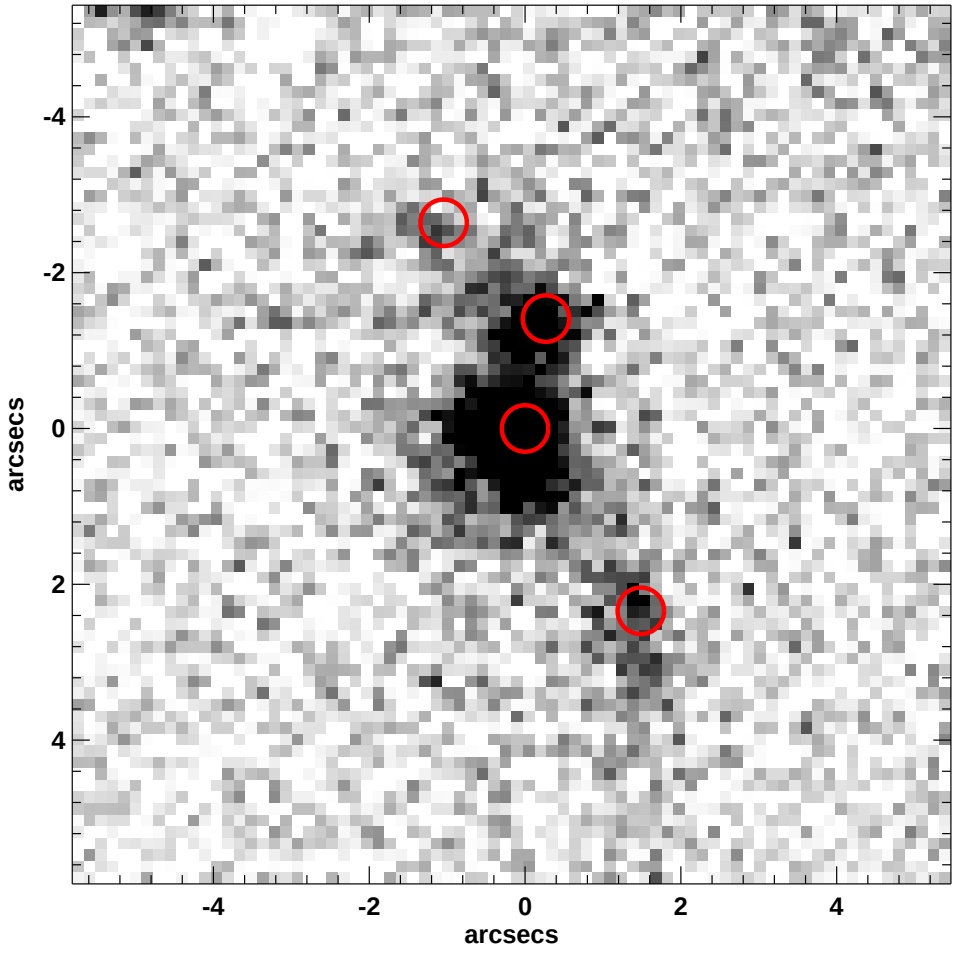

Figure 4.6: NB image of the radio galaxy MRC 2104−242 and its three companion sources, all circled in red.

4.4.3 Comparison of the Hα emitters in the protocluster and control fields

In this section I perform a detailed comparison of the protocluster and control galaxies, including their stellar masses, SFRs, dust extinction, and sSFRs. In all following analysis the radio galaxy and three companions (see Figure 4.6) have been removed from the protocluster sample. These objects are likely to be affected by the radio jets and my objective in this chapter is to study the environmental impact of the protocluster rather than the influence of the RLAGN on nearby galaxies.

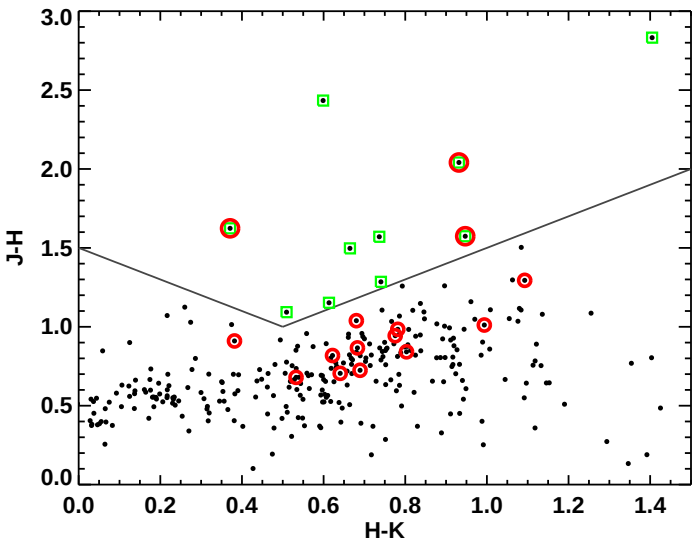

Figure 4.7: Near IR colours of galaxies in the MRC 2104−242 field. Lines mark the JHK criterion used to select galaxies at high redshift; galaxies selected this way are shown by green squares. Hα emitters are highlighted with red circles.

4.4.3.1 Galaxy stellar masses

I find that the protocluster galaxies are on average more massive than the control field galaxies (shown in Figure 4.8a). A two-sided Kolmogorov-Smirnov (K-S) test shows a significant difference between the two samples: K-S $p = 2.2 \times 10^{-5}$. The SED fits at masses $M < 10^9 M_\odot$ have large errors associated with them, but even if these galaxies are excluded from the analysis there is still a significant difference (K-S $p = 1.1 \times 10^{-4}$) between these samples. A similar difference between the masses of protocluster and control galaxies has been found in other $z > 2$ studies, including Steidel *et al.* (2005); Hatch *et al.* (2011b) and Koyama *et al.* (2013a).

The protocluster contains a large number of $M > 10^{10.5} M_\odot$ objects and no objects with $M < 10^{10} M_\odot$ within the observed 7 sq. arcmin field-of-view. My detection method selects on Hα equivalent width and galaxies below the completeness limit in SFR ($< 7\,\mathrm{M}_\odot\,\mathrm{yr}^{-1}$) may not be selected. The Hα sample is therefore incomplete at all masses and particularly at low masses due to the mass-SFR relation. However I emphasise that both the protocluster and the control fields are incomplete to the same level as I have ensured that the selection method is identical in all fields. Hence the difference in mass functions in different environments is physical, rather than an artefact, and is discussed further in Section 4.5.2.

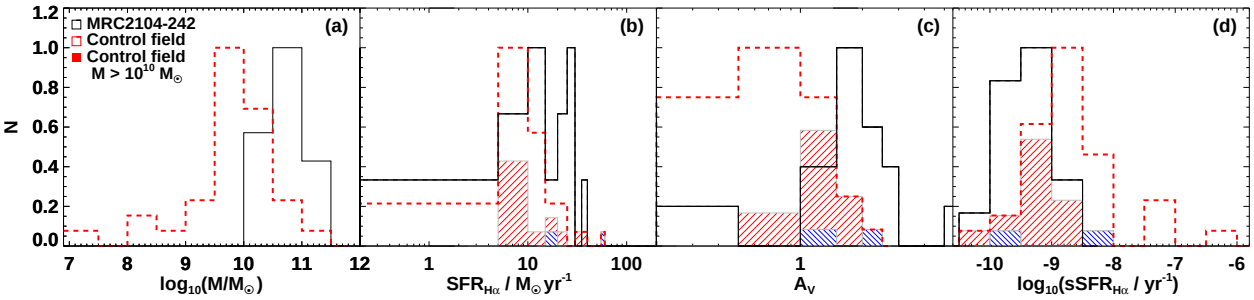

Figure 4.8: A comparison of the properties of the protocluster galaxies (black) and control galaxies (red dashed lines) including: (a) Mass, (b) Hα SFR (dust corrected), (c) A_V, (d) sSFR. Shaded in red are the mass-selected control field histograms for SFR, A_V and sSFR ($\log(M/\mathrm{M}_\odot) > 10$). Blue shaded histograms show the two AGN candidates. Each histogram is normalised to 1.

4.4.3.2 Dust content

The protocluster galaxies typically have higher dust extinction, as calculated from their UV slopes, than the field galaxies, with a median A_V that is twice as large (see Figure 4.8c). A K-S test shows a significant difference in the dust content between the two environments: K-S $p = 3.2 \times 10^{-6}$.

Dust extinction correlates strongly with galaxy mass (e.g. Garn & Best, 2010) so I tested whether the observed trend was a symptom of the mass difference found in Section 4.4.3.1 by limiting my analysis to galaxies with $M \geq 10^{10}\,\mathrm{M}_\odot$. Figure 4.9 shows the values of A_V in both the protocluster and control fields as a function of mass, with filled red squares highlighting the control field galaxies with $M \geq 10^{10}\,\mathrm{M}_\odot$. The range of A_V reduces for this mass-limited sample and the control field galaxies are more consistent with those in the protocluster. There remains a significant difference in the dust extinction measured in the protocluster and control galaxies for this sample, however only at a 2σ level (K-S $p = 0.02$).

4.4.3.3 Dust-corrected SFRs

The Hα SFRs corrected for dust extinction using the UV slope are plotted in Figures 4.8b and 4.10; there is little difference between the protocluster and control galaxies. A K-S test results in a probability of 0.1, indicating no significant difference.

Plotted in Figure 4.10 are the dust-corrected Hα SFRs against the SED-derived stellar masses for both the protocluster and control field galaxies. The Daddi *et al.* (2007) and

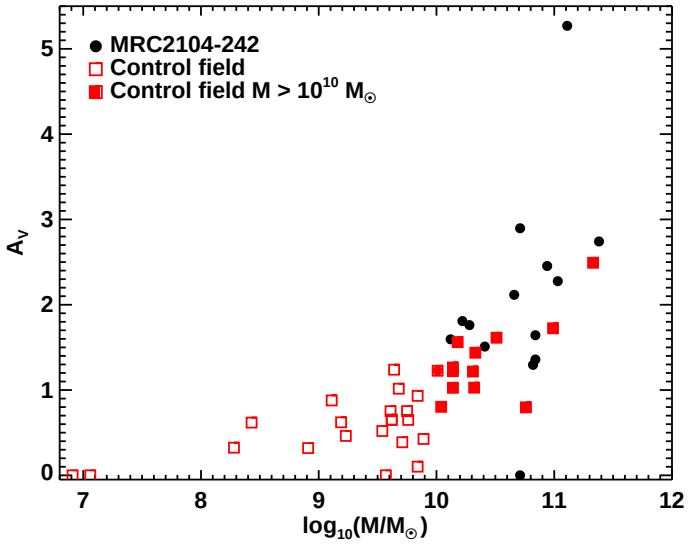

Figure 4.9: A_V as a function of galaxy mass for the protocluster (black circles) and control field (red squares) galaxies. There is a trend for increasing dust extinction with galaxy mass, with the trend becoming steeper at higher masses.

Santini *et al.* (2009) correlations showing the "main-sequence" for $z \sim 2$ galaxies are also plotted for comparison. The scatter of Hα emitters with $M < 10^{10.5}\,\mathrm{M}_{\odot}$ is consistent with the main sequence, but at higher masses both the protocluster and control field galaxies appear to lie below this relation. This suggests that the applied dust-correction for the high-mass Hα emitters is not sufficient and there may be additional star formation that is heavily optically obscured. It is extremely difficult to correct for dust extinction using the UV slope alone (Elbaz *et al.*, 2011) and a far more accurate measurement of the total SFR is obtained through the IR luminosity.

Figure 4.11 shows the total SFR derived by combining the raw Hα SFRs with SFRs derived through the IR $24\,\mu$m and $250\,\mu$m luminosities. SFRs derived using $24\,\mu$m have two values depending on whether we assume they have ULIRG SEDs or whether they have main-sequence SEDs. The *Herschel* $250\,\mu$m protocluster SFR estimate is in better agreement with the $24\,\mu$m IR SFR estimate based on local ULIRGs (Rieke *et al.*, 2009), although all of these IR estimates are in agreement with the main sequence relationship. Whilst the $24\,\mu$m signal could be due to AGN-heated warm dust, the detection of $250\,\mu$m flux (rest-frame $70\,\mu$m) in the protocluster galaxies indicates that I must be detecting cooler dust heated by UV emission from young, hot stars.

The IR+Hα SFRs are comparable to the dust-corrected Hα SFRs in the control fields,

but in the protocluster I find a large discrepancy. The IR+Hα SFRs are at least twice as fast (and up to ten times as fast) as the dust-corrected Hα SFRs which implies the protocluster galaxies contain more optically obscured star formation than those in the control galaxies. These results imply that the total SFR of the massive galaxies which reside in dense regions cannot be derived from Hα estimates alone; the protocluster galaxies have higher masses with large dust extinctions, therefore far-IR or sub-millimetre data are required to probe the optically-obscured star formation. Note that the large amount of dust extinction may have implications for studies which aim to detect protoclusters and study them through Lyman α emission from their member galaxies, as Lyα is more sensitive to dust extinction than Hα.

The IR SFRs reveal a different picture to the Hα SFRs: the protocluster galaxies are forming stars more rapidly than the control galaxies but much of this star formation is hidden from optical view. Figure 4.11 reveals that once this obscured star formation is taken into account the protocluster galaxies lie on the same main sequence of the mass-SFR relation as the control galaxies.

The IR SFR estimates for both control and protocluster galaxies are consistent with the main-sequence of the SFR-mass relation, suggesting that the majority of these Hα emitters are not undergoing a "bursty" mode of star formation but rather forming stars at the expected rate for their mass. This is in agreement with previous protocluster studies (Koyama *et al.*, 2013a,b). However, note that the SFR$_{IR}$ are derived from median stacks, thus my method would not be able to find starbursting galaxies if the majority of the Hα emitters were main sequence galaxies. A few of the protocluster galaxies have 2σ detections at $250\,\mu$m, and one has a 3σ detection at $24\,\mu$m. If I remove those Hα emitters with nearby (≤ 10 arcsec) 2σ detections from the $250\,\mu$m stack, the signal decreases and I do not find a signal above 3σ (where 3σ corresponds to an upper limit of $98\,\mathrm{M}_{\odot}\,\mathrm{yr}^{-1}$). I discuss these IR luminous and highly star-forming galaxies further in Section 4.4.4.

4.4.3.4 sSFRs

Figure 4.8d compares the specific star formation rates (sSFR) of the protocluster and control galaxies. When the entire mass range of galaxies is taken into account there is a

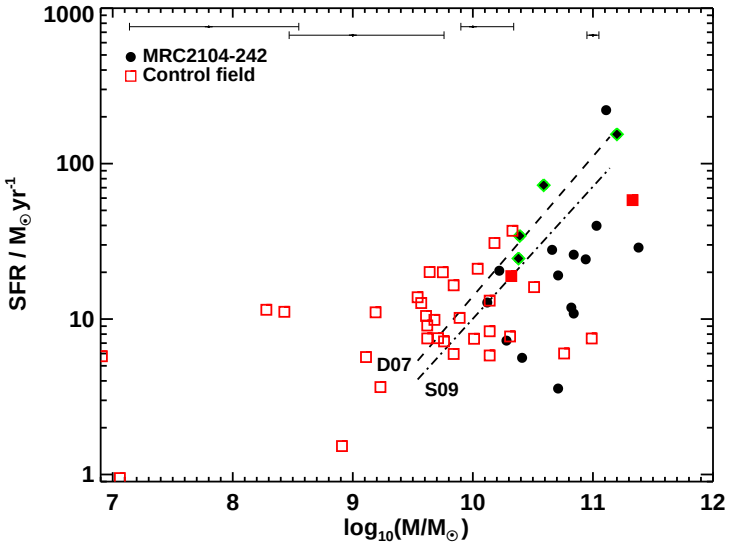

Figure 4.10: Dust corrected Hα SFRs against stellar mass. The protocluster galaxies are plotted as filled, black circles and lie mostly at the high mass end of the plot. The control fields are plotted as open, red squares. The radio galaxy and three companion galaxies are highlighted with green diamonds. The COSMOS AGN candidates are plotted as filled red squares. Median error bars at the top show the typical uncertainty on the SED mass estimates in four mass bins ($6.5 \leq \log_{10}(M/\mathrm{M}_{\odot}) < 8.5$, $8.5 \leq \log_{10}(M/\mathrm{M}_{\odot}) < 9.5$, $9.5 \leq \log_{10}(M/\mathrm{M}_{\odot}) < 10.5$, $10.5 \leq \log_{10}(M/\mathrm{M}_{\odot}) < 12$). Overplotted are relations from previous studies, (Daddi *et al.*, 2007; Santini *et al.*, 2009, labelled D07; S09), valid above $M \sim 10^{9.5}$ $\mathrm{M}_{\odot}$.

significant difference in the sSFRs between the two populations (K-S $p = 6.8 \times 10^{-4}$). However this difference is driven by the disparate mass distributions of galaxies in the two environments. The shaded red histogram shows the distribution of sSFRs of galaxies with masses $M \geq 10^{10}\,\mathrm{M}_{\odot}$. For this population there is no significant difference in the sSFRs: K-S $p = 0.15$.

4.4.4 Highly starforming galaxies

No Hα emitters in the protocluster or control fields are detected above 3σ significance at $250\,\mu$m, however there are a few detections with signals $> 2\sigma$. In the MRC 2104−242 field there are three 2σ sources, one of which has a 3σ $24\,\mu$m detection of $0.11\,\mu$Jy$= 145 \pm 60\,\mathrm{M}_{\odot}\ \mathrm{yr}^{-1}$ (main sequence estimate for SFR) or $= 1200 \pm 775\,\mathrm{M}_{\odot}\ \mathrm{yr}^{-1}$ (ULIRG estimate). Their $250\,\mu$m SFRs are plotted in Figure 4.11 as small black diamonds.

In the control fields we only find one source with a $>2\sigma$ detection. The $250\,\mu$m-derived SFR is plotted as a small red diamond in Figure 4.11. This source is one of the

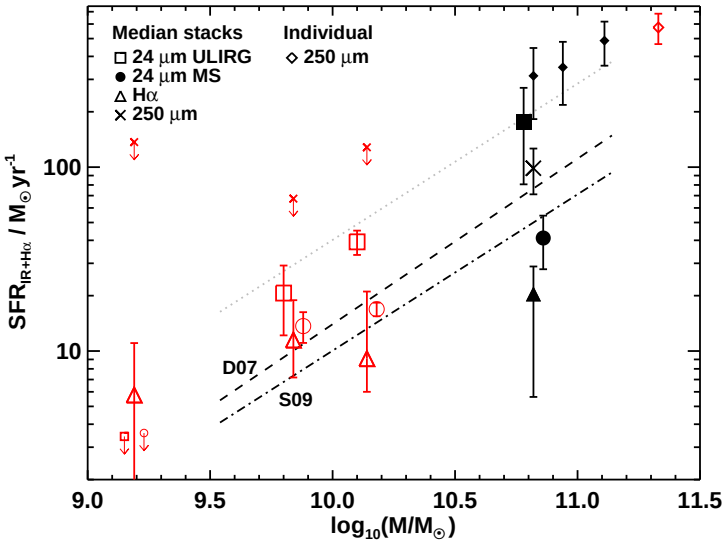

Figure 4.11: The IR+Hα SFRs plotted against median mass values for the protocluster (black filled symbols) and control fields (red open symbols). From left to right: GOODS-S, COSMOS, UDS. 3σ upper limits are plotted if no signal is observed. Circles and squares (offset in the x-axis for clarity) are SFRs calculated from $24\,\mu$m using Rujopakarn *et al.* (2013) and Rieke *et al.* (2009) respectively. Triangles are the dust-corrected Hα SFRs, with error bars enclosing 68% of the data. The crosses are the SFRs derived from *Herschel* $250\,\mu$m stacks of Hα emitters. Overplotted are Daddi *et al.* (2007) and Santini *et al.* (2009) relations, labelled D07 and S09. Also plotted are the *Herschel* SFRs (IR+Hα) and 1σ error bars for sources with $250\,\mu$m signal $> 2\sigma$ above the background noise: black/red diamonds are protocluster/COSMOS galaxies. These sources are consistent with being starbursts ($\sim 4\times$ the main sequence); the grey dotted line shows the Santini *et al.* (2009) relation multiplied by 4.

AGN candidates in the COSMOS field.

Five percent of the Hα emitters (i.e. < 1 of the Hα emitters) are expected to be detected at the 2σ level due to noise in the $250\,\mu$m data. In the protocluster I find three, suggesting that at least two of them are real sources and not noise. All three sources have $250\,\mu$m SFRs which are consistent with starbursting galaxies, defined such that they lie four times above the main sequence (Rodighiero *et al.*, 2011). This suggests that the fraction of starbursts is several times higher in the protocluster, with 21% of the Hα emitters being starburst galaxies, compared to just $\sim 3\%$ in the control field.

4.4.5 Robustness checks

4.4.5.1 Effect of AGN on measured A_V and SFRs

Removing the two AGN detected in the COSMOS field from the control sample does not significantly change my results. There is still a significant difference in dust content

estimated from the UV slope (K-S $p = 2 \times 10^{-6}$) which remains at a 2σ level when considering the mass-limited galaxy samples. Furthermore the trends for the sSFRs remain the same: K-S $p = 2.5 \times 10^{-4}$ and K-S $p = 0.1$ for the full sample and mass-limited sample respectively. The average IR and Hα SFRs decrease for the COSMOS field[2] and the Hα SFR distributions become significantly different at a 2σ level (K-S $p = 0.05$). However, in the mass-limited sample (M$> 10^{10}\,$M$_\odot$) there is still no significant difference in the SFRs between the two distributions: K-S $p = 0.43$. Excluding the COSMOS AGN, the starburst galaxy fraction is still higher in the protocluster than the control field.

4.4.5.2 Luminosity distances

The NB filters used for the control fields have different central wavelengths from the NB229 filter used to select the protocluster galaxies. Since I select galaxies at slightly different redshifts, the luminosity distance to the control field galaxies is slightly less than to the protocluster galaxies. As the control field galaxies are at lower redshifts than the protocluster, I probe further down the luminosity function of the control field for the same cuts in apparent magnitude. I have tested how this may affect the results by taking this difference in magnitude into account and applying a cut to the control fields at brighter magnitudes. These cuts remove five control field galaxies from the sample, increasing the level of overdensity measured in the protocluster field to 9 ± 0.8 times the control field density. The masses and star formation properties of the remaining galaxies remain within the error margins calculated. So the difference in luminosity distance between the protocluster and control fields does not affect my other conclusions.

The star formation rate of the Universe evolves over time, so using control fields at lower redshift than the protocluster may cause a bias in the number of Hα emitters selected due to the lower SFR density of the Universe. The cosmic star formation rate density, however, is relatively constant over the range $z = 2$–3 and evolves by $\sim 3\%$ between the redshift of MRC 2104−242 and the lowest redshift field, GOODS-S (Hopkins & Beacom, 2006). This effect is far less than the effect of cosmic variance,

[2]The median dust-corrected Hα SFR for the COSMOS field decreases by $< 1\,$M$_\odot$ yr^{-1} and the 24 μm + Hα SFR decreases by $\sim 2\,$M$_\odot$ yr^{-1}.

where the number of star-forming galaxies can fluctuate by $\sim 50\%$ between fields (e.g. Table 4.2).

4.5 Discussion

4.5.1 Galaxy growth in protoclusters

I have shown that the star forming protocluster galaxies at $z = 2.5$ are more massive than similarly selected galaxies in the field. The SFRs and sSFRs of the protocluster galaxies are consistent with the control galaxies once the difference in galaxy mass is taken into account by only comparing galaxy samples of similar mass.

The high-mass protocluster galaxies include a larger amount of dust-obscured star formation than the lower-mass control galaxies. Once this has been included in the total SFRs by adding the IR SFRs from the $24\,\mu$m and *Herschel* $250\,\mu$m data, I find that on average, protocluster and control galaxies lie on the same main-sequence of the SFR-mass relation. This means that at $z \sim 2.5$, galaxy growth in terms of star formation is regulated predominantly by galaxy mass and is not greatly affected by the environment of the host galaxy.

Figures 4.8a and 4.10 show that the protocluster galaxies typically have higher masses than the control field galaxies, and there are more than twice as many protocluster galaxies than field galaxies with $M > 10^{10.5}\,\mathrm{M}_{\odot}$ (10 protocluster galaxies compared to only 4 control field galaxies even though the protocluster area surveyed is only 4% of the control area). This poses a conundrum: if the SFR is governed by galaxy mass alone at $z \sim 2.5$, then how did the protocluster galaxies gain so much mass so rapidly? The early formation of these galaxies must be dependent on their environments at higher redshift, even though at $z \sim 2.5$ their growth proceeds in the same way.

I find three 2σ detections at $250\,\mu$m in the protocluster, suggesting the presence of starbursting galaxies. If the fraction of galaxies undergoing a starburst is much greater in denser environments, this may explain the higher masses. Deeper sub-millimetre observations of protocluster galaxies are essential to understanding this issue.

4.5.2 Overdensity and the lack of low mass star forming galaxies in protocluster

In this section I examine why, on average, galaxy masses differ between the two environments. I find no difference at the high mass end of the distributions; taking a mass selected sample of all Hα emitters with $M \geq 10^{10}\,\mathrm{M}_{\odot}$ there is no significant difference in the mass distributions. However, I find no low mass ($M < 10^{10}\,\mathrm{M}_{\odot}$) galaxies in my protocluster sample. This skew in the mass distribution means that the strength of the overdensity that I detect depends on the mass range examined, e.g. the protocluster number density is ~ 25 times the control field if only objects with $M > 10^{10}\,\mathrm{M}_{\odot}$ are considered and ~ 55 times the control field at $M > 10^{10.5}\,\mathrm{M}_{\odot}$ (see Figure 4.12). This large excess of high-mass galaxies suggests the presence of a galaxy protocluster, as discussed in Section 4.4.1. If the MRC 2104−242 field does contain a protocluster then we also expect to find an overdensity of low mass galaxies within the field. Although I am incomplete in mass, particularly at low masses, I am incomplete to the same level in the protocluster and the control fields. The fraction of the cluster obscured by cluster members, assuming each member obscures 3×3 sq. arcsec, is 0.5–0.7% of the surveyed area and so is negligible. Since I detect 22 Hα emitters at $M < 10^{10}\,\mathrm{M}_{\odot}$ in the control fields, I expect to detect $\sim$ 21–22 Hα emitters in the protocluster[3], assuming an overdensity of 24, whereas I do not detect any (Figure 4.8a). This work is not the only study to find a lack of low-mass star forming galaxies: Koyama *et al.* (2013a) also show that the protocluster around MRC 1138−262 (the Spiderweb galaxy) lacks low-mass objects. The difference I find in the average masses between the MRC 2104−242 field and the control field is due to this lack of low mass galaxies in the protocluster, rather than a population of extremely massive galaxies.

In the following subsections, I consider three possible reasons for this difference in the protocluster and control field mass distributions: an intrinsic difference in mass functions between the protocluster and the field galaxies; observational effects, such as the higher value of dust extinction in protocluster galaxies or low mass galaxies which may have already shut down their star formation; and mass segregation, with

[3]I still expect to detect 21–22 Hα emitters once the area of the protocluster obscured by cluster members is accounted for.

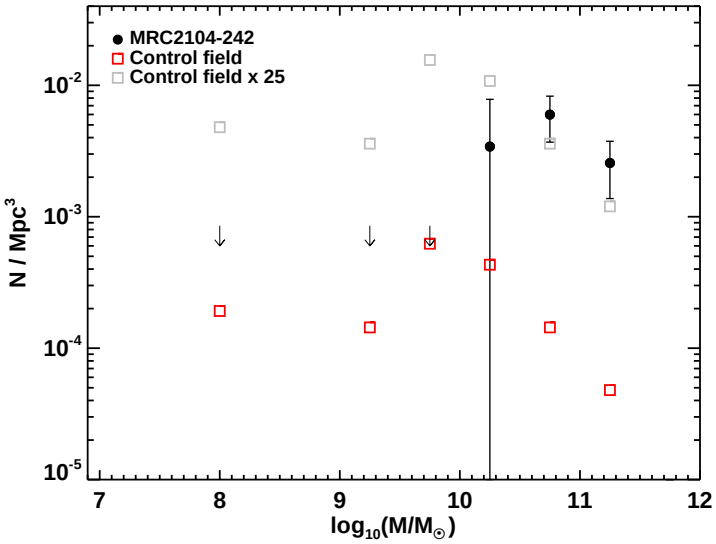

Figure 4.12: Galaxy number densities per mass bin for the control field (red squares) and the protocluster (black circles). In grey I also show the control field distribution, scaled by a factor of 25, to illustrate the expected number densities in the protocluster. This figure shows a clear excess of galaxies in the protocluster at the high mass end, however there appears to be a lack of low mass objects in the protocluster, whereas I detect many low mass objects in the field.

high mass galaxies preferentially clustered around the radio galaxy.

4.5.2.1 Environmental dependence of the galaxy mass functions

In order to determine an expected mass function for protoclusters at $z \sim 2.5$, I analysed the mass distributions of a protocluster and the surrounding field from semi-analytic models. The semi-analytic model output was created by S. Muldrew, which I describe below. I then analysed the resulting mass functions.

We have taken the $z = 2.42$ output of the Guo *et al.* (2011) semi-analytic model applied to the Millennium Dark Matter Simulation (Springel *et al.*, 2005). This semi-analytic model is an updated version of the Croton *et al.* (2006) and De Lucia & Blaizot (2007) models. The Millennium Simulation uses a flat ΛCDM cosmology with $\Omega_0 = 0.25$, $\Omega_\Lambda = 0.75$, $\sigma_8 = 0.9$, $n = 1$, and $h = 0.73$. This is consistent with the Two-Degree Field Galaxy Redshift Survey (2dFGRS; Colless *et al.*, 2001) and the Wilkinson Microwave Anisotropy Probe first year results (WMAP; Spergel *et al.*, 2003), but differs slightly from Planck Collaboration *et al.* (2014) measurements. Chiang, Overzier & Gebhardt (2013) found that the results derived for protoclusters from these different cosmologies are very similar for $z < 3$ and so are unlikely to greatly affect our results.

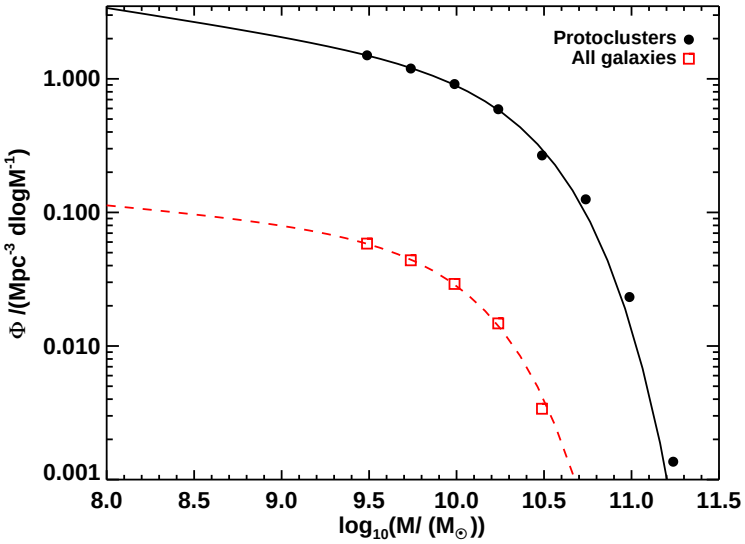

Figure 4.13: Semi-analytic derived mass distributions for all galaxies (red squares) and protocluster galaxies (black circles, see text for details). Solid and dashed lines show the fitted Schechter functions. The values of M_* and Φ differ by 0.4 dex and 0.14 dex respectively. The difference in α is 0.08 dex.

The Millennium Simulation follows the evolution of 2160^3 dark matter particles from $z = 127$ to the present day in a box of side length $500\,h^{-1}\mathrm{Mpc}$ comoving. Haloes were identified using a Friends-of-Friends algorithm (FoF; Davis *et al.*, 1985) with a linking length of 0.2, which were then analysed for bound substructures using SUBFIND (Springel *et al.*, 2001). Only haloes containing ≥ 20 particles were considered.[4]

Traditionally semi-analytic models have been unable to accurately reproduce the redshift evolution of the galaxy stellar mass function. As shown in figure 23 of Guo *et al.* (2011), the high mass end of the galaxy stellar mass function fits the observations well in this redshift range, but there is an over-abundance of lower mass galaxies. In order to minimise the effect of this over-abundance of low mass galaxies, we limit our sample to galaxies with stellar masses greater than $10^{9.5}\,h^{-1}\mathrm{M}_\odot$.

We identify 1938 clusters in the $z = 0$ catalogue by selecting clusters as those haloes with masses greater $10^{14}\,h^{-1}\mathrm{M}_\odot$. We then trace the merger tree back in time to $z = 2.42$ and select the highest mass progenitor galaxy in the $z = 2.42$ catalogue as the central protocluster galaxy and all galaxies that will merge to form the $z = 0$ cluster as protocluster members. To compare to the observations, we subsample cubes of side

[4]We note that similar results can be found with other halo finders (Muldrew, Pearce & Power, 2011; Knebe *et al.*, 2011).

length $3.5\,h^{-1}\mathrm{Mpc}$ comoving centred on the central protocluster galaxy and compare the mass function with that of the whole volume.

I fit a Schechter curve to the semi-analytic derived mass distributions (Figure 4.13) and found that the expected mass function of the protocluster shows no turnover at the faint end. Indeed, I find the faint end slope for protocluster galaxies tends to be slightly steeper (by ~ 0.1 dex) than that for the whole volume. The distributions differ significantly in the value of M_* and normalisation (differences of 0.4 dex and 0.14 dex respectively). This means that the difference in number densities that I observe is not due to a fundamental difference in the shape of the mass functions at $z \sim 2.5$. The shape of the expected mass function is dependent on the volume sampled and the SFR of the galaxies that are selected. I will further examine how the star forming fraction, and hence galaxy mass function, changes as a function of volume sampled in Section 4.5.2.4 (see also Muldrew, Hatch & Cooke, 2015).

4.5.2.2 Mass segregation

Protoclusters at high redshift are not dynamically evolved and so it is unlikely that large-scale mass segregation has had enough time to occur: the 2.65 arcmin $\times$ 2.65 arcmin area corresponds to 1.28 Mpc $\times 1.28$ Mpc in physical coordinates. Assuming an average galaxy velocity of $500\,\mathrm{km\,s^{-1}}$, this gives a crossing time of 2.5 Gyr. At $z = 2.49$, the age of the Universe is 2.58 Gyr. This means that there has not been enough time for virialization to occur and any dynamical friction effects will not be strong enough to produce mass segregation in the protocluster at this redshift.

Substructure has, however, been found around radio galaxies at high redshift. Hayashi *et al.* (2012) reported the discovery of a protocluster where there were three distinct "clumps" of galaxies on scales of ~ 8–10 Mpc. They found that the highest mass objects resided in the densest clump at $z = 2.53$, suggesting that higher mass objects may preferentially form in denser environments. Kuiper *et al.* (2010) also found that the most massive and highly star forming galaxies were located near the radio galaxy of a $z \sim 3$ protocluster. It may be that protoclusters have more high mass galaxies forming through monolithic collapse, or experience many more mergers in the early years of their formation. Measuring galaxy sizes in protoclusters compared to the field may

provide more information on galaxy formation mechanisms in different environments.

4.5.2.3 Dust and low mass quiescent galaxies

In deep, wide field surveys of star forming galaxies, typically a cut in sSFR is taken to define passive or star-forming samples of galaxies (e.g. Lani *et al.*, 2013). The selection of galaxies used in this chapter is instead based on their NB flux, and corresponds to a cut in SFR, regardless of stellar mass. This causes a difference between the intrinsic and observed shapes of the stellar mass function. This can be seen in Figure 4.14 (taken from Muldrew, Hatch & Cooke, 2015) where the fraction of galaxies selected from the Millennium Simulation that are star-forming is shown for a fixed cut in sSFR and SFR. Using a cut in sSFR reveals that the mass functions of star-forming galaxies are expected to be the same shape in the protocluster and the field. Using a SFR cut, however, causes a bias against low mass star-forming galaxies being selected. This is seen in the observations in Figure 4.12, where both the field and protocluster mass functions are incomplete at lower masses (shown by the turnover in the distributions below $\sim 10\,\mathrm{M}_{\odot}$). This incompleteness, as previously discussed, affects the protocluster and field samples in the same way- they are incomplete to the same level at all masses, and so does not explain the observed lack of low mass galaxies in the protocluster.

My NB survey selects star forming galaxies with Hα emission, down to a dust-uncorrected star formation rate of $\sim 7\,\mathrm{M}_{\odot}\,\mathrm{yr}^{-1}$. If the low mass protocluster galaxies were passive or heavily obscured by dust, the NB survey would not detect them. To test if these galaxies are missing in my NB survey, I compared the galaxy luminosity functions in the protocluster field to the control field (Figure 4.15).

I compared the luminosity functions in the K_s band, using a $(J - H > H - K_s - 0.15)_{Vega}$ cut to remove galaxies at redshifts below ~ 1, and at $4.5\,\mu$m, taking a $([3.6] - [4.5])_{AB} > -0.1$ colour cut (selecting galaxies at $z > 1.3$). These wavebands select passive galaxies, as well as the star-forming NB emitters in my sample, albeit with a large contamination rate. I find an overdensity of bright galaxies ($K_s < 21.9$ and $4.5\,\mu\mathrm{m} < 20.5$) and a lack of faint galaxies in both K_s and $4.5\,\mu$m at magnitudes fainter than 21.9 (AB) and 20.5 (AB) respectively. The lack of faint galaxies, at mag-

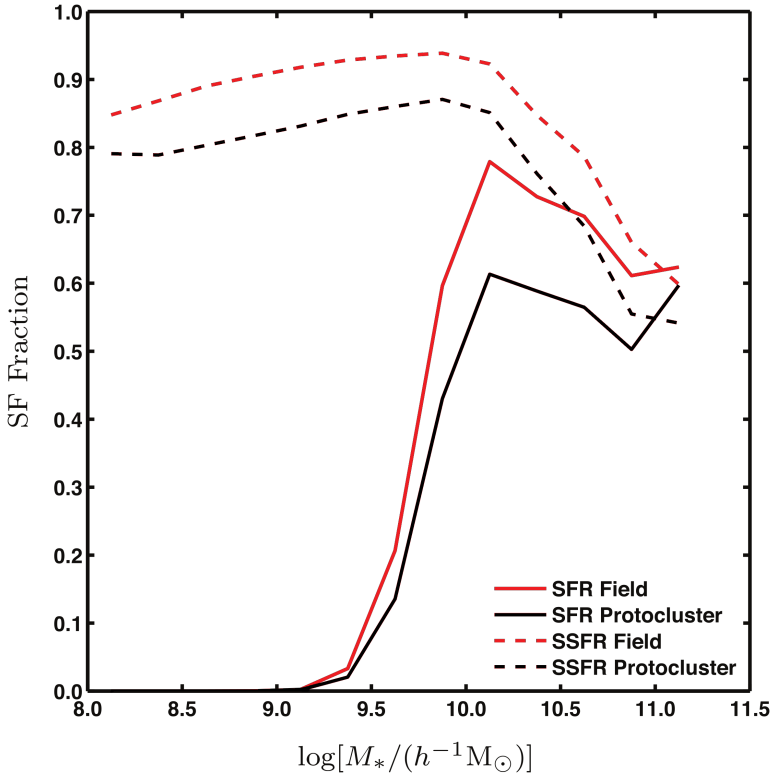

Figure 4.14: From Muldrew, Hatch & Cooke (2015): the star forming fraction in the field and protocluster from the Millennium Simulation as a function of mass for two different selection criteria. Dashed lines show the effect of a constant sSFR cut, frequently used in the literature (e.g. Lani *et al.*, 2013). Solid lines show the effect of a cut in SFR, as used in this chapter. This SFR cut causes an artificial loss of low mass galaxies, but both field and protocluster are affected in the same way.

nitudes brighter than the 80% completeness limits (shown by the vertical dashed lines in Figure 4.15), suggests that this protocluster lacks both star forming and passive low mass galaxies. A K-S test indicates that the difference between the protocluster and control field is significant for both the K_s and $[4.5]$ luminosity functions for magnitudes brighter than the 80% completeness ($p = 3.3 \times 10^{-3}$ and $p = 5 \times 10^{-3}$ respectively). This significance remains at 95% completeness for the $[4.5]$ luminosity function, however rapidly decreases for the K_s luminosity function ($p = 0.8$). This suggests that incompleteness at faint luminosities may be affecting the K_s band comparison. However, since the effect is still present in the $[4.5]$ luminosity function, which probes the rest-frame NIR, the observed lack of low mass galaxies remains.

Kulas *et al.* (2013) found that the metallicity of protocluster galaxies did not vary with galaxy mass, whereas field galaxy metallicity decreases with decreasing mass. They found no difference between the two environments at high masses, but at low masses

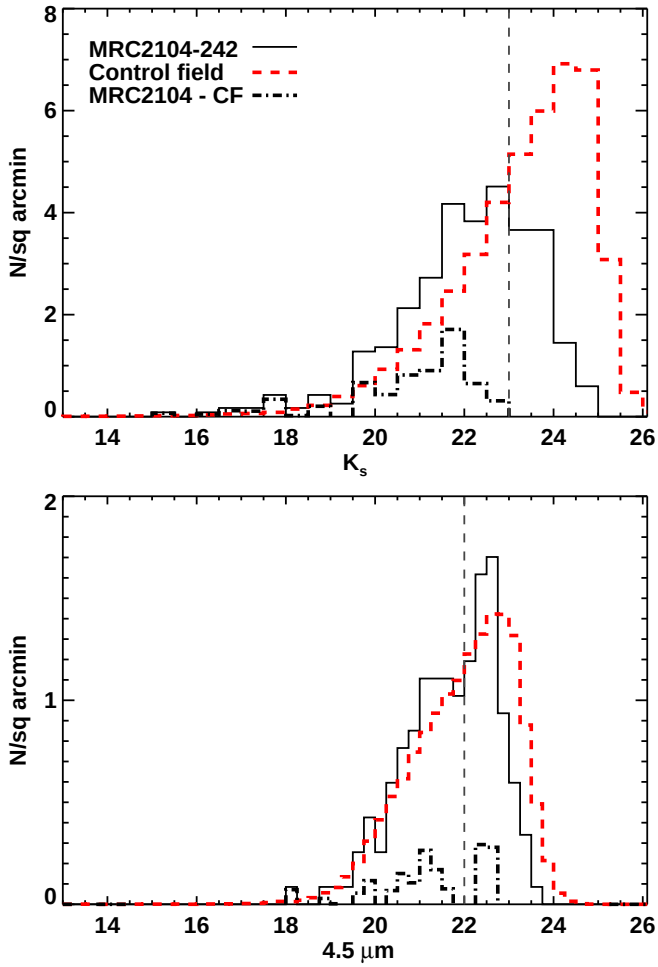

Figure 4.15: Number density histograms in the K_s band and at 4.5 μm for galaxies with colours $J-H > H-K_s-0.15$ (Vega) and $[3.6]-[4.5] > -0.1$ (AB) respectively. These criteria select passive, as well as star-forming, galaxies. Black histograms are for the MRC 2104−242 field, red dashed is the control field and black dot-dashed is the difference between the two, indicating protocluster candidates. Completeness is shown by the vertical dashed lines. The lack of protocluster galaxies at magnitudes brighter than the completeness limits, shown by the drop in the dot-dashed histograms, suggests a lack of faint galaxies in this protocluster.

found a significant difference in metallicity (but see also Tran *et al.*, 2015, who found no evidence for a difference in metallicity in a protocluster environment).

This suggests that low mass galaxies are more metal rich in protocluster environments than in the field. This may also mean that the low mass galaxies in protoclusters are dustier than those in the field. However, with this current data I find no evidence to suggest this and it is difficult to test as I do not detect any low mass galaxies in the protocluster.

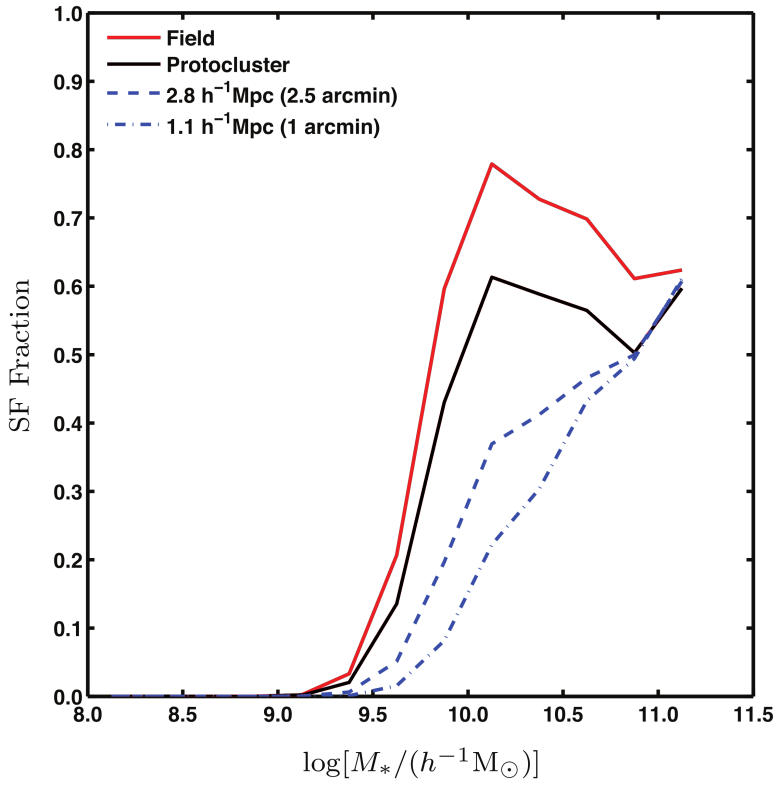

Figure 4.16: From Muldrew, Hatch & Cooke (2015): the star forming fraction in the field and protocluster from the Millennium Simulation as a function of mass, showing the effect of the observational field-of-view. Solid red and black lines are the same as in Figure 4.14. Blue dashed and dot-dashed lines show the expected observations for an area around the central galaxy with radius 2.5 arcmin and 1 arcmin respectively. A small field-of-view can dramatically affect the number of star forming galaxies selected in the models.

4.5.2.4 Observational effects on mass distributions

The protocluster observations in this chapter are limited by the field-of-view around MRC 2104−242. I have imaged an area of 2.65×2.65 arcmin^2 around the HzRG, which is $\sim 4.5 \times 4.5$ Mpc^2 in comoving coordinates at this redshift. This corresponds to a small fraction of the predicted protocluster. At $z = 2.5$, protoclusters can extend over 40 Mpc comoving (Muldrew, Hatch & Cooke, 2015). In Figure 4.16 I show the effect of this limited field-of-view on the fraction of star-forming galaxies selected by a constant cut in SFR in the Millennium Simulation (taken from Muldrew, Hatch & Cooke, 2015). The blue lines show two different fields-of-view: a 2.5 arcmin radius aperture and a 1 arcmin radius aperture. By only observing the central core of the protocluster, the star-forming galaxy fraction is dramatically suppressed compared to the field. In the Millennium Simulation, galaxies are prescribed to undergo environmental effects, such as ram pressure stripping, when they are within one virial radius of the

central galaxy (Guo *et al.*, 2011). By observing only the protocluster core in the simulation, a higher fraction of low mass galaxies are quiescent compared to the field or the wider protocluster structure. This may explain the lack of low mass star-forming galaxies around MRC 2104−242, however it does not explain why I do not observe a population of low mass red galaxies (Figure 4.15).

4.5.2.5 Where are the low mass galaxies?

In the previous subsections I have established that the MRC 2104−242 protocluster galaxy mass function differs from that of the control field for both star forming and passive galaxies. A higher level of dust extinction in only the low mass protocluster galaxies could produce this effect observationally; with my current data I only find a 2σ difference in the dust extinction between the protocluster and control field galaxies at high masses, and cannot test this at lower masses. Alternatively, protocluster environments may form more high mass galaxies through monolithic collapse or protocluster galaxies may undergo many more mergers in the early stages of their growth compared to the field. I find tentative evidence that the fraction of starburst galaxies is higher in the protocluster, indicating a more rapid growth of galaxies in denser environments.

Recently, Husband *et al.* (2016) studied Hα emitters around seven HzRGs at $z \sim 2.2$. They used a large field of view ($12.2 \times 12.2\,\mathrm{Mpc}^2$) and found that the H$\alpha$ mass function does not appear different in shape to the field, once incompleteness is corrected for. They do not, however, probe below $10^{10}\,\mathrm{M}_\odot$. Nevertheless, this suggests that the observed lack of low mass galaxies may be due to both our small field of view (Section 4.5.2.4) and incompleteness at the low mass end. In this chapter I do not perform any completeness corrections but the protocluster and field should be directly comparable as neither have been corrected. Koyama *et al.* (2013a) also show a similar lack of star-forming galaxies with low masses in the MRC 1138−262 protocluster, and Rudnick *et al.* (2012) find a lack of low mass red galaxies in a (proto)cluster at $z = 1.6$. With only three protoclusters, however, it is difficult to come to any firm conclusions as to why I find this result and this remains an open question. In future studies it is important that we now progress towards larger samples of protoclusters, in order to overcome the effects of cosmic variance and obtain a meaningful statistical understanding of the

formation and evolution of these structures.

4.6 Conclusions and summary

I have undertaken a near-infrared narrowband survey of the field around the HzRG MRC 2104−242 to locate Hα emitting galaxies in the surrounding protocluster. I selected star-forming galaxies and compared their properties with those of a field sample at similar redshifts. My key results are:

1. The field around the HzRG MRC 2104−242 is overdense compared to blank control fields, with a level of overdensity of 8.0 ± 0.8 times the average blank field, which is consistent with this field being the progenitor of a low redshift cluster, i.e. a protocluster.

2. The protocluster galaxies around MRC 2104−242 are more massive and have more hidden star formation than control field galaxies at the same redshift. When I take a mass selected field sample I find no difference in the SFR and sSFR between the two environments, and only a minor difference in the dust content.

3. Star formation at $z \sim 2.5$ is governed predominantly by galaxy mass, not environment. After including dust-extincted star formation using $24\,\mu$m and *Herschel* data I find that the average SFR-mass relations are the same irrespective of environment and both the protocluster and control field galaxies lie close to the main sequence.

4. I find a large difference in the mass distributions between environments: I expect to find $\sim$ 21–22 galaxies in the protocluster at masses $M < 10^{10}\,\mathrm{M}_{\odot}$ and detect none. This could indicate a higher level of dust extinction in low mass galaxies in the protocluster. It may alternatively be due to galaxies in the protocluster forming more high mass galaxies through monolithic collapse or undergoing many more mergers in the early stages of their growth.

5. I find tentative evidence of a larger fraction of starburst galaxies in the protocluster than in the control field. Further data is required to confirm the $250\,\mu$m

detections, however a more rapid mode of star formation in denser environments may explain how protocluster galaxies build up their mass quicker than in the field.

6. The overdensity I detect in this small area is highly dependent on the mass range we consider. It can range from an overdensity of 0 (at $M < 10^{10}\,\mathrm{M}_{\odot}$) to 55 ($M > 10^{10.5}\,\mathrm{M}_{\odot}$). It is important when quantifying protoclusters to compare their mass functions, rather than simply number overdensities.

Chapter 5

Hα emitters in protoclusters at $z \sim 1.6$

5.1 Introduction

In Chapter 3 I showed that RLAGN can reside in clusters of various stages of collapse. This means that they are not solely found in young, forming clusters. It is still uncertain, however, whether radio galaxy-selected (proto)clusters are representative of the full cluster population. For example, even if they are mostly star-forming, are the star formation properties of the member galaxies comparable to typical cluster galaxies? Most protocluster candidates to date have been discovered in the vicinity of RLAGN (Wylezalek *et al.*, 2013, Chapter 1). In the last few years progress has been made towards larger samples of "normal" clusters at $z > 1.5$ (e.g. Wilson *et al.*, 2009; Fassbender *et al.*, 2011, see Chapter 1), but it will be difficult to extend these samples to $z > 2$, and certainly not to $z \geq 5$, where the highest redshift protoclusters have been discovered (e.g. Mayo *et al.*, 2012). Although *Euclid*, LSST and DES are predicted to discover tens of thousands of galaxy clusters at $z < 2$, at higher redshifts, our studies of galaxy formation in the densest environments will be limited to protoclusters around RLAGN. This means that it is crucially important to understand whether results derived from these structures may be extrapolated to the full cluster population.

RLAGN may preferentially reside in the most massive cluster haloes (Chapter 1), so the properties of their surrounding galaxies may experience stronger environmental effects than those of typical clusters without a RLAGN. The radio galaxy itself may

also influence the galaxies around it, causing bursts of star formation from interactions with the radio jet (Chapter 4), or suppressing star formation in the cluster core (e.g. Kashikawa *et al.*, 2007). We are now obtaining significant samples of clusters selected via the SZ effect, red sequence matching, and X-ray detections out to $z \sim 1.5$. These samples mean it is now possible to study the properties of galaxies in clusters around RLAGN compared to galaxies in clusters with no RLAGN.

In 2013–2014 we submitted 3 proposals to ESO with an aim of comparing the star-forming properties of galaxies in clusters around RLAGN at $z = 1.5$ to a sample of galaxies in clusters with no RLAGN to identify any differences. Unfortunately only a small subset of these observations were obtained. In this chapter I will present the data and initial results from this project. I will present NB data on two protocluster candidate fields around RLAGN at $z \sim 1.5$–1.6. One is a CARLA field (not studied in Chapter 2), 3C 008, and one has previously been found to be situated in an overdensity of red galaxies (Best *et al.*, 2003). I will present the selection of Hα emitters around these two RLAGN and analyse some of the protocluster properties. These RLAGN are at a similar redshift to CARLA J1753+6311 (Chapter 3) which has a large quiescent population. With the NB observations of these fields, I am examining the star-forming population alone.

5.2 Data

3C 008 and PKS 2025−155 were observed as part of a study of five radio galaxy fields during the course of five observing runs between 2013 March and 2015 July (PIs J. Kurk and E. Cooke) with the Son of ISAAC instrument (SofI; Moorwood, Cuby & Lidman, 1998) on the 3.6 m New Technology Telescope (NTT) at La Silla, Chile. Of these observing runs, I was the observer for two and PI for one. To detect Hα emission in galaxies surrounding these HzRGs, narrow-band filters were used: the NB Fe II H (width $0.25\,\mu$m) and NB 1.71 (width $0.26\,\mu$m) filters cover Hα at $z = 1.5$ and $z = 1.59$ respectively. Of the five fields proposed, I only got sufficient data on two: 3C 008 and PKS 2025−155. The details of the observations, including the additional three fields, are given in Table 5.1. In the rest of this chapter I only discuss 3C 008 and

Target	RA	DEC	z	NB filter	Exp. time NB (H)	Depth NB (H)
PKS 2025−155	20:28:07.4	−15:21:23.0	1.500	NB Fe II H	32.9h (3.5h)	23.6 (23.5)
3C 008	00:18:51.3	−12:42:34.0	1.589	NB 1.71	25.3h (4.5h)	23.0 (23.6)
BRL 1131−17	11:31:52.0	−17:11:15.0	1.618	NB 1.71	8h (1.5h)	N/A*
BRL 0949+002	09:49:25.0	+00:12:37.0	1.487	NB Fe II H	1h (1h)	N/A*
PKS 2128−208	21:28:12.0	−20:50:10.0	1.615	NB 1.71	No data	N/A

Table 5.1: Details of the observations for the radio galaxy fields. Depths are 3σ, as measured from the flux in ~ 10000 random apertures on the images. The exposure times and depths in brackets are for the H band. Only two fields, PKS 2025−155 and 3C 008, had sufficient exposure times to attempt any further analysis.
* These data are not deep enough to be usable for this project so the images have not been calibrated.

PKS 2025−155.

The data were reduced by N. Hatch using the ESO/MVM data reduction pipeline (Vandame, 2004). The field of view of the NB data around both HzRGs is $\sim 5 \times 5$ arcmin^2. I flux calibrated the broadband H images using 2MASS stars in the field of view. I then calibrated the NB images by fitting a function of the form $NB = a \times (H - K) + H + b$, where a and b are constants determined for each field and set of filters individually from a range of Pickles (1998) stellar templates. All images were rescaled to have a zeropoint of 23.9 (AB).

The depths of the images were determined from flux measurements in ~ 10000 randomly-placed 2 arcsec diameter apertures. 3σ depths are reached at ~ 23 mag for all images; details are in Table 5.1.

5.2.1 Selection of Hα emitters

NB sources were selected using SExtractor in dual-image mode, using the NB image as the detection image and measuring fluxes in 2 arcsec diameter apertures. Sources exhibiting excess NB emission were selected as in Chapter 4, using Equation 4.1. Hα emitters were selected as those sources with $\Sigma \geq 3$, Hα EW≥ 25 Å and NB magnitudes brighter than the measured 3σ depths (Table 5.1). After visual inspection of the selected Hα emitters, one was removed from the PKS 2025−155 field as it appears to be a bright emission source in a tidal stream of a lower redshift galaxy. Figures 5.1 and 5.2 show the selection of Hα emitters around 3C 008 and PKS 2025−155 respectively; 3C 008 is surrounded by 11 Hα emitters and PKS 2025−155 has six Hα

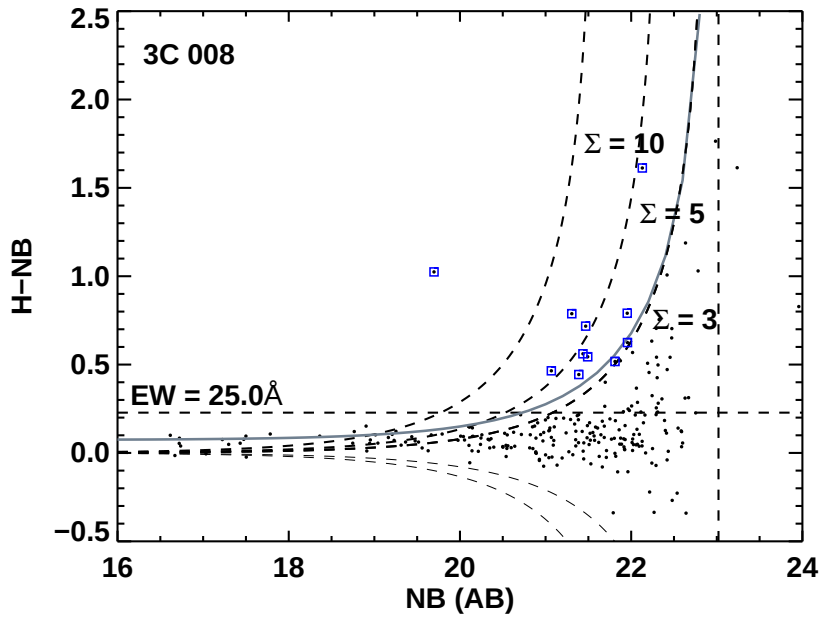

Figure 5.1: Selection of Hα emitters in the field around 3C 008. Black points show all sources detected in the NB image. Curved dashed lines show lines of excess NB flux compared to the H band (Σ). Sources are selected as Hα emitters (blue squares) if they have an excess of NB flux such that $\Sigma \geq 3$ and EW ≥ 25 Å. The radio galaxy is the bright source at NB ~ 19.7 mag. The vertical lines show the 80% completeness (dot-dashed) and 3σ depth (dashed) of the NB. The solid grey line indicates a line of constant $SFR = 10\,\mathrm{M}_{\odot}\,\mathrm{yr}^{-1}$.

emitters besides the central radio galaxy.

5.3 Results

5.3.1 Do these RLAGN reside in protoclusters?

Figure 5.3 shows the Hα luminosity functions of 3C 008 and PKS 2025−155 compared to field Hα emitters at $z \sim 1.6$. The dotted line shows the field luminosity function scaled to fit the 3C 008 data points[1]. From this best fit, 3C 008 is 4.9 times the density of the field at this redshift. PKS 2025−155 is only 1.3 times the field density of Hα emitters, and is consistent with the field at a 1σ level.

It is difficult to interpret whether or not PKS 2025−155 is likely to be a protocluster. Best *et al.* (2003) found a significant overdensity of galaxies within 20 arcsec of the radio galaxy, however without significant numbers of excess galaxies at large radii that

[1]The RLAGN is the only source in the highest luminosity bin. This data point is therefore excluded from the fitting of the luminosity function.

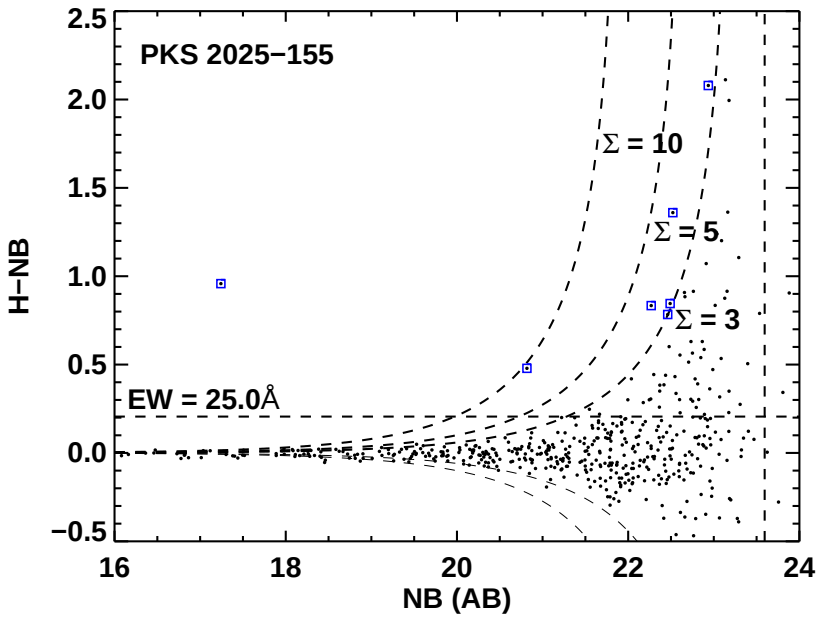

Figure 5.2: Selection of Hα emitters in the field around PKS 2025−155. Black points show all sources detected in the NB image. Curved dashed lines show lines of excess NB flux compared to the H band (Σ). Sources are selected as Hα emitters (blue squares) if they have an excess of NB flux such that $\Sigma \geq 3$ and EW ≥ 25 Å. There are six Hα emitters selected, plus the radio galaxy (NB ~ 17.2 mag). The vertical dashed line shows the 3σ depth of the NB.

will be able to collapse and feed cluster growth, the galaxies within 20 arcsec are not sufficient to produce a protocluster. I find a slightly higher number of Hα emitters in the field around PKS 2025−155 than expected from a blank field, but the majority of these are more than 2 arcmin from the radio galaxy and show no obvious connection to the central RLAGN. 3C 008, on the other hand, lies within an overdensity of Hα emitters, which suggests it may evolve into a protocluster.

5.3.2 Analysis of PKS 2025−155

Best *et al.* (2003) observed PKS 2025−155 to reside within a compact overdensity of red galaxies. To determine whether there is any Hα emission in these galaxies, I selected red galaxies using the NIR K band as a detection image and placed 2 arcsec apertures on the H and NB images to measure their Hα flux. Only the radio galaxy is selected as an Hα emitter using the criteria in Section 5.2.1. The remaining sources were stacked in both H and the NB, but no excess NB emission was detected above the continuum measured in the H-band. These red sources are therefore consistent with

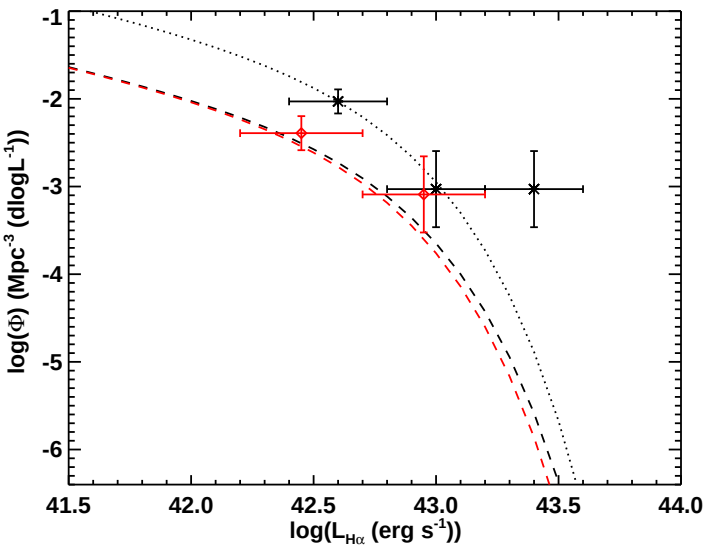

Figure 5.3: The Hα luminosity functions of Hα emitters around 3C 008 (black crosses) and PKS 2025−155 (red diamonds). Error bars in the x-direction show the bin size. The field luminosity functions are shown by the dashed lines for $z = 1.59$ (black) and $z = 1.50$ (red), corrected for redshift from Sobral *et al.* (2013). The dotted line shows the best fit to the Hα luminosity function around 3C 008, scaling the $z = 1.59$ field luminosity function to the data points (excluding the radio galaxy at $\log(L_{H\alpha}) \sim 43.5$). From this best fit, 3C 008 is 4.9 times the density of the field at this redshift. PKS 2025−155 is only 1.3 times the field density.

being quiescent satellite galaxies surrounding PKS 2025−155.

Chiang, Overzier & Gebhardt (2013) showed that protoclusters are extended structures; cluster growth is fuelled by the in-fall of galaxies from this surrounding structure. Muldrew, Hatch & Cooke (2015) showed that 90% of the $z = 0$ stellar mass of a 1–4 $\times$ $10^{14}\,h^{-1}\,\mathrm{M}_{\odot}$ cluster is within a radius of 5 Mpc (comoving) at $z = 1.5$. The lack of an extended structure in the observed 5×5 arcmin^2 ($\sim 2.5 \times 2.5$ Mpc^2 comoving) around PKS 2025−155, either of red galaxies or Hα emitters, suggests that this field will not collapse to form a cluster by $z = 0$ and therefore PKS 2025−155 is unlikely to reside within a protocluster. Instead, it is surrounded by many red satellites within 20 arcsec. To determine the properties of these satellites and disentangle projection effects and signatures of feedback, future integral field unit spectroscopy would be required, or deep photometric SED fitting. For the purposes of this chapter, PKS 2025−155 is unlikely to be surrounded by a protocluster and I do not discuss it further.

5.3.3 Analysis of 3C 008

3C 008 is a RLAGN targeted by the CARLA survey. It has a 3σ overdensity of red IRAC-selected sources which lie at $z > 1.3$ as measured by Wylezalek *et al.* (2014). This is approximately 1.5 times the average field density. Figure 5.3 shows that 3C 008 is 4.9 times the density of the field in the narrow redshift slice $1.58 < z < 1.63$ covered by the narrow-band filter.

The *Spitzer* IRAC selection of the CARLA survey detects both star-forming and passive galaxies, as well as those obscured by dust. The NB selection used in this chapter is only sensitive to a dust-uncorrected SFR of $\sim 10\,\mathrm{M}_{\odot}\,\mathrm{yr}^{-1}$ (Figure 5.1). To look for lower levels of star formation in the structure around 3C 008, I stacked all red IRAC-selected sources with no individually detected NB emission and measured the total NB and H fluxes. The flux measurements from the stack show no excess NB emission compared to the broadband H band. This means that the majority of the remaining IRAC-selected sources are likely to be passive galaxies in the protocluster, or interloper galaxies with no strong emission lines within the NB filter. To find passive galaxies in the protocluster further deep photometry would be required in order to fit the SEDs of the galaxies.

5.3.4 Comparison sample: a cluster without a RLAGN

In order to compare clusters containing a RLAGN to those which do not, we have data on a cluster at $z = 1.6$ with no RLAGN: Cl 0332−2742 (Kurk *et al.*, 2009). NB observations of this cluster discovered 80 NB emitters, more than 50 of which were Hα emitters at $z = 1.6$. Figure 5.4 shows a map of the Hα emitters, the selection of Hα emitters, and the Hα luminosity function for this cluster. These data are much deeper than the RLAGN-selected fields. From the Hα luminosity function, Cl 0332−2742 is 2.5 times the density of the control field from Sobral *et al.* (2013), lower than the overdensity measured around 3C 008.

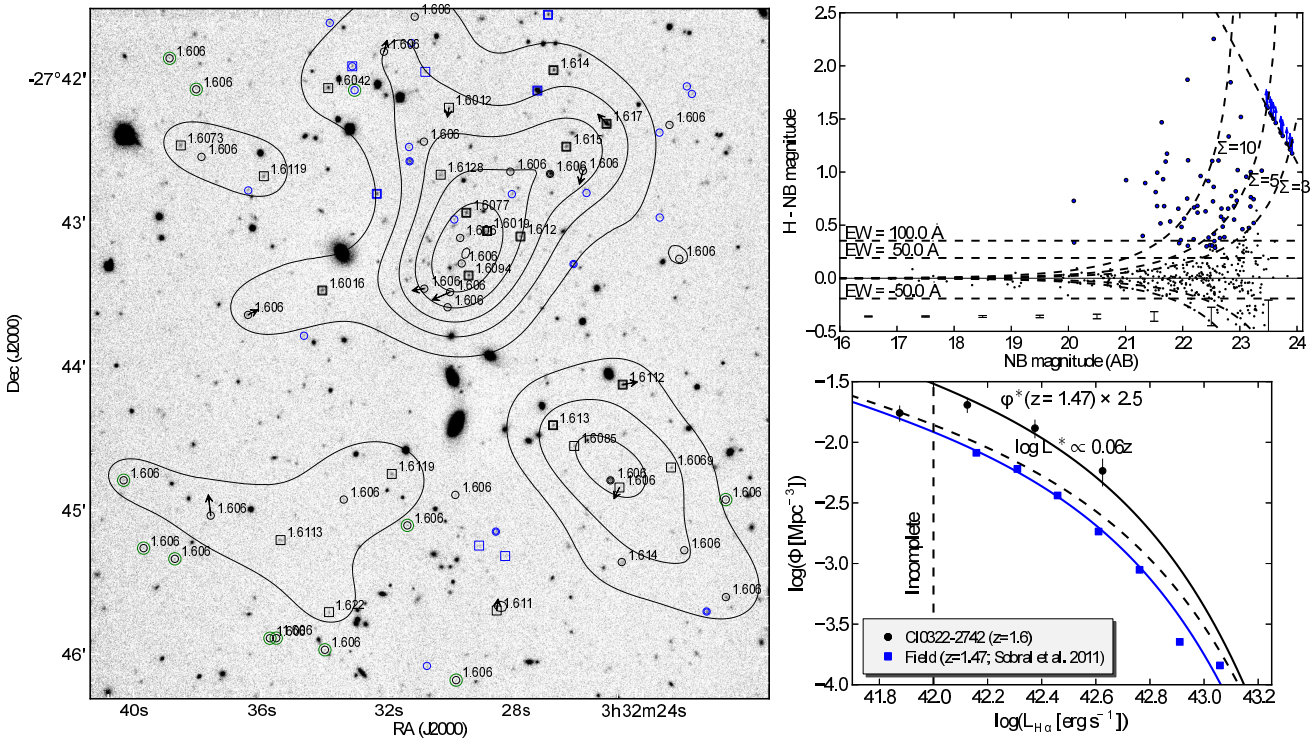

Figure 5.4: The figures from the original telescope proposal, created by J. Kurk, for Cl 0332−2742 at $z = 1.61$ (Kurk *et al.*, 2009). *Left:* Map of the eighty NB emitters selected in this field: squares/ circles show those with/without spectroscopic redshifts. Numbers indicate the measured redshift for sources at $z \sim 1.61$ (the redshift is set to $z = 1.606$ if there is no spectroscopic measurement). Contours indicate the surface density of Hα emitters, with levels at $5, 10, 15, 20, 25\times$ the average density of the field. *Top right:* Selection of Hα emitters. Curved dashed lines show the $3, 5$ and 10Σ significance levels. Horizontal lines show EWs of 50 Å and 100 Å. Typical errors in the colours are indicated at the bottom. *Bottom right:* Hα luminosity functions for the field at $z = 1.47$ (squares; Sobral *et al.*, 2013), extrapolated to $z = 1.6$ (dashed line), and for the 5×5 arcmin^2 region around Cl 0332−2742 (circles).

5.4 Discussion

I do not compare the two structures 3C 008 and Cl 0332−2742 here because the amount of cluster-to-cluster variation (e.g. Chapter 3) requires larger samples in order to draw any reasonable conclusions. The original idea was to compare the five radio galaxy fields with several $z \sim 1.5$–1.6 (proto)clusters. We have submitted three telescope proposals in order to observe these fields with the appropriate NB filters. None of the proposals were awarded the full amount of time requested, and several of the awarded nights were lost to poor weather. Instead, in the following sections, I will examine the structure and galaxies around 3C 008 in more detail.

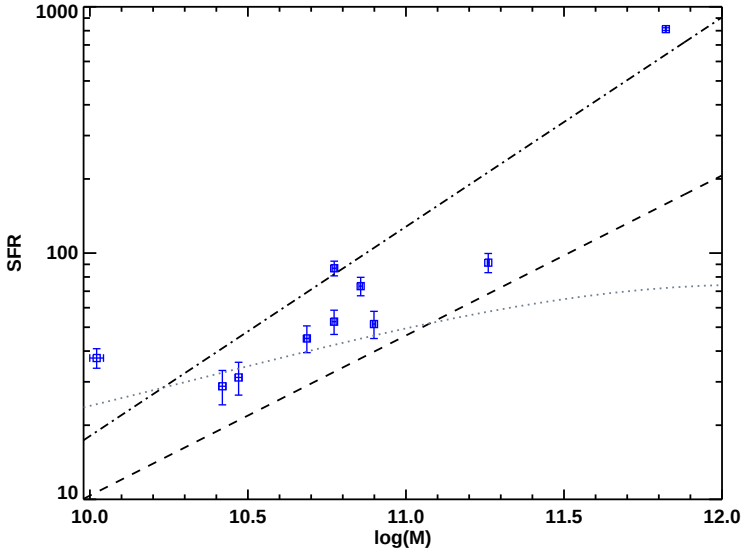

Figure 5.5: SFR-mass relation for Hα emitters around 3C 008. Overlaid are lines from Santini *et al.* (2009), showing the field SFR-mass relation at $z \sim 1.5$ (derived for galaxies at $1 < z < 1.5$ [dashed line] and $1.5 < z < 2.5$ [dot-dashed line]). Masses were derived from the $4.5\,\mu$m magnitudes following the method of Cooke *et al.* (2016), using a relation for only star-forming galaxies. There is ~ 0.2 dex scatter in this relation which is not shown in the error estimates. The SFRs have been corrected for dust extinction using the relation from Garn & Best (2010). Due to the selection criteria I am complete to a dust-uncorrected SFR of $\sim 10\,\mathrm{M}_\odot\,\mathrm{yr}^{-1}$. This corresponds to the grey dotted line for dust-corrected SFR. The radio galaxy's SFR measurement ($\sim 800\,\mathrm{M}_\odot\,\mathrm{yr}^{-1}$) may be contaminated by the AGN. The cluster Hα emitters are consistent with the field SFR-mass relation at this redshift.

5.4.1 SFR-mass relation

All of the Hα emitters surrounding 3C 008 are detected at $4.5\,\mu$m, so I use the $4.5\,\mu$m flux to determine a stellar mass for each of them (as described in Chapter 3). SFRs were measured as in Chapter 4: I calculated the continuum in the H-band and converted the NB signal to an Hα flux using Equations 4.8 and 4.9. These SFRs were corrected for dust extinction using the relation with stellar mass from Garn & Best (2010). Due to the selection criteria the data are complete to a dust-uncorrected SFR of $\sim 10\,\mathrm{M}_\odot\,\mathrm{yr}^{-1}$ (Figure 5.1). The radio galaxy's SFR measurement ($\sim 800\,\mathrm{M}_\odot\,\mathrm{yr}^{-1}$) may be contaminated by the central AGN. The remaining Hα emitters are consistent with the field SFR-mass relation at this redshift (Figure 5.5).

In Chapter 4 I showed that the SFR-mass relations for protocluster galaxies and field galaxies were the same at $z = 2.5$. I note that the data in this chapter are not as deep as those in Chapter 4, and I do not have a measure of any potential quiescent galaxies. From the star-forming galaxies I do detect, however, I find no difference between the

field and the galaxies surrounding 3C 008 at $z = 1.6$. These studies imply that the SFR-mass relation does not depend on environment at $1.6 \leq z \leq 2.5$, which would suggest that at every epoch $1.6 \leq z \leq 2.5$ galaxy growth proceeds in the same way for cluster and field galaxies. Further, deeper data examining the star-forming population around 3C 008 would be required in order to better measure the relationship between SFR and stellar mass in this structure.

In Chapter 4 the mass distributions of Hα emitters in the protocluster and the field were significantly different due to a lack of low mass galaxies in the protocluster. I do not probe below $M \sim 10^{10.5}\,\mathrm{M}_{\odot}$, so cannot comment on the existence of low mass galaxies around 3C 008.

5.4.2 Structure around 3C 008

3C 008 is overdense both in the *Spitzer* IRAC selection and in Hα emitters. Figure 5.6 shows the distributions of the Hα emitters selected in this chapter, overlaid on a density map, created as in Chapter 3, using the coordinates of IRAC-selected sources (selected using the criteria in Section 1.4). Although there is a large amount of line-of-sight contamination in the underlying density map, the Hα emitters in Figure 5.6 appear to trace the structure of the IRAC-selected galaxies.

The distribution of Hα emitters appears strongly correlated with the underlying density of IRAC-selected galaxies. To test whether this correlation is real, I scaled the density map to a probability density map by scaling each pixel such that the sum of all pixels was unity. I then randomly populated the field with 12 sources and noted the probability at each source's position. The product of these probabilities was then the total probability of obtaining that distribution of 12 Hα emitters given the underlying density of IRAC-selected galaxies. A random sample of 12 Hα emitters has a probability of 0.0013 of having the distribution I find in the observations. The Hα emitters and CARLA IRAC-selected sources are therefore highly likely to be tracing the same structure. Given the narrow redshift slice in which Hα lies within the NB filter ($\Delta z \lesssim 0.03$), this is confirmation that the structure is at $z \sim 1.6$ and associated with the radio galaxy, rather than a line-of-sight projection.

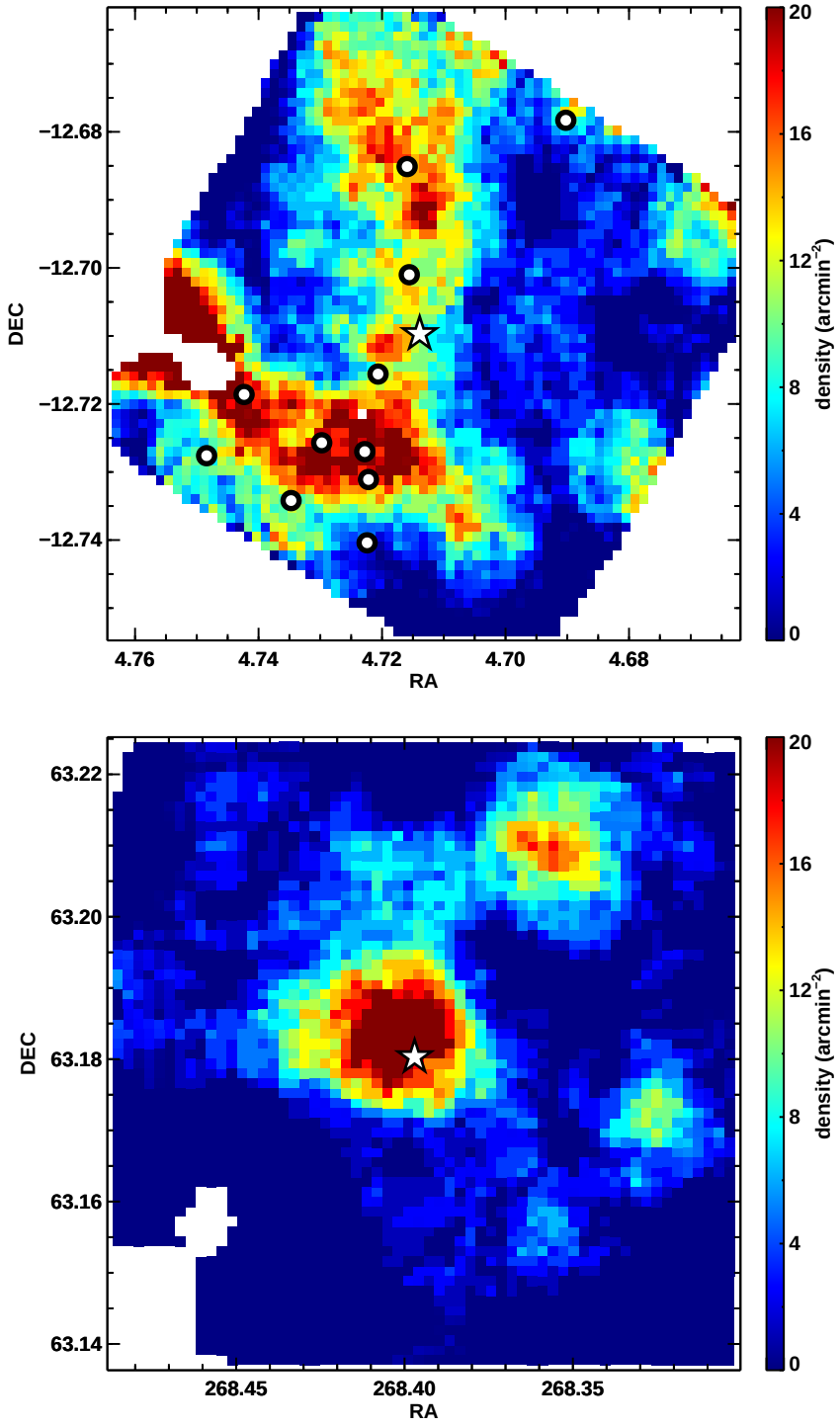

Figure 5.6: *Top:* Map of Hα emitters around 3C 008 compared to IRAC-selected galaxies. The white points show the positions of Hα emitters, the underlying density map shows the distribution of IRAC-selected galaxies selected as in Section 1.4. The white star indicates the RLAGN 3C 008. *Bottom:* The distribution of IRAC-selected galaxies selected in CARLA J1753+6311. The white star is the RLAGN.

Figure 5.6 shows the density maps of the field around 3C 008 and CARLA J1753+6311. Both are structures selected around RLAGN at $z \sim 1.58$, however the two structures appear very different. Whereas 7C 1753+6311 is surrounded by a dense core ~ 1 Mpc in diameter, the structure around 3C 008 is more extended and may be composed of a filamentary structure, or a merger of smaller group-sized haloes. From the overdensity in the field around 3C 008 alone, I cannot determine if 3C 008 will evolve into a cluster by $z = 0$. It is certainly not a collapsed cluster but may instead be a protocluster or perhaps a proto-group. In order to determine the future evolution, the wider structure around 3C 008 needs to be mapped in order to determine how much mass is available to collapse and form a group or cluster.

Interestingly, 7C 1753+6311 resides in the centre of the overdensity measured by CARLA, whereas 3C 008 does not reside in the densest region. This has implications for studies using RLAGN to detect (proto)clusters: although the RLAGN may indeed reside in an overdensity or (proto)cluster, it does not always appear in the centre of the overdensity. Wide fields-of-view around the RLAGN are required to find and fully study these structures.

5.5 Conclusions and future work

5.5.1 Conclusions

In this chapter, I have presented NB imaging of Hα emitters surrounding the RLAGN 3C 008 and PKS 2025−155. PKS 2025−155 is surrounded by a compact overdensity (< 20 arcsec radius) of red galaxies, found by Best *et al.* (2003). I do not detect any Hα emission from these galaxies, suggesting they are quiescent satellites of PKS 2025−155. The surrounding field is consistent with the field density of Hα emitters at $z = 1.5$ and so PKS 2025−155 is unlikely to reside within a protocluster. Several studies have found that not all RLAGN reside in protoclusters (e.g. Venemans *et al.*, 2007; Hatch *et al.*, 2011a; Galametz *et al.*, 2012). Although this radio galaxy showed a promising overdensity of red galaxies, this was not reflected in the number of Hα emitters.

3C 008 was detected as residing in a significant overdensity of red IRAC-selected galaxies by the CARLA survey. The narrow redshift range probed by the NB filter confirms this overdensity resides at $z \sim 1.6$, and so is likely to be associated with the RLAGN. I find an overdensity of Hα emitters of 4.9 times the field density at this redshift, which may suggest this structure is a protocluster, although further data is required to confirm this. The star-forming galaxies surrounding 3C 008 lie on the same SFR-mass relation as field galaxies at $z \sim 1.6$, suggesting there is no difference in the star formation processes of field galaxies and those in the structure around 3C 008.

This field contains an interesting, immature structure. The structure of the overdensity, as traced by both red *Spitzer* IRAC-selected galaxies and Hα emitters, is diffuse with no collapsed dense cores or groups. It may be formed of a merger of two smaller haloes or perhaps a filamentary structure. Further work looking at the wider field around this overdensity is required to determine the form of the structure. In the future I will be applying for KMOS and *Spitzer* time to examine the surrounding regions of this structure. Future work will use spectra to confirm the star-forming members, and photometry to examine any potential quiescent members, such as in Chapter 3. With a wider field-of-view and a measure of both the star-forming and passive populations, comparisons with semi-analytic models will allow me to determine how this structure is likely to evolve in the future (e.g. Hatch *et al.*, 2016).

Chapter 6

Conclusions and future work

In this thesis I have set out to study the formation and evolution of cluster galaxies at high redshift. To do this I have used a sample of high redshift radio-loud active galactic nuclei (RLAGN) to select fields likely to contain galaxy clusters and proto-clusters. As shown in Chapter 1, these RLAGN are proven beacons for (proto)clusters and are theorised to be the progenitors of local brightest cluster galaxies. By using this targeted approach, the required telescope time to observe these structures is drastically reduced compared to wide and deep field surveys searching for (proto)clusters. Wylezalek *et al.* (2013, 2014) showed that nearly half (45%) of RLAGN in the Clusters Around Radio-Loud AGN (CARLA) survey at $1.3 < z < 3.2$ reside in structures with densities suggestive of (proto)clusters. In this thesis I have observed a sample of the densest candidates from the CARLA survey, obtaining follow-up i' and J-band images, as well as analysing in depth the star-forming members of a protocluster selected from the *Spitzer* high redshift radio galaxy survey, the precursor to CARLA. I have studied the formation history of the massive cluster members by comparing the average colours of cluster galaxies across an 11 Gyr period (Chapter 2). I then examined one of the CARLA clusters in detail using the rest-frame UBJ wavebands to measure the fraction of cluster galaxies which are quiescent (Chapter 3). Finally I compared the star-forming properties of Hα emitters surrounding a RLAGN at $z = 2.49$ to those in the field, finding no difference in the overall star-formation mode, but a significant difference in the mass functions for cluster and field galaxies (Chapter 4). In the following sections I will summarise my main conclusions and finish by looking ahead to

the next stage of this research.

6.1 Cluster formation timescales

In Chapter 2 I examined the evolution of the average observed $i' - [3.6]$ colour of protocluster and cluster galaxies over $0 < z < 3.2$. I used a sample of (proto)clusters from the CARLA survey selected to be among the densest candidates at $1.3 \leq z \leq 3.2$. I showed that these clusters are likely to represent an evolutionary sequence, whereby the protoclusters at $z \sim 3.2$ are likely to evolve into structures like the (proto)clusters at $z \sim 1.3$. This means that, when analysing their average colours, one evolutionary model is required to explain all the data. The average observed colour does not significantly evolve with redshift at $z > 1.3$. This is in contrast to lower redshift surveys which predict a bluer average colour at higher redshifts.

Comparing the colour data to simple galaxy formation models I showed that single burst models, which are frequently used to fit red sequence galaxies at $z < 1$, cannot explain the CARLA data. Instead, a more extended model, involving many bursts of star formation, is required. This means that clusters formed over longer periods of time than extrapolated from low redshift surveys, but individual galaxies may have formed rapidly. I also showed that cluster formation, as measured using the average $i' - [3.6]$ colour, is consistent with the cosmic star formation history, with a truncation in star formation somewhere in the range $1 < z < 2$. I compared these CARLA clusters to results from the IRAC Shallow Cluster Survey at $z < 1.5$ (ISCS; Eisenhardt *et al.*, 2008). I found that the extended cluster formation models were also consistent with low redshift results.

This evidence for an extended, bursty formation period for cluster galaxies is similar to results found using semi-analytic models. De Lucia *et al.* (2006) showed that massive ellipticals in the Millennium Simulation form their stars through multiple bursts of star formation. In future work it would be interesting to analyse the observed colours of cluster galaxies in semi-analytic models, and compare the evolution to the observed trends in Chapter 2.

Further work analysing the rest-frame optical and NIR colours of these clusters will

allow me to better differentiate between different formation histories. The $i' - [3.6]$ colour spans a wide range in rest-frame colour and so many different galaxy formation models can fit the data. In addition, spectroscopic confirmation of the CARLA cluster members (on-going with *HST*; G. Noirot *et al.* in preparation) will allow a more detailed examination of their formation histories without relying on statistical subtraction of field contamination.

6.1.1 Cluster galaxy formation mechanisms

Another important result from Chapter 2 is that the significance of dry mergers for massive galaxies assembling their stellar mass is redshift dependent. The average galaxy colours at $z > 2$ only allow for rapid assembly of the stellar populations: massive galaxies must have assembled within 0.5 Gyr of them forming a significant fraction of their stars. This means that dry mergers are not the dominant formation mechanism for massive cluster galaxies at $z > 2$. Studies of the luminosity function at high redshift have shown that the bright end of the luminosity function is established within 5 Gyr of the Big Bang (e.g. Muzzin *et al.*, 2008, Chapter 2). This qualitatively agrees with my results showing that massive galaxies are already in place by $z \sim 3$. This is in contrast to cluster galaxies formed in semi-analytic models, which form their stars very early, but build up their mass over much longer periods of time (typically ≥ 1 Gyr, e.g. De Lucia *et al.*, 2006). At $z < 2$, dry merging may be a more significant mechanism for cluster galaxies assembling their stellar mass, as the average colours allow for a longer period of time. This is more consistent with semi-analytic models of galaxy formation.

6.2 RLAGN as beacons for (proto)clusters

In this thesis I have detected (proto)clusters using RLAGN as beacons for these overdensities. However, in the literature there is some debate as to whether these powerful radio galaxies preferentially reside in clusters of a certain age or stage of collapse (e.g. Simpson & Rawlings, 2002; van Breukelen *et al.*, 2009). In Chapter 3 I investigated a structure around the RLAGN 7C 1753+6311 and found it to be consistent with a collapsed, mature cluster, with a high quiescent fraction of galaxies. This showed that

RLAGN can reside in a range of clusters, at various stages of maturity, and not just in very young, or merging, clusters.

7C 1753+6311 was selected from the sample of CARLA (proto)clusters used in Chapter 2 as a pilot study examining the quiescent fraction of high redshift clusters and protoclusters. The structure of the cluster surrounding 7C 1753+6311 (CARLA J1753+6311) is very dense and compact, with 28 ± 6 galaxies within 0.9 arcmin of the RLAGN. This is more dense and more compact than other forming clusters at the same redshift, indicating that CARLA J1753+6311 is at least as massive as confirmed (proto)clusters such as ClG 0218.3−0530 (Papovich *et al.*, 2010; Tanaka, Finoguenov & Ueda, 2010) and is likely to evolve into a structure of similar mass to the Virgo cluster.

I examined the red and quiescent fractions of galaxies in CARLA J1753+6311, finding that this cluster has properties consistent with other "normal" clusters, with no central RLAGN, at $z \sim 1.6$. The red fraction is double that of the field, indicating environmental colour differences are well-established by $z = 1.6$. By using the rest-frame UBJ colours of galaxies in this field, I showed that 80% of the red galaxies are quiescent, compared to only 60% of red field galaxies. This shows that the observed red colours are due to an evolved galaxy population and not a large fraction of dust-obscured star forming galaxies.

Interestingly, in studying CARLA J1753+6311 I found signs of environmental effects being mass-dependent. In Chapter 3 I showed that the quiescent fraction in CARLA J1753+6311 is higher than the field, but only at high masses ($M_* > 10^{10.5}$ M$_\odot$). This is in contrast to lower redshift studies which have shown that mass and environmental effects on quenching star formation are separable out to $z \sim 0.7$ (Peng *et al.*, 2010; Kovač *et al.*, 2014).

These results form a pilot study of the quiescent fraction in $z > 1.5$ (proto)clusters and need to be further analysed in a large sample of clusters. At $z > 1.5$ our study of cluster properties has so far been limited to studies of individual structures, providing a range of results, sometimes contradictory (e.g. Papovich *et al.*, 2012; Newman *et al.*, 2014). In a future project I will extend the UVJ analysis of 7C 1753+6311 to a sample of 20 clusters and protoclusters from CARLA. The NIR data (rest-frame V/B) for these clusters is in the process of being reduced (G. Noirot *et al.* in preparation) and

I have applied for rest-frame U data for 12 CARLA (proto)clusters. Along with the 8 (proto)clusters for which we already have optical data, these will form the first large, uniform sample of $z > 1.5$ clusters and protoclusters and allow us to study the evolution of the quiescent fraction and build up of the red sequence across $2.5 > z > 1.3$.

6.3 Star forming properties of (proto)clusters

In Chapters 4 and 5 I examined the properties of Hα emitters in (proto)clusters at $z = 2.5$ and $z \sim 1.6$. In Chapter 4 I measured the star formation rate relation with stellar mass in a protocluster at $z = 2.49$. At $z < 1$, this relationship is the same for star forming galaxies, regardless of their environment. In Chapter 4 I showed that this holds even at $z \sim 2.5$. This means that at $z = 2.5$, star formation in massive galaxies is governed predominantly by galaxy mass rather than environment.

The mass functions of protocluster and field galaxies studied in Chapter 4 were significantly different. I showed that protocluster galaxies at $z = 2.5$ are more massive, and therefore more star-forming, than those in the field. This is because the protocluster lacks low-mass star-forming galaxies compared to the field. By examining the mass functions of protocluster and field galaxies using semi-analytic models I showed that this lack of low mass galaxies may be caused by the small field of view examined around the RLAGN. Low mass galaxies in the central regions of the protocluster are quenched in the models and therefore have no detectable Hα emission. In order to establish whether this is the case in the observations, further deep photometric studies are required to probe the low mass quiescent cluster populations at this redshift.

In Chapter 5 I presented data on the RLAGN 3C 008 at $z = 1.59$ and Hα emitters surrounding it. The Hα emitters detected in this study are also consistent with the field relation between SFR and stellar mass, although further data are required to probe the lower mass star forming galaxies as well as measure the quiescent population.

The structure around 3C 008 appears to be immature, formed of a few diffuse groups which are perhaps merging, or maybe a filamentary structure. This structure is traced by both star-forming Hα emitters and red IRAC-selected galaxies. The diffuse structure around 3C 008 has interesting implications for surveys such as CARLA, which

use RLAGN to detect (proto)clusters. 3C 008 does not reside in the centre, or densest region of the surrounding structure, meaning the overdensity measured in an aperture centred on the RLAGN will be underestimated. There are also indications that the overdensity extends beyond the $\sim 5 \times 5$ arcmin^2 field of view. This means that future studies of (proto)clusters around RLAGN should use larger fields of view in order to establish the existence of a (proto)cluster. Some protoclusters may be missed as their dense cores are offset from the RLAGN.

6.4 Future work

In Chapters 3 and 5 I showed that RLAGN reside in a range of environments—from dense cores of quiescent galaxy overdensities, to more extended, star-forming structures. The initial plan for Chapter 5 remains an interesting open question: are RLAGN-selected (proto)clusters representative of the cluster population as a whole? The ideal epoch in which to study this question is $z \sim 1.5$. At this redshift there are tens of "normal" clusters now known from surveys such as SpARCS and XDCP (Chapter 1), as well as several clusters around RLAGN from CARLA. With further photometric and spectroscopic information on the CARLA sample a direct comparison would be possible and it would be very interesting to determine what, if any, impact the presence of a RLAGN has on the surrounding structure.

Another open question in the research of protoclusters is when does the quiescent fraction diverge from the field? With incoming NIR data on 20 CARLA clusters and protoclusters I aim to expand on the pilot study from Chapter 3 and study the build-up of the quiescent population. With these data I will also examine the importance of red/dusty star-forming galaxies at $1.3 < z < 2.5$. Comparisons to field samples will also allow me to measure the relative importance of mass and environment at different times in the Universe. By comparing these data to semi-analytic models I hope to determine the main processes by which galaxies in (proto)clusters build up their stellar mass.

In addition to studying the galaxy populations in high redshift protoclusters, it would be interesting to study the intra-cluster medium (ICM). Measurements of the ICM

at high redshift are very difficult due to the X-ray signal declining rapidly. At high redshift the gas is also more diffuse, making detections using the SZ effect increasingly difficult. Some suggestions have been made to study the early stages of the ICM's formation using bright sources such as quasars that lie behind the forming cluster. When we have large samples of confirmed (proto)clusters, comparing the spectra of quasars behind them to those with no structure in the line of sight may allow us to measure the ICM gas before it collapses.

Other questions that will be interesting to answer in the coming years include: what are the different processes occurring at the highest redshifts, compared to lower redshift, in forming the high mass cluster galaxies? Are any of the high mass galaxies at high redshift quiescent, or are clusters dominated by star formation? Can we explain the differences we see between cluster and field galaxies locally simply by an earlier formation time, or is there some kind of effect on galaxies due to their protocluster environment at high redshift? Is there a larger incidence of starbursting, or sub-millimeter galaxies in (proto)clusters? Upcoming surveys such as eROSITA and DES will be invaluable in answering these questions. The large numbers of clusters and protoclusters expected from these surveys will allow us to systematically study dense environments out to $z \sim 3$.

Appendices

Appendix A

Colour magnitude diagrams

The $i' - [3.6]$ vs. $[3.6]$ colour-magnitude diagrams for the 37 CARLA fields (including those in Figure 2.2) are shown in Figure A.1. There is a large scatter in the colours of sources, suggesting that each of these clusters still has continuing star formation.

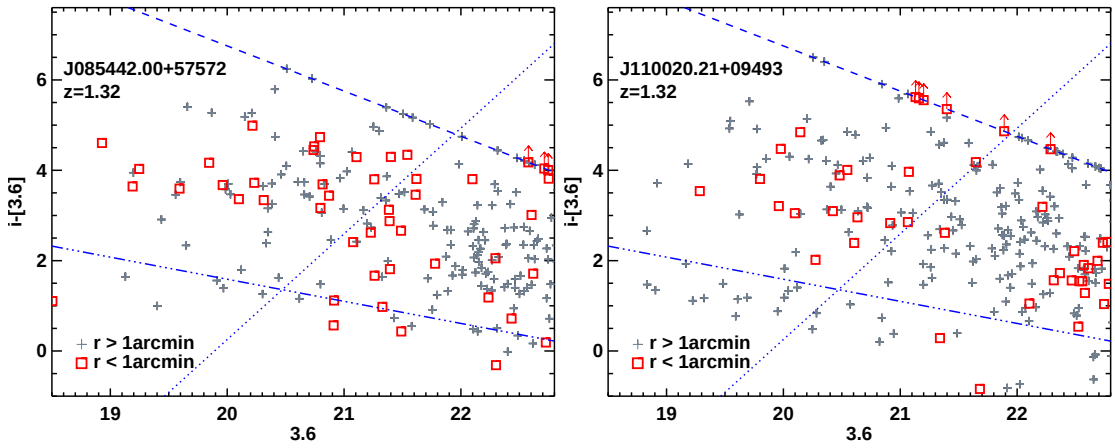

Figure A.1: $i' - [3.6]$ colour-magnitude diagrams. Red squares show sources within 1 arcmin of the RLAGN. Grey plus symbols show those sources lying further than 1 arcmin from the RLAGN, which are more likely to be contaminants. The blue dashed lines show the 1σ i' median depth. Sources fainter than the 1σ median depth are set to $1\sigma_{med}$ and shown as lower limits. The dotted blue lines show a $M_* > 10^{10.5}\,\mathrm{M}_\odot$ mass cut and the dash-triple dotted blue lines show the cut used to remove low redshift contaminants. The RLAGN is shown by a red star. In some diagrams, the AGN is too bright to fit on the scale and so is not shown. For 7C1756+6520 confirmed cluster members from Galametz *et al.* (2010a) are shown by green circles.

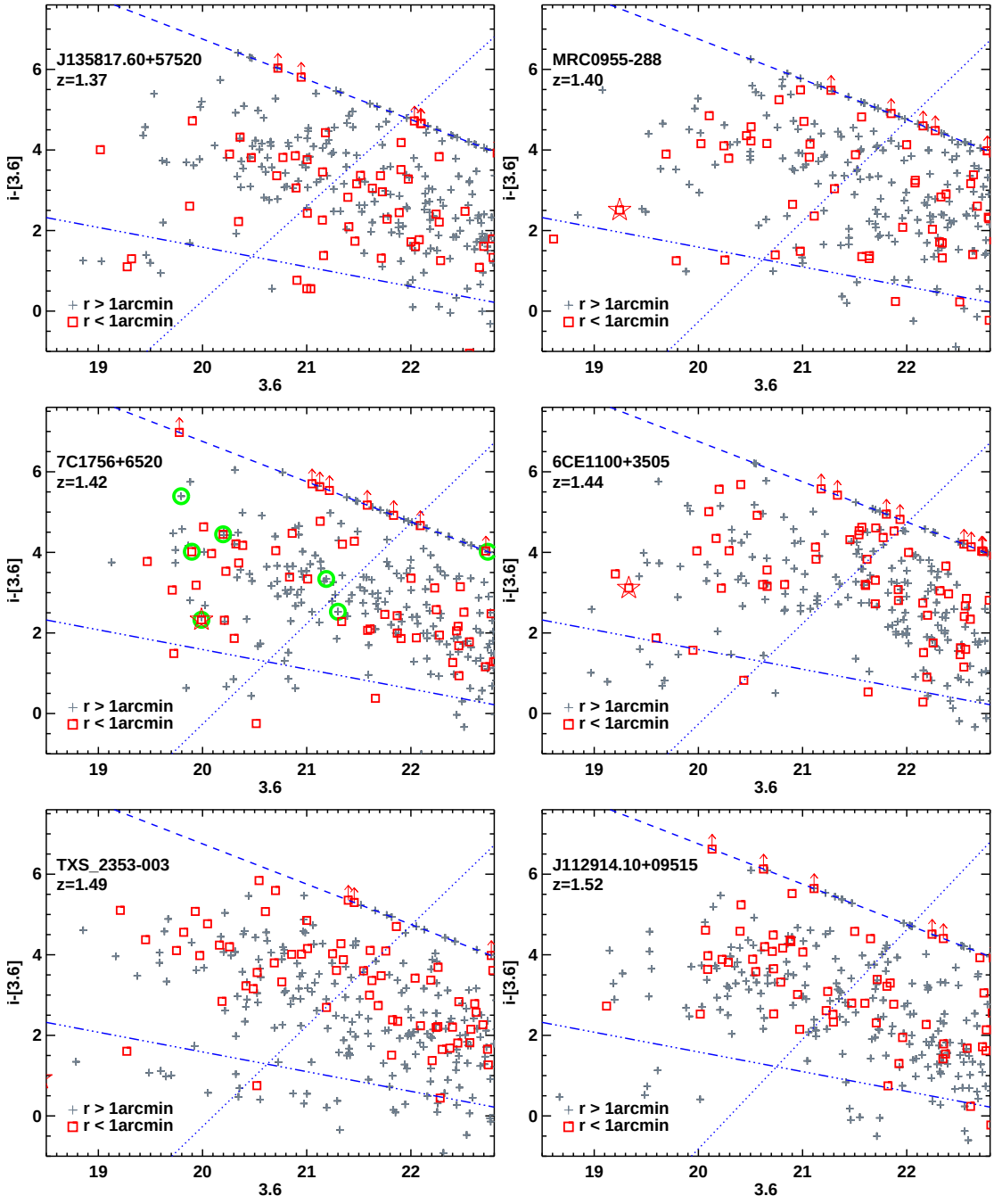

Figure A.1: continued.

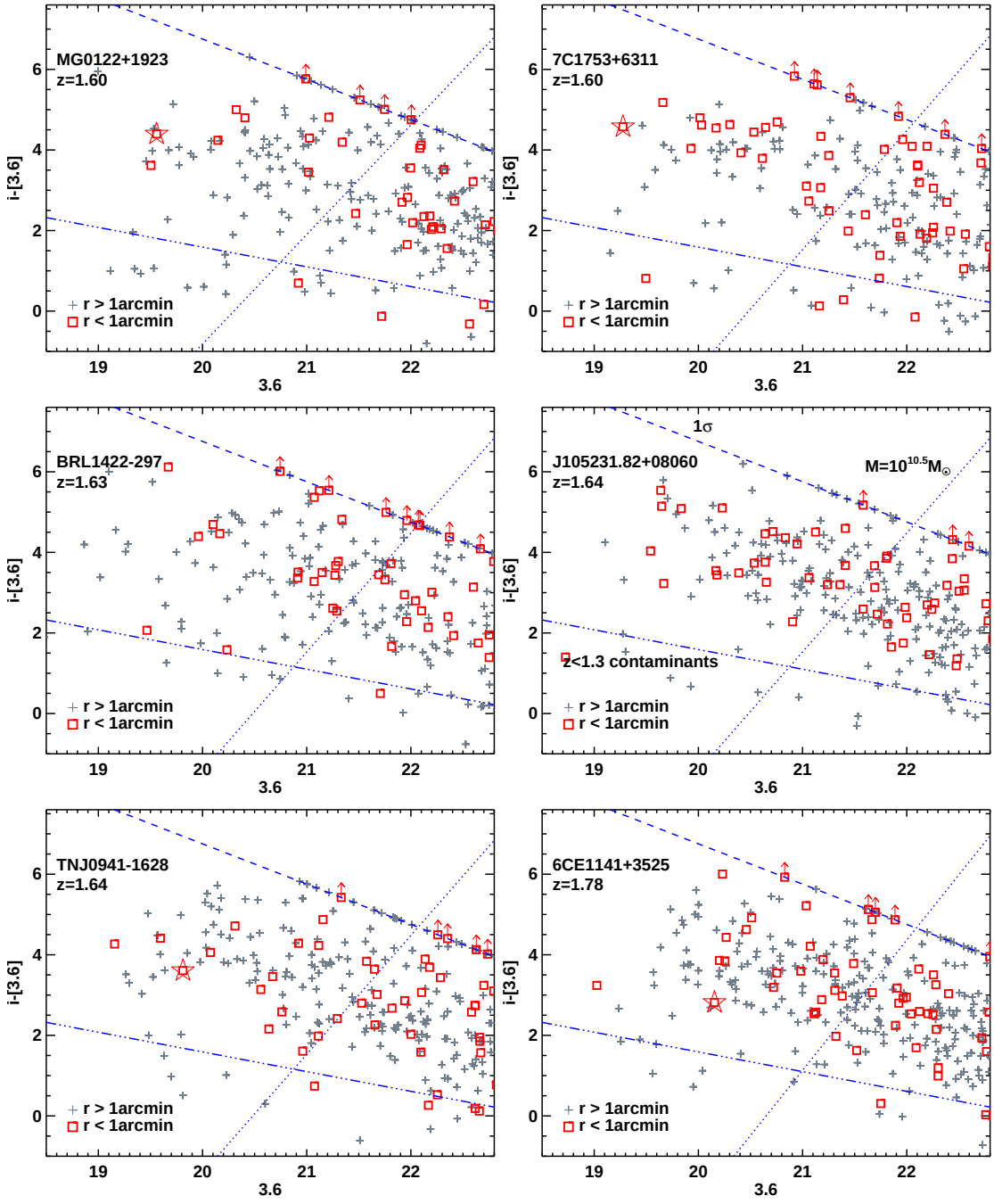

Figure A.1: continued.

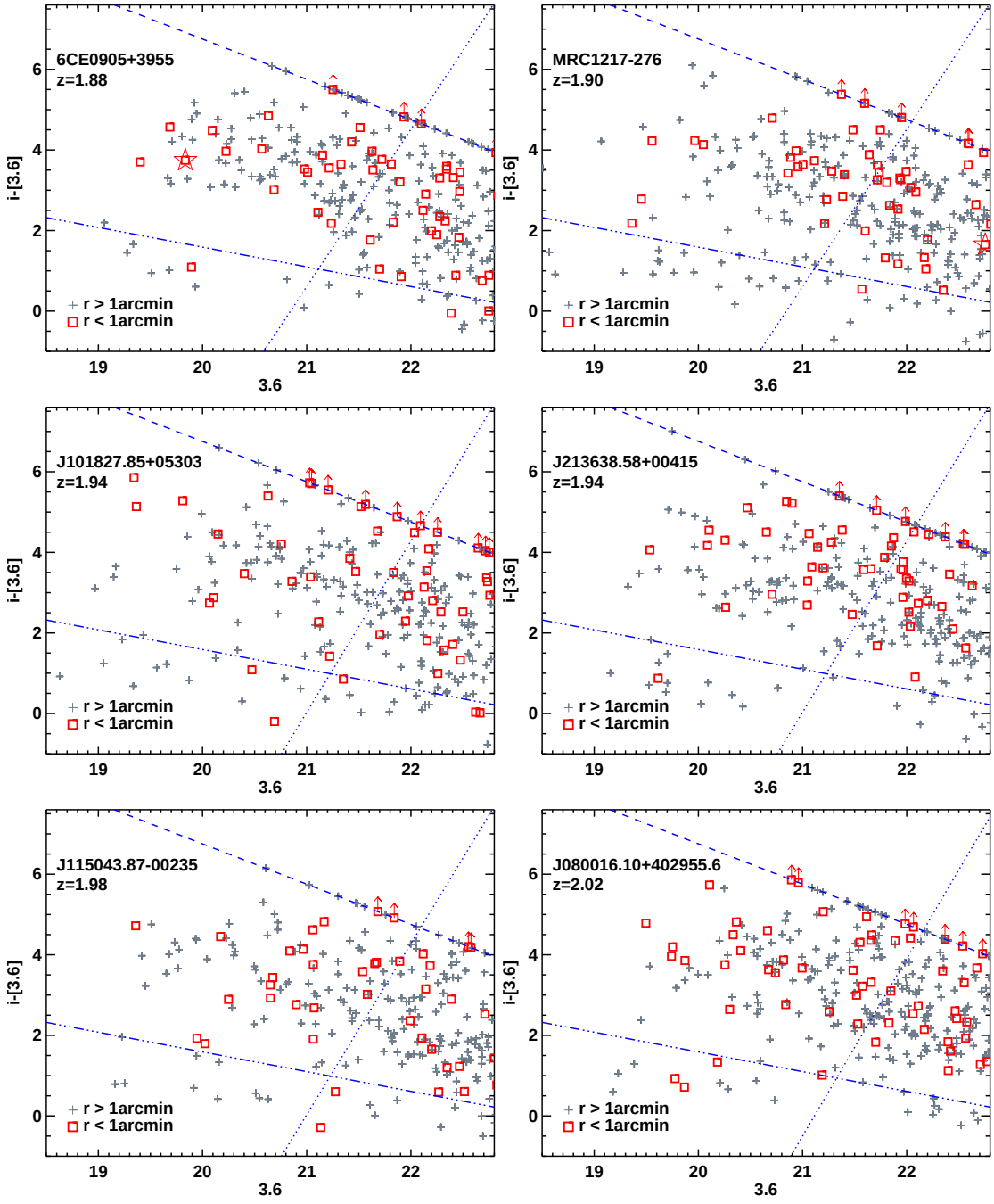

Figure A.1: continued.

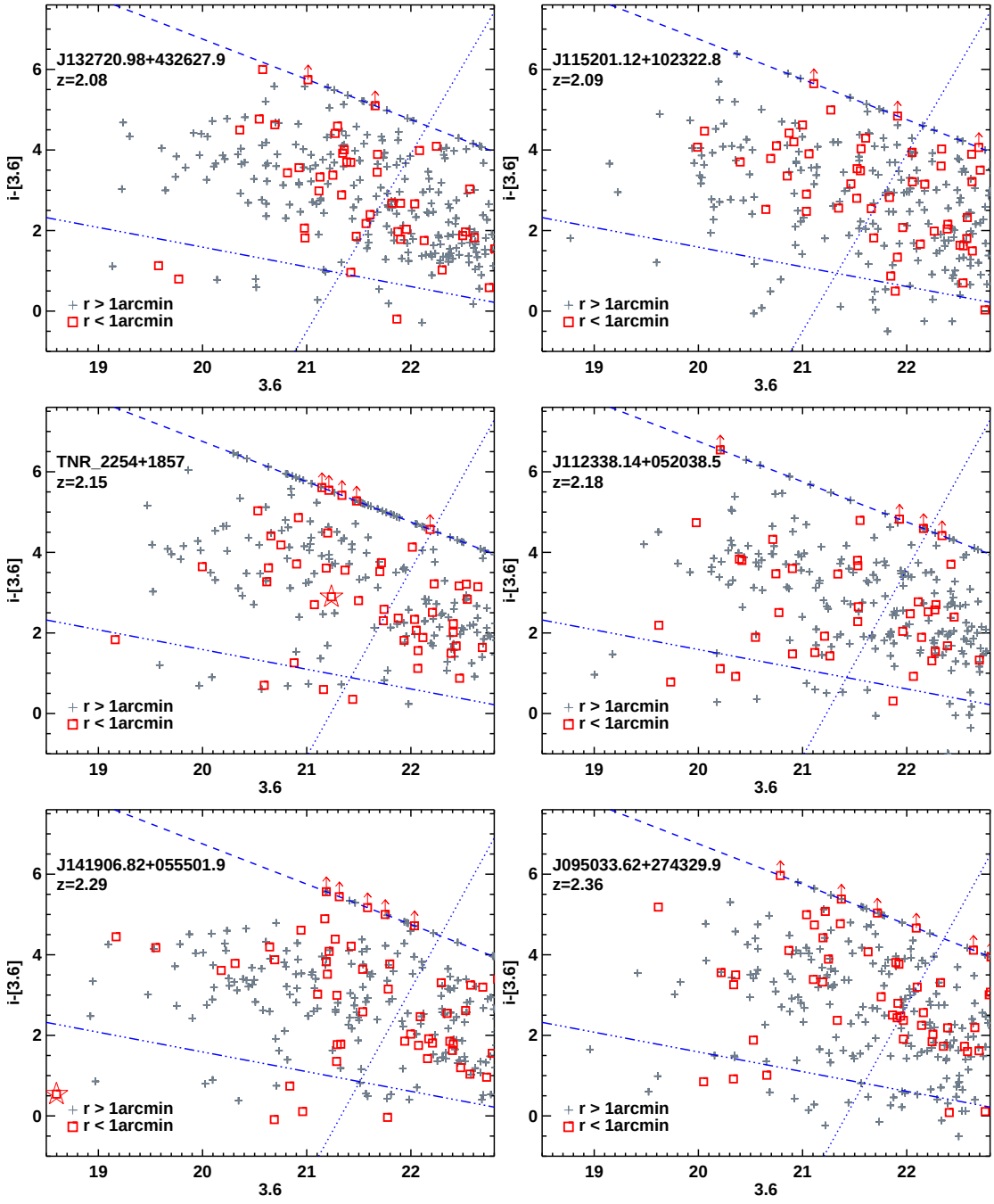

Figure A.1: continued.

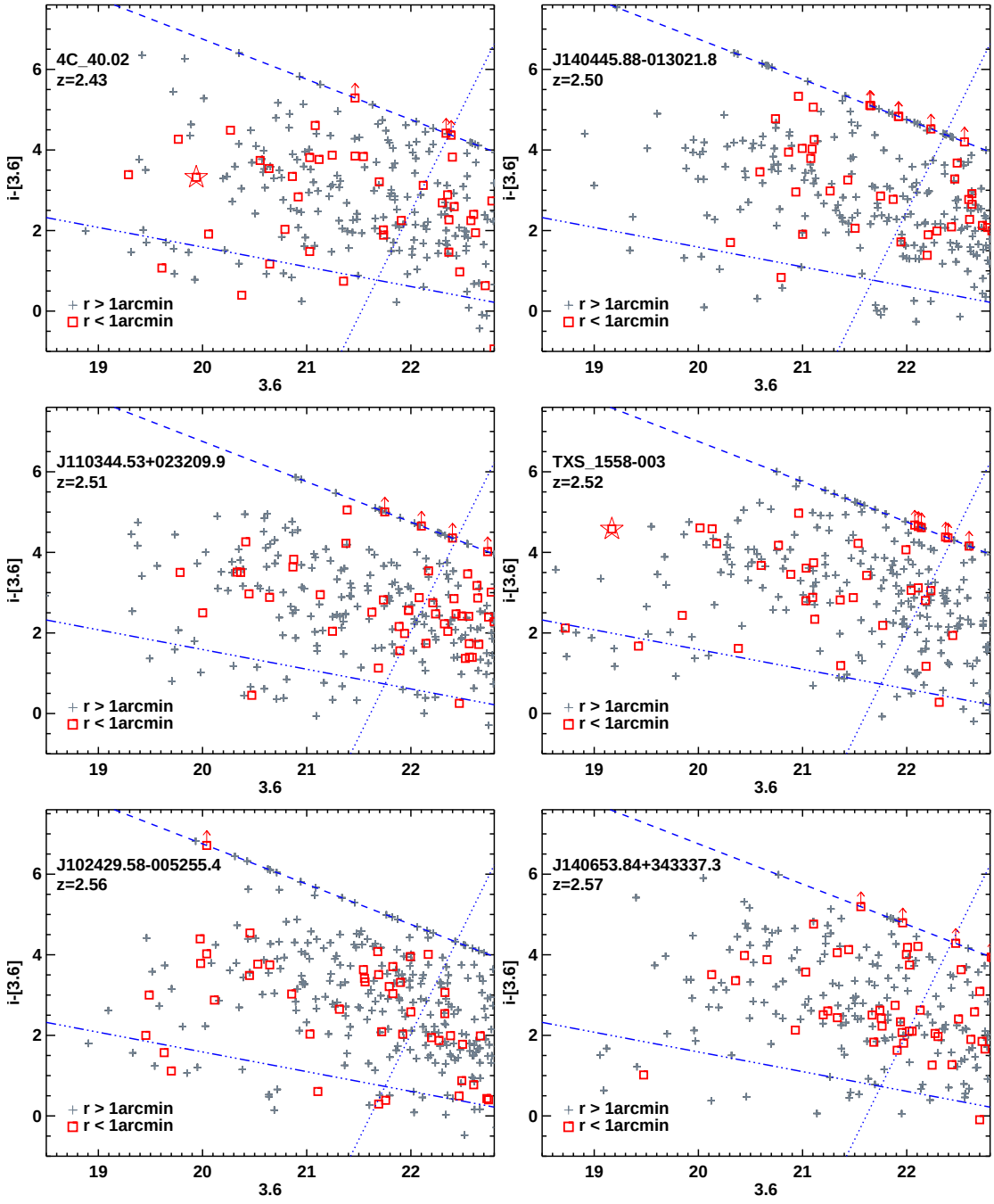

Figure A.1: continued.

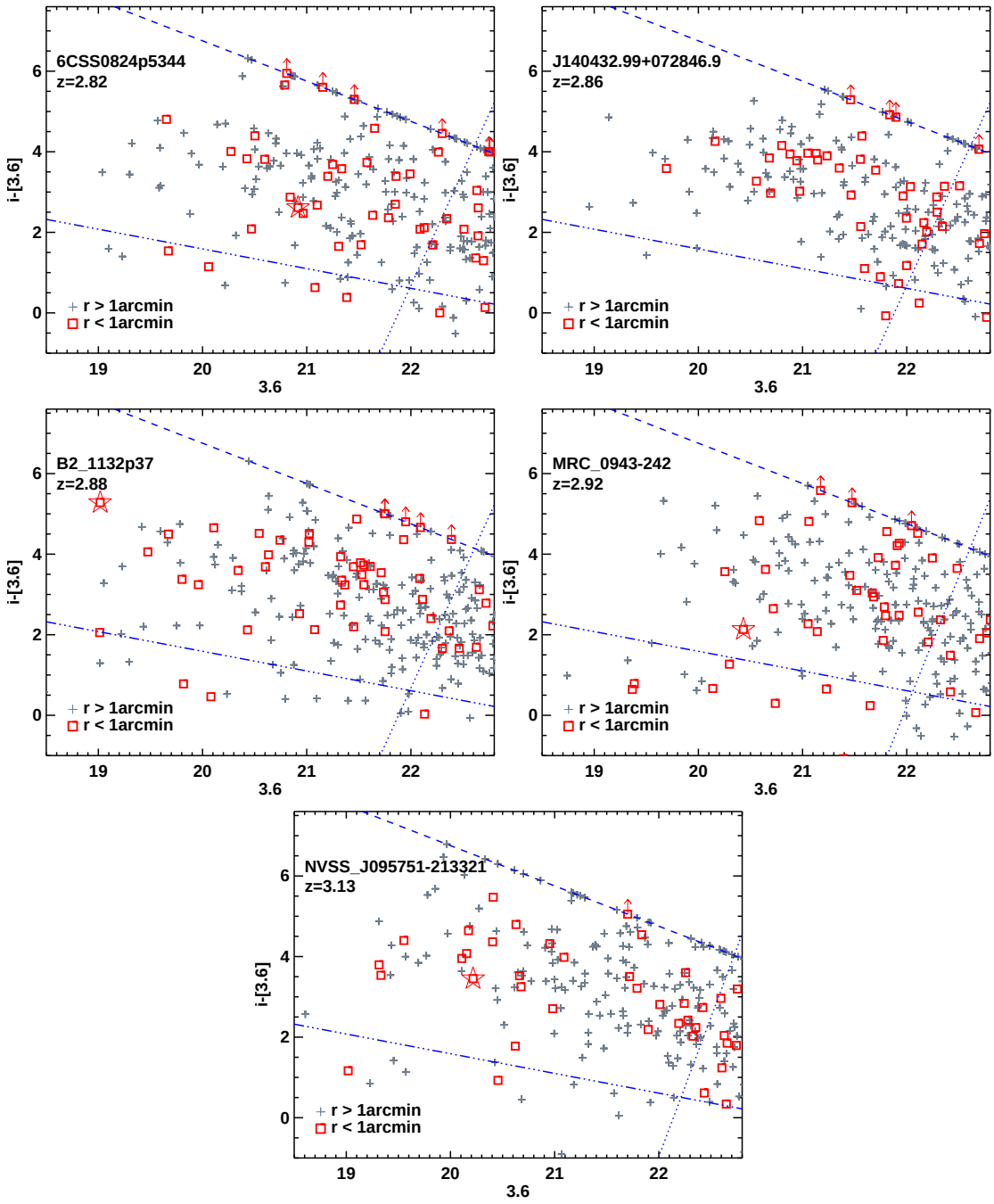

Figure A.1: continued.

“Get out of my office”

– Dr. N. Hatch

Bibliography

Abell G. O., Corwin, Jr. H. G., Olowin R. P., 1989. *ApJS*, **70**, 1.

Abell G. O., 1958. *ApJS*, **3**, 211.

Abramson A., Kenney J. D. P., Crowl H. H., Chung A., van Gorkom J. H., Vollmer B., Schiminovich D., 2011. *AJ*, **141**, 164.

Adelman-McCarthy J. K., Agüeros M. A., Allam S. S., Allende Prieto C., Anderson K. S. J., Anderson S. F., Annis J., Bahcall N. A., Bailer-Jones C. A. L., Baldry I. K., Barentine J. C., Bassett B. A., Becker A. C., Beers T. C., Bell E. F., Berlind A. A., Bernardi M., Blanton M. R., Bochanski J. J., Boroski W. N., Brinchmann J., Brinkmann J., Brunner R. J., Budavári T., Carliles S., Carr M. A., Castander F. J., Cinabro D., Cool R. J., Covey K. R., Csabai I., Cunha C. E., Davenport J. R. A., Dilday B., Doi M., Eisenstein D. J., Evans M. L., Fan X., Finkbeiner D. P., Friedman S. D., Frieman J. A., Fukugita M., Gänsicke B. T., Gates E., Gillespie B., Glazebrook K., Gray J., Grebel E. K., Gunn J. E., Gurbani V. K., Hall P. B., Harding P., Harvanek M., Hawley S. L., Hayes J., Heckman T. M., Hendry J. S., Hindsley R. B., Hirata C. M., Hogan C. J., Hogg D. W., Hyde J. B., Ichikawa S.-i., Ivezić Ž., Jester S., Johnson J. A., Jorgensen A. M., Jurić M., Kent S. M., Kessler R., Kleinman S. J., Knapp G. R., Kron R. G., Krzesinski J., Kuropatkin N., Lamb D. Q., Lampeitl H., Lebedeva S., Lee Y. S., French Leger R., Lépine S., Lima M., Lin H., Long D. C., Loomis C. P., Loveday J., Lupton R. H., Malanushenko O., Malanushenko V., Mandelbaum R., Margon B., Marriner J. P., Martínez-Delgado D., Matsubara T., McGehee P. M., McKay T. A., Meiksin A., Morrison H. L., Munn J. A., Nakajima R., Neilsen, Jr. E. H., Newberg H. J., Nichol R. C., Nicinski T., Nieto-Santisteban M., Nitta A., Okamura S., Owen R., Oyaizu H., Padmanabhan N., Pan K., Park C., Peoples, Jr. J., Pier J. R., Pope A. C., Purger N., Raddick M. J., Re Fiorentin P., Richards G. T., Richmond M. W., Riess A. G., Rix H.-W., Rockosi C. M., Sako M., Schlegel D. J., Schneider D. P., Schreiber M. R., Schwope A. D., Seljak U., Sesar B., Sheldon E., Shimasaku K., Sivarani T., Allyn Smith J., Snedden S. A., Steinmetz M., Strauss M. A., SubbaRao M., Suto Y., Szalay A. S., Szapudi I., Szkody P., Tegmark M., Thakar A. R., Tremonti C. A., Tucker D. L., Uomoto A., Vanden Berk D. E., Vandenberg J., Vidrih S., Vogeley M. S., Voges W., Vogt N. P., Wadadekar Y., Weinberg D. H., West A. A., White S. D. M., Wilhite B. C., Yanny B., Yocum D. R., York D. G., Zehavi I., Zucker D. B., 2008. *ApJS*, **175**, 297.

Alberts S., Pope A., Brodwin M., Atlee D. W., Lin Y.-T., Dey A., Eisenhardt P. R. M., Gettings D. P., Gonzalez A. H., Jannuzi B. T., Mancone C. L., Moustakas J., Snyder G. F., Stanford S. A., Stern D., Weiner B. J., Zeimann G. R., 2014. *MNRAS*, **437**, 437.

Amendola L., Appleby S., Bacon D., Baker T., Baldi M., Bartolo N., Blanchard A., Bonvin C., Borgani S., Branchini E., Burrage C., Camera S., Carbone C., Casarini L., Cropper M., de Rham C., Di Porto C., Ealet A., Ferreira P. G., Finelli F., García-Bellido J., Giannantonio T., Guzzo L., Heavens A., Heisenberg L., Heymans C., Hoekstra H., Hollenstein L., Holmes R., Horst O., Jahnke K., Kitching T. D., Koivisto T., Kunz M., La Vacca G., March M., Majerotto E., Markovic K., Marsh D., Marulli F., Massey R., Mellier Y., Mota D. F., Nunes N., Percival W., Pettorino V., Porciani C., Quercellini C., Read J., Rinaldi M., Sapone D., Scaramella R., Skordis C., Simpson F., Taylor A., Thomas S., Trotta R., Verde L., Vernizzi F., Vollmer A., Wang Y., Weller J., Zlosnik T., 2013. *Living Reviews in Relativity*, **16**.

Andreon S., Congdon P., 2014. *A&A*, **568**, A23.

Andreon S., Newman A. B., Trinchieri G., Raichoor A., Ellis R. S., Treu T., 2014. *A&A*, **565**, A120.

Andreon S., 2006. *A&A*, **448**, 447.

Aragon-Salamanca A., Ellis R. S., Couch W. J., Carter D., 1993. *MNRAS*, **262**, 764.

Bahcall N. A., Dong F., Bode P., Kim R., Annis J., McKay T. A., Hansen S., Schroeder J., Gunn J., Ostriker J. P., Postman M., Nichol R. C., Miller C., Goto T., Brinkmann J., Knapp G. R., Lamb D. O., Schneider D. P., Vogeley M. S., York D. G., 2003. *ApJ*, **585**, 182.

Balogh M. L., Baldry I. K., Nichol R., Miller C., Bower R., Glazebrook K., 2004. *ApJL*, **615**, L101.

Bamford S. P., Nichol R. C., Baldry I. K., Land K., Lintott C. J., Schawinski K., Slosar A., Szalay A. S., Thomas D., Torki M., Andreescu D., Edmondson E. M., Miller C. J., Murray P., Raddick M. J., Vandenberg J., 2009. *MNRAS*, **393**, 1324.

Bellagamba F., Maturi M., Hamana T., Meneghetti M., Miyazaki S., Moscardini L., 2011. *MNRAS*, **413**, 1145.

Benson B. A., de Haan T., Dudley J. P., Reichardt C. L., Aird K. A., Andersson K., Armstrong R., Ashby M. L. N., Bautz M., Bayliss M., Bazin G., Bleem L. E., Brodwin M., Carlstrom J. E., Chang C. L., Cho H. M., Clocchiatti A., Crawford T. M., Crites A. T., Desai S., Dobbs M. A., Foley R. J., Forman W. R., George E. M., Gladders M. D., Gonzalez A. H., Halverson N. W., Harrington N., High F. W., Holder G. P., Holzapfel W. L., Hoover S., Hrubes J. D., Jones C., Joy M., Keisler R., Knox L., Lee A. T., Leitch E. M., Liu J., Lueker M., Luong-Van D., Mantz A., Marrone D. P., McDonald M., McMahon J. J., Mehl J., Meyer S. S., Mocanu L., Mohr J. J., Montroy T. E., Murray S. S., Natoli T., Padin S., Plagge T., Pryke C., Rest A., Ruel J., Ruhl J. E., Saliwanchik B. R., Saro A., Sayre J. T., Schaffer K. K., Shaw L., Shirokoff E., Song J., Spieler H. G., Stalder B., Staniszewski Z., Stark A. A., Story K., Stubbs C. W., Suhada R., van Engelen A., Vanderlinde K., Vieira J. D., Vikhlinin A., Williamson R., Zahn O., Zenteno A., 2013. *ApJ*, **763**, 147.

Bertin E., Arnouts S., 1996. *A&AS*, **117**, 393.

Bertin E., Mellier Y., Radovich M., Missonnier G., Didelon P., Morin B., 2002. In: *Astronomical Data Analysis Software and Systems XI*, 228, eds Bohlender D. A., Durand D., Handley T. H.

Bertin E., 2006. In: *Astronomical Data Analysis Software and Systems XV*, 112, eds Gabriel C., Arviset C., Ponz D., Enrique S.

Best P. N., Lehnert M. D., Miley G. K., Röttgering H. J. A., 2003. *MNRAS*, **343**, 1.

Best P. N., Longair M. S., Röttgering H. J. A., 1998. *MNRAS*, **295**, 549.

Blakeslee J. P., Anderson K. R., Meurer G. R., Benítez N., Magee D., 2003. In: *Astronomical Data Analysis Software and Systems XII*, p. 257, eds Payne H. E., Jedrzejewski R. I., Hook R. N.

Blandford R. D., Znajek R. L., 1977. *MNRAS*, **179**, 433.

Bleem L. E., Stalder B., de Haan T., Aird K. A., Allen S. W., Applegate D. E., Ashby M. L. N., Bautz M., Bayliss M., Benson B. A., Bocquet S., Brodwin M., Carlstrom J. E., Chang C. L., Chiu I., Cho H. M., Clocchiatti A., Crawford T. M., Crites A. T., Desai S., Dietrich J. P., Dobbs M. A., Foley R. J., Forman W. R., George E. M., Gladders M. D., Gonzalez A. H., Halverson N. W., Hennig C., Hoekstra H., Holder G. P., Holzapfel W. L., Hrubes J. D., Jones C., Keisler R., Knox L., Lee A. T., Leitch E. M., Liu J., Lueker M., Luong-Van D., Mantz A., Marrone D. P., McDonald M., McMahon J. J., Meyer S. S., Mocanu L., Mohr J. J., Murray S. S., Padin S., Pryke C., Reichardt C. L., Rest A., Ruel J., Ruhl J. E., Saliwanchik B. R., Saro A., Sayre J. T., Schaffer K. K., Schrabback T., Shirokoff E., Song J., Spieler H. G., Stanford S. A., Staniszewski Z., Stark A. A., Story K. T., Stubbs C. W., Vanderlinde K., Vieira J. D., Vikhlinin A., Williamson R., Zahn O., Zenteno A., 2015. *ApJS*, **216**, 27.

Bower R. G., Lucey J. R., Ellis R. S., 1992. *MNRAS*, **254**, 601.

Brodwin M., Gonzalez A. H., Moustakas L. A., Eisenhardt P. R., Stanford S. A., Stern D., Brown M. J. I., 2007. *ApJL*, **671**, L93.

Brodwin M., Gonzalez A. H., Stanford S. A., Plagge T., Marrone D. P., Carlstrom J. E., Dey A., Eisenhardt P. R., Fedeli C., Gettings D., Jannuzi B. T., Joy M., Leitch E. M., Mancone C., Snyder G. F., Stern D., Zeimann G., 2012. *ApJ*, **753**, 162.

Brodwin M., Stanford S. A., Gonzalez A. H., Zeimann G. R., Snyder G. F., Mancone C. L., Pope A., Eisenhardt P. R., Stern D., Alberts S., Ashby M. L. N., Brown M. J. I., Chary R.-R., Dey A., Galametz A., Gettings D. P., Jannuzi B. T., Miller E. D., Moustakas J., Moustakas L. A., 2013. *ApJ*, **779**, 138.

Bruzual G., Charlot S., 2003. *MNRAS*, **344**, 1000.

Bunker A. J., Warren S. J., Hewett P. C., Clements D. L., 1995. *MNRAS*, **273**, 513.

Butcher H., Oemler, Jr. A., 1978. *ApJ*, **219**, 18.

Butcher H., Oemler, Jr. A., 1984. *ApJ*, **285**, 426.

Calzetti D., Armus L., Bohlin R. C., Kinney A. L., Koornneef J., Storchi-Bergmann T., 2000. *ApJ*, **533**, 682.

Capak P., Aussel H., Ajiki M., McCracken H. J., Mobasher B., Scoville N., Shopbell P., Taniguchi Y., Thompson D., Tribiano e. a., 2007. *ApJS*, **172**, 99.

Capak P., Mobasher B., Scoville N. Z., McCracken H., Ilbert O., Salvato M., Menéndez-Delmestre K., Aussel H., Carilli C., Civano F., Elvis M., Giavalisco M., Jullo E., Kartaltepe J., Leauthaud A., Koekemoer A. M., Kneib J.-P., LeFloch E., Sanders D. B., Schinnerer E., Shioya Y., Shopbell P., Tanaguchi Y., Thompson D., Willott C. J., 2011. *ApJ*, **730**, 68.

Carlstrom J. E., Ade P. A. R., Aird K. A., Benson B. A., Bleem L. E., Busetti S., Chang C. L., Chauvin E., Cho, H.-M., Crawford T. M., Crites A. T., Dobbs M. A., Halverson N. W., Heimsath S., Holzapfel W. L., Hrubes J. D., Joy M., Keisler R., Lanting T. M., Lee A. T., Leitch E. M., Leong J., Lu W., Lueker M., Luong-Van D., McMahon J. J., Mehl J., Meyer S. S., Mohr J. J., Montroy T. E., Padin S., Plagge T., Pryke C., Ruhl J. E., Schaffer K. K., Schwan D., Shirokoff E., Spieler H. G., Staniszewski Z., Stark A. A., Tucker C., Vanderlinde K., Vieira J. D., Williamson R., 2011. *PASP*, **123**, 568.

Cerulo P., Couch W. J., Lidman C., Demarco R., Huertas-Company M., Mei S., Sánchez-Janssen R., Barrientos L. F., Muñoz R. P., 2016. *MNRAS*, **457**, 2209.

Chabrier G., 2003. *PASP*, **115**, 763.

Chiang Y.-K., Overzier R., Gebhardt K., 2013. *ApJ*, **779**, 127.

Chiang Y.-K., Overzier R., Gebhardt K., 2014. *ApJL*, **782**, L3.

Cimatti A., Daddi E., Renzini A., Cassata P., Vanzella E., Pozzetti L., Cristiani S., Fontana A., Rodighiero G., Mignoli M., Zamorani G., 2004. *Nature*, **430**, 184.

Cirasuolo M., McLure R. J., Dunlop J. S., Almaini O., Foucaud S., Simpson C., 2010. *MNRAS*, **401**, 1166.

Colless M., Dalton G., Maddox S., Sutherland W., Norberg P., Cole S., Bland-Hawthorn J., Bridges T., Cannon R., Collins C., Couch W., Cross N., Deeley K., De Propris R., Driver S. P., Efstathiou G., Ellis R. S., Frenk C. S., Glazebrook K., Jackson C., Lahav O., Lewis I., Lumsden S., Madgwick D., Peacock J. A., Peterson B. A., Price I., Seaborne M., Taylor K., 2001. *MNRAS*, **328**, 1039.

Cooke E. A., Hatch N. A., Muldrew S. I., Rigby E. E., Kurk J. D., 2014. *MNRAS*, **440**, 3262.

Cooke E. A., Hatch N. A., Stern D., Rettura A., Brodwin M., Galametz A., Wylezalek D., Bridge C., Conselice C. J., De Breuck C., Gonzalez A. H., Jarvis M., 2016. *ApJ*, **816(2)**, 83.

Cooper M. C., Newman J. A., Coil A. L., Croton D. J., Gerke B. F., Yan R., Davis M., Faber S. M., Guhathakurta P., Koo D. C., Weiner B. J., Willmer C. N. A., 2007. *MNRAS*, **376**, 1445.

Cooper M. C., Gallazzi A., Newman J. A., Yan R., 2010. *MNRAS*, **402**, 1942.

Couch W. J., Sharples R. M., 1987. *MNRAS*, **229**, 423.

Croom S. M., Smith R. J., Boyle B. J., Shanks T., Miller L., Outram P. J., Loaring N. S., 2004. *MNRAS*, **349**, 1397.

Croton D. J., Springel V., White S. D. M., De Lucia G., Frenk C. S., Gao L., Jenkins A., Kauffmann G., Navarro J. F., Yoshida N., 2006. *MNRAS*, **365**, 11.

Crowl H. H., Kenney J. D. P., van Gorkom J. H., Vollmer B., 2005. *AJ*, **130**, 65.

Cucciati O., Iovino A., Marinoni C., Ilbert O., Bardelli S., Franzetti P., Le Fèvre O., Pollo A., Zamorani G., Cappi A., Guzzo L., McCracken H. J., Meneux B., Scaramella R., Scodeggio M., Tresse L., Zucca E., Bottini D., Garilli B., Le Brun V., Maccagni D., Picat J. P., Vettolani G., Zanichelli A., Adami C., Arnaboldi M., Arnouts S., Bolzonella M., Charlot S., Ciliegi P., Contini T., Foucaud S., Gavignaud I., Marano B., Mazure A., Merighi R., Paltani S., Pellò R., Pozzetti L., Radovich M., Bondi M., Bongiorno A., Busarello G., de la Torre S., Gregorini L., Lamareille F., Mathez G., Mellier Y., Merluzzi P., Ripepi V., Rizzo D., Temporin S., Vergani D., 2006. *A&A*, **458**, 39.

Daddi E., Cimatti A., Renzini A., Fontana A., Mignoli M., Pozzetti L., Tozzi P., Zamorani G., 2004. *ApJ*, **617**, 746.

Daddi E., Dickinson M., Morrison G., Chary R., Cimatti A., Elbaz D., Frayer D., Renzini A., Pope A., Alexander D. M., Bauer F. E., Giavalisco M., Huynh M., Kurk J., Mignoli M., 2007. *ApJ*, **670**, 156.

Dannerbauer H., Kurk J. D., De Breuck C., Wylezalek D., Santos J. S., Koyama Y., Seymour N., Tanaka M., Hatch N., Altieri B., Coia D., Galametz A., Kodama T., Miley G., Röttgering H., Sanchez-Portal M., Valtchanov I., Venemans B., Ziegler B., 2014. *A&A*, **570**, A55.

Davis M., Efstathiou G., Frenk C. S., White S. D. M., 1985. *ApJ*, **292**, 371.

De Breuck C., van Breugel W., Röttgering H., Stern D., Miley G., de Vries W., Stanford S. A., Kurk J., Overzier R., 2001. *AJ*, **121**, 1241.

De Breuck C., van Breugel W., Stanford S. A., Röttgering H., Miley G., Stern D., 2002. *AJ*, **123**, 637.

De Breuck C., Seymour N., Stern D., Willner S. P., Eisenhardt P. R. M., Fazio G. G., Galametz A., Lacy M., Rettura A., Rocca-Volmerange B., Vernet J., 2010. *ApJ*, **725**, 36.

De Lucia G., Blaizot J., 2007. *MNRAS*, **375**, 2.

De Lucia G., Springel V., White S. D. M., Croton D., Kauffmann G., 2006. *MNRAS*, **366**, 499.

De Lucia G., Poggianti B. M., Aragón-Salamanca A., White S. D. M., Zaritsky D., Clowe D., Halliday C., Jablonka P., von der Linden A., Milvang-Jensen B., Pelló R., Rudnick G., Saglia R. P., Simard L., 2007. *MNRAS*, **374**, 809.

De Propris R., Colless M., Driver S. P., Couch W., Peacock J. A., Baldry I. K., Baugh C. M., Bland-Hawthorn J., et al., 2003. *MNRAS*, **342**, 725.

Desai V., Dalcanton J. J., Aragón-Salamanca A., Jablonka P., Poggianti B., Gogarten S. M., Simard L., Milvang-Jensen B., Rudnick G., Zaritsky D., Clowe D., Halliday C., Pelló R., Saglia R., White S., 2007. *ApJ*, **660**, 1151.

Dickinson M., Papovich C., Ferguson H. C., Budavári T., 2003. *ApJ*, **587**, 25.

Donley J. L., Koekemoer A. M., Brusa M., Capak P., Cardamone C. N., Civano F., Ilbert O., Impey C. D., Kartaltepe J. S., Miyaji T., Salvato M., Sanders D. B., Trump J. R., Zamorani G., 2012. *ApJ*, **748**, 142.

Douglas L. S., Bremer M. N., Lehnert M. D., Stanway E. R., Milvang-Jensen B., 2010. *MNRAS*, **409**, 1155.

Dressler A., Oemler, Jr. A., Couch W. J., Smail I., Ellis R. S., Barger A., Butcher H., Poggianti B. M., Sharples R. M., 1997. *ApJ*, **490**, 577.

Dressler A., 1980. *ApJ*, **236**, 351.

Eales S., Dunne L., Clements D., Cooray A., de Zotti G., Dye S., Ivison R., Jarvis M., Lagache G., Maddox S., Negrello M., Serjeant S., Thompson M. A., van Kampen E., Amblard A., Andreani P., Baes M., Beelen A., Bendo G. J., Benford D., Bertoldi F., Bock J., Bonfield D., Boselli A., Bridge C., Buat V., Burgarella D., Carlberg R., Cava A., Chanial P., Charlot S., Christopher N., Coles P., Cortese L., Dariush A., da Cunha E., Dalton G., Danese L., Dannerbauer H., Driver S., Dunlop J., Fan L., Farrah D., Frayer D., Frenk C., Geach J., Gardner J., Gomez H., González-Nuevo J., González-Solares E., Griffin M., Hardcastle M., Hatziminaoglou E., Herranz D., Hughes D., Ibar E., Jeong W.-S., Lacey C., Lapi A., Lawrence A., Lee M., Leeuw L., Liske J., López-Caniego M., Müller T., Nandra K., Panuzzo P., Papageorgiou A., Patanchon G., Peacock J., Pearson C., Phillipps S., Pohlen M., Popescu C., Rawlings S., Rigby E., Rigopoulou M., Robotham A., Rodighiero G., Sansom A., Schulz B., Scott D., Smith D. J. B., Sibthorpe B., Smail I., Stevens J., Sutherland W., Takeuchi T., Tedds J., Temi P., Tuffs R., Trichas M., Vaccari M., Valtchanov I., van der Werf P., Verma A., Vieria J., Vlahakis C., White G. J., 2010. *PASP*, **122**, 499.

Ebeling H., Edge A. C., Mantz A., Barrett E., Henry J. P., Ma C. J., van Speybroeck L., 2010. *MNRAS*, **407**, 83.

Eggen O. J., Lynden-Bell D., Sandage A. R., 1962. *ApJ*, **136**, 748.

Eisenhardt P. R., De Propris R., Gonzalez A. H., Stanford S. A., Wang M., Dickinson M., 2007. *ApJS*, **169**, 225.

Eisenhardt P. R. M., Brodwin M., Gonzalez A. H., Stanford S. A., Stern D., Barmby P., Brown M. J. I., Dawson K., Dey A., Doi M., Galametz A., Jannuzi B. T., Kochanek C. S., Meyers J., Morokuma T., Moustakas L. A., 2008. *ApJ*, **684**, 905.

Elbaz D., Daddi E., Le Borgne D., Dickinson M., Alexander D. M., Chary R., Starck J., Brandt W. N., Kitzbichler M., MacDonald E., Nonino M., Popesso P., Stern D., Vanzella E., 2007. *A&A*, **468**, 33.

Elbaz D., Dickinson M., Hwang H. S., Díaz-Santos T., Magdis G., Magnelli B., Le Borgne D., Galliano F., Pannella M., Chanial P., Armus L., Charmandaris V., Daddi E., Aussel H., Popesso P., Kartaltepe J., Altieri B., Valtchanov I., Coia D., Dannerbauer H., Dasyra K., Leiton R., Mazzarella J., Alexander D. M., Buat V., Burgarella D., Chary R.-R., Gilli R., Ivison R. J., Juneau S., Le Floc'h E., Lutz D., Morrison G. E., Mullaney J. R., Murphy E., Pope A., Scott D., Brodwin M., Calzetti D., Cesarsky C., Charlot S., Dole H., Eisenhardt P., Ferguson H. C., Förster Schreiber N., Frayer D., Giavalisco M., Huynh M., Koekemoer A. M., Papovich C., Reddy N., Surace C., Teplitz H., Yun M. S., Wilson G., 2011. *A&A*, **533**, A119.

Ellis R. S., Smail I., Dressler A., Couch W. J., Oemler, Jr. A., Butcher H., Sharples R. M., 1997. *ApJ*, **483**, 582.

Erben T., Schirmer M., Dietrich J. P., Cordes O., Haberzettl L., Hetterscheidt M., Hildebrandt H., Schmithuesen O., Schneider P., Simon P., Deul E., Hook R. N., Kaiser N., Radovich M., Benoist C., Nonino M., Olsen L. F., Prandoni I., Wichmann R., Zaggia S., Bomans D., Dettmar R. J., Miralles J. M., 2005. *Astronomische Nachrichten*, **326**, 432.

Fanidakis N., Baugh C. M., Benson A. J., Bower R. G., Cole S., Done C., Frenk C. S., 2011. *MNRAS*, **410**, 53.

Fassbender R., Böhringer H., Nastasi A., Šuhada R., Mühlegger M., de Hoon A., Kohnert J., Lamer G., Mohr J. J., Pierini D., Pratt G. W., Quintana H., Rosati P., Santos J. S., Schwope A. D., 2011. *New Journal of Physics*, **13(12)**, 125014.

Fassbender R., Nastasi A., Santos J. S., Lidman C., Verdugo M., Koyama Y., Rosati P., Pierini D., Padilla N., Romeo A. D., Menci N., Bongiorno A., Castellano M., Cerulo P., Fontana A., Galametz A., Grazian A., Lamastra A., Pentericci L., Sommariva V., Strazzullo V., Šuhada R., Tozzi P., 2014. *A&A*, **568**, A5.

Fazio G. G., Hora J. L., Allen L. E., Ashby M. L. N., Barmby P., Deutsch L. K., Huang J.-S., Kleiner S., Marengo M., Megeath S. T., Melnick G. J., Pahre M. A., Patten B. M., Polizotti J., Smith H. A., Taylor R. S., Wang Z., Willner S. P., Hoffmann W. F., Pipher J. L., Forrest W. J., McMurty C. W., McCreight C. R., McKelvey M. E., McMurray R. E., Koch D. G., Moseley S. H., Arendt R. G., Mentzell J. E., Marx C. T., Losch P., Mayman P., Eichhorn W., Krebs D., Jhabvala M., Gezari D. Y., Fixsen D. J., Flores J., Shakoorzadeh K., Jungo R., Hakun C., Workman L., Karpati G., Kichak R., Whitley R., Mann S., Tollestrup E. V., Eisenhardt P., Stern D., Gorjian V., Bhattacharya B., Carey S., Nelson B. O., Glaccum W. J., Lacy M., Lowrance P. J., Laine S., Reach W. T., Stauffer J. A., Surace J. A., Wilson G., Wright E. L., Hoffman A., Domingo G., Cohen M., 2004. *ApJS*, **154**, 10.

Fernandes C. A. C., Jarvis M. J., Rawlings S., Martínez-Sansigre A., Hatziminaoglou E., Lacy M., Page M. J., Stevens J. A., Vardoulaki E., 2011. *MNRAS*, **411**, 1909.

Ferré-Mateu A., Sánchez-Blázquez P., Vazdekis A., de la Rosa I. G., 2014. *ApJ*, **797**, 136.

Foltz R., Rettura A., Wilson G., van der Burg R. F. J., Muzzin A., Lidman C., Demarco R., Nantais J., DeGroot A., Yee H., 2015. *ApJ*, **812**, 138.

Furusawa H., Kosugi G., Akiyama M., Takata T., Sekiguchi K., Tanaka I., Iwata I., Kajisawa M., Yasuda N., Doi M., Ouchi M., Simpson C., Shimasaku K., Yamada T., Furusawa J., Morokuma T., Ishida C. M., Aoki K., Fuse T., Imanishi M., Iye M., Karoji H., Kobayashi N., Kodama T., Komiyama Y., Maeda Y., Miyazaki S., Mizumoto Y., Nakata F., Noumaru J., Ogasawara R., Okamura S., Saito T., Sasaki T., Ueda Y., Yoshida M., 2008. *ApJS*, **176**, 1.

Galametz A., De Breuck C., Vernet J., Stern D., Rettura A., Marmo C., Omont A., Allen M., Seymour N., 2009. *A&A*, **507**, 131.

Galametz A., Stern D., Stanford S. A., De Breuck C., Vernet J., Griffith R. L., Harrison F. A., 2010a. *A&A*, **516**, A101.

Galametz A., Vernet J., De Breuck C., Hatch N. A., Miley G. K., Kodama T., Kurk J., Overzier R. A., Rettura A., Röttgering H. J. A., Seymour N., Venemans B. P., Zirm A. W., 2010b. *A&A*, **522**, A58.

Galametz A., Stern D., De Breuck C., Hatch N., Mayo J., Miley G., Rettura A., Seymour N., Stanford S. A., Vernet J., 2012. *ApJ*, **749**, 169.

Galametz A., Stern D., Pentericci L., De Breuck C., Vernet J., Wylezalek D., Fassbender R., Hatch N., Kurk J., Overzier R., Rettura A., Seymour N., 2013. *A&A*, **559**, A2.

Gao L., Springel V., White S. D. M., 2005. *MNRAS*, **363**, L66.

Garn T., Best P. N., 2010. *MNRAS*, **409**, 421.

Giovanelli R., Haynes M. P., Chincarini G. L., 1986. *ApJ*, **300**, 77.

Gladders M. D., Yee H. K. C., 2005. *ApJS*, **157**, 1.

Gladders M. D., Yee H. K. C., Majumdar S., Barrientos L. F., Hoekstra H., Hall P. B., Infante L., 2007. *ApJ*, **655**, 128.

Gobat R., Daddi E., Onodera M., Finoguenov A., Renzini A., Arimoto N., Bouwens R., Brusa M., Chary R.-R., Cimatti A., Dickinson M., Kong X., Mignoli M., 2011. *A&A*, **526**, A133.

Gonzalez A. H., Stanford S. A., Brodwin M., Fedeli C., Dey A., Eisenhardt P. R. M., Mancone C., Stern D., Zeimann G., 2012. *ApJ*, **753**, 163.

Griffin M. J., Abergel A., Abreu A., Ade P. A. R., André P., Augueres J.-L., Babbedge T., Bae Y., Baillie T., Baluteau J.-P., Barlow M. J., Bendo G., Benielli D., Bock J. J., Bonhomme P., Brisbin D., Brockley-Blatt C., Caldwell M., Cara C., Castro-Rodriguez N., Cerulli R., Chanial P., Chen S., Clark E., Clements D. L., Clerc L., Coker J., Communal D., Conversi L., Cox P., Crumb D., Cunningham C., Daly F., Davis G. R., de Antoni P., Delderfield J., Devin N., di Giorgio A., Didschuns I., Dohlen K., Donati M., Dowell A., Dowell C. D., Duband L., Dumaye L., Emery R. J., Ferlet M., Ferrand D., Fontignie J., Fox M., Franceschini A., Frerking M., Fulton T., Garcia J., Gastaud R., Gear W. K., Glenn J., Goizel A., Griffin D. K., Grundy T., Guest S., Guillemet L., Hargrave P. C., Harwit M., Hastings P., Hatziminaoglou

E., Herman M., Hinde B., Hristov V., Huang M., Imhof P., Isaak K. J., Israelsson U., Ivison R. J., Jennings D., Kiernan B., King K. J., Lange A. E., Latter W., Laurent G., Laurent P., Leeks S. J., Lellouch E., Levenson L., Li B., Li J., Lilienthal J., Lim T., Liu S. J., Lu N., Madden S., Mainetti G., Marliani P., McKay D., Mercier K., Molinari S., Morris H., Moseley H., Mulder J., Mur M., Naylor D. A., Nguyen H., O'Halloran B., Oliver S., Olofsson G., Olofsson H.-G., Orfei R., Page M. J., Pain I., Panuzzo P., Papageorgiou A., Parks G., Parr-Burman P., Pearce A., Pearson C., Pérez-Fournon I., Pinsard F., Pisano G., Podosek J., Pohlen M., Polehampton E. T., Pouliquen D., Rigopoulou D., Rizzo D., Roseboom I. G., Roussel H., Rowan-Robinson M., Rownd B., Saraceno P., Sauvage M., Savage R., Savini G., Sawyer E., Scharmberg C., Schmitt D., Schneider N., Schulz B., Schwartz A., Shafer R., Shupe D. L., Sibthorpe B., Sidher S., Smith A., Smith A. J., Smith D., Spencer L., Stobie B., Sudiwala R., Sukhatme K., Surace C., Stevens J. A., Swinyard B. M., Trichas M., Tourette T., Triou H., Tseng S., Tucker C., Turner A., Vaccari M., Valtchanov I., Vigroux L., Virique E., Voellmer G., Walker H., Ward R., Waskett T., Weilert M., Wesson R., White G. J., Whitehouse N., Wilson C. D., Winter B., Woodcraft A. L., Wright G. S., Xu C. K., Zavagno A., Zemcov M., Zhang L., Zonca E., 2010. *A&A*, **518**, L3.

Gunn J. E., Gott, III J. R., 1972. *ApJ*, **176**, 1.

Gunn J. E., Hoessel J. G., Oke J. B., 1986. *ApJ*, **306**, 30.

Guo Y., McIntosh D. H., Mo H. J., Katz N., van den Bosch F. C., Weinberg M., Weinmann S. M., Pasquali A., Yang X., 2009. *MNRAS*, **398**, 1129.

Guo Q., White S., Boylan-Kolchin M., De Lucia G., Kauffmann G., Lemson G., Li C., Springel V., Weinmann S., 2011. *MNRAS*, **413**, 101.

Hartley W. G., Almaini O., Mortlock A., Conselice C. J., Grützbauch R., Simpson C., Bradshaw E. J., Chuter R. W., Foucaud S., Cirasuolo M., Dunlop J. S., McLure R. J., Pearce H. J., 2013. *MNRAS*, **431**, 3045.

Hasselfield M., Hilton M., Marriage T. A., Addison G. E., Barrientos L. F., Battaglia N., Battistelli E. S., Bond J. R., Crichton D., Das S., Devlin M. J., Dicker S. R., Dunkley J., Dünner R., Fowler J. W., Gralla M. B., Hajian A., Halpern M., Hincks A. D., Hlozek R., Hughes J. P., Infante L., Irwin K. D., Kosowsky A., Marsden D., Menanteau F., Moodley K., Niemack M. D., Nolta M. R., Page L. A., Partridge B., Reese E. D., Schmitt B. L., Sehgal N., Sherwin B. D., Sievers J., Sifón C., Spergel D. N., Staggs S. T., Swetz D. S., Switzer E. R., Thornton R., Trac H., Wollack E. J., 2013. *JCAP*, **7**, 8.

Hatch N. A., De Breuck C., Galametz A., Miley G. K., Overzier R. A., Röttgering H. J. A., Doherty M., Kodama T., Kurk J. D., Seymour N., Venemans B. P., Vernet J., Zirm A. W., 2011a. *MNRAS*, **410**, 1537.

Hatch N. A., Kurk J. D., Pentericci L., Venemans B. P., Kuiper E., Miley G. K., Röttgering H. J. A., 2011b. *MNRAS*, **415**, 2993.

Hatch N. A., Wylezalek D., Kurk J. D., Stern D., De Breuck C., Jarvis M. J., Galametz A., Gonzalez A. H., Hartley W. G., Mortlock A., Seymour N., Stevens J. A., 2014. *MNRAS*, **445**, 280.

Hatch N. A., Muldrew S. I., Cooke E. A., Hartley W. G., Almaini O., Simpson C. J., Conselice C. J., 2016. *MNRAS*, **459**, 387.

Hayashi M., Kodama T., Tadaki K.-i., Koyama Y., Tanaka I., 2012. *ApJ*, **757**, 15.

Hilton M., Lloyd-Davies E., Stanford S. A., Stott J. P., Collins C. A., Romer A. K., Hosmer M., Hoyle B., Kay S. T., Liddle A. R., Mehrtens N., Miller C. J., Sahlén M., Viana P. T. P., 2010. *ApJ*, **718**, 133.

Holden B. P., Stanford S. A., Eisenhardt P., Dickinson M., 2004. *AJ*, **127**, 2484.

Hook I. M., Jørgensen I., Allington-Smith J. R., Davies R. L., Metcalfe N., Murowinski R. G., Crampton D., 2004. *PASP*, **116**, 425.

Hopkins A. M., Beacom J. F., 2006. *ApJ*, **651**, 142.

Hubble E., Humason M. L., 1931. *ApJ*, **74**, 43.

Huertas-Company M., Shankar F., Mei S., Bernardi M., Aguerri J. A. L., Meert A., Vikram V., 2013. *ApJ*, **779**, 29.

Husband K., Bremer M. N., Stott J. P., Murphy D. N. A., 2016. *arXiv:1606.07452*.

Jaffé Y. L., Aragón-Salamanca A., Kuntschner H., Bamford S., Hoyos C., De Lucia G., Halliday C., Milvang-Jensen B., Poggianti B., Rudnick G., Saglia R. P., Sanchez-Blazquez P., Zaritsky D., 2011. *MNRAS*, **417**, 1996.

Jannuzi B. T., Dey A., 1999. In: *Photometric Redshifts and the Detection of High Redshift Galaxies*, 111, eds Weymann R., Storrie-Lombardi L., Sawicki M., Brunner R.

Kajisawa M., Yamada T., 2006. *ApJ*, **650**, 12.

Kashikawa N., Kitayama T., Doi M., Misawa T., Komiyama Y., Ota K., 2007. *ApJ*, **663**, 765.

Kauffmann G., Heckman T. M., White S. D. M., Charlot S., Tremonti C., Brinchmann J., Bruzual G., Peng E. W., Seibert M., Bernardi M., Blanton M., Brinkmann J., Castander F., Csábai I., Fukugita M., Ivezic Z., Munn J. A., Nichol R. C., Padmanabhan N., Thakar A. R., Weinberg D. H., York D., 2003. *MNRAS*, **341**, 33.

Kauffmann G., White S. D. M., Heckman T. M., Ménard B., Brinchmann J., Charlot S., Tremonti C., Brinkmann J., 2004. *MNRAS*, **353**, 713.

Kenney J. D. P., van Gorkom J. H., Vollmer B., 2004. *AJ*, **127**, 3361.

Kennicutt, Jr. R. C., 1998. *ARAA*, **36**, 189.

Kissler-Patig M., Pirard J., Casali M., Moorwood A., Ageorges N., Alves de Oliveira C., Baksai P., Bedin L. R., Bendek E., Biereichel P., Delabre B., Dorn R., Esteves R., et al., 2008. *A&A*, **491**, 941.

Knebe A., Knollmann S. R., Muldrew S. I., Pearce F. R., Aragon-Calvo M. A., Ascasibar Y., Behroozi P. S., Ceverino D., Colombi S., Diemand J., Dolag K., Falck B. L., Fasel P., Gardner J., Gottlöber S., Hsu C.-H., Iannuzzi F., Klypin A., Lukić Z., Maciejewski M., McBride C., Neyrinck M. C., Planelles S., Potter D., Quilis V., Rasera Y., Read J. I., Ricker P. M., Roy F., Springel V., Stadel J., Stinson G., Sutter P. M., Turchaninov V., Tweed D., Yepes G., Zemp M., 2011. *MNRAS*, **415**, 2293.

Kodama T., Arimoto N., 1997. *A&A*, **320**, 41.

Kodama T., Bower R. G., Bell E. F., 1999. *MNRAS*, **306**, 561.

Kodama T., Tanaka I., Kajisawa M., Kurk J., Venemans B., De Breuck C., Vernet J., Lidman C., 2007. *MNRAS*, **377**, 1717.

Kovač K., Lilly S. J., Knobel C., Bschorr T. J., Peng Y., Carollo C. M., Contini T., Kneib J.-P., Le Févre O., Mainieri V., Renzini A., Scodeggio M., Zamorani G., Bardelli S., Bolzonella M., Bongiorno A., Caputi K., Cucciati O., de la Torre S., de Ravel L., Franzetti P., Garilli B., Iovino A., Kampczyk P., Lamareille F., Le Borgne J.-F., Le Brun V., Maier C., Mignoli M., Oesch P., Pello R., Montero E. P., Presotto V., Silverman J., Tanaka M., Tasca L., Tresse L., Vergani D., Zucca E., Aussel H., Koekemoer A. M., Le Floc'h E., Moresco M., Pozzetti L., 2014. *MNRAS*, **438**, 717.

Koyama Y., Kodama T., Tadaki K.-i., Hayashi M., Tanaka M., Smail I., Tanaka I., Kurk J., 2013a. *MNRAS*, **428**, 1551.

Koyama Y., Smail I., Kurk J., Geach J. E., Sobral D., Kodama T., Nakata F., Swinbank A. M., Best P. N., Hayashi M., Tadaki K.-i., 2013b. *MNRAS*, **434**, 423.

Kriek M., van Dokkum P. G., Franx M., Illingworth G. D., Marchesini D., Quadri R., Rudnick G., Taylor E. N., Förster Schreiber N. M., Gawiser E., Labbé I., Lira P., Wuyts S., 2008. *ApJ*, **677**, 219.

Kriek M., van Dokkum P. G., Labbé I., Franx M., Illingworth G. D., Marchesini D., Quadri R. F., 2009. *ApJ*, **700**, 221.

Kriek M., Labbé I., Conroy C., Whitaker K. E., van Dokkum P. G., Brammer G. B., Franx M., Illingworth G. D., Marchesini D., Muzzin A., Quadri R. F., Rudnick G., 2010. *ApJL*, **722**, L64.

Kroupa P., 2001. *MNRAS*, **322**, 231.

Kuiper E., Hatch N. A., Röttgering H. J. A., Miley G. K., Overzier R. A., Venemans B. P., De Breuck C., Croft S., Kajisawa M., Kodama T., Kurk J. D., Pentericci L., Stanford S. A., Tanaka I., Zirm A. W., 2010. *MNRAS*, **405**, 969.

Kuiper E., Hatch N. A., Venemans B. P., Miley G. K., Röttgering H. J. A., Kurk J. D., Overzier R. A., Pentericci L., Bland-Hawthorn J., Cepa J., 2011. *MNRAS*, **417**, 1088.

Kulas K. R., McLean I. S., Shapley A. E., Steidel C. C., Konidaris N. P., Matthews K., Mace G. N., Rudie G. C., Trainor R. F., Reddy N. A., 2013. *ApJ*, **774**, 130.

Kurk J. D., Röttgering H. J. A., Pentericci L., Miley G. K., van Breugel W., Carilli C. L., Ford H., Heckman T., McCarthy P., Moorwood A., 2000. *A&A*, **358**, L1.

Kurk J. D., Pentericci L., Overzier R. A., Röttgering H. J. A., Miley G. K., 2004a. *A&A*, **428**, 817.

Kurk J. D., Pentericci L., Röttgering H. J. A., Miley G. K., 2004b. *A&A*, **428**, 793.

Kurk J., Cimatti A., Zamorani G., Halliday C., Mignoli M., Pozzetti L., Daddi E., Rosati P., Dickinson M., Bolzonella M., Cassata P., Renzini A., Franceschini A., Rodighiero G., Berta S., 2009. *A&A*, **504**, 331.

Lacy M., Rawlings S., Hill G. J., Bunker A. J., Ridgway S. E., Stern D., 1999. *MNRAS*, **308**, 1096.

Lani C., Almaini O., Hartley W. G., Mortlock A., Häußler B., Chuter R. W., Simpson C., van der Wel A., Grützbauch R., Conselice C. J., Bradshaw E. J., Cooper M. C., Faber S. M., Grogin N. A., Kocevski D. D., Koekemoer A. M., Lai K., 2013. *MNRAS*, **435**, 207.

Lee S.-K., Im M., Kim J.-W., Lotz J., McPartland C., Peth M., Koekemoer A., 2015. *ApJ*, **810**, 90.

Lidman C., Rosati P., Tanaka M., Strazzullo V., Demarco R., Mullis C., Ageorges N., Kissler-Patig M., Petr-Gotzens M. G., Selman F., 2008. *A&A*, **489**, 981.

Lilly S. J., Longair M. S., 1984. *MNRAS*, **211**, 833.

Lonsdale C. J. e. a., 2003. *PASP*, **115**, 897.

Lotz J. M., Jonsson P., Cox T. J., Croton D., Primack J. R., Somerville R. S., Stewart K., 2011. *ApJ*, **742**, 103.

Lotz J. M., Papovich C., Faber S. M., Ferguson H. C., Grogin N., Guo Y., Kocevski D., Koekemoer A. M., Lee K.-S., McIntosh D., Momcheva I., Rudnick G., Saintonge A., Tran K.-V., van der Wel A., Willmer C., 2013. *ApJ*, **773**, 154.

Mancone C. L., Gonzalez A. H., 2012. *PASP*, **124**, 606.

Mancone C. L., Gonzalez A. H., Brodwin M., Stanford S. A., Eisenhardt P. R. M., Stern D., Jones C., 2010. *ApJ*, **720**, 284.

Mancone C. L., Baker T., Gonzalez A. H., Ashby M. L. N., Stanford S. A., Brodwin M., Eisenhardt P. R. M., Snyder G., Stern D., Wright E. L., 2012. *ApJ*, **761**, 141.

Maraston C., Daddi E., Renzini A., Cimatti A., Dickinson M., Papovich C., Pasquali A., Pirzkal N., 2006. *ApJ*, **652**, 85.

Maraston C., 2005. *MNRAS*, **362**, 799.

Marriage T. A., Acquaviva V., Ade P. A. R., Aguirre P., Amiri M., Appel J. W., Barrientos L. F., Battistelli E. S., Bond J. R., Brown B., Burger B., Chervenak J., Das S., Devlin M. J., Dicker S. R., Bertrand Doriese W., Dunkley J., Dünner R., Essinger-Hileman T., Fisher R. P., Fowler J. W., Hajian A., Halpern M., Hasselfield M., Hernández-Monteagudo C., Hilton G. C., Hilton M., Hincks A. D., Hlozek R., Huffenberger K. M., Handel Hughes D., Hughes J. P., Infante L., Irwin K. D., Baptiste

Juin J., Kaul M., Klein J., Kosowsky A., Lau J. M., Limon M., Lin, Y.-T., Lupton R. H., Marsden D., Martocci K., Mauskopf P., Menanteau F., Moodley K., Moseley H., Netterfield C. B., Niemack M. D., Nolta M. R., Page L. A., Parker L., Partridge B., Quintana H., Reese E. D., Reid B., Sehgal N., Sherwin B. D., Sievers J., Spergel D. N., Staggs S. T., Swetz D. S., Switzer E. R., Thornton R., Trac H., Tucker C., Warne R., Wilson G., Wollack E., Zhao Y., 2011. *ApJ*, **737**, 61.

Martini P., Miller E. D., Brodwin M., Stanford S. A., Gonzalez A. H., Bautz M., Hickox R. C., Stern D., Eisenhardt P. R., Galametz A., Norman D., Jannuzi B. T., Dey A., Murray S., Jones C., Brown M. J. I., 2013. *ApJ*, **768**, 1.

Matthews T. A., Morgan W. W., Schmidt M., 1964. *ApJ*, **140**, 35.

Mayo J. H., Vernet J., De Breuck C., Galametz A., Seymour N., Stern D., 2012. *A&A*, **539**, A33.

McCarthy P. J., Kapahi V. K., van Breugel W., Subrahmanya C. R., 1990. *AJ*, **100**, 1014.

McCracken H. J., Milvang-Jensen B., Dunlop J., Franx M., Fynbo J. P. U., Le Fèvre O., Holt J., Caputi K. I., Goranova Y., Buitrago F., Emerson J. P., Freudling W., Hudelot P., López-Sanjuan C., Magnard F., Mellier Y., Møller P., Nilsson K. K., Sutherland W., Tasca L., Zabl J., 2012. *A&A*, **544**, A156.

Mei S., Blakeslee J. P., Stanford S. A., Holden B. P., Rosati P., Strazzullo V., Homeier N., Postman M., Franx M., Rettura A., Ford H., Illingworth G. D., Ettori S., Bouwens R. J., Demarco R., Martel A. R., Clampin M., Hartig G. F., Eisenhardt P., Ardila D. R., Bartko F., Benítez N., Bradley L. D., Broadhurst T. J., Brown R. A., Burrows C. J., Cheng E. S., Cross N. J. G., Feldman P. D., Golimowski D. A., Goto T., Gronwall C., Infante L., Kimble R. A., Krist J. E., Lesser M. P., Menanteau F., Meurer G. R., Miley G. K., Motta V., Sirianni M., Sparks W. B., Tran H. D., Tsvetanov Z. I., White R. L., Zheng W., 2006. *ApJ*, **639**, 81.

Mei S., Holden B. P., Blakeslee J. P., Ford H. C., Franx M., Homeier N. L., Illingworth G. D., Jee M. J., Overzier R., Postman M., Rosati P., Van der Wel A., Bartlett J. G., 2009. *ApJ*, **690**, 42.

Mei S., Scarlata C., Pentericci L., Newman J. A., Weiner B. J., Ashby M. L. N., Castellano M., Conselice C. J., Finkelstein S. L., Galametz A., Grogin N. A., Koekemoer A. M., Huertas-Company M., Lani C., Lucas R. A., Papovich C., Rafelski M., Teplitz H. I., 2015. *ApJ*, **804**, 117.

Mihos J. C., Hernquist L., 1994. *ApJL*, **425**, L13.

Miley G., De Breuck C., 2008. *A&AR*, **15**, 67.

Moore B., Lake G., Katz N., 1998. *ApJ*, **495**, 139.

Moorwood A., Cuby J.-G., Lidman C., 1998. *The Messenger*, **91**, 9.

Mortlock A., Conselice C. J., Hartley W. G., Ownsworth J. R., Lani C., Bluck A. F. L., Almaini O., Duncan K., Wel A. v. d., Koekemoer A. M., Dekel A., Davé R., Ferguson H. C., de Mello D. F., Newman J. A., Faber S. M., Grogin N. A., Kocevski D. D., Lai K., 2013. *MNRAS*, **433**, 1185.

Muldrew S. I., Croton D. J., Skibba R. A., Pearce F. R., Ann H. B., Baldry I. K., Brough S., Choi Y.-Y., Conselice C. J., Cowan N. B., Gallazzi A., Gray M. E., Grützbauch R., Li I.-H., Park C., Pilipenko S. V., Podgorzec B. J., Robotham A. S. G., Wilman D. J., Yang X., Zhang Y., Zibetti S., 2012. *MNRAS*, **419**, 2670.

Muldrew S. I., Hatch N. A., Cooke E. A., 2015. *MNRAS*, **452**, 2528.

Muldrew S. I., Pearce F. R., Power C., 2011. *MNRAS*, **410**, 2617.

Mundy C. J., Conselice C. J., Ownsworth J. R., 2015. *MNRAS*, **450**, 3696.

Muzzin A., Wilson G., Lacy M., Yee H. K. C., Stanford S. A., 2008. *ApJ*, **686**, 966.

Muzzin A., Wilson G., Yee H. K. C., Hoekstra H., Gilbank D., Surace J., Lacy M., Blindert K., Majumdar S., Demarco R., Gardner J. P., Gladders M., Lonsdale C., 2009. *ApJ*, **698**, 1934.

Muzzin A., Wilson G., Yee H. K. C., Gilbank D., Hoekstra H., Demarco R., Balogh M., van Dokkum P., Franx M., Ellingson E., Hicks A., Nantais J., Noble A., Lacy M., Lidman C., Rettura A., Surace J., Webb T., 2012. *ApJ*, **746**, 188.

Muzzin A., Wilson G., Demarco R., Lidman C., Nantais J., Hoekstra H., Yee H. K. C., Rettura A., 2013. *ApJ*, **767**, 39.

Nair P. B., van den Bergh S., Abraham R. G., 2010. *ApJ*, **715**, 606.

Newman A. B., Ellis R. S., Andreon S., Treu T., Raichoor A., Trinchieri G., 2014. *ApJ*, **788**, 51.

Oemler, Jr. A., 1974. *ApJ*, **194**, 1.

Orsi Á. A., Fanidakis N., Lacey C. G., Baugh C. M., 2016. *MNRAS*, **456**, 3827.

Overzier R. A., Harris D. E., Carilli C. L., Pentericci L., Röttgering H. J. A., Miley G. K., 2005. *A&A*, **433**, 87.

Overzier R. A., Bouwens R. J., Cross N. J. G., Venemans B. P., Miley G. K., Zirm A. W., Benítez N., Blakeslee J. P., Coe D., Demarco R., Ford H. C., Homeier N. L., 2008. *ApJ*, **673**, 143.

Overzier R. A., Shu X., Zheng W., Rettura A., Zirm A., Bouwens R. J., Ford H., Illingworth G. D., Miley G. K., Venemans B., White R. L., 2009. *ApJ*, **704**, 548.

Papovich C., Momcheva I., Willmer C. N. A., Finkelstein K. D., Finkelstein S. L., Tran K.-V., Brodwin M., Dunlop J. S., Farrah D., Khan S. A., Lotz J., McCarthy P., McLure R. J., Rieke M., Rudnick G., Sivanandam S., Pacaud F., Pierre M., 2010. *ApJ*, **716**, 1503.

Papovich C., Bassett R., Lotz J. M., van der Wel A., Tran K.-V., Finkelstein S. L., Bell E. F., Conselice C. J., Dekel A., Dunlop J. S., Guo Y., Faber S. M., Farrah D., Ferguson H. C., Finkelstein K. D., Häussler B., Kocevski D. D., Koekemoer A. M., Koo D. C., McGrath E. J., McLure R. J., McIntosh D. H., Momcheva I., Newman J. A., Rudnick G., Weiner B., Willmer C. N. A., Wuyts S., 2012. *ApJ*, **750**, 93.

Papovich C., 2008. *ApJ*, **676**, 206.

Peng Y.-j., Lilly S. J., Kovač K., Bolzonella M., Pozzetti L., Renzini A., Zamorani G., Ilbert O., Knobel C., Iovino A., Maier C., Cucciati O., Tasca L., Carollo C. M., Silverman J., Kampczyk P., de Ravel L., Sanders D., Scoville N., Contini T., Mainieri V., Scodeggio M., Kneib J.-P., Le Fèvre O., Bardelli S., Bongiorno A., Caputi K., Coppa G., de la Torre S., Franzetti P., Garilli B., Lamareille F., Le Borgne J.-F., Le Brun V., Mignoli M., Perez Montero E., Pello R., Ricciardelli E., Tanaka M., Tresse L., Vergani D., Welikala N., Zucca E., Oesch P., Abbas U., Barnes L., Bordoloi R., Bottini D., Cappi A., Cassata P., Cimatti A., Fumana M., Hasinger G., Koekemoer A., Leauthaud A., Maccagni D., Marinoni C., McCracken H., Memeo P., Meneux B., Nair P., Porciani C., Presotto V., Scaramella R., 2010. *ApJ*, **721**, 193.

Pentericci L., Kurk J. D., Röttgering H. J. A., Miley G. K., van Breugel W., Carilli C. L., Ford H., Heckman T., McCarthy P., Moorwood A., 2000. *A&A*, **361**, L25.

Pentericci L., McCarthy P. J., Röttgering H. J. A., Miley G. K., van Breugel W. J. M., Fosbury R., 2001. *ApJS*, **135**, 63.

Pickles A. J., 1998. *PASP*, **110**, 863.

Pierre M., Clerc N., Maughan B., Pacaud F., Papovich C., Willmer C. N. A., 2012. *A&A*, **540**, A4.

Piffaretti R., Arnaud M., Pratt G. W., Pointecouteau E., Melin J.-B., 2011. *A&A*, **534**, A109.

Pillepich A., Porciani C., Reiprich T. H., 2012. *MNRAS*, **422**, 44.

Planck Collaboration, Ade P. A. R., Aghanim N., Alves M. I. R., Armitage-Caplan C., Arnaud M., Ashdown M., Atrio-Barandela F., Aumont J., Aussel H., et al., 2014. *A&A*, **571**, A1.

Planck Collaboration, Ade P. A. R., Aghanim N., Arnaud M., Ashdown M., Aumont J., Baccigalupi C., Banday A. J., Barreiro R. B., Barrena R., et al., 2015. *ArXiv e-prints*.

Poggianti B. M., Bridges T. J., Carter D., Mobasher B., Doi M., Iye M., Kashikawa N., Komiyama Y., Okamura S., Sekiguchi M., Shimasaku K., Yagi M., Yasuda N., 2001. *ApJ*, **563**, 118.

Poggianti B. M., Fasano G., Bettoni D., Cava A., Dressler A., Vanzella E., Varela J., Couch W. J., D'Onofrio M., Fritz J., Kjaergaard P., Moles M., Valentinuzzi T., 2009. *ApJL*, **697**, L137.

Postman M., Franx M., Cross N. J. G., Holden B., Ford H. C., Illingworth G. D., Goto T., Demarco R., Rosati P., Blakeslee J. P., Tran K.-V., Benítez N., Clampin M., Hartig G. F., Homeier N., Ardila D. R., Bartko F., Bouwens R. J., Bradley L. D., Broadhurst T. J., Brown R. A., Burrows C. J., Cheng E. S., Feldman P. D., Golimowski D. A., Gronwall C., Infante L., Kimble R. A., Krist J. E., Lesser M. P., Martel A. R., Mei S., Menanteau F., Meurer G. R., Miley G. K., Motta V., Sirianni M., Sparks W. B., Tran H. D., Tsvetanov Z. I., White R. L., Zheng W., 2005. *ApJ*, **623**, 721.

Quadri R. F., Williams R. J., Franx M., Hildebrandt H., 2012. *ApJ*, **744**, 88.

Rettura A., Martinez-Manso J., Stern D., Mei S., Ashby M. L. N., Brodwin M., Gettings D., Gonzalez A. H., Stanford S. A., Bartlett J. G., 2014. *ApJ*, **797**, 109.

Retzlaff J., Rosati P., Dickinson M., Vandame B., Rité C., Nonino M., Cesarsky C., GOODS Team, 2010. *A&A*, **511**, A50+.

Rieke G. H., Young E. T., Engelbracht C. W., Kelly D. M., Low F. J., Haller E. E., Beeman J. W., Gordon K. D., Stansberry J. A., Misselt K. A., Cadien J., Morrison J. E., Rivlis G., Latter W. B., Noriega-Crespo A., Padgett D. L., Stapelfeldt K. R., Hines D. C., Egami E., Muzerolle J., Alonso-Herrero A., Blaylock M., Dole H., Hinz J. L., Le Floc'h E., Papovich C., Pérez-González P. G., Smith P. S., Su K. Y. L., Bennett L., Frayer D. T., Henderson D., Lu N., Masci F., Pesenson M., Rebull L., Rho J., Keene J., Stolovy S., Wachter S., Wheaton W., Werner M. W., Richards P. L., 2004. *ApJS*, **154**, 25.

Rieke G. H., Alonso-Herrero A., Weiner B. J., Pérez-González P. G., Blaylock M., Donley J. L., Marcillac D., 2009. *ApJ*, **692**, 556.

Rigby E. E., Hatch N. A., Röttgering H. J. A., Sibthorpe B., Chiang Y. K., Overzier R., Herbonnet R., Borgani S., Clements D. L., Dannerbauer H., De Breuck C., De Lucia G., Kurk J., Maschietto F., Miley G., Saro A., Seymour N., Venemans B., 2014. *MNRAS*, **437**, 1882.

Robotham A. S. G., Norberg P., Driver S. P., Baldry I. K., Bamford S. P., Hopkins A. M., Liske J., Loveday J., Merson A., Peacock J. A., Brough S., Cameron E., Conselice C. J., Croom S. M., Frenk C. S., Gunawardhana M., Hill D. T., Jones D. H., Kelvin L. S., Kuijken K., Nichol R. C., Parkinson H. R., Pimbblet K. A., Phillipps S., Popescu C. C., Prescott M., Sharp R. G., Sutherland W. J., Taylor E. N., Thomas D., Tuffs R. J., van Kampen E., Wijesinghe D., 2011. *MNRAS*, **416**, 2640.

Rodighiero G., Daddi E., Baronchelli I., Cimatti A., Renzini A., Aussel H., Popesso P., Lutz D., Andreani P., Berta S., Cava A., Elbaz D., Feltre A., Fontana A., Förster Schreiber N. M., Franceschini A., Genzel R., Grazian A., Gruppioni C., Ilbert O., Le Floch E., Magdis G., Magliocchetti M., Magnelli B., Maiolino R., McCracken H., Nordon R., Poglitsch A., Santini P., Pozzi F., Riguccini L., Tacconi L. J., Wuyts S., Zamorani G., 2011. *ApJL*, **739**, L40.

Roettgering H. J. A., van Ojik R., Miley G. K., Chambers K. C., van Breugel W. J. M., de Koff S., 1997. *A&A*, **326**, 505.

Rosati P., Della Ceca R., Norman C., Giacconi R., 1998. *ApJL*, **492**, L21.

Rudnick G., von der Linden A., Pelló R., Aragón-Salamanca A., Marchesini D., Clowe D., De Lucia G., Halliday C., Jablonka P., Milvang-Jensen B., Poggianti B., Saglia R., Simard L., White S., Zaritsky D., 2009. *ApJ*, **700**, 1559.

Rudnick G. H., Tran K.-V., Papovich C., Momcheva I., Willmer C., 2012. *ApJ*, **755**, 14.

Rujopakarn W., Rieke G. H., Weiner B. J., Pérez-González P., Rex M., Walth G. L., Kartaltepe J. S., 2013. *ApJ*, **767**, 73.

Saintonge A., Tran K.-V. H., Holden B. P., 2008. *ApJL*, **685**, L113.

Salpeter E. E., 1955. *ApJ*, **121**, 161.

Santini P., Fontana A., Grazian A., Salimbeni S., Fiore F., Fontanot F., Boutsia K., Castellano M., Cristiani S., de Santis C., Gallozzi S., Giallongo E., Menci N., Nonino M., Paris D., Pentericci L., Vanzella E., 2009. *A&A*, **504**, 751.

Santos J. S., Altieri B., Tanaka M., Valtchanov I., Saintonge A., Dickinson M., Foucaud S., Kodama T., Rawle T. D., Tadaki K., 2014. *MNRAS*, **438**, 2565.

Santos J. S., Altieri B., Valtchanov I., Nastasi A., Böhringer H., Cresci G., Elbaz D., Fassbender R., Rosati P., Tozzi P., Verdugo M., 2015. *MNRAS*, **447**, L65.

Schechter P., 1976. *ApJ*, **203**, 297.

Schirmer M., 2013. *ApJS*, **209**, 21.

Schneider D. P., Richards G. T., Hall P. B., Strauss M. A., Anderson S. F., Boroson T. A., Ross N. P., Shen Y., Brandt W. N., Fan X., Inada N., Jester S., Knapp G. R., Krawczyk C. M., Thakar A. R., Vanden Berk D. E., 2010. *AJ*, **139**, 2360.

Seymour N., Stern D., De Breuck C., Vernet J., Rettura A., Dickinson M., Dey A., Eisenhardt P., Fosbury R., Lacy M., McCarthy e. a., 2007. *ApJS*, **171**, 353.

Seymour N., Altieri B., De Breuck C., Barthel P., Coia D., Conversi L., Dannerbauer H., Dey A., Dickinson M., 2012. *ApJ*, **755**, 146.

Shapley A. E., Steidel C. C., Erb D. K., Reddy N. A., Adelberger K. L., Pettini M., Barmby P., Huang J., 2005. *ApJ*, **626**, 698.

Siana B., Smail I., Swinbank A. M., Richard J., Teplitz H. I., Coppin K. E. K., Ellis R. S., Stark D. P., Kneib J.-P., Edge A. C., 2009. *ApJ*, **698**, 1273.

Simpson C., Eisenhardt P., 1999. *PASP*, **111**, 691.

Simpson C., Rawlings S., 2002. *MNRAS*, **334**, 511.

Smail I., Geach J. E., Swinbank A. M., Tadaki K., Arumugam V., Hartley W., Almaini O., Bremer M. N., Chapin E., Chapman S. C., Danielson A. L. R., Edge A. C., Scott D., Simpson C. J., Simpson J. M., Conselice C., Dunlop J. S., Ivison R. J., Karim A., Kodama T., Mortlock A., Robson E. I., Roseboom I., Thomson A. P., van der Werf P. P., Webb T. M. A., 2014. *ApJ*, **782**, 19.

Smith R. J., Hudson M. J., Lucey J. R., Nelan J. E., Wegner G. A., 2006. *MNRAS*, **369**, 1419.

Smith D. J. B., Hardcastle M. J., Jarvis M. J., Maddox S. J., Dunne L., Bonfield D. G., Eales S., Serjeant S., Thompson M. A., Baes M., Clements D. L., Cooray A., De Zotti G., Gonzàlez-Nuevo J., van der Werf P., Virdee J., Bourne N., Dariush A., Hopwood R., Ibar E., Valiante E., 2013. *MNRAS*, **436**, 2435.

Snyder G. F., Brodwin M., Mancone C. M., Zeimann G. R., Stanford S. A., Gonzalez A. H., Stern D., Eisenhardt P. R. M., Brown M. J. I., Dey A., Jannuzi B., Perlmutter S., 2012. *ApJ*, **756**, 114.

Sobral D., Smail I., Best P. N., Geach J. E., Matsuda Y., Stott J. P., Cirasuolo M., Kurk J., 2013. *MNRAS*, **428**, 1128.

Songaila A., Cowie L. L., Hu E. M., Gardner J. P., 1994. *ApJS*, **94**, 461.

Spergel D. N., Verde L., Peiris H. V., Komatsu E., Nolta M. R., Bennett C. L., Halpern M., Hinshaw G., Jarosik N., Kogut A., Limon M., Meyer S. S., Page L., Tucker G. S., Weiland J. L., Wollack E., Wright E. L., 2003. *ApJS*, **148**, 175.

Spitler L. R., Labbé I., Glazebrook K., Persson S. E., Monson A., Papovich C., Tran K.-V. H., Poole G. B., Quadri R., van Dokkum P., Kelson D. D., Kacprzak G. G., McCarthy P. J., Murphy D., Straatman C. M. S., Tilvi V., 2012. *ApJL*, **748**, L21.

Springel V., White S. D. M., Tormen G., Kauffmann G., 2001. *MNRAS*, **328**, 726.

Springel V., White S. D. M., Jenkins A., Frenk C. S., Yoshida N., Gao L., Navarro J., Thacker R., Croton D., Helly J., Peacock J. A., Cole S., Thomas P., Couchman H., Evrard A., Colberg J., Pearce F., 2005. *Nature*, **435**, 629.

Stanford S. A., Eisenhardt P. R., Dickinson M., 1998. *ApJ*, **492**, 461.

Stanford S. A., Eisenhardt P. R., Brodwin M., Gonzalez A. H., Stern D., Jannuzi B. T., Dey A., Brown M. J. I., McKenzie E., Elston R., 2005. *ApJL*, **634**, L129.

Stanford S. A., Brodwin M., Gonzalez A. H., Zeimann G., Stern D., Dey A., Eisenhardt P. R., Snyder G. F., Mancone C., 2012. *ApJ*, **753**, 164.

Stanford S. A., Gonzalez A. H., Brodwin M., Gettings D. P., Eisenhardt P. R. M., Stern D., Wylezalek D., 2014. *ApJS*, **213**, 25.

Steidel C. C., Adelberger K. L., Shapley A. E., Erb D. K., Reddy N. A., Pettini M., 2005. *ApJ*, **626**, 44.

Sunyaev R. A., Zeldovich Y. B., 1972. *Comments on Astrophysics and Space Physics*, **4**, 173.

Tanaka M., Finoguenov A., Ueda Y., 2010. *ApJL*, **716**, L152.

Taylor M. B., 2005. In: *Astronomical Data Analysis Software and Systems XIV*, 29, eds Shopbell P., Britton M., Ebert R.

Terlevich A. I., Forbes D. A., 2002. *MNRAS*, **330**, 547.

Tozzi P., Santos J. S., Jee M. J., Fassbender R., Rosati P., Nastasi A., Forman W., Sartoris B., Borgani S., Boehringer H., Altieri B., Pratt G. W., Nonino M., Jones C., 2015. *ApJ*, **799**, 93.

Tran K., Papovich C., Saintonge A., Brodwin M., Dunlop J. S., Farrah D., Finkelstein K. D., Finkelstein S. L., Lotz J., McLure R. J., Momcheva I., Willmer C. N. A., 2010. *ApJL*, **719**, L126.

Tran K.-V. H., Nanayakkara T., Yuan T., Kacprzak G. G., Glazebrook K., Kewley L. J., Momcheva I., Papovich C. J., Quadri R., Rudnick G., Saintonge A., Spitler L. R., Straatman C., Tomczak A., 2015. *ApJ*, **811**, 28.

Trenti M., Bradley L. D., Stiavelli M., Shull J. M., Oesch P., Bouwens R. J., Muñoz J. A., Romano-Diaz E., Treu T., Shlosman I., Carollo C. M., 2012. *ApJ*, **746**, 55.

Urry C. M., Padovani P., 1995. *PASP*, **107**, 803.

Valentinuzzi T., Fritz J., Poggianti B. M., Cava A., Bettoni D., Fasano G., D'Onofrio M., Couch W. J., Dressler A., Moles M., Moretti A., Omizzolo A., Kjærgaard P., Vanzella E., Varela J., 2010. *ApJ*, **712**, 226.

van Breukelen C., Simpson C., Rawlings S., Akiyama M., Bonfield D., Clewley L., Jarvis M. J., Mauch T., Readhead T., Stobbart A.-M., Swinbank M., Watson M., 2009. *MNRAS*, **395**, 11.

van der Burg R. F. J., Muzzin A., Hoekstra H., Lidman C., Rettura A., Wilson G., Yee H. K. C., Hildebrandt H., Marchesini D., Stefanon M., Demarco R., Kuijken K., 2013. *A&A*, **557**, A15.

van Dokkum P. G., Franx M., 2001. *ApJ*, **553**, 90.

van Dokkum P. G., Franx M., Kelson D. D., Illingworth G. D., Fisher D., Fabricant D., 1998. *ApJ*, **500**, 714.

Vandame B., 2004. *PhD Thesis, Nice University, France*.

Vanderlinde K., Crawford T. M., de Haan T., Dudley J. P., Shaw L., Ade P. A. R., Aird K. A., Benson B. A., Bleem L. E., Brodwin M., Carlstrom J. E., Chang C. L., Crites A. T., Desai S., Dobbs M. A., Foley R. J., George E. M., Gladders M. D., Hall N. R., Halverson N. W., High F. W., Holder G. P., Holzapfel W. L., Hrubes J. D., Joy M., Keisler R., Knox L., Lee A. T., Leitch E. M., Loehr A., Lueker M., Marrone D. P., McMahon J. J., Mehl J., Meyer S. S., Mohr J. J., Montroy T. E., Ngeow C.-C., Padin S., Plagge T., Pryke C., Reichardt C. L., Rest A., Ruel J., Ruhl J. E., Schaffer K. K., Shirokoff E., Song J., Spieler H. G., Stalder B., Staniszewski Z., Stark A. A., Stubbs C. W., van Engelen A., Vieira J. D., Williamson R., Yang Y., Zahn O., Zenteno A., 2010. *ApJ*, **722**, 1180.

Venemans B. P., Röttgering H. J. A., Miley G. K., van Breugel W. J. M., de Breuck C., Kurk J. D., Pentericci L., Stanford S. A., Overzier R. A., Croft S., Ford H., 2007. *A&A*, **461**, 823.

von der Linden A., Wild V., Kauffmann G., White S. D. M., Weinmann S., 2010. *MNRAS*, **404**, 1231.

Vulcani B., Marchesini D., De Lucia G., Muzzin A., Stefanon M., Brammer G. B., Labbé I., Le Fèvre O., Milvang-Jensen B., 2016. *ApJ*, **816**, 86.

Weinmann S. M., Kauffmann G., van den Bosch F. C., Pasquali A., McIntosh D. H., Mo H., Yang X., Guo Y., 2009. *MNRAS*, **394**, 1213.

Williams R. J., Quadri R. F., Franx M., van Dokkum P., Labbé I., 2009. *ApJ*, **691**, 1879.

Willis J. P., Clerc N., Bremer M. N., Pierre M., Adami C., Ilbert O., Maughan B., Maurogordato S., Pacaud F., Valtchanov I., Chiappetti L., Thanjavur K., Gwyn S., Stanway E. R., Winkworth C., 2013. *MNRAS*, **430**, 134.

Wilson G., Muzzin A., Yee H. K. C., Lacy M., Surace J., Gilbank D., Blindert K., Hoekstra H., Majumdar S., Demarco R., Gardner J. P., Gladders M. D., Lonsdale C., 2009. *ApJ*, **698**, 1943.

Wylezalek D., Galametz A., Stern D., Vernet J., De Breuck C., Seymour N., Brodwin M., Eisenhardt P. R. M., Gonzalez A. H., Hatch N., Jarvis M., Rettura A., Stanford S. A., Stevens J. A., 2013. *ApJ*, **769**, 79.

Wylezalek D., Vernet J., De Breuck C., Stern D., Brodwin M., Galametz A., Gonzalez A. H., Jarvis M., Hatch N., Seymour N., Stanford S. A., 2014. *ApJ*, **786**, 17.

Zeimann G. R., Stanford S. A., Brodwin M., Gonzalez A. H., Snyder G. F., Stern D., Eisenhardt P., Mancone C., Dey A., 2012. *ApJ*, **756**, 115.

Zeimann G. R., Stanford S. A., Brodwin M., Gonzalez A. H., Mancone C., Snyder G. F., Stern D., Eisenhardt P., Dey A., Moustakas J., 2013. *ApJ*, **779**, 137.